Proceedings of International Symposium

FORGES 2008

Forecasting of the Radiation and Geomagnetic Storms by networks of particle detectors

Nor-Amberd, Armenia

September 29-October 3

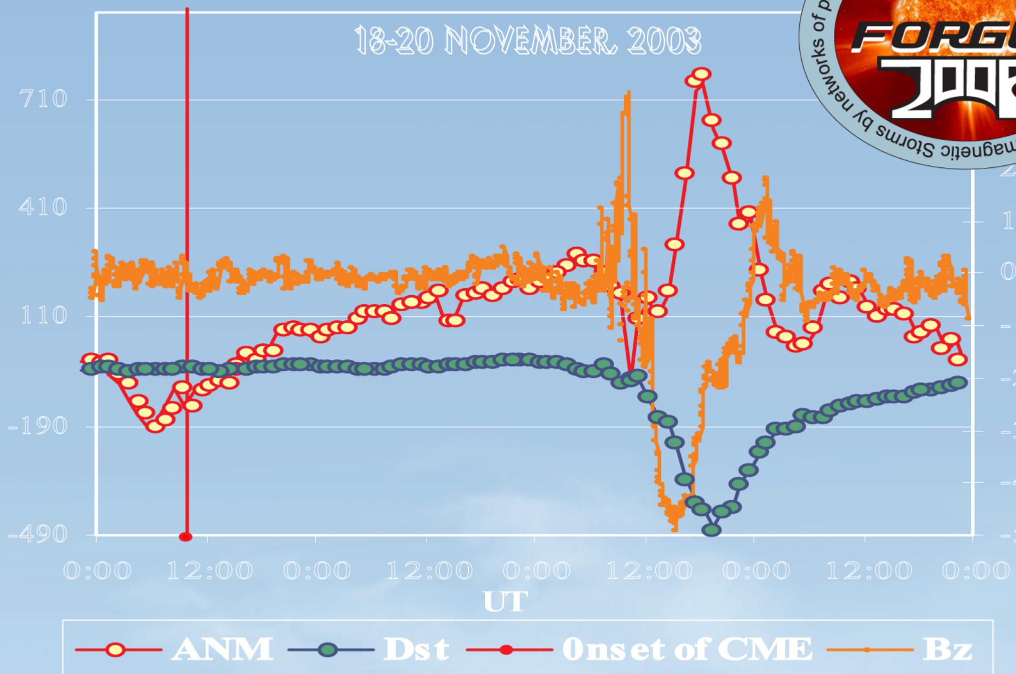

Edited by A. Chilingarian

Cosmic Ray Division,

Alikhanyan Physics Institute

Artem Alikhanyan, Sketched by Arto Chakmakchyan

The Book of Proceedings is dedicated to centennial of Artem Alikhanyan (1908-1978), the founder of Yerevan Physics Institute and the initiator of high-energy physics schools in Nor–Amberd where FORGES-2008 was held.

Proceedings of International Symposium

FORGES 2008

Forecasting of the Radiation and Geomagnetic Storms by networks of particle detectors

Nor-Amberd, Armenia
September 29-October 3

Edited by A. Chilingarian

Cosmic Ray Division, Alikhanyan Physics Institute

Published by CRD
Cosmic Ray Division, Alikhanyan Physics Institute,
Alikhanyan Brothers Street 2, Yerevan, Armenia

Printed by **TIGRAN METS**
2, Arshakouniats Avenue, Yerevan, Armenia
Tel. (37410) 521 775

ISBN ?? – ? – ??– ? July 2009

Copies 150
Pages ???

INTERNATIONAL SCIENTIFIC ADVISORY COMMITTEE

Joe Kunches,
Space Weather Prediction Center, NOAA, USA
Joseph.Kunches@noaa.gov

Michail Panasuk,
MSU, Russia
panasyuk@sinp.msu.ru

Nat Gopalswami,
NASA GSFC, USA
gopals@ssedmail.gsfc.nasa.gov

Karel Kudela,
Institute of Experimental Physics, Slovakia
kkudela@upjs.sk

Rainer Hippler,
University of Greifswald, Germany
hippler@physik.uni-greifswald.de

Hartmut Gemmeke,
Research Center Karlsruhe, Germany,
Hartmut.Gemmeke@ipe.fzk.de

Helene Mavromichalaki,
National & Kapodistrian University of Athens, Greece
emavromi@phys.uoa.gr

Lev Dorman,
Israel Cosmic Ray Center
lid@physics.technion.ac.il

Vahe' Petrosian,
Stanford University, USA
vahe@astronomy.stanford.edu

Valery Karepanov,
Lviv Centre of Institute of Space Research, Ukraine
vakor@isr.lviv.ua

Ashot Chilingarian,
Cosmic Ray Division of Alikhanian Physics Institute, Armenia
chili@aragats.am

Caro Lucas,
Tehran University, Iran,
lucas@mail.ipm.ir

Vahe Peroomian,
University of California, Los Angeles, USA
vahe@igpp.ucla.edu

Preface

The International Workshop: “Forecasting of Radiation and Geomagnetic Storms by networks of particle detectors” (FORGES-2008) was held from 29 September to 3 October, 2008 in the International Conference Center in Nor Amberd, Armenia, 40 km from Armenia's capital Yerevan. The foci of the meeting were the drivers of space weather and the possibility that the networks of particle detectors can provide warning of impending severe radiation and geomagnetic storms. Some 40 scientists and students from Germany, Italy, Great Britain, Croatia, Greece, Ukraine, Russia, USA, Costa-Rica and Armenia listened to eight invited lectures and 25 original Papers covering the following topics:

(I) The Physics of the Interplanetary Coronal Mass Ejections (ICME), their origin and propagation in the interplanetary space and interaction with the cosmic rays and the magnetosphere; modulation effects posed on the galactic cosmic rays; classification of the geomagnetic storms (GMSs). The aims of these papers were to explore in detail the characteristics of the Solar flares (SF) and ICMEs, and the conditions of the Interplanetary Magnetic Field (IMF) and of Magnetosphere that lead to severe GMSs; as well as to discuss which combination of SF, ICME, and IMF parameters unleash severe geomagnetic storms.

(II) Characteristics of ground-based networks of particle detectors; experimental methods of measuring count rates and energies of secondary cosmic rays; the efficiency of detecting various species of secondary cosmic rays, detection of the most important solar transient events of the 23rd solar activity cycle; recommendations for the further development of the Aragats Space Environmental Center (ASEC). These presentations focused on the location and design of particle detector networks required for the early recognition of approaching ICME “patterns”. These patterns should reflect the size, direction and “frozen” magnetic field in ICMEs. Registering simultaneously charged and neutral fluxes of secondary cosmic rays with particle detectors located at different latitudes and longitudes can help solve this extremely difficult problem.

(III) Mathematical methods of the prediction; feature selection; Bayesian and Neural Network models of interpolation and extrapolation; multivariate regression methods. For solving the forecasting problems, most convenient are multivariate nonparametric models, trained on the data bases of recorded geomagnetic storms with all related solar and geophysical parameters. The key problem is the selection of the optimal feature subset for prediction.

(IV) Training. The UN Office of Outer Space Affairs and the International Heliophysical Year (IHY) has launched a small instrument programme as one of UN’s Basic Space Science (UNBSS) activities. A network of particle detectors located at middle to low latitudes, the Space Environmental Viewing and Analysis Network (SEVAN) aims to improve the fundamental research on particle acceleration in the vicinity of the Sun and space environment conditions. First SEVAN modules are being tested at the Aragats Space Environmental Center in Armenia. The network grows in 2008 with detectors deployed in Croatia and Bulgaria. In 2009 SEVAN detectors are to be installed in Slovakia and India.

Research groups from Croatia and Costa-Rica were introduced to the SEVAN detector operation and data analysis. During numerous discussions, the answers to the main topic of the workshop and recommendation to ASEC development materialized in the following statements.

The key issue of the Space Weather (SW) research is to seek a better understanding of the physics of the most energetic process on the Sun, the mechanism of propagation of the ICME in the interplanetary space and its interactions with magnetosphere. The excellent facilities of the ongoing and planned space missions will bring direct information about processes on the Sun and in vicinity of the Earth. Secondary fluxes of elementary particles measured on the Earth’s surface provide compatible information on highest energy solar cosmic rays and on the modulation effects solar activity poses on the ambient population of the galactic cosmic rays.

Particle detectors located at the Aragats Space Environmental Center (ASEC) measure charged and neutral secondary fluxes and access wide energy domain of the primary cosmic rays. The planned SEVAN particle detectors network will also measure different components of secondary cosmic rays at different latitudes longitudes and altitudes. Such networks, one located in one place and the others distributed world-wide, can be used for intercalibration and to provide detailed information on transient solar events (Forbush decreases, Geomagnetic Storms, Ground Level Enhancements) and detect precursors of approaching Geomagnetic and Radiation storms.

Taking into account the importance of measurement of electromagnetic fields for monitoring space particles fluxes, it was recommended that special funds be made available for the installation of electromagnetic stations at the Nor Amber and Aragats observatories.

Ashot Chilingarian
Yerevan Physics Institute

Table of Contents

I. Physics of the Interplanetary Coronal Mass Ejections (ICME), their Propagation in the Interplanetary Space and Interaction with Cosmic Rays and Magnetosphere; Modulation Effects Posed on the Galactic Cosmic Rays; Classification of the Geomagnetic Storms (GMS).

Cosmic Ray Transmissivity in Variable Magnetosphere

K. Kudela

Department of Space Physics, Institute of Experimental Physics, SAS,
Watsonova 47, 04001 Košice, Slovakia
(e-mail: kkudela@kosice.upjs.sk)

Abstract: Selected results of computations of variable transmissivity of the magnetosphere for cosmic rays are presented. The long term variability of cosmic ray flux accessing the atmosphere indicates the increase of the global transmission function over past 2000 years, but its description is limited by the available models for the past period. At some positions the cut-off rigidity was steadily increasing while at another positions it was decreasing. During strong geomagnetic storms different models of external geomagnetic field provide different estimates of the time profile of cut-off rigidity decrease and of the asymptotic directions. At neutron monitor energies the measurements are affected by superposition of the interplanetary anisotropy and of the changes in magnetospheric transmissivity. For purposes of checking the validity of different geomagnetic field models during the strong geomagnetic storms by the network of neutron monitors at low and middle latitudes, the estimates based on interpolation of anisotropy at high energies (muon telescope network) and at low energies (neutron monitors at high latitudes) can be useful.

1. INTRODUCTION

Classification of charged particles in the magnetosphere of the Earth can be done according to characteristic dimensions of their trajectories (d–curvature radius or Larmor radius) with respect to the dimension of magnetosphere (dm)or to Stormer length(ls),

$$l_s = (\mu_o M \left|q\right| / (4\pi m v))^{1/2}$$

where $M=8.1.\ 10^{22} A.m^2$ is the moment of the Earth's magnetic dipole, *m,v* are mass and velocity of particle with the charge *q*. Within the magnetosphere there occur the charged particles in wide energy range from plasma particles up to cosmic rays with high energy (Falthammar, 1973).

On one end there are particles satisfying clearly the condition $d_m << l_s$. Their trajectory can be suitably described using the guiding center system (GCS) approach with the drift of first two orders (Schulz and Lanzerotti, 1974) and the three adiabatic invariants related to three cyclic motions, e.g. for trapped particles to the gyromotion, bounce and azimuthally drift. This approximation provides the information about the motion of the guiding center, not on the phases of the cyclic motions. When the particle "feels" the changes of the outer magnetic field on the time scale of one of the periodicities, the resonance leads to the violation of the invariance of the corresponding adiabatic invariant due to wave-particle interaction. The GCS is limited to the case when the three periodicities of the cyclic motions are very different from each other.

When this condition is not satisfied, the trajectory tracing is probably the only approach to understand the "fate" of the particle within the magnetosphere. This is the case (fig.6. in the book by Schulz and Lanzerotti, 1974) of the outer magnetosphere for the protons with kinetic energy of several hundreds MeV. This is the other extreme case, the trajectories of typical cosmic rays. The simplest estimate of the cut-off rigidity is the Stormer cut-off. Below that the direct access for any proton from outside the field to the given point in vicinity of the dipole from the given direction is forbidden (Cooke et al., 1991). The estimate is restricted to the dipolar field and no shadow of the Earth body for the trajectories.

The trajectory tracing is well known procedure which was used for the first time in sixties-seventies of the last century (e.g. McCracken, Rao and Shea, 1962; Shea and Smart, 1970; Smart and Shea, 1975). The set of differential equations describing trajectory of particle in static magnetic field is solved by numerical techniques, starting from the point of observation with reversing the charge sign and the vector of arrival to the border of magnetosphere where the asymptotic directions are obtained for allowed trajectories. System of allowed and forbidden trajectories is computed assuming the presence of the Earth's body in given geomagnetic field. There are several numerical integration techniques used. Here we use the technique described by Kassovicova and Kudela (1998) and by Bobik (2001).

The access of cosmic rays of various energies at different times to different sites on the Earth is important knowledge for space weather studies utilizing ground based system of detection of secondary cosmic rays (described e.g. by Chilingarian and Reymers, 2008; De Witt, Chilingarian and Karapetyan, 2008; Storini, 2006; Mavromichalaki et al., 2005; Kudela et al., 2000 among others) as well as for the satellite measurements of high energy particles especially at low polar orbits. In the next two sections we illustrate the different long term and short term changes of conditions for the cosmic ray access to the Earth using the selected available geomagnetic field models. The question how to approach to the testing of the validity of geomagnetic field models during strong disturbances is shortly discussed.

2. LONG TERM VARIATIONS OF GEOMAGNETIC CUT-OFFS

The long term variations of cosmic rays are important for studies of solar terrestrial environment (e.g. Usoskin, 2004; 2008; Storini, Metteo and Moreno, 2008). The estimates of cutoffs depend on the precision of the knowledge of geomagnetic field in the past. For simplicity we will discuss only vertical cutoff changes. There are positions on the Earth where the geomagnetic cut-offs are changing over past century more dramatically than in another positions and the changes at different positions are of opposite directions (decreasing or increasing the cutoff).

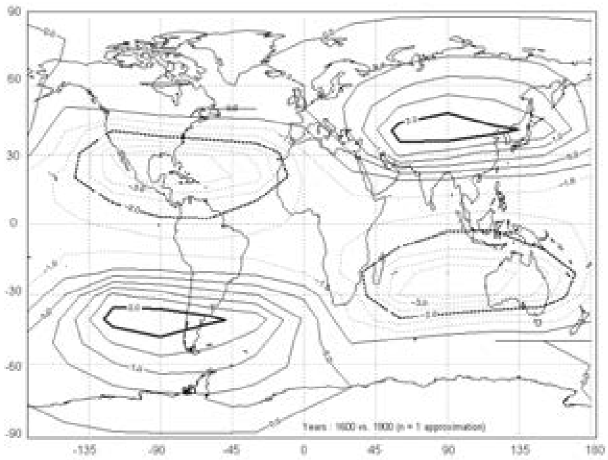

Figure 1. Contours of the change in vertical effective cutoff rigidity between years 1600 and 1900 by trajectory computations using dipolar field (according to the model by Bloxham and Jackson (1992).

Since 1900 there is more precise presentation of the static geomagnetic field model, IGRF. It was shown that the cut-off rigidity R can be approximated as a function of the Mc Ilwain‘s parameter L (Shea et al., 1987). First approach is $R \sim L^{-n}$, where n is approximately 2. Figure 2 shows how the L parameter evolves differently over half a century at two positions where neutron monitors are measuring.

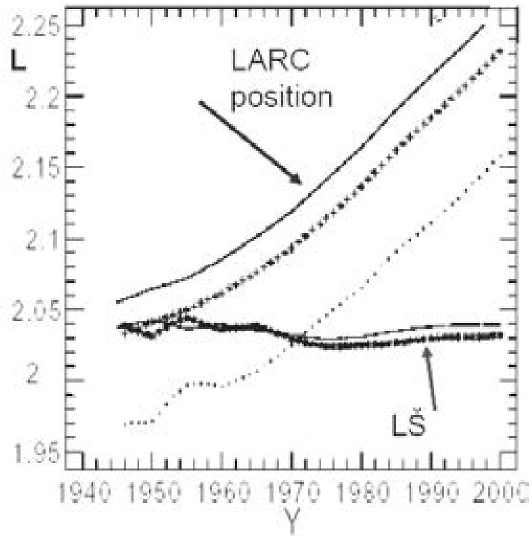

Figure 2. While around 1950 the L paramater at LARC (southern hemisphere) and Lomnicky Stit (LS) positions (northern hemisphere) were almost equal, the increase of L at LARC lead to the significant decrease of cut-off at that position over half century while at LS the cut-off was not changing much (Kudela and Storini, 2001).

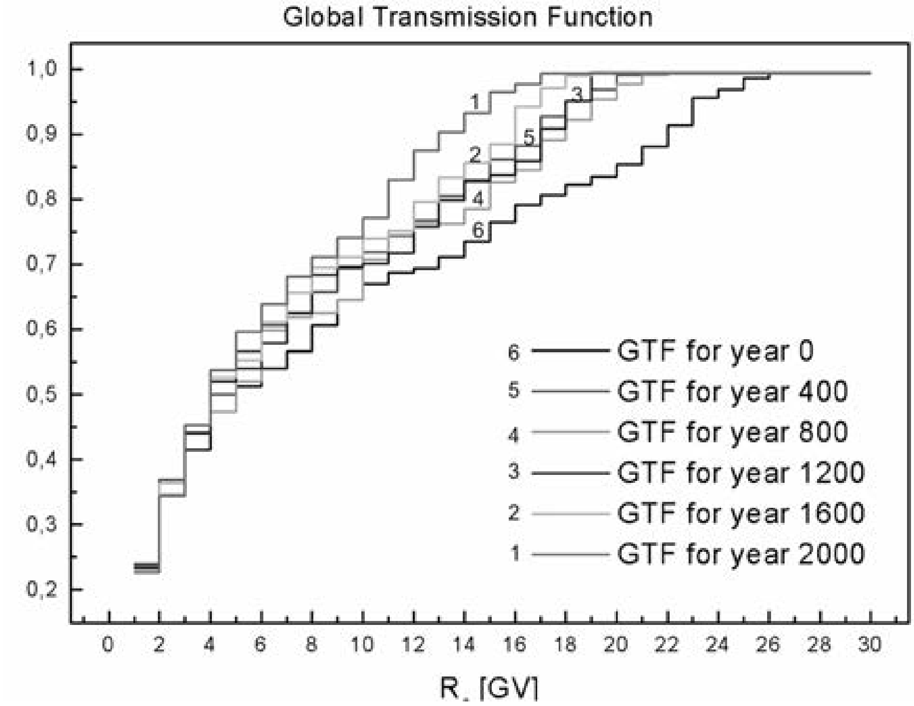

Figure 3. The „Global Transmission Function“ representing the fraction of the Earth’s surface which was exposed to galactic cosmic rays above the given rigidity was changing over long time scale. More details about the temporal evolution of vertical cutoff at different posistions at Earth can be found in paper by Kudela and Bobik (2004).

3. VARIATIONS OF GEOMAGNETIC CUT-OFFS ON SHORT TIME SCALES

For the geomagnetic field of internal sources it is straightforward to use the IGRF model available from the site http://www.ngdc.noaa.gov/IAGA/vmod/igrf.html, where the potential of the field is represented by a truncated series expansion from year 2000 to the degree of n=13. Before that the coefficient of expansion was up to 8 or 10. These coefficients and the codes of the library (http://geo.phys.spbu.ru/~tsyganenko/modeling.html and references therein) were used here for the contributions of external field sources. Kudela, Bučík and Bobík (2008) have shown how the use of different external field models is affecting (i) the transmissivity function, (ii) time of maximum of the increase at high geomagnetic cut-off neutron monitors during the Dst depression and (iii) the changes in asymptotic directions during the disturbance, if various models are used. The increases are seen during some of the geomagnetic disturbances at high cut-off stations as it is e.g. described by Zazyan and Chilingarian (2005) for the event of November 20, 2003 due to the improvement of transmissivity of the magnetosphere. Usually it is seen as superposition of the Forbush decrease with another increase close to the time of minimum Dst at middle or high cut-off stations. However it is not observed in all cases of geomagnetic storms (Miyasaka et al., 2005).

Here we illustrate the differences of expected cosmic ray access in two cases, namely in the geomagnetic storm on April 6, 2000 and that on November 7, 2004.

An important advantage of the Tsyganenko 2004 model (Tsyganenko and Sitnov, 2005) with the older models, e. g. (Tsyganenko, 1989; 1995) is that the „prehistory“ of the storm represented by the contribution of different current systems and based on IMF and solar wind before and at the beginning of the storm is taken into account.

Desorgher, Flückiger and Bütikofer (2005) studied in detail the estimates of cutoffs for the model Ts04 (Tsyganenko and Sitnov, 2005) during the storm on April 6, 2000. Kudela, Bučík and Bobík (2008) compared the predictions by models (Tsyganenko and Sitnov, 2005) and (Tsyganenko, 1995), respectively. It was indicated that the model with trajectory code used here gives expected intensity profiles at middle latitude neutron monitors consistent with the result reported earlier using the code described by McCracken, Rao and Shea (1962). For that event the Ts96 model (Tsyganenko, 1995) gives overestimation of the improved magnetospheric transmissivity if compared with neutron monitor profiles. This is illustrated in Fig. 4. Ts04 model better fits the observed profile at least at middle latitudes for the main phase.

A simple comparison of the timing of maximum increase at neutron monitors due to the improvement of magnetospheric transmissivity during the geomagnetic storms for the two storms, namely November 20-23 , 2003 and November 8, 2004 gives no clear conclusion about validity of the models with the prehistory and of the “usual” external field models. It may be of interest that even the timing of the maximum at different positions and high cut-off stations is not the same. This is illustrated in Figure 7 for the event of November 8, 2004.

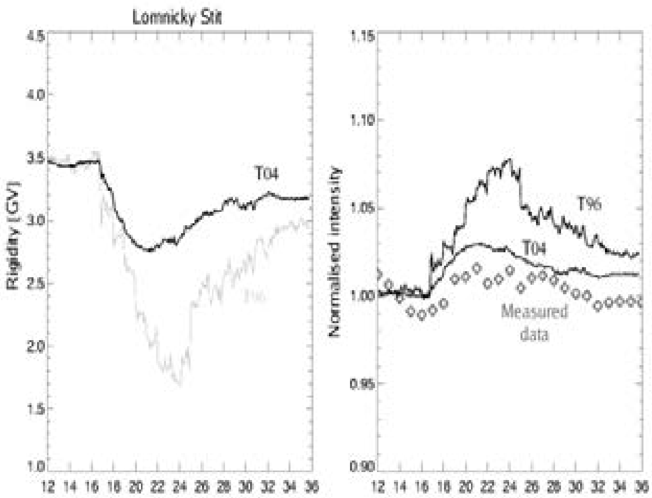

Figure 4. Ts04 model (Tsyganenko, 1995) is better fitting the observed profile at least at middle latitudes for the main phase of the storm on April 6, 2000. Both, Ts96 and Ts04 predict longer recovery phase than observed by neutron monitors. Similar comparison is obtained for Jungfraujoch. Time is in hours from 00:00 UT on April 6.

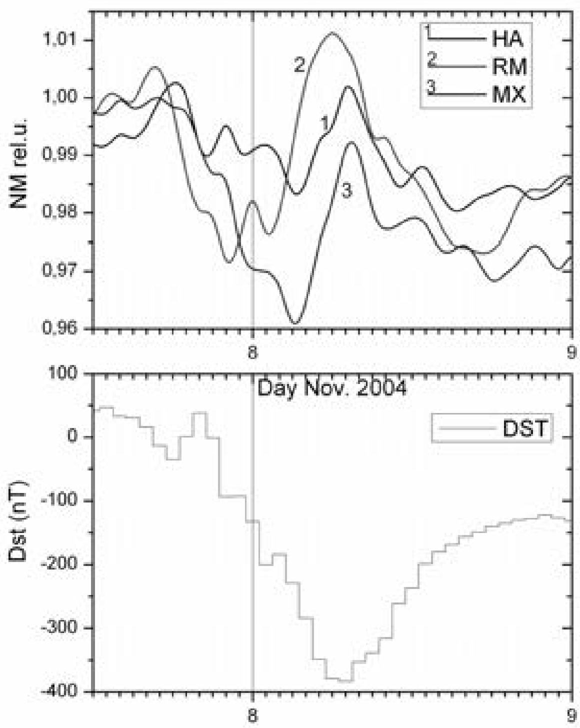

Figure 5. The smoothed (B-spline) data of neutron monitor count rates for Rome, Mexico and Haleakala and corresponding Dst for November 7-8, 2004. The normalization to unity is for the first half of November 7 for each station. The time of maximum for Rome (and similarly for other European stations) is different from those at different longitudes. There is probably some longitudinal anisotropy for the access of cosmic rays even at higher energy, which is difficult to characterise by a single universal value as Dst is.

Moreover, the structure of the allowed and forbidden trajectories affecting the access of particles is rather strongly changed during the storm and different pattern for different models used is found. Such example is in Fig.7 of the paper (Kudela, Bučík and Bobík, 2008). The difference in the asymptotic directions for the two models of the field is clearly seen from Figure 6.

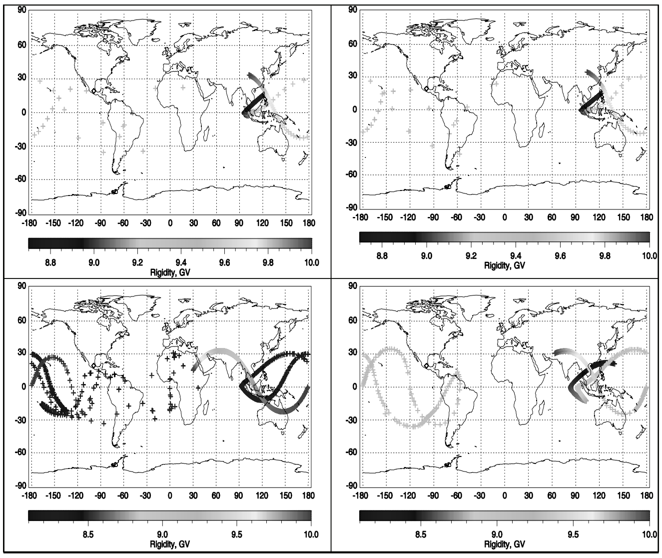

Asymptotic directions for Mexico ($R>R_U$) *before* the disturbance (*upper* panels, Nov. 7, 2004, 12 UT) and at *minimum Dst* (*lower* panels, Nov. 8, 06 UT) for Ts89+Dst model (*left*) and Ts04 model (*right*).

Figure 6. While the upper panels show consistency of the asymptotic during quiet time intervals for two different models, the asymptotic directions are quite different during the interval of minimum Dst when models (Boberg et al., 1995) and Ts04 are used. Thus, for the given anisotropy in the interplanetary space, the different responses at various neutron monitors with nominal high cutoff position is expected.

4. DISCUSSION AND CONCLUSION

The precision of the geomagnetic filter effect estimate in the past for cosmic ray access, which is related to the debates of the impact of cosmic rays on the Earth climate, depends on the available models of geomagnetic field. We illustrate the trends of the cut-off change over few centuries.

Regarding the short term changes observed by network of neutron monitors, muon telescopes and other ground based cosmic ray measurement devices, there is still much work to be done in attempt to use the extensive measurement files from different sites and epochs for checking the existing models of the geomagnetic field, especially those constructed from plenty of magnetic field measurements during the last two decades. Simple approaches like “which model gives better timing of increase and better correspondence of neutron monitor count rate profiles at different sites” are useful as case studies assuming the correct responses of neutron monitors.

However, this disregards the interplanetary anisotropy. In the energy range where neutron monitors are sensitive, there is an “overlap” of interplanetary anisotropy and anisotropy of “access of particles during the geomagnetic disturbances”, which makes the forecast of space weather effects not easy just by measurements of neutron monitors. One of the potential possibilities to overcome this problem is to use the estimates of interplanetary anisotropy at higher energies produced by muon telescope network (Munakata et al., 2000). The geomagnetic disturbances are not very strong for these high energies of primaries. On the other hand, the anisotropy obtained from the low cut-off stations for which the extent of asymptotic longitudes is rather narrow and the atmospheric cut-off is above the geomagnetic one, can give the clear low energy anisotropy of cosmic rays in interplanetary space (e.g. Spaceship Earth described by Bieber and Evenson, 1995). The interpolation of interplanetary anisotropy between these two sets of devices is worth to be checked in future studies of the question of de-convolution of the two types of anisotropies observed by the neutron monitors, for the checking of validity of external geomagnetic field models and for possibilities to use neutron monitor data for the space weather forecasts.

ACKNOWLEDGEMENT

The author wishes to acknowledge the VEGA grant Agency project 2/7063/27 for support. The PIs of the neutron monitors which data are used in paper are acknowledged.

REFERENCES

Bieber J.W., Evenson P., Spaceship Earth – an optimized network of neutron monitors. Proc. 24th ICRC, Rome, vol. 4, 1316-1319, 1995

Bloxham J., Jackson A., Time-dependent mapping of the magnetic field at the core- Mantle boundary, J. Geophys. Res., 97, 19537-19563, 1992

Boberg P.R., Tylka A.J., Adams J.H. Jr., Flückiger E.O., Kobel E., 1995. Geomagnetic transmission of solar energetic protons during the geomagnetic disturbance of October 1989, Geophys. Res. Lett., vol. 22, No 9, 1133-1136, 1995

Bobik P., PhD Thesis, 2001. University P.J. Safarik, Kosice. Cooke D.J., Humble J.E., Shea M.A., Smart D.F., Lund N., Rasmussen I.L., Byrnak B., Goret P., Petrou N., On cosmic ray cutoff terminology. Il Nuovo Cimento, 14 C, N 3, 213-233, 1991

Chilingarian A., Reymers A., Investigations of the response of hybrid particle detectors for Space Environmental Viewing and Analysis Network (SEVAN), Ann. Geophysicae, 26**,** 2, 249-257, 2008

Desorgher L., Flückiger E.O., Bütikofer R., Cosmic Ray Trajectory Tracing in various geomagnetic fiield models, IAGA, GAV06, 2005

De Wit Dudok, Chilingarian A., Karpetyan G., 2008. Techniques for characterizing weak transients in cosmic ray records, as measured by neutron monitor networks, Acta Geophysica, 07, 2008

Falthammar K.G., 1973. In Cosmical Geophysics, editors A. Egeland, O. Holter, A. Omholt, Oslo, 1973, Russian translation, 1976

http://www.ngdc.noaa.gov/IAGA/vmod/igrf.html

http://geo.phys.spbu.ru/~tsyganenko/modeling.html and references therein

Kassovicova J., Kudela K., 1998. On the computations of cosmic ray trajectories in the geomagnetic field, preprint IEP SAS, Kosice, pp. 27, May 1998

Kudela K., Storini, M., Hofer, Y., Belov, A., 2000. Cosmic ray in relation to space weather, Space Sci. Rev., 93, 153-174, 2000

Kudela, K., Storini, M., 2001. Long-term cutoff changes and L parameter at LARC neutron monitor locatiobn, Proc. ICRC, Hamburg, vol. 9, 4106, 2001

Kudela K., Bobík P., Long term variations of geomagnetic rigidity cutoffs. Solar Physics, 224(1), 423–431, 2004.

Kudela K., Bučík R., Bobík P., On the transmissivity of low energy cosmic rays in disturbed magnetosphere. Adv. Space Res., 42, 1300-1306, 2008

Kudela K., Bobík P., Bučík R., Transmissivity predictions for cosmic rays in disturbed magnetosphere: a case study, EGU2007-A-03230, 2007

Mavromichalaki H., Yanke V., Dorman L., Iucci N., Chilingaryan A., Kryakunova O., Neutron Monitor Network in Real Time and Space Weather,http://crd.yerphi.am/files/Publication/2005/2004/mavro_ESP.pdf, 2005

McCracken K.G., Rao U.R., Shea M.A., 1962. The Trajectories of Cosmic Rays in a High Degree Simulation of the Geomagnetic Field, Massachusetts Institute of Technology, Technical Report No. 77, NYO-2670, August 1962

Miyasaka, H. et al, Geomagnetic Cutoff Variation Observed with TIBET Neutron Monitor, Proc. 28th ICRC vol. 6, JP Universal Academy Press, Inc, Tsukuba, 3609–3612, 2005

Munakata K., Bieber J.W., Yasue S.-I., Kato C., Koyama M., Akahane S., Fujimoto K., Humble J.E., Duldig M.L., 2000. Precursorsof geomagnetic storms observed by the muon detector network, J. Geophys. Res., 105, 27,457, 2000

Shea M.A., Smart D.F., Secular Variations in Cosmic Ray Cutoff Rigidities. J. Geophys. Res., 75, 3921-3922, 1970

Shea M.A., Smart D.F., Gentile L.C., 1987. Estimating cosmic-ra vertical cutoff rigidities as a function of the McIlwain L – parameter for different epochs of the geomagnetic field, Phys, Earth and Planet. Interiors, 48, 200-205

Schulz M., Lanzerotti L.J., Particle diffusion in radiation belts, Springer, 1974

Smart D.F., Shea M.A., Cosmic-Ray Penumbral Effects for Selected Balloon Launching Locations, 14th International Cosmic Ray Conference, vol. 4, 1304-1308, 1975

Storini M., The relevance of cosmic rays to space and earth weather, paper at 20th ECRS, Lisbon, www.lip.pt/events/2006/ecrs/talks/192.ppt, 2006

Storini M., Metteo P., Moreno G., Effects of geomagnetic secular variations on cosmic ray access to the terrestrial environment. Advances in Space Research Vol. 41, Issue 1, 70-75, 2008

Tsyganenko N.A. and Sitnov M.I., Modeling the dynamics of the inner magnetosphere during strong geomagnetic storms, J. Geophys. Res., 110, A032208, doi:10.1029/2004JA010798, 2005

Tsyganenko N. A., A magnetospheric magnetic field model with a warped tail current Sheet, Planet. Space Sci., v.37(1), 5-20, 1989

Tsyganenko N.A., Modeling the Earth's magnetosphereic magnetic field confined within a realistic magnetopause, J. Geophys. Res., 100, No A4, 5599-5612, 1995

Usoskin I., Long-Term Variations of Cosmic Rays and Terrestrial Environment. In: Frontiers of Cosmic Ray Science, (eds..Kajita T., Asaoka Y., Kawachi A., Matsubara Y., Sasaki M.), Universal Academy Press, Tokyo, p.205-228, 2004

Usoskin, I., History of Solar Activity over Millennia, Living Rev. Solar Phys., 5, 3, 2008

Zazyan M., Chilingarian A., Calculation of the Aragats Space Environmental Center Monitors response to galactic and solar cosmic rays. Proc. 29th ICRC Pune, 2005

Solar 1-20 MeV Protons as a Source of the Proton Radiation Belt

L. Lazutin, Ju. Logachev, E. Muravieva

Abstract: After several strong magnetic storms of the last solar cycle (SC), the 1-20 MeV proton belt intensity was enhanced by one or two order higher than the prestorm level. Solar cosmic ray (SCR) capture is supposed to be the source of this new proton belts. Using particle measurements of the low-altitude satellites we summarize findings of particle trapping and acceleration mechanisms and the lifetime of the enhanced proton belt. Approximation of the measurements onto the last three solar cycles shows that the classical mechanism of the proton belt creation by slow radial diffusion is dominating only half of a cycle time. On the other half the proton belt enhanced population was created by solar protons. We conclude that existing radiation belt model must be revised, which is important for the radiation belt physics and space weather applications.

1. INTRODUCTION

Extreme magnetic storms at the end of the last solar cycle have revived interest to the problem of the contribution of solar protons with energy of 1-20 MeV into Earth's radiation belts. At a quiet magnetosphere the penetration boundary of solar protons with energy up to 100 MeV is limited to field lines with L ≈ 5-7. During magnetic storms penetration of the boundary position decreases. So, for several magnetic storms the SCR penetration boundary into the magnetosphere was just at L=2-3 and after a storm the outer proton belt was renewed, intensified and there are no doubts that the SCR are sources of this new proton population. There are different explanations of process of SCR capture. More widespread model is based on radial injection and additional acceleration of particles during the moment of SC (Blake et al., 1992, Pavlov et al., 1993, Hudson et al., 1997). The model of a direct transition of SCR protons to the closed drift shells on a recovery phase of a magnetic storm without injection (Lazutin et al., 2006, 2007) was offered in the work reported and published in the proceedings of the previous conference in Nor-Amberd in 2005. Continuation of this work has brought in new results. First, it was found, that additional acceleration of trapped protons before the end of a storm or a series of storms took place so that the new belt of 1-20 MeV has intensity in 2-3 order higher than a normal one. Secondly, it became clear, that the new belt is concerved much longer, than we assumed earlier and by that SCR contribution to the proton belt can be rather essential in comparison with the traditional mechanism of radial diffusion, and in some intervals it can be dominating. Thus, existing model of the outer proton belt formation based on the mechanism of radial transport of particles from the auroral magnetosphere into the inner magnetosphere require revision, which is important as well for space weather applied models of radiation in near space.

2. CHARACTERISTICS OF SCR BELTS

Reports on possible contribution of SCR in the proton belt have appeared since 80th years (Mineev et al., 1983, Pavlov et al., 1993), but there were no necessary information, to estimate mechanism and duration of existence of the solar protons belt. New data have appeared in a number of publications of the last decade (Lorentzen et al., 2002, Slocum et al., 2002) confirming the solar origin of a new belts.

Results of the analysis of solar proton radial structures of by measurements on low-altitude satellites CORONAS-F and SERVIS-1 during strong storms of 2001-2004 have shown, that, at least in five storms there were real captures of SCR protons. In table 1 we give characteristics of SCR belts by publications in the works (Lazutin et al. 2008, Hasede et al., 2008).

Table 1

Data, Tmin,	UT	Dst	Lmin
06.11.2001	07	-292	2.2
24.11.2001	17	-221	2.4
29.10.2003	10	-180	2.6
30.10.2003	01	-363	2.2
30.10.2003	23	-401	2.0
22.07.2004	03	-101	3.2
25.07.2004	12	-148	2.9
27.07.2004	14	-197	2.6
08.11.2004	07	-373	2.3
10.11.2004	10	-289	2.1

Fig. 1 shows an example of the measurement of proton radial profiles before the beginning of the magnetic storm on October, 29, 2003 and on the recovery phase of the last storm of a series as measured at the longitude of the Brazilian Magnetic Anomaly. The dashed line shows a profile in the maximum of the main phase of the last storm, indicating the depth of SCR protons penetration. The first profile has classical structure with a maximum at L=3. The last profile has an increased intensity and it is shifted to L=2.4, that supposes capture of SCR protons that had penetration boundary at L =2.

Analysis of protons capture development during the chain of magnetic storms on July 23-27, 2004 allows to found consecutive acceleration of the trapped protons caused by the radial shift or diffusion of protons toward the Earth, (Kuznetsov et al. 2008). Relativistic electron acceleration at the magnetic storm recovery phase was known for years, while similar simultaneous solar proton acceleration inside the magnetosphere has been registered for the first time. The same effect was observed during the magnetic storm on November 7-12, 2004.

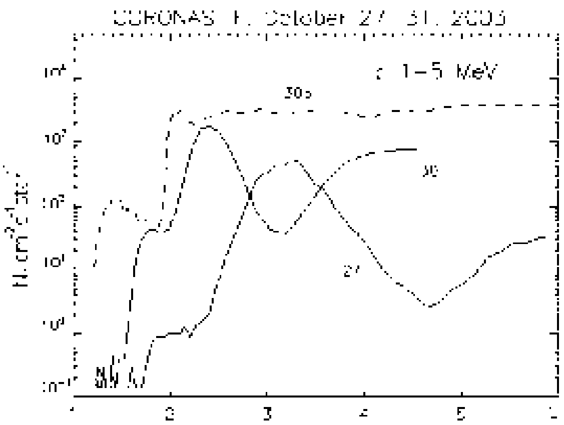

Figure 1. Radial profiles of the 1-5 MeV protons measured by KORONAS-F before and after the October 2003 magnetic storms over Brazilian Magnetic Anomaly. By brocken line radial profile with maximal approach to the Earth of the proton penetration boundary is shown.

Fig. 2 presents radial structures of protons with energy of 12.5 MeV measured on SERVIS-1 at altitude of 1000 km which is twice higher than altitude of CORONAS-F satellite. The flux of protons before the storm at L=2.9 was a bit more than the background level, but after the first storm the flux of trapped protons increases by two order, and after the second storm - again 30 times. Accordingly the maximum of a new proton belt was displaced closer to the Earth at first to L = 2.8 and after that to L = 2.4-2.6. Similar transformation undergo protons with energy of 1 MeV , though total intensity increase was lower.

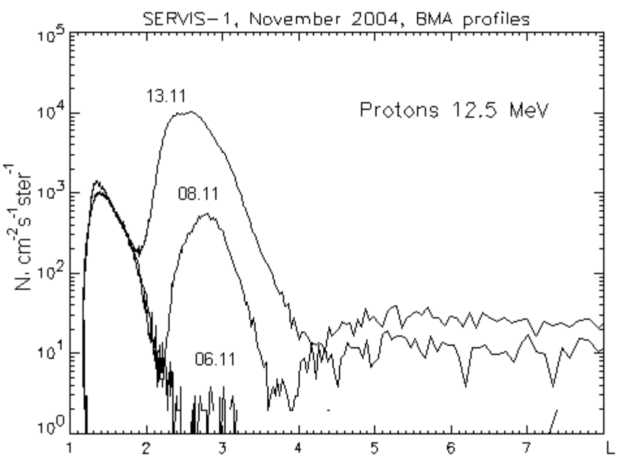

Figure 2. Radial profiles of the 12.5 MeV protons measured by SERVIS-1on November 07, 08 u 11 2004.

Displacement of the maximum of the proton belt toward the Earth was observed also during a storm on 20.11.2003. There were no SCR protons in the vicinities of the Earth, and, accordingly, there were no new capture to the proton belt, however the belt, formed during a storm on October 29, has moved from L=2.1 to L=1.9, and proton intensity at the maximum has increased twice (Lazutin et al. 2006).

3. LIFETIME OF SCR PROTONS BELTS

Fig. 3 shows an example of change of protons intensity after the capture and acceleration during July, 2004 storms (Hasebe et al., 2008). The capture effect was observed in two energy channels. Only the 24 MeV channel increase during the storm was caused by the approach of penetration boundary to L<3, so the flux of particles equal to a flux in interplanetary space was measured and right after the end of a storm it returned to the pre-storm level.

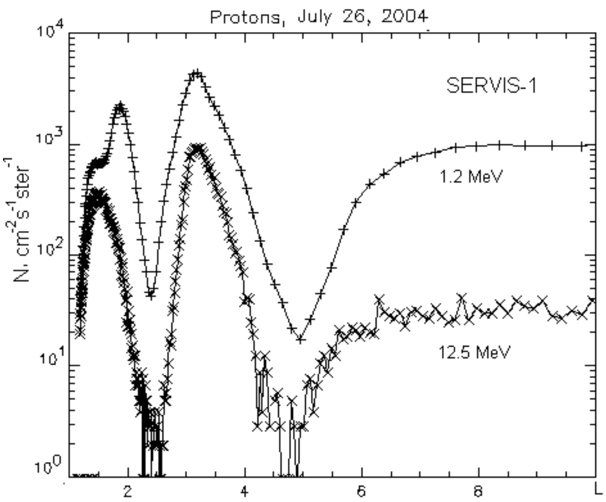

Figure 3. Temporal evolution of the proton intensity after November 22-27, 2004 magnetic storm. Daily maximum intensities at L=3 are shown.

The particles flux in new SCR proton belts decreases at first rather quickly, probably caused by excitation of ion-cyclotron instability, then, after 10-15 day protons flux becomes insufficient for excitation of instability and the diffusion passes in the slow mode. As a result the increased protons flux remains within weeks and months, depending on energy of particles and a drift shell distance from the Earth. From the presented example one can see that in three months the 12.5 MeV protons fluxes come back to a normal level, and the flux of 1 MeV protons remains at a level that exceed the quiet level by an order. On deeper shells the decay of SCR belt went even more slowly.

At the analysis of a temporal variations of the proton belt formed 30-31.10.2003 it was found that new proton belt at L = 1.9-2.1 kept intensity constant prior to the beginning of the storm of 20.12.2003, and then intensity started to decrease, and for 2 months a flux 1 MeV protons decreased to the background level (Lazutin et al, 2006). Therefore from the CORONAS-F satellite data we concluded that new proton belt is not long living. However at the analysis of SERVIS-1 satellite data, launched in December 2003 at the altitude two times higher it was found out, that this October-03 belt has not disappeared, and was there more than a year.

On fig. 4 radial structures of protons of 1 and 12.5 MeV measured on July, 2004 are shown. The maximum at L = 1.5 is not real, created by penetration into detector of high energy protons of the inner proton belt. At L =3.2 there is seen SCR belt formed just during the July storm, and at L =1.8 we found old October-03 SCR belt discussed above. And half-year later, in the November event, this belt has not disappeared, but has been covered by the new SCR belt of the greater intensity. Therefore, the disappearance of enhance proton flux measured by CORONAS-F detector is a consequence of the pitch-angle redistribution.

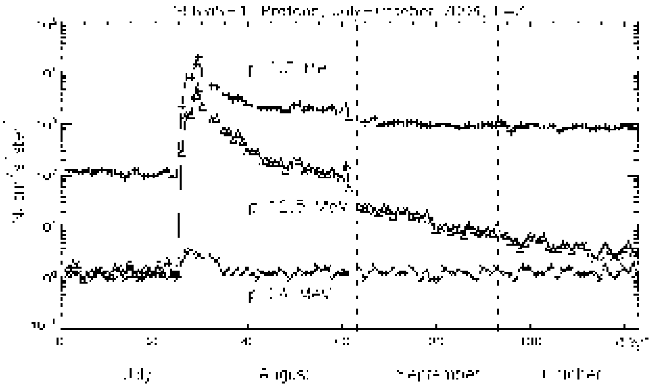

Figure 4. Radial profiles of 1.2 and 12.5 MeV protons, 26.07.2004

Results of the analysis of SCR protons belts life time allow us to assume that during strong magnetic storms with Dst_{min} < 250 nT the probability of appearance of SCR belt is great, if there are SCR protons in the vicinity of the Earth and that such belt can exist not less than a year. Fig. 5 shows the occurrence of such events since 1976 with the last 3 solar cycles indicated. As it was shown in work (Lazutin, Logachev, 2009), it is possible to expect, that during half of the cycle, from a years of the maximum to the end of a cycle, a proton belt of the Earth may be dominantly populated by SCR, and only half of a cycle - by the mechanism of radial diffusion from the auroral zone.

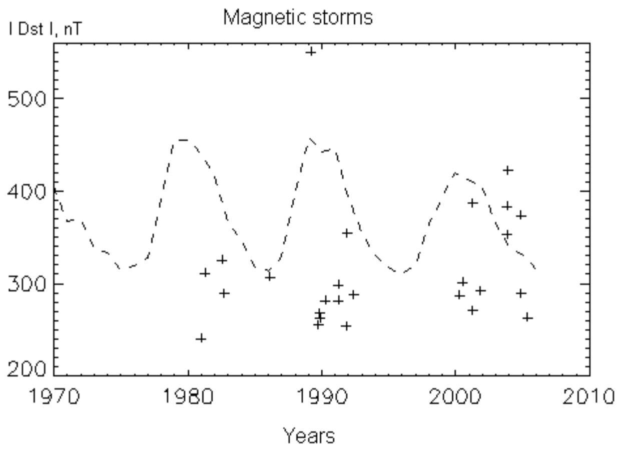

Figure 5. Occurrence of the strong magnetic storms during last three solar cycles. By broken line Wolfs numbers are shown.

4. CONCLUSION

After several strong magnetic storms of the last solar cycle, the 1-20 MeV proton belt intensity was enhanced by one or two order higher than the prestorm level. Solar cosmic ray capture is supposed to be the source of this new proton belts. Using particle measurements of the low-altitude satellites we summarize findings of particle trapping and acceleration mechanisms and the lifetime of the enhanced proton belt.

- Trapping of the SCR protons with energy of 1-20 MeV onto the closed drift shells of proton belts occurs on the recovery phase of strong magnetic storms without injection.
- In some cases additional acceleration of the new belt protons was observed after the capture.
- SCR belts in the inner magnetosphere at L=2-3 can keep the enhanced intensity level about one year and more.
- SCR capture is essential as the proton belt source about half of solar cycles.

REFERENCES

Blake J.B.,.Kolasinski W.A,,.Fillius R.W, and.Mullen E.G, Injection of electrons and protons with energies of tens of MeV into L > 4 on 24 March 1991, Geophys. Res. Lett., 19, 821, 1992.

Hasebe N., Sukurai K., Hareyama M., Lazutin L., Muravieva E., Gotselyuk Yu., Myagkova I.and Jushkov B., Variations of energetic particles in the radiation belts after the July 22-30, 2004 magnetic storms, In: “Physics of Auroral Phenomena”, Proc. XXXI Annual Seminar, Apatity, pp. 33-37, 2008

Hudson M.K. , Elkington S.R., Lyon J.G. et al. Simulations of proton radiation belt formation during storm sudden commencements, J. Geophys. Res. 102, 14087-14102, 1997.

Kuznetsov S.N, Lazutin L.L., Panasyuk M.I.,. Starostin L.I, Gotseliuk Yu.V., Hasebe N., Sukurai K. and Hareyama M., Solar particle dynamics during magnetic storms of July 23-27, J. Adv. Space Res. (2008), doi:10.1016/j.asr.2008.09.014, 2004.

Lazutin L.L., Kuznetsov S.N. and Podorolsky A.N., Solar proton belts in the inner magnetosphere during magnetic storms.Proceedings of the 2d International Symposium Solar Extreme Events: Fundamental Science and Applied Aspects, Nor-Amberd, Armenia, 2005, Ed. by Chilingarian A.and Karapetyan G., Erevan, p.63-67, 2006.

Lazutin L., Muravjeva E., Panasyuk M., Hasebe N., Sukurai K. and Hareyama M., Comparative analysis of the energetic electron and solar proton dynamics during strong magnetic storms. In: “Physics of Auroral Phenomena”, Proc. XXXI Annual Seminar, Apatity, pp. 17-21, Proceedings of Apatity-08, 2008.

Lazutin L.L., Kuznetsov S.N., and Podorolsky A.N., Dynamics of the radiation belt created by solar protons during magnetic storms, Geom. & Aeronomie, V. 47, № 2, p.187-197, 2007

Lazutin L.L., Logachev Yu.I. On the input of solar cosmic rays into the Earths proton belt creation, accepted to Geom. & Aeronomie, 2009

Lorentzen, K.R., Mazur J.E., Loper M.E., Fennell J.F., and Blake J.B., Multisatellite observations of MeV ion injections during storms, J. Geophys. Res., 107, 1231, 2002.

Mineev Yu.V., Spirkova E.S., Glukhov G.A., Kratenko Yu.P., Features of solar cosmic ray penetration into the high-latitude regions of the Earth's magnetosphere inferred from Intercosmos-19 data. Proc. of 18-th Intern. Cosmic Ray Conf., Bangalore, India, v.3 p. 262-265, 1983.

Pavlov N.N., Tverskaya L.V., Tverskoy B.A., Chuchkov E.A., Variations of the radiation belt particles during strong magnetic storm of March 24, 1991. Geomagnetism and Aeronomie 33, #6, 41-45, 1993 (in Russion).

Slocum P.L., Lorentzen K.R., Blake J.B., Fennell J.F., Hudson M.K, Looper M.D., Masson G.M., and Mazur J.E., Observations of ion injections during large solar particle events, AGU Fall Meeting, SH61A-0501, 2002.

Modulation of the Cosmic Ray Flux at the Beginning of the 24-th Solar Activity Cycle

Y. Stozhkov

Lebedev Physical Institute of the Russian Academy of Sciences,
Moscow, 119991, Leninsky Prospect, 53, Russia, (e-mail: stozhkov@fian.fian.dns.mipt.ru)

Abstract : The data on cosmic ray fluxes from the measurements in the atmosphere made at the northern and southern polar latitudes and the middle latitude in 1957 - 2008 are presented. The deep minimum in cosmic ray fluxes and solar activity observed during 2006 – present time is discussed. New idea on sunspot production is suggested and low forthcoming solar maximum is predicted.

1. INTRODUCTION

At the present time there are several sets of experimental data on the long-term modulation of cosmic ray fluxes. These sets were obtained with the neutron monitor network on the ground level, in the atmosphere (Charakhchyan et al., 1976; Stozhkov et al., 2007), and in space:RoiEi8TFar8J:voyager.jpl.nasa.gov/+Voyager1+data &hl = en&ct=clnk&cd=1).

Below the time dependences of cosmic ray fluxes observed during the present solar activity minimum are analyzed and comparison of these fluxes with ones observed in the past minima is made. The experimental data obtained in cosmic ray flux measurements in the atmosphere are mainly used.

As solar activity level defines cosmic ray flux at 1 a.u., the question on the solar activity in the new 24-th solar cycle is very important. The new idea of sunspot production was suggested by Dr. Victor Ermakov and the prediction on the new 24-th solar activity cycle based on this idea is given. It is predicted that maximal daily number of sunspot in the forthcoming solar cycle will be low, less than 30, and it is possible that we have the start of the new Maunder minimum in the solar activity.

2. EXPERIMENTAL DATA ON COSMIC RAY FLUXES

The group of researches of Lebedev Physical Institute of the Russian Academy of Sciences has made the regular measurements of cosmic ray fluxes in the atmosphere at the altitudes from the ground level up to (30 – 35) km. The standard devices (radiosonds) shown in Figure 1 have been used in these experiments (Stozhkov et al., 2007). The flux of charged particles as a function of altitude or atmospheric pressure is measured. The regular radiosond launchings are performed at the polar latitudes (northern hemisphere, geomagnetic cutoff R_c = 0.5 GV; southern hemisphere, R_c = 0.04 GV) and the middle latitude (R_c = 2.4 GV).

There are the homogeneous sets of data on cosmic ray fluxes in the Earth's atmosphere from the middle of 1957 till present time. Here we will use the cosmic ray flux values in the maximum of particle absorption curve in the atmosphere, so-called Pfotzer's maximum N_{max}. We have used the data on fluxes of particles coming to our detector from all directions, so-called omnidirectional fluxes. The experimental data are presented in Figure 2.

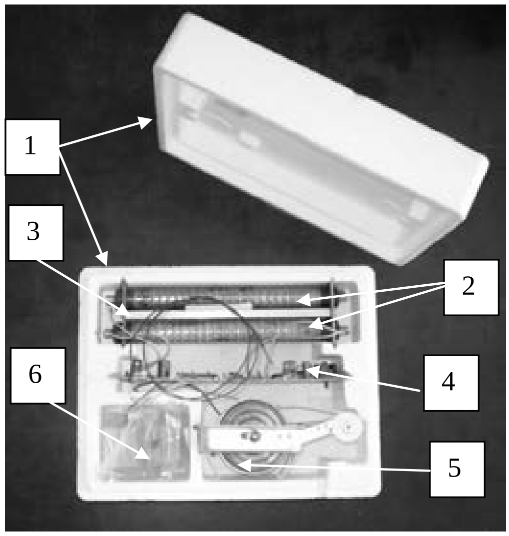

Figure 1. A standard radiosond for measurements of charged particle flux in the atmosphere: 1 – a foam plastic box; 2 – detectors of charged particles (gas-discharged counters); 3 – an aluminum plate of 7 mm thickness; 4 – electronic scheme with high voltage source and transmitter; 5 – atmospheric pressure sensor; 6 – chemical

As one can see from Figure 2 the values of geomagnetic cutoff rigidities R_c at the polar northern latitude (R_c = 0.5 GV) and at the southern one (R_c = 0.04 GV) are different. But the maximum cosmic ray fluxes N_{max} at these latitudes is recorded at the atmospheric pressure x ≈ 25 g/cm^2. Only the particles with R_c > 0.5 GV can penetrate at these depths in the atmosphere. So, in our case the residual atmospheric pressure (not the Earth's magnetic field) defines the value of cutoff for particles. Because of this, we have the same atmospheric cutoff at the northern and southern latitudes. The measurements of cosmic ray fluxes have been made almost every day and the monthly averaged values of N_{max} are presented in Figure 2.

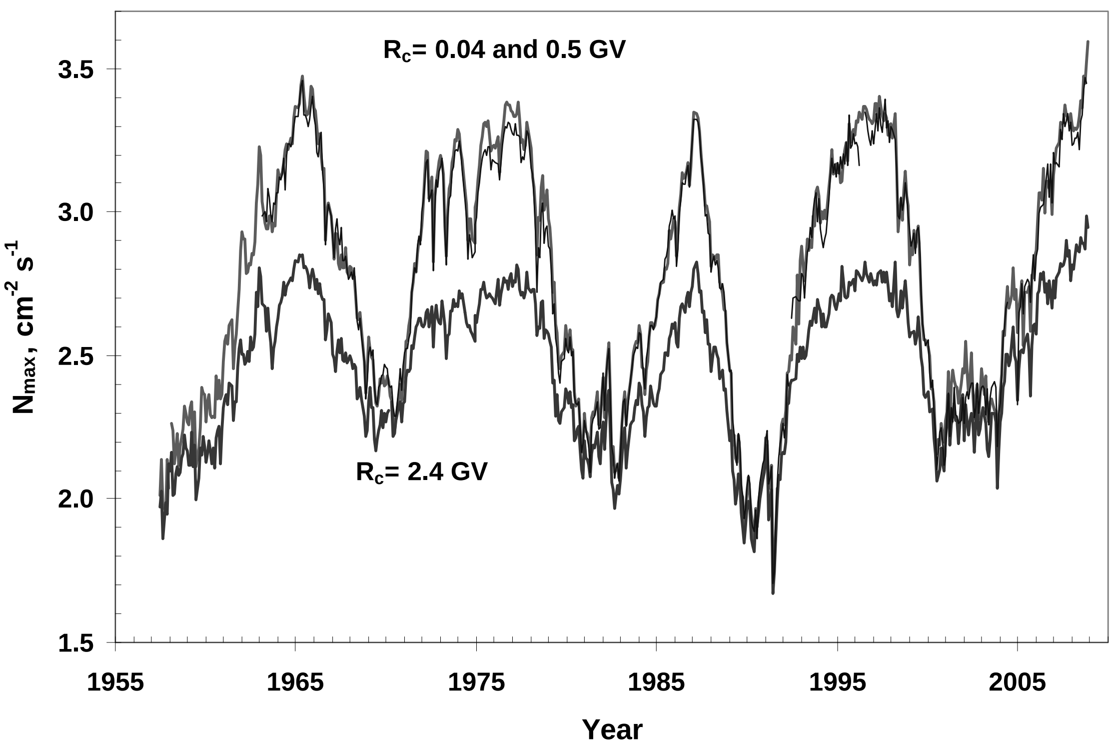

Figure 2. Time dependences of monthly averaged omnidirectional cosmic ray fluxes at the maximum of the absorption curve in the atmosphere, N_{max}, measured at the polar northern and southern latitudes (2 upper curves), and the middle northern latitude (underneath curve).

The data under discussion span the four solar activity cycles: part of the 19-th solar cycle – (1957 -1964); the 20-th solar cycle – (1964 – 1976); the 21-st solar cycle – (1976 – 1986); the 22-nd solar cycle – (1986 -1996); the 23-rd solar cycle – (1996- 2006); and the part of 24-th solar cycle – (2006 – 2008).

As one can see from Figure 2 during each cycle the large amplitude of cosmic ray modulation from solar activity minimum to maximum is observed. The amplitudes measured in the atmosphere exceed the ones inferred from neutron monitor data in several times.

It follows from the data presented that there are two types of the time profiles of cosmic ray flux, namely, the profiles with the sharp maxima (1965 and 1987, 20-th and 22-nd solar activity cycles) and with the flat ones (1977 and 1997, 21-st and 23-rd solar activity cycles). The directions of magnetic field lines in the heliosphere or the phase of the 22-yearly solar magnetic cycle define these profile types. When we have the negative phases of the 22-yearly solar magnetic cycle (magnetic lines come out from the solar northern polar latitudes) the sharp maxima are observed, and, vice versa, when magnetic lines enter into the solar northern polar latitudes (it corresponds to the positive phases) the flat time dependences in cosmic rays are observed.

However, we have unusual situation with the cosmic ray time dependence in the current solar cycle. From 2001 there is the negative phase of the 22-yearly solar magnetic cycle and during the current solar activity minimum we have to observe the sharp profile of cosmic ray changes. In Figure 3 the comparison of time dependences of cosmic ray fluxes measured in the several minima of solar activity in negative phases of the solar magnetic cycles is given. One can see that during present time we observe unprecedented long-term maximum in cosmic ray flux (see red points in Figure 3). Such situation was not observed in the previous solar cycles. The cosmic ray flux increase observed at the end of 2008 is due to the deep solar activity minimum. The low solar activity (low number of sunspots) and the weak interplanetary magnetic field is responsible for the effect observed.

It is well known that there is a tight relationship between cosmic ray flux and solar activity level. In our case the sunspot number R_z defines solar activity. For the long-term sets of data on cosmic ray fluxes, for example, as it is shown in Figure 2, the correlation coefficient r of N_{max} and R_z is rather high. It equals to $r \approx 0.9$ with the time shift between these values $\Delta t \approx 6$ months (cosmic ray changes are delayed relative to solar activity ones) (Stozhkov, Okhlopkov, 2004). Thus, we can expect that cosmic ray flux will be high in 2009.

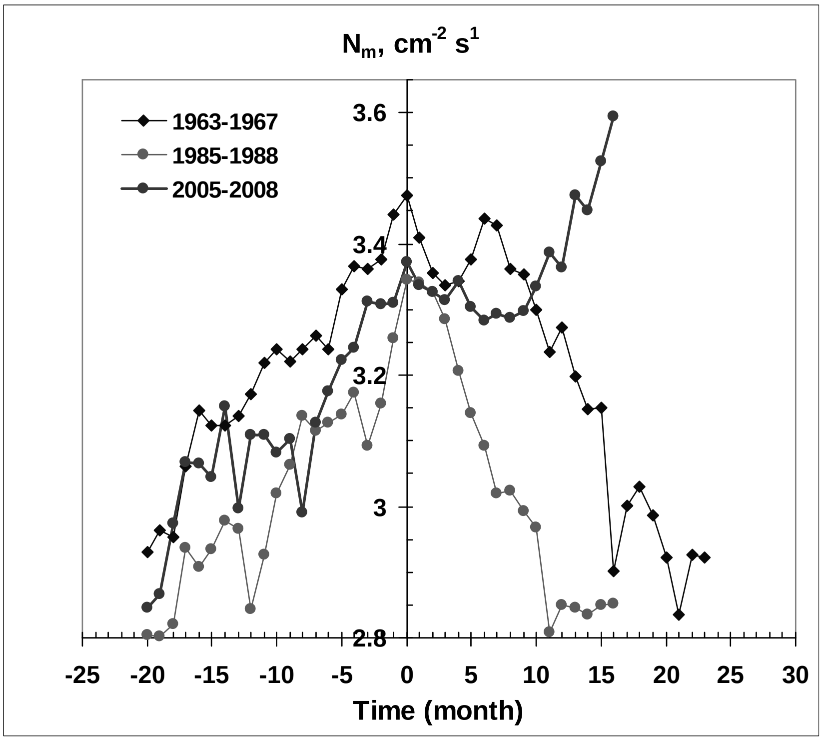

Figure 3. The time dependences of the monthly averages of cosmic ray fluxes N_m. The measurements were made at the polar northern latitude during several solar activity minima in negative phases of the solar magnetic cycles. The "0" time corresponds to May 1965, February 1987 and August 2007 (strictly upp going curve).

3. ABOUT SOLAR ACTIVITY IN THE PAST AND PRESENT TIME

From 2007 – present time we observe high level of cosmic ray fluxes (see Figures 2 and 3). The deep solar activity minimum is responsible for this effect. This minimum is due to the absence of high latitudinal sunspots.

It has been well established that the sunspots of each new solar cycle arise at the high heliolatitudes about (25^o - 35^o). During some period (from several months up to 1 year) low and high heliolatitudinal sunspots are observed simultaneously. The analysis of heliolatitudinal distribution of sunspots data in solar activity minima observed from 1875 to 2008 was made and it confirms this conclusion. The data on heliolatitudes of sunspots were taken from (http://solarscience.msfc.nasa.gov/ greenwch.shtml). As an example, in Figure 4 the heliolatitudinal distribution of sunspots is shown for the period of solar activity minimum of the 22 – 23 solar cycles.

During several months the overlapping of the old sunspots and new ones are seen (red and blue dots in Figure 4 in 1996-1997). The same situations are observed for the other solar activity minima for the periods 1875 – 2000 for which there is the information on the heliolatitudinal distribution of sunspots.

However, for the present period of the solar activity minimum of the 23-rd and 24-th solar cycles such overlapping is almost absent. There are vanishingly few high latitudinal sunspots during this minimum as it is shown in Figure 5.

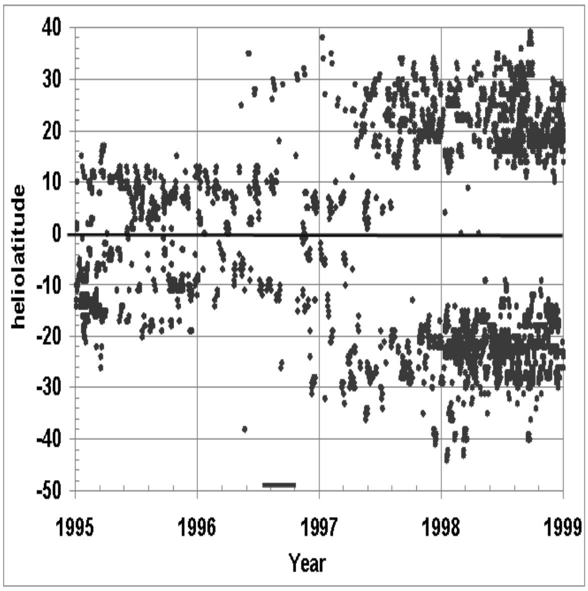

Figure 4. Heliolatitudinal distribution of sunspots for the period of solar activity minimum of the 22-dsolar cycle (points around solar equator to the left) and 23-rd (points to the right) solar cycles. The bar near horizontal axes shows the minimum of sunspot number.

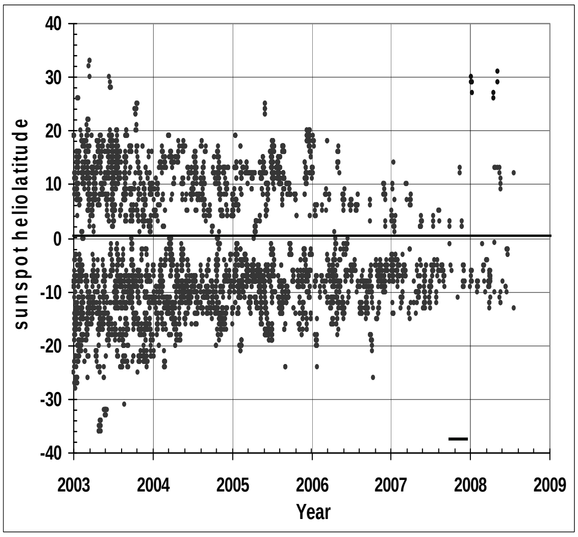

Figure 5. Heliolatitudinal distribution of sunspots for the period of the solar activity minimum of 23-rd cycle (points around solar equator to the left) and very few spots of starting 24-th (points to the right) solar cycles. The bar near horizontal axes shows the minimum of sunspot number.

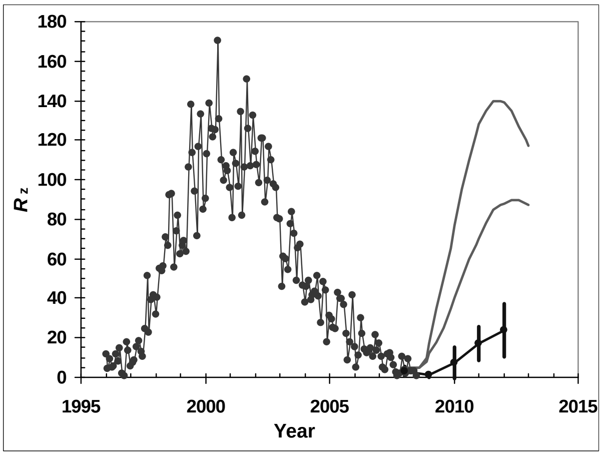

Figure 6. Monthly averages of sunspot number R_z of the 23-rd solar cycle. Predictions for 24-th solar cycle from **http://www.swpc.noaa.gov/SolarCycle/ index.html*; curve with error bars – from this paper.***

4. DISCUSSION

My colleague, Dr. Victor Ermakov, put forward the new idea about sunspot appearance. The sunspot arises after falling of a comet on the solar surface. The heavy planets in our solar system control the comet motion coming to the solar system from Oort's cloud. It could be expected that owing it, we have the quasi-periodical changes in the number of comets falling on the Sun and, as a consequence, the quasi-periodical changes of sunspot number (~11 – year solar cycle). In the current minimum of the solar activity the disposition of planets does not focus comet on the Sun and we do not have high latitudinal sunspots. It is unusual situation.

The possible explanation of it could be the following. If we consider the disposition of the Sun and center mass of the solar system at the present time, we find that during the recent several years the center mass of the solar system does not coincide with the Sun. It is outside of the Sun (the calculations were made by my colleague Dr. V. Okhlopkov). It could be the cause of the absence of high latitudinal sunspots.

In the nearest future the positions of the center mass and the Sun will overlap. It could be the cause of the appearance of low latitudinal sunspots. In this case the amplitude of the forthcoming 24-th solar cycle will be due to these sunspots. Using the time dependences of sunspot number observed at low heliolatitudes ($-10^o \le \Lambda \le 10^o$) in the previous solar cycles, the prediction on the growth phase of the current solar cycle can be done. It is shown in Figure 6. The very low sunspot number is expected during the 24-th solar cycle ($R_z \le 30$).

The nearest future will prove or disprove this hypothesis.

5. CONCLUSION

The comparison of cosmic ray fluxes measured in the atmosphere in the region of the polar latitudes during the several minima of solar activity (1964-1965; 1976-1977; 1986-1987; 1996-1997; 2007-present time) shows that at the present time we have very high cosmic ray flux in comparison with the previous periods of low solar activity. These high cosmic ray fluxes observed are due to the deep minimum of solar activity (sunspot number). As we have the time shift about 6 months between solar activity and cosmic ray flux, it is expected high cosmic ray fluxes during 2009.

Based on the new idea of sunspot production (the comets falling on the Sun causes sunspot appearance), the prediction on the maximum of forthcoming 24-th solar cycle is made. The new solar cycle will have very low sunspot number ($R_z \le 30$).

ACKNOWLEDGMENT

The author thanks coworkers of Lebedev Physical Institute RAS for the experimental data on cosmic ray fluxes in the atmosphere and useful discussion. This work was supported by Russian Foundation for Basic Research, grant 07-02-01019"a".

REFERENCES

Charakhchyan A.N., Bazilevskaya G.A., Stozhkov Y.I., Charakhchyan T.N. Cosmic rays in the stratosphere and in the near-Earth space during 19th and 20th cycles of solar activity. Trudy FIAN 88, Nauka, Moscow, 3-50, 1976. (In Russian).

Stozhkov Y.I., Okhlopkov V.P., Svirzhevsky N.S. Cosmic ray fluxes in present and past times. Solar Physics. 224 (1-2), 323-333, 2004.

Stozhkov Yu.I., Svirzhevsky N.S., Bazilevskaya G.A., Svirzhevskaya A.K., Kvashnin A.N., Krainev M.B., Makhmutov V.S., Klochkova T.I. Fluxes of cosmic rays in the maximum of absorption curve in the atmosphere and at the atmosphere boundary (1957-2007). Preprint LPI RAS No. 14, 77 p., 2007.

The Energization of Magnetotail Ions During the 28 October 2001 Sudden Storm Commencement

V. Peroomian and M. El-Alaoui

Institute of Geophysics and Planetary Physics, University of California, Los Angeles, 405 Hilgard Ave., Los Angeles, CA 90095-1567, USA (e-mail: vahe@igpp.ucla.edu)

Abstract: The effect of the sudden storm commencement (SSC) of the 28 October 2001 geomagnetic storm was investigated by carrying out a large-scale kinetic particle tracing study of the storm event. We launched H^+ ions from the solar wind and O^+ ions from the ionosphere in global time-dependent electric and magnetic fields obtained from a global magnetohydrodynamic (MHD) simulation of the storm. We found that the in-situ population of H^+ and O^+ ions was rapidly energized along the night side ring current, and that energy densities obtained from our calculations were consistent with those obtained from the MHD simulation. The energy densities and injection regions obtained in our simulation were consistent with observations of the storm-time ring current. An examination of ion velocity distributions showed for the first time the dramatic effect of the SSC in energizing ions to > 100 keV energies at geosynchronous orbit.

1. INTRODUCTION

The largest disturbances affecting the Earth's magnetosphere-ionosphere system are magnetic storms. These are primarily driven by strong coupling of the magnetosphere and the interplanetary magnetic field (IMF) due to strong, extended southward magnetic field (*Kamide*, 2001). Storms are often associated with a large increase in the dynamic pressure due to the arrival of an interplanetary shock, causing a sudden compression of the magnetosphere and, a consequent sudden increase in the magnetic field near the Earth: the storm sudden commencement (SSC). The largest space weather events occur when either a coronal mass ejection (CME), an immense expanding mass of plasma that erupt from the Sun, or a corotating interaction region (CIR), a high velocity stream of plasma originating at coronal holes, arrives at the Earth (*Tsurutani and Gonzales,* 1997).

The effects of dynamic pressure pulses and other transient features of SSCs on the ion populations of the near-Earth magnetotail have not been fully explored. *Hudson et al*. (1996) used fields from a global MHD simulation of the 24 March 1991 SSC to investigate radiation belt formation during this storm and showed that the inductive electric fields in the inner magnetosphere were sufficiently large to form the radiation belts in less than one drift period. *Daglis* (1996) and *Daglis et al.* (1997) examined observations of the acceleration of ions during SSCs, focusing on the effect of sudden storm commencement on the energization of ionospheric O^+ ions and the changes in H^+/O^+ energy density ratios in the near-Earth magnetotail during large storms. More recently, *Nosé et al*. (2005) investigated the October, 2003 superstorm using data from the IMAGE/LENA and Geotail/EPIC instruments and found that during this event, the O^+ energy density in the near-Earth plasma sheet increased to ~100 keV.cm^{-3}, up to two orders of magnitude higher than pre-storm values. Moreover, the ratio of O^+/H^+ energy density reached as high as 10-20 near the peak of the storm, indicating that O^+ carried over 90% of the energy density during this event. *Denton et al.* (2005) carried out a superposed epoch analysis of 283 geomagnetic storms occurring between 1991 and 2001 and found that the densities of 1 eV – 45 keV ions was highest in the dawn sector during peak Dst, indicating that ion injection into the inner magnetosphere occurred through this sector. *Denton et al.* (2006) further examined the characteristics of storms driven by CMEs and CIRs and found that CME-driven storms produced significant modulation of plasma density in the near-Earth region.

The acceleration of ions from the ionosphere and their transport into the plasma sheet and ring current have been investigated by particle tracing calculations (*Delcourt et al*., 1989, *Cladis and Francis*, 1992; *Peroomian*, 1994; *Peroomian and Ashour-Abdalla*, 1995, 1996; *Moore and Delcourt*, 1995; *Moore et al.*, 2005; *Peroomian et al*., 2006b, 2007) and multi-fluid MHD calculations (*Winglee*, 2000, 2002; *Winglee et al*., 2005). *Peroomian et al*. (2006a, 2007) evaluated the contribution of the solar wind and the dayside ionosphere to the plasma sheet and ring current for the 24 – 25 September 1998 magnetic storm and found that solar wind H^+ was the dominant species for the first three hours of the storm, after which ionospheric O^+ ions became the dominant carrier of energy density in the ring current. Except for the recent *Peroomian et al.* investigations, the above studies of ion access and acceleration only considered quiescent intervals.

In this paper, we consider the effect of the 28 October 2001 SSC on the ion distributions in the near-Earth magnetosphere. Our methodology, detailed below, mirrors that of *Peroomian et al*. (2007). Section 2 of this paper introduces this event, section 3 details the methodology used in our study, and section 4 presents our simulation results. We summarize our findings in section 5.

2. THE 28 OCTOBER 2001 GEOMAGNETIC STORM

Figure 1 shows the interplanetary magnetic field (IMF) and solar wind data measured by the Geotail spacecraft on 28 October 2001.

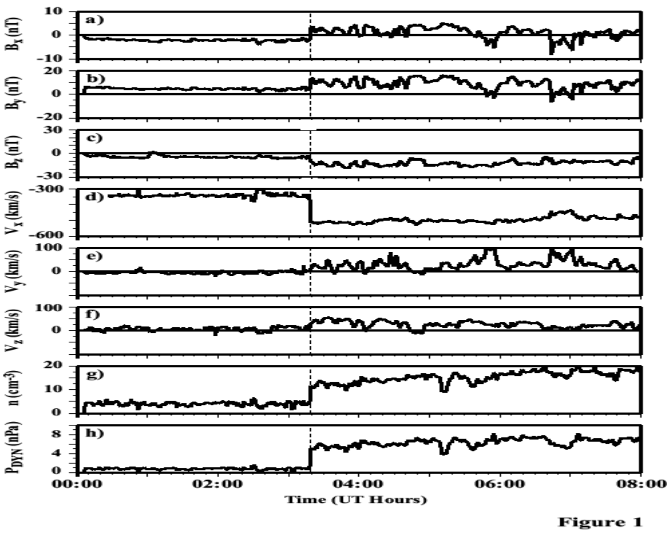

Figure 1. IMF and solar wind data from the Geotail spacecraft for 8 hours on 28 October 2001. The SSC is indicated by the vertical dashed curve.

Geotail was upstream of the Earth, in the solar wind just upstream of the bow shock at (X_{GSM} = 22.7 R_E, Y_{GSM} = -17.1 R_E, Z_{GSM} = 10.0 R_E). Prior to the sudden storm commencement (SSC) occurring at ~03:20 UT (shown with dashed curve in Figure 1), the IMF was southward ($B_z < 0$), with significant westward ($B_y > 0$) and anti-sunward ($B_x < 0$) components (panels a-c of Figure 1). The solar wind velocity was ~325 km/s (Figure 1d), and the solar wind density was measured to be ~5 cm^{-3} (Figure 1g), resulting in a solar wind dynamic pressure of ~1 nPa (Figure 1h). With the arrival of the interplanetary shock and the commencement of the storm, the IMF B_z component became more strongly southward, the B_x component became positive, and the B_y component became more strongly westward but variable. The jump in solar wind velocity to ~550 km/s and solar wind density to ~15-18 cm^{-3} resulted in a relatively low storm-time dynamic pressure of 6-7 nPa. Dst, measuring the energy stored in the storm-time ring current decreased to -157 nT at 12:00 UT, indicating that this was a moderate-sized geomagnetic storm.

3. METHODOLOGY

Our methodology for investigating the acceleration and transport of magnetotail ions is carried out in two steps. First, we use the IMF and solar wind observations shown in Figure 1 as input into our global three-dimensional magnetohydrodynamic (MHD) simulation of Earth's magnetosphere. Next, we use the global time dependent electric and magnetic fields obtained from our MHD simulation to carry out a large-scale kinetic (LSK) test particle trajectory calculation from sources in the solar wind and in the ionosphere.

a) MHD Model

Our coupled magnetosphere-ionosphere, three-dimensional global MHD code is based on a one-fluid description of the interaction between the solar wind and Earth's magnetosphere (*Raeder et al.*, 1995; *Frank et al.*, 1995; *Berchem et al.*, 1998; *Ashour-Abdalla et al.*, 1999a, b; *El-Alaoui*, 2001). The thoroughly benchmarked, parallelized production code uses a conservative finite difference method to solve the gas dynamic part of the MHD equations as an initial value problem. The numerical resistivity is so low that anomalous resistivity must be introduced when modeling substorms (*Raeder et al.*, 1995; 1997). The ionospheric part of the model takes into account three sources of ionospheric conductance: solar EUV ionization is modeled by using the empirical model of *Moen and Brekke* (1993), diffuse auroral precipitation is modeled by assuming strong pitch angle scattering at the inner boundary (2.2 R_E) of the MHD simulation, and accelerated electron precipitation associated with upward field-aligned currents is modeled in accordance with the approach of *Knight* (1972). We use the empirical relations developed by *Robinson et al.* (1987) to calculate ionospheric conductances from mean electron energies and energy fluxes. We note that in the MHD simulation, the total electric field is comprised of convective as well as resistive terms, and is given by: $\mathbf{E} = -\mathbf{v} \times \mathbf{B} + \eta\mathbf{J}$, where **v** is the bulk flow velocity, **B** is the magnetic field, **J** is the current density, and is the resistivity. The resistivity is proportional to the square of the total current; resistive (**J**) contributions to **E** become significant only near the magnetopause and near X- and O-type neutral lines (see *Raeder et al.* (2001) for a comprehensive discussion of the MHD simulation and the resistivity model used within it). To validate the MHD simulation, we compare magnetic fields, flows, densities and temperatures from virtual spacecraft placed in the simulation to those from spacecraft observations of the magnetotail (see, e.g., *Ashour-Abdalla et al.*, 1997, 1999a, b, *El-Alaoui*, 2001).

b) The LSK Particle Tracing Technique

The three-dimensional, time-dependent magnetic and electric fields used in the particle tracing are obtained directly from the global MHD simulation. Field data are saved with 30-second resolution in order to capture the rapid changes that occur in the magnetosphere during storms.

Because the magnetospheric topology, especially near the magnetopause and the magnetotail current sheet, causes ions to behave nonadiabatically and to violate the conservation of the first adiabatic invariant (*Speiser*, 1965; *Lyons and Speiser*, 1982; *Chen and Palmadesso*, 1986; *Büchner and Zelenyi*, 1986, 1989) it is necessary to follow the exact motion of ions. Therefore, for each particle we integrated the full equation of motion given by $d\mathbf{V}/dt = q\mathbf{V}$ **B** + $q\mathbf{E}$. We use linear interpolation in both space and time to determine the instantaneous values of the MHD fields on scales smaller than the grid spacing (typically 0.12 – 0.15 R_E; previous studies have found linear interpolation to be more than adequate for this purpose (e.g. *Ashour-Abdalla et al.*, 1993; *Peroomian*, 1994)). We use a fourth-order Runge-Kutta method to calculate the ion trajectories in the evolving magnetic and electric fields. The time step for the calculation is nominally set at 0.002 times the local ion gyro-period, with an upper limit imposed to ensure that the time step does not get too large in weak field regions. This ensures that all the particles in the simulation conserve energy (to 6 significant figures) and that the trajectory is calculated correctly in the model. The exact method for calculating particle trajectories insures that the particles' phase information is preserved, even as they move through the non-adiabatic regions. This is of primary importance when resolving the narrow ionospheric loss cone, because even a small deviation in phase would scatter a particle out of the loss cone.

c) Ion launch scheme

Our paradigm for launching ionospheric O^+ ions is as follows. We use the formulae developed by *Strangeway et al*. (2005) and the precipitating density and downward Poynting flux into the ionosphere obtained from the MHD simulation to calculate O^+ outflow. The Poynting flux parameterization captures the O^+ outflow from the dayside ion fountain, whereas the precipitating electron parameterization reproduces outflow from the polar wind and the auroral zone. Figure 2 plots the total ionospheric outflow rates calculated from the *Strangeway et al.* (2005) formulae for Poynting flux (red curve) and electron precipitation (black curve) for this event. Prior to storm onset, the ionospheric outflow is ~10^{26} ions/s, and increases sharply by a factor of ~5 at the SSC. Both the electron precipitation and Poynting Flux curves show short and long time scale variations that reflect changes in the solar wind and IMF and the dynamics of the magnetotail. Using these outflow rates, we launched ~50,000 O^+ ions per hemisphere at 1-minute intervals beginning just after 0:00 UT and continuing until 07:00 UT on 28 October 2001. A total of 4.2×10^7 O^+ ions were launched during this event.

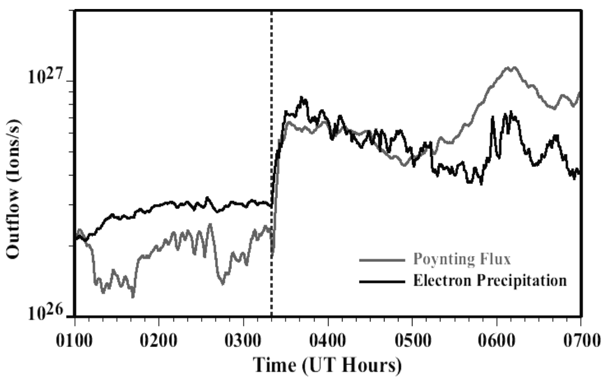

Figure 2. Total O+ ion outflow rates computed from the Poynting flux and precipitation at the MHD ionospheric boundary and the Strangeway et al. [2005] formulae. The SSC is indicated by the vertical dashed curve.

The launch grid used in our previous studies of solar wind ion entry into the magnetosphere during quiet (*Peroomian*, 2003a, b) and storm-time (*Peroomian et al.*, 2006a, 2007) conditions was also used in this study. We launched 100 H^+ ions in drifting Maxwellian distributions from gridpoints spaced 0.5 R_E apart in the x = 17 R_E plane, covering an 80 $R_E \times 80$ R_E (-40 $R_E < y < 40$ R_E, -40 $R_E < z < 40$ R_E) area in the y–z direction. Solar wind H^+ ions were launched at 1-minute intervals during the same interval as the ionospheric O^+ ions. The temperature, velocity, and density of the solar wind ions was obtained from the solar wind input used in the MHD simulation at the time of launch. We launched ~1.0×10^9 solar wind protons during this storm event.

4. SIMULATION RESULTS

The solar wind and IMF data shown in Figure 1 were used as input into our MHD simulation run, extending from 00:00 UT to 1200 UT on 28 October 2001. Figure 3 shows four snapshots the MHD pressure (in pPa) in the noon-midnight meridian (Y_{GSM} = 0) plane.

The black curve in each panel shows the location of the bow shock. Figure 3a shows the configuration of the magnetosphere 10 minutes prior to the SSC. During this time, the IMF is southward and has a positive y-component. The bow shock standoff distance is ~14 R_E, nominal for quiet solar wind conditions, and the magnetotail lobes have very low density. Figure 3b, at 03:20 UT, coincides with the arrival of the interplanetary shock and shows increased solar wind particle pressure and an Earthward movement of the bow shock. The magnetotail remains unaffected at this time. Ten minutes later, at 03:30 UT (Figure 3c), the bow shock has been pushed inward to ~10 R_E, and the magnetopause standoff distance (not shown in the figure) has decreased from 10.3 RE at 03:10 UT to 6.7 R_E at 03:30, or just outside geosynchronous orbit. The tail cross-section has also decreased from its pre-storm value of ~55 R_E at X_{GSM} = -20 R_E to ~47 R_E at that location. In the magnetotail, the lobes have significantly more plasma, and the plasma sheet Earthward of X_{GSM} ~ -20 R_E has expanded. Figure 3d, at 03:40 UT, shows a similar configuration to the previous panel, except that the plasma sheet has enlarged considerably in the previous 10 minutes.

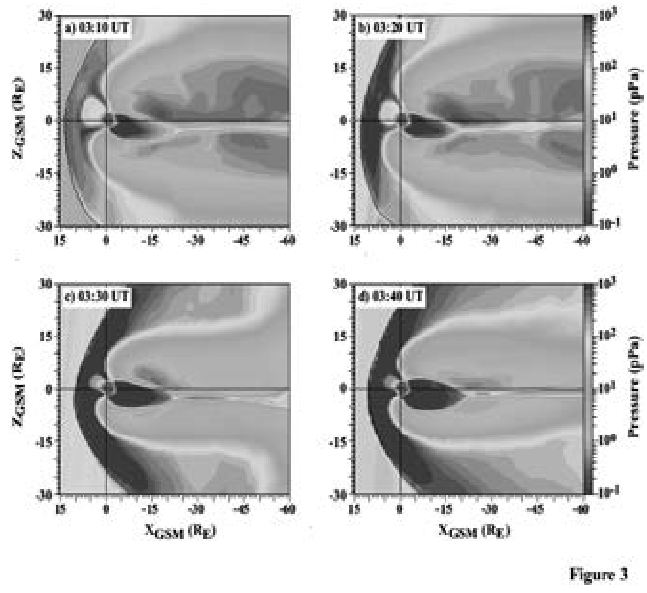

Figure 3. XGSM – ZGSM Snapshots of the MHD pressure (in pPa) in the YGSM = 0 plane at (a) 03:10 UT, (b) 03:20 UT, (c) 03:30 UT, and (d) 03:40 UT. The location of the bow shock is shown with the black curve in each panel. The color coding is identical for all four panels and is shown to the right of each row.

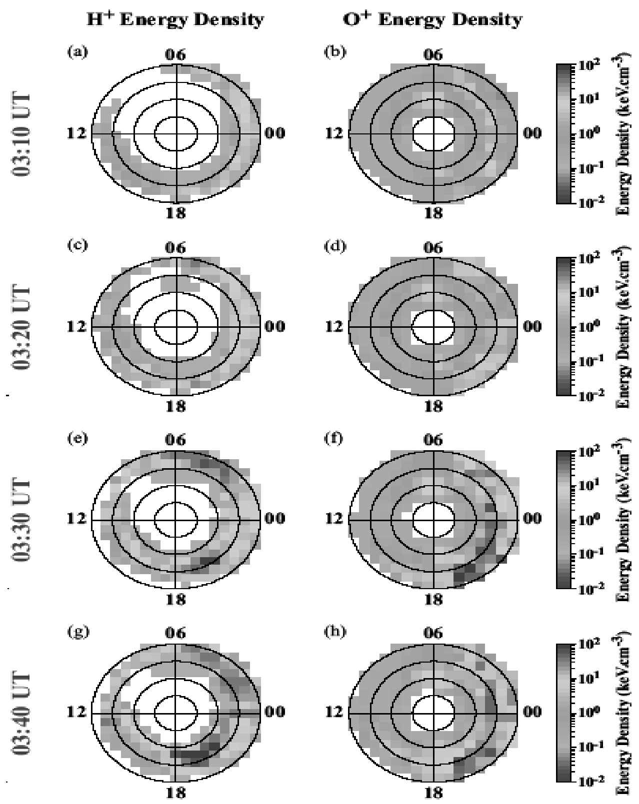

Figure 4

Figure 4. Profiles of energy density (in keV.cm-3) in the near-Earth (RXY < 8 RE) equatorial plane for solar wind H+ (left-hand column) and ionospheric O+ (right-hand column) for the four times shown in Figure 3. The color coding, is identical for all four panels and is shown

Figure 4 shows the results of our LSK particle tracing calculation in the near-Earth region. Each panel of the figure shows the energy density of ions in the equatorial plane at $R_{GSM} < 8\ R_E$ averaged over a 2-minute time interval centered on the time shown to the left and color-coded according to the scale on the right of the panel. The left-hand column shows solar wind H^+ ions, and the right-hand column shows ionospheric O^+ ions. Panels a and b of Figure 4 show results at 03:10 UT, prior to the SSC, and indicate that the solar wind ions populated the partial ring current with peak energy densities of ~10 keV.cm^{-3} in the pre-midnight sector, whereas a much colder O^+ population populated the ring current to very low *L* shells. Many of the O^+ ions, especially those at low *L* shells, were directly injected into this region. The SSC, occurring at 03:20 UT, has an immediate effect on the near-Earth ions. An injection of both H^+ (Figure 4c) and O^+ (Figure 4d) ions can be seen in the dawn sector. Both species also show significant energization, especially in the 1800 – 0000 MLT sector for O^+ and throughout the night side for H^+ ions. Ten minutes after the SSC begins, the energy density of both H^+ and O^+ ions has increased tenfold, and exceeds 100 keV.cm^{-3} in the dawn and pre-midnight sectors for H^+ and in the pre-midnight sector for O^+ ions (Figures 4e and 4f). Also, H^+ ions have now been injected into a full ring current encircling the Earth. This pattern persists at 03:40 UT (Figures 4g and 4h), and in fact continues during the next hour of the SSC. The principal difference in the energization pattern of solar wind H^+ and ionospheric O^+ ions during the SSC is that H^+ ions is that in addition to energization and injection from the magnetotail, a hot population of solar wind H^+ ions also appears to be injected from the dawn flank (Figures 4c and 4e). This injection mechanism has been observed for other storms, and was reported in *Peroomian and El-Alaoui* (2008) as resulting from the direct access of magnetosheath ions to the inner magnetosphere via an elongated reconnection region in the dawn flank. The injection into the dawn sector is also consistent with observational results reported by *Denton et al.* (2005).

The average energy densities for the near-Earth region shown in Figure 4 and plasma sheet are plotted in Figure 5.

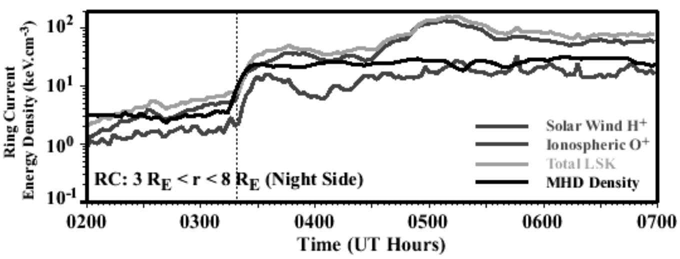

Figure 5

Figure 5. Ring current energy densities (in keV.cm-3) of solar wind H+ (red curve), ionospheric O+ (blue curve), total LSK ions (H+ + O+, green curve) from the LSK simulation compared with the energy density obtained from the MHD simulation (black curve) for 5 hours during the 28 October 2001 event. The ring current is defined as 3 RE < RGSM < 8 RE; XGSM < 0 in the equatorial plane.

The top panel of this figure shows the energy densities of solar wind H^+ ions (red curve), ionospheric O^+ ions (blue curve), and the total LSK energy density (green curve) averaged over the nightside ring current (defined as $3\ R_E < R_{GSM} < 8\ R_E$; $X_{GSM} < 0$ in the equatorial plane). The average energy density from the MHD simulation is also shown for reference (black curve). Prior to the SSC, the total LSK energy density is in excellent agreement with the MHD result, and the jump in energy density at the onset of the SSC is of equal magnitude. However, the absence of a ring current in the MHD simulation results in a flat energy density profile, whereas continuous injection of hot ions into the ring current increases the LSK energy density, especially after a substorm that occurs at 04:30 UT. In the nightside ring current, our results show that prior to the SSC, O^+ ions carried ~30% of the total energy density. Minutes after the onset of the SSC, oxygen ions briefly carried ~40% of the energy density, and during the next four hours, O^+ ions carried ~20% - 30% of the energy density. The O^+/H^+ energy density ratio was smallest just after the 04:30 UT substorm, when an injection of hot H^+ ions into the region disproportionately increased the H^+ energy density. Nosé et al. (2005) compiled storm observations spanning two decades to show that the O^+/H^+

energy density ratio was a function of storm strength (as measured by Dst), and was ~0.3 – 1.0 for storms comparable to the 28 October 2001 event (their Figure 7). Our results are in excellent agreement with these observations.

We now concentrate on the rapid energization of ions seen at the onset of the SSC. To do so, we plot in Figure 6 Vx – Vy cuts of the velocity distribution function for solar wind H^+ ions at 2100 MLT (left-hand column), 0000 MLT (middle column), and 0300 MLT (right-hand column) in geosynchronous orbit.

The top row of Figure 6, obtained at 03:18 UT just prior to the SSC, shows a ring-type distribution of hot ions at 2100 MLT, and a warm distribution at 0000 MLT. As was seen in Figure 4, there are very few ions in the 0300 MLT sector at this time. However, the first distribution to show significant change at the onset of the SSC (second row, 03:20 UT) is in fact the 0300 MLT distribution (Figure 6f), indicating the injection of new particles into the region. The 2100 MLT and 0000 MLT distributions (Figures 6d and 6e) only show a modest change from the previous snapshots. At 03:22 UT (Figures 6g – 6i), the 2100 MLT and 0000 MLT are warmer, and the 0300 MLT distribution shows a significant injection of hot ions into that sector. This is in fact the dawnside source that was seen in Figure 4. From this point onward, the distributions continue to increase in energy, so that at 03:26 UT (bottom row), all three MLT sectors show very hot plasma with a significant fraction of ions with E > 50 keV. It is interesting to note that after 03:22 UT, and continuing through the first four hours of the SSC, the distribution at 0000 MLT is colder that those of its neighboring sectors. This feature is consistent with the near-Earth energy densities shown in Figures 6e and 4g. The energization of ions during their duskward drift in the ring current can explain the increase in energy from 0000 MLT to 2100 MLT. However, the hotter population on dawn side of midnight apparently mixes with a cooler population during its duskward drift, as both Figure 4 and Figure 6 show a decrease in energy density toward midnight.

5. SUMMARY AND DISCUSSION

We carried out an MHD+LSK simulation of the 28 October 2001 sudden storm commencement by launching ions from the solar wind and the ionosphere in global electric and magnetic fields obtained from a global MHD simulation of the event. We found that

1. The SSC resulted in the injection and energization of solar wind H^+ ions at all local times on the night side, but especially in the dawn and pre-midnight sectors. O^+ ions were injected predominantly in the pre-midnight sector. Injection into the dawn sector is consistent with observations reported by *Denton et al.* (2005) and modeling of ion entry by *Peroomian and El-Alaoui* (2008).

The energy densities obtained from our LSK calculations in the nightside ring current were consistent with those found in the MHD simulation prior to and just after storm onset, including the jump at the onset of the SSC. The LSK ion energy density increased in response to a substorm that occurred at 04:30 UT, forming a ring current absent in the MHD simulation. The energy densities obtained in our calculations are in the range reported by *Nosé et al*. (2005) for comparable storms.

2. Velocity distributions obtained at geosynchronous orbit showed the rapid energization of ions to ~ 50 keV – 100 keV, and the role of particle transport on ion velocity distributions in the near-Earth region.

The results shown in this paper highlight the dramatic effect of the SSC on ions in the near-Earth magnetotail. In addition to obtaining bulk parameters in the near-Earth region and examining the effect of the SSC on these quantities, we report for the first time the changes in ion velocity distributions caused by acceleration and injection during the SSC. One of the primary acceleration mechanisms operating during the SSC are large-scale transient electric fields, and especially large inductive electric fields. These, combined with the compression of the magnetosphere, result in the inward injection and acceleration of ions into trapped orbits in the ring current. The subsequent relaxation of the magnetosphere following shock passage results in an outward motion of the trapping boundary but does not affect ions that are already in trapped orbits. A more complete analysis of the 28 October 2001 storm event, including entry paths of solar wind ions into the magnetosphere, is the subject of a forthcoming paper.

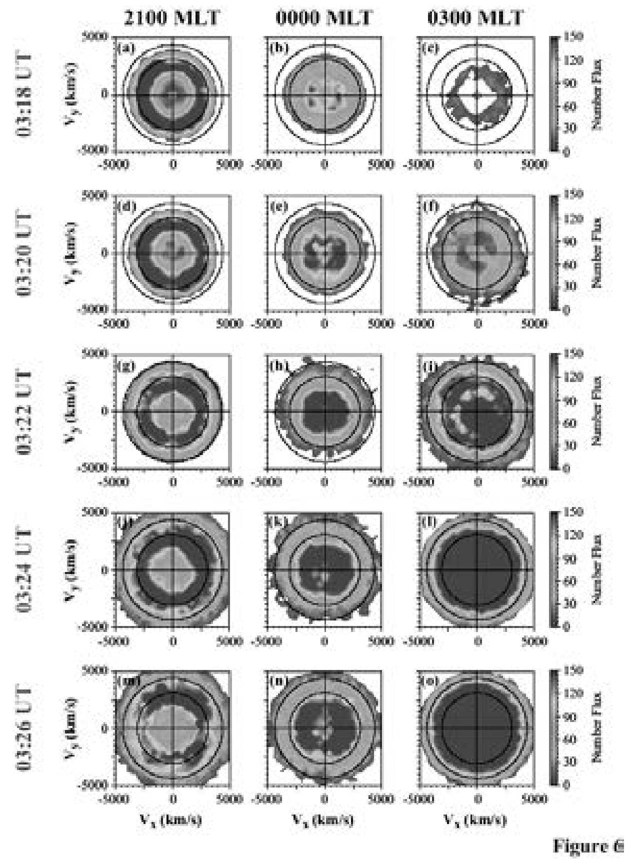

Figure 6. Solar wind H^+ ion velocity distributions at geosychronous orbit obtained at 2100 MLT (left-hand column), 0000 MLT (middle column), and 0300 MLT (right-hand column) during the SSC. Each distribution function is obtained from a 2 $R_E \times 2$ R_E square centered on the given MLT and a radial distance of 6.6 R_E from Earth, and represents a 2-minute average centered on the time given to the left of each row. The color coding is the same for all panels, and is given to the right of each row for reference, and the two circles in each panel represent 50 keV and 100 keV energies, respectively.

ACKNOWLEDGEMENTS

This study was supported by NASA Living with a Star grant NNX08AP95G. Computing support was provided by the San Diego Supercomputer Center and by the UCLA Academic Technology Services.

REFERENCES

Ashour-Abdalla M., Berchem J., Büchner J. and Zelenyi L.M., Shaping of the magnetotail from the mantle: Global and local structuring, J. Geophys. Res., 98, 5651, 1993.

Ashour-Abdalla M., et al. Ion sources and acceleration mechanisms inferred from local distribution functions, Geophys. Res. Lett., 24(8**)**, 955–958, 1997.

Ashour-Abdalla M., El-Alaoui M., Peroomian V., Walker R. J., Raeder J., Frank L. A., and. Paterson W. R, Source distributions of substorm ions observed in the near-Earth magnetotail, Geophys. Res. Lett., 26, 955, 1999a.

Ashour-Abdalla, M., El-Alaoui M., Peroomian V., Walker R. J.,. Zelenyi L. M,. Frank L. A, and Paterson W. R. , Localized reconnection and substorm onset on Dec. 22, 1996, Geophys. Res. Lett., 26, 3545., 1999b.

Berchem J.,. Raeder J, Ashour-Abdalla M,. Frank L. A W., Paterson R., Ackerson K. L., Kokubun S., Yamamoto T., and Lepping R. P., Large-scale dynamics of the magnetospheric boundary: Comparisons between global MHD simulation results and ISTP observations, in Geospace Mass and Energy Flow: Results From the International Solar-Terrestrial Physics Program, edited by Horwitz J. L., Gallagher D. L., and Peterson W. K., Geophys. Monogr. *Ser.*, vol.104**,** 247, AGU, Washington, D. C., 1998.

Büchner J., and Zelenyi L. M., Deterministic chaos in the dynamics of charged particles near a magnetic field reversal, Phys. Lett. A, 118**,** 395, 1986.

Büchner, J., and Zelenyi L. M., Regular and chaotic charged particle motion in magnetotail-like field reversal, 1, Basic theory of trapped motion, J. Geophys. Res., 94, 11,821, 1989.

Chen J., and Palmadesso P. J., Chaos and nonlinear dynamics of single-particle orbits in a magnetotaillike magnetic field, J. Geophys. Res., 91, 1499, 1986.

Cladis J. B. and Francis W. E., Distribution in magnetotail of O^+ ions from cusp/cleft ionosphere: a possible substorm trigger, J. Geophys. Res., 97, 123, 1992.

Daglis I. A., The role of magnetosphere-ionosphere coupling in magnetic storm dynamics, in *Magnetic Storms*, edited by Tsurutani B. T.,. Gonzales W. D, Kamide Y., and Arballo J. K., *Geophys. Monogr. Ser.*, vol. 98, 107, AGU, Washington, D. C., 1996.

Daglis I. A., Axford W. I., Sarris E. T., Livi S.and Wilken B. Particle acceleration in geospace and its association with solar events, Solar Phys., 172, 287-296, 1997

Delcourt D. C., Chappell C. R., Moore T. E., and Waite J. H. Jr., A three-dimensional numerical model of ionospheric plasma in the magnetosphere, J. Geophys. Res., 94**,** 11,893, 1989.

Denton M. H., Thomsen M. F., Korth H., Lynch S., Zhang J. C., and Liemohn M. W. Bulk plasma properties at geosynchronous orbit, J. Geophys. Res., 110, A07223, doi:10.1029/2004JA010861, 2005

Denton M. H., Borovsky J. E., Skoug R. M, Thomsen M. F., Lavraud B., Henderson M. G., McPherron R. L., Zhang J. C., and Liemohn M. W. Geomagnetic storms driven by ICME- and CIR-dominated solar wind, J. Geophys. Res., 111, A07S07, doi:10.1029/2005JA011436, 2006.

El-Alaoui, Current disruption during November 24, 1996, substorm, J. Geophys. Res., 106, 6229, 2001.

Hudson M. K., Elkington S. R.,. Lyon J. G., Marchenko V. A., Roth I., Temerin M., and Gussenhoven M. S., MHD/Particle simulations of radiation belt formation during a storm sudden commencement, in *Radiation Belts: Models and Standards*, edited by j. F. Lemaire, D. Heynderickx, and D. N. Baker, Geophys. Monogr. Ser., 97, p. 57, AGU, Washington, D.C., 1996.

Kamide Y. Interplanetary and magnetospheric electric fields during geomagnetic storms: what is more important, steady-state fields or fluctuating fields, J. Atmos. Sol.-Terr. Phys., 63, 413-20, 2001.

Knight S., Parallel electric fields, Planet. Space Sci., 21, 741, 1972.

Lyons L. R., and Speiser T. W., Evidence for current sheet acceleration in the geomagnetic tail, J. Geophys. Res., 87, 2276, 1982.

Moen J., and Brekke A., The solar flux influence on quiet time conductances in the auroral ionosphere, Geophys. Res. Lett., 20, 971, 1993.

Moore T. E., and Delcourt D. C., The Geopause, Rev. Geophys., 33, 175, 1995.

Moore, T. E., et al, Plasma sheet and (nonstorm) ring current formation from solar and polar wind sources, J. Geophys. Res., 110, A02210, doi:10.1029/2004JA010563, 2005.

Nosé M., Taguchi S., Hosokawa K., Christon S. P., McEntire R. W.,. Moore T. E, and Collier M. R. Overwhelming O^+ contribution to the plasma sheet energy density during the October 2003 superstorm: Geotail/EPIC and IMAGE/LENA observations, J. Geophys. Res., 110, A09S24, doi:10.1029/2004JA010930, 2005.

Peroomian V., Large Scale Kinetic Modeling of Magnetospheric Plasma, Ph.D. thesis, University of California at Los Angeles, March 1994.

Peroomian V., Interplanetary magnetic field-dependent impact of solar wind ions on Earth's magnetosphere, in *The Low-Latitude Boundary Layer*, edited by P. Newell and T. Onsager, *Geophys. Monogr. Ser.*, 133, DOI 10.1029/133GM04, 2003a.

Peroomian, V., The influence of the interplanetary magnetic field on the entry of solar wind ions into the magnetosphere, *Geophys. Res. Lett.* 30, 10.1029/2002GL016627, 2003b.

Peroomian V., and El-Alaoui M. The storm-time access of solar wind ions to the nightside ring current and plasma sheet, *J. Geophys. Res.*, *113*, A06215, doi:10.1029/2007JA012872, 2008.

Peroomian V., and Ashour-Abdalla M., Relative contribution of the solar wind and the auroral zone to near-Earth plasmas, in Cross-Scale Coupling in Space Plasmas, edited by J. Horwitz et al., Geophys. Monogr.

Ser., vol. 93, pp. 213-217, AGU, Washington, D. C., 1995.

Peroomian V., and Ashour-Abdalla M., Population of the near-Earth magnetotail from the auroral zone, J. Geophys. Res., 101, 15,387, 1996.

Peroomian V., El-Alaoui M., Ashour-Abdalla, and Zelenyi L. M., Ion dynamics during the September 24-25, 1998 magnetic storm, Proceedings of the 2005 Solar Extreme Events Conference, Nor Amberd, Armenia, p. 147, 2006a.

Peroomian V., El-Alaoui M., Abdalla M. A., and Zelenyi L. M. Dynamics of ionospheric O^+ ions in the magnetosphere during the 24–25 September 1998 magnetic storm, J. Geophys. Res., 111, A12203, doi:10.1029/2006JA011790, 2006b.

Peroomian V., El-Alaoui M., Ashour-Abdalla M., and Zelenyi L. M. A comparison of solar wind and ionospheric plasma contributions to the September 24-25, 1998 magnetic storm, J. Atmos. Sol.-Terr. Phys., doi:10.1016/j.jastp.2006.07.02, 2007.

Raeder J., Walker R. J., and Ashour-Abdalla M., The structure of the distant geomagnetic tail during long periods of northward IMF, Geophys. Res. Lett., 22, 349, 1995.

Raeder J., Berchem J., Ashour-Abdalla M., Frank L. A., Paterson W. R., Ackerson K. L., Bosqued J. M., Lepping R. P., Kokubun S., Yamamoto T., Slavin S. A., Boundary layer formation in the magnetotail: Geotail observations and comparisons with a global MHD model, Geophys. Res. Lett., *24*, 951, 1997.

Raeder J., McPherron R. L.,. Frank L. A, Kokubun S., Lu G., Mukai T., Paterson W. R.,. Sigwarth J. B,. Singer H. J, and. Slavin J. A, Global simulation of the Geospace Environment Modeling substorm challenge event, J. Geophys. Res., 106(A1), 381–396, 2001.

Robinson R. M., Vondrak R. R., Miller K., Dabbs T., and Hardy D., On calculating ionospheric conductances from the flux and energy of precipitating electrons, J. Geophys. Res., 92, 2565, 1987.

Speiser T. W., Particle trajectories in model current sheets, J. Geophys. Res., 70, 4219, 1965.

Strangeway R. J., Ergun R. E., Y.-J. Su, Carlson C. W., Elphic R. C. (2005), Factors controlling ionospheric outflows as observed at intermediate altitudes, J. Geophys. Res., 110, A03221, doi:10.1029/2004JA 010829.

Tsurutani B. T. and Gonzales W. D., The Interplanetary Causes of Magnetic Storms: A Review, Geophys. Monogr., *98*, edited by Tsurutani B. T., Gonzales W. D., Kamide Y,and. Arballo J. K, pg. 77, AGU, 1997.

Winglee R. M., Multi-fluid simulations of the magnetosphere: the identification of the geopause and its variation with IMF, Geophys. Res. Lett., *25*, 4441, 1998.

Winglee R. M., Mapping of ionospheric outflows into the magnetosphere for varying IMF conditions, J. Atmos. And Solar Terr. Phys., 62, 527, 2000.

Winglee R. M., Lewis W., and G. Lu, Mapping of the heavy ion outflows as seen by IMAGE and multifluid global modeling for the 17 April 2002 storm, J. Geophys. Res., 110, A12S24, doi:10.1029/2004JA 010909, 2005.

Acceleration of CMEs and Eruptive Prominences

D. Maričić [1], B. Vršnak [2], D Roša .

[1]*Astronomical Observatory Zagreb, Opatička 22, HR-10000 Zagreb, Croatia*
(e-mail: darije.maricic@zg.t-com.hr, drosa@hpd.botanic.hr*)*
[2]*Hvar Observatory, Faculty of Geodesy, Kačićeva 26, HR-10000 Zagreb, Croatia*
(e-mail: bvrsnak@geodet.geof.hr)

Abstract: We present a statistical analysis of the relationship between the acceleration of the leading edge of coronal mass ejections (CMEs) and eruptive prominences (EPs). We study the main acceleration phase of 18 CMEs in which kinematics was measured from the pre-eruption stage up to the post-acceleration phase using the data provided by the Extreme Ultraviolet Imaging Telescope, the Mark-IV K-coronameter of the Mauna Loa Solar Observatory, and the Large Angle and Spectrometric Coronagraph. We find a distinct correlation between the duration of the leading edge acceleration phase and prominence acceleration phase. In the majority of events (78%) the acceleration phase of the leading edge is very closely synchronized with the acceleration of the prominence (±20 min). However, in two events acceleration of the leading edge started earlier than the acceleration of the prominence (>50 min), and in two events prominence acceleration started earlier than the acceleration of the leading edge (>40 min).

Key words:: Sun: coronal mass ejection (CMEs)

1. INTRODUCTION

Coronal mass ejections (CMEs) are eruptions of large-scale coronal magnetic field structures, capable of launching 10^{13} kg of plasma into the interplanetary (IP) space at speeds ranging from several tens of km s^{-1}, to more than ~2000 km s^{-1} (see Gopalswamy, et al, 2003) The height-time measurements show that kinematics of CMEs is characterized by three distinct phases: (1) a slow rising motion (this phase may last for hours, and is usually considered to be an quasi-stationary evolution of the pre-eruptive structure through a series of equilibrium states), (2) the main acceleration phase (most often starting by an exponential-like development), and (3) a post-acceleration phase (CME showing approximately constant velocity, or weak residual acceleration/deceleration) (see Maričić,, et al, 2004). The first two phases occur mainly in the inner corona (at radial distances <2 solar radii), while the third phase characterizes the motion in the outer corona.

CMEs often expose a three-part structure: the eruptive prominence (hereinafter, EP), the cavity, and the leading edge (hereinafter, LE). Observations in EUV, soft X-rays, as well as the solar eclipse observation, have revealed an analogous quiescent prominence/corona structure (the EP is usually found in a coronal void nested in the helmet streamer), indicating that the basic CME morphology has its roots in the pre-eruption magnetic field configuration. A comparison of the height, speed, and acceleration time profiles of these three CME components provides an important information on the CME initiation process and the CME dynamics.

A number of studies presented evidence of synchronized kinematics of different parts of the CME (see Dere, et al, 1999), (see Fisher, et al, 1981), (see Gopalswamy, et al, 2003), (see Illing, et al, 1985), (see Koutchmy, et al, 2008), (see Low, et al, 1987) (see Maričić, et al, 2004), (see Plunkett, et al, 1997), (see Plunkett, et al, 2000), (see Schmahl, et al, 1977), (see Srivastava, et al, 2000) and (see Wood, et al, 1999). However, observations were not always elaborated quantitatively and different sets of instruments were used, making comparison and systematization of empirical results difficult and ambiguous.

In this paper, we systematize the synchronization of the main acceleration of the LE and the EP (as a basic parts of CME) using a relatively large sample of events, all observed by the same set of the three instruments. We employ the data from the Extreme Ultraviolet Imaging Telescope (EIT) onboard Solar and Heliospheric Observatory (SoHO), the Mark-IV K-coronameter (MK-IV) of the Mauna Loa Solar Observatory (MLSO, and the Large Angle and Spectrometric Coronagraph (LASCO) onboard SoHO. The main advantage of using these data is the overlapping field-of-view of these three instruments, see Table 1.

2. OBSERVATIONS

The analysis of the kinematics is based on the distance-time measurements of the top of the leading edge and the top of the eruptive prominence. After the corresponding features in EIT, MK-IV, and LASCO C2/C3 images were properly associated, the height-time data, $h(t)$, were joined for a given feature and smoothed. The smooth function uses a symmetric n nearest-neighbor linear least-squares fitting procedure (in which n is adaptively chosen) to make a series of line segments through our data. Then, we have determined the speed by using two successive smoothed data points: $v(t_{vi}) = (r(t_{i+1})-r(t_i))/(t_{i+1}-t_i)$, where $r(t_i)$ is the radial distance at the time t_i, whereas t_{vi} is defined as $t_{vi} = (t_{i+1}+t_i)/2$. In the following step, we have determined the acceleration by applying: $a(t_{ai}) = (v(t_{vi+1})-v(t_{vi}))/(t_{vi+1}-t_{vi})$, where $v(t_{vi})$ is the speed at the time t_{vi} and $t_{ai} = (t_{vi+1}+t_{vi})/2$.

From the acceleration time-profile we determined the times of the onset, the maximum, and the end of the acceleration phase (t_e, t_b, and t_e, respectively), as well as the peak acceleration (a_m), and the durtion of the acceleration phase (T_a=t_e-t_b). The average accelerationis is calculated as a_{aver} = (v_m-v_b)/(t_{vm}-t_b), where v_m is the peak velocity, v_b is the velocity at the onset of the acceleration phase, whereas t_{vm} and t_b are the corresponding times. Note that in an ideal situation t_{vm} and t_e should be identical. However, in a real situation they usually differ, since $a(t)$ often shows several "oscillations" around a=0 at the end of the acceleration stage, so it is often difficult to estimate t_e.

3. RESULTS

The acceleration phase duration, T_a, for LEs vary from 35 min up to 10 h, and for EPs from 50 min up to 10 h. The distribution peaks, for both LEs and the EPs at the bin 100 – 200 min (the average value for the leading edge amounts to 180 min, while for the prominence amounts to 173 min). The distribution of delays between the LE and EP peak-accelerations, Δt_m, has maximum at Δt = 0 and shows a slight asymmetry towards Δt < 0 (Fig. 1). The distribution is characterized by Δt_m= -9 ± 14 min (negative value means that the acceleration-peak of LE occurs before the acceleration-peak of EP). However, we emphasize that the time lag in some events is larger than 30 min.

In the majority of events (14 out of 18; 78%) the beginning of the acceleration phase of the leading edge and the prominence are strongly synchronized (within ±20 min). However, in the two events (11%) the LE acceleration starts 50 min earlier than the EP acceleration, and in the remaining two events EP starts to accelerated 40 min earlier than the LE. So, in four events there was a considerable mismatch between the acceleration phases of the leading edge and the prominence. The distributions of the delays of the onsets and ends of the acceleration phase are characterised by Δt_b = -1 ± 26 min and Δt_e = -14 ± 52 min, respectively. Thus, the onset and the end of the acceleration phase of LE and EP also tend to be synchronized.

We also find that normalized time lags between acceleration-peaks of LE and EP, $\Delta t_m/T_a$, range from -0.69 to +0,08. The distributions of $\Delta t_b/T_a$, $\Delta t_m/T_a$, and $\Delta t_e/T_a$, are shown in Figures 2a-c, respectively. Distributions are characterized by mean values $\Delta t_b/T_a$ = 0.09 ± 0.32, $\Delta t_m/T_a$ = -0.14 ± 0.22, and $\Delta t_e/T_a$ = 0.08 ± 0.43. This clearly shows that in most events LE and EP acceleration phases are well synchronized, with lags ranging on average around ± 10 %.

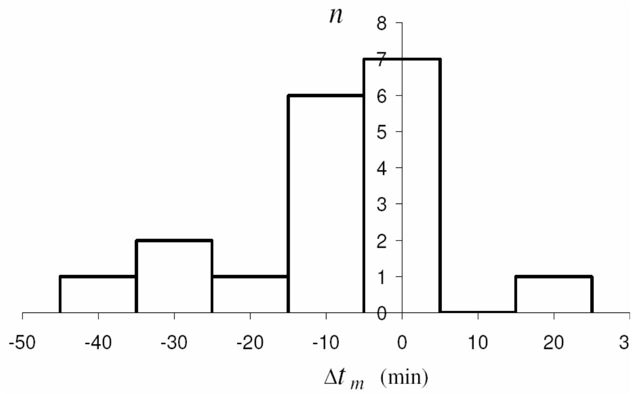

Figure 1. Distribution of the time lag between the acceleration peak of the leading edge and the prominence. Negative values mean that the LE acceleration peak occurs before the EP acceleration peak.

In the Figure 3a we show the relationship between peak- speeds of LEs and EPs.
The graph shows a linear dependence between these two parameters, i.e., larger LE speeds, on average are associated with larger EP speeds. The linear dependence is characterized by the slope k = 1.31. Note that if the event of the largest v_{mLE} would be removed, the correlation coefficient would increase from C= 0.71 to C = 0.84, and the linear coefficient than would become k = 1.24.

The correlation of the LE peak acceleration and the EP peak acceleration is shown in Figure 3b. The graph reveals a distinct correlation, where the LE accelerations are almost twice larger than EP accelerations. If the data would be fitted by the power-law one would get a_{mLE} = 2.14 × $a_{mEP}^{0,92}$, with correlation coefficient C=0.79.
In Figure 3c we present the correlation between the acceleration phase duration of LEs and EPs.

On average, longer acceleration phase of LE is associated with longer acceleration phase of EP.

The graph shows a linear dependence between these two parameters, characterized by the slope k = 1.05, the correlation coefficient C = 0.92, and F-test statistical significance larger than 99%. This reveals that the acceleration phase duration is practically equal for LEs and EPs.

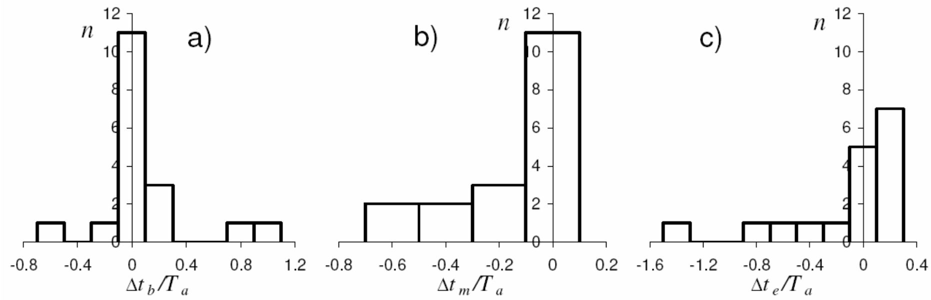

Figure 2. Distribution of the normalized time lags between: a) beginning of the acceleration phase of LEs and EPs; b) the acceleration peak of LEs and EPs; c) the end of the acceleration phase of LEs and the EPs.

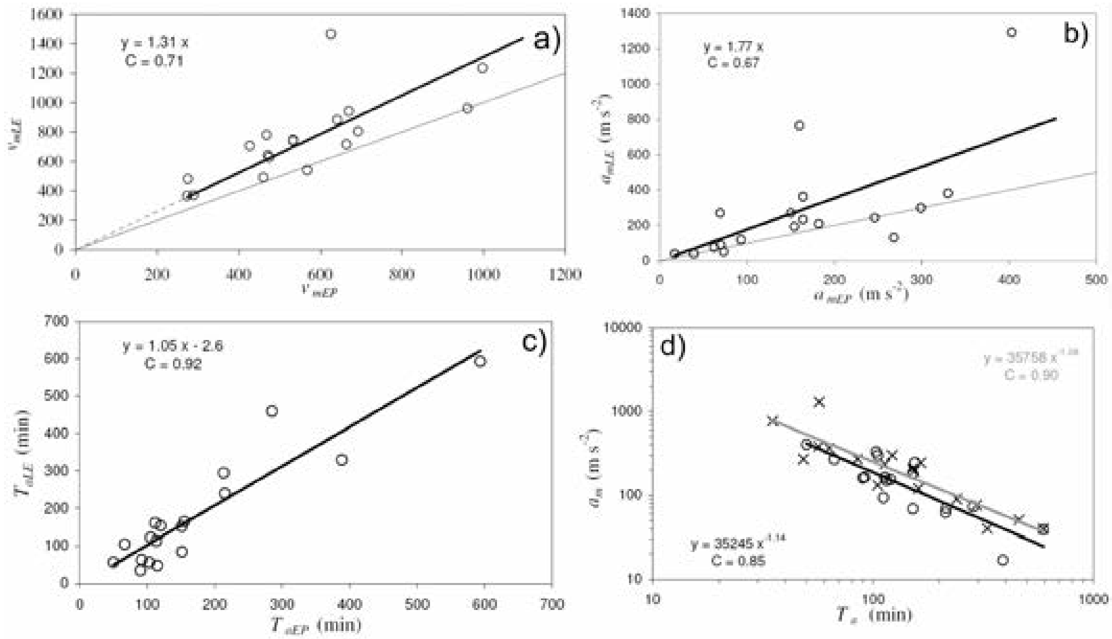

Figure 3. a) Leading edge peak-velocities shown as a function of the prominence peak-velocities; b) Leading edge peak acceleration show as a function of the prominence peak acceleration.; c) Relationship between the leading edge acceleration phase duration and the prominence acceleration phase duration; d) Leading edge peak acceleration (dots) and prominence peak acceleration (crosses) show as a function of the leading edge acceleration phase duration and the prominence acceleration phase duration, respectively. In the insets the linear last squares fit is shown, together with correlation coefficients, C. The F-test of statistical significance of all correlations is P > 99%. The gray line in a) and b) represents y=x line. Errors of individual values in od graphs are smaller then the scatter of data-points.

TABLE 1 Kinematical properties of the analyzed events

date	LASCO UT	v_{mLE} kms^{-1}	v_{mEP} kms^{-1}	a_{mLE} ms^{-2}	a_{mEP} ms^{-2}	T_{aLE} [min]	T_{aEP} [min]	Δt_b [min]	Δt_m [min]	Δt_e [min]	$\Delta t_b/T_a$	$\Delta t_m/T_a$	$\Delta t_e/T_a$
26 02 2000	23:54	778	469	234	164	113	113	18.3	-6.7	18.3	0.16	-0.06	0.16
28 06 2000	19:31	1466	626	1293	403	57	50	9.6	-8.3	16.7	0.17	-0.15	0.29
23 04 2001	19:09	365	273	40	17	330	388	41.7	3.3	-16.7	0.13	0.01	-0.05
25 05 2001	17:26	958	961	300	299	122	105	-1.3	-4.7	15.9	-0.01	-0.04	0.13
08 01 2002	18:30	480	275	120	93	161	112	3.2	-5.6	52.5	0.02	-0.04	0.33
09 03 2002	22:30	371	290	270	150	48	115	3.3	-33.3	-63.3	0.07	-0.69	-1.31
06 06 2002	17:54	745	534	90	70	240	215	-8.3	18.3	16.7	-0.04	0.08	0.07
16 02 2003	23:08	491	461	270	69	85	152	5	-15	-61.7	0.06	-0.18	-0.73
18 02 2003	2:42	802	693	209	182	151	151	0	0.5	0	0	0	0
14 03 2003	18:06	881	642	382	330	57	103	43.3	-36.7	-3.3	0.77	-0.65	-0.06
15 03 2003	21:54	629	475	76	62	295	213	-3.3	-15	78.3	-0.01	-0.05	0.27
26 04 2003	21:50	705	427	193	154	153	120	-10	-16.7	23.3	-0.07	-0.11	0.15
15 07 2003	22:30	540	568	132	268	105	67	-63.3	-31.7	-25	-0.6	-0.3	-0.24
21 10 2003	19:54	640	471	51	73	460	285	-51.7	-1.7	123.3	-0.11	0	0.27
12 11 2003	18:30	940	670	363	164	63	92	1.7	-1.7	-26.7	0.03	-0.03	-0.42
18 08 2004	17:54	740	534	766	160	35	90	35	-11.7	-20	1	-0.33	-0.57
06 09 2005 I	20:00	1235	998	244	246	165	155	-3.3	3.3	6.7	-0.02	0.02	0.04
06 09 2005 II	21:12	715	665	40	39	593	593	-1.7	3.3	116.7	0	0.01	0.2
aver.		749	557	281	136	179	173	1	-8.9	14	0.09	-0.14	-0.08
st.dev.		282	202	305	108	152	133	26.8	14.2	51.9	0.33	0.22	0.43

In Figure 3d we display the dependence of the peak acceleration on the acceleration phase duration for LEs and EPs. The correlations for LEs and EPs are characterized by the power-law fits $a_{LE} = 3.6 \times 10^4 \times T_{aLE}^{-1,08}$ and $a_{EP} = 3.5 \times 10^4 \times T_{aEP}^{-1,14}$, respectively. We find that weaker accelerations of LEs and EPs are associated with longer acceleration phase durations.

4. CONCLUSION

In this paper, we analyzed the synchronization of the main acceleration phase of LEs and EPs (as a basic parts of CMEs) using a relatively large sample of events, all observed by the same set of instruments (MLSO MKIV, SOHO LASCO C2/C3, and SOHO EIT). We summarize the results as follows:

- The highest speed of the LE is on average 190 km/s larger than the highest speed of the EP;
- The peak acceleration of the LE is on average 140 ms^{-2} larger than the peak acceleration of the EP;
- The highest speed of the LE is proportional to the highest speed of the EP, showing a correlation $v_{mLE} = 1.31 \times v_{mEP}$;
- The peak accelerations of LEs and EPs are strongly correlated and for the analyzed sample show a dependence $a_{LE} = 1.77 \times a_{EP}$;
- The duration of the LE acceleration phase is proportional to the duration of the EP acceleration phase, $T_{aLE} = 1,05 \times T_{aEP}$ (on average, durations of the LE and EP acceleration phases are nearly equal);
- In the majority of events (78%) the acceleration of the LE and the EP began almost simultaneously (within ±20 min); however, in two events the LE acceleration began considerably earlier than the acceleration of the EP (>50 min), while in two events the EP acceleration began before the LE acceleration (>40 min);
- The LE and EP acceleration peaks are on average highly synchronized (the distribution peaks at $\Delta t = 0$). However, the time lag in some events is larger than 30 min.
- Durations of the LE and EP acceleration phases are anti-correlated with the peak acceleration.

Our results show that acceleration phases of LEs and EPs are closely correlated in the majority of events, confirming the suggestion by (Gopalswamy, N., Shimojo, M., Lu, W., et al, 2003) that the prominence eruption starts simultaneously with the CME take-off. Moreover, the results indicate that in most events the eruption proceeds in a “self-similar" manner, e.g., like in the event described by (Krall, J., Chen, J., Duffin, et al, 2001)

This means that LE and EP behave as parts of a common erupting magnetic structure, as e.g., in the flux-rope model proposed by (Chen, J., 1989).

Since during the eruption the flux-rope broadens, its outer parts propagate faster than its central parts, implying that the measured acceleration and velocity are higher for LE than for EP that is nested below the flux-rope axis.

On the other hand, our results might indicate that EP acceleration peaks somewhat later than the LE acceleration, which might be related to a larger inertia of the dense EP plasma. Furthermore, in two events the EP could be considered as a driver of the eruption since EP acceleration starts significantly earlier than LE acceleration. On the other hand, in two events the prominence eruption seems to be a consequence of the CME take-off, since it started to accelerate significantly later than the LE.

ACKNOWLEDGEMENT

We would like to thank the GOES, MLSO, SOHO, and Yohkoh teams for developing and operating the instruments and we are grateful for their open data policy.

REFERENCES

Chen J., Effects of toroidal forces in curren loops embedded in a background plasma.Astrophys. J. 338, 453 – 470. doi:10.1086/167211, 1989.

Der K.P.,Brueckner G.E., Howard R.A., Michels D.J., Delaboudiniere J.P., LASCO and EIT Observations of Helical Structure in Coronal Mass Ejections. Astrophys. J. 516, 465 – 474. doi:10.1086/307101, 1999.

Fisher R., Garcia C.J., Seagraves P., On the coronal transient-eruptive prominence of 1980 August 5. Astrophys. J. Lett. 246,L161 – L164. doi:10.1086/ 183575, 1981.

Gopalswamy N., Shimojo M., Lu W., Yashiro S., Shibasaki K., Howard R.A., Prominence Eruptions and Coronal Mass Ejection: A Statistical Study Using Microwave Observations. Astrophys. J. 586, 562 – 578. doi:10.1086/367614, 2003.

Gopalswamy N., Space Science Reviews, 124, Issue 1-4, 145, 2006.

Illing R.M.E., Hundhausen A.J., Observation of a coronal transient from 1.2 to 6 solar radii. J. Geophys. Res. 90, 275 – 282, 1985.

Koutchmy S., Slemzin V., Filippov B., Noens J.C., Romeuf, D., Golub, L., Analysis and interpretation of a fast limb CME with eruptive prominence, C-flare, and EUV dimming. Astron. Astrophys., 483, 599 – 608, doi:10.1051/0004-6361:20078311, 2008.

Krall J., Chen J., Duffin R.T., Howard R.A., Thompson B.J., Erupting Solar Magnetic Flux Ropes: Theory and Observation. Astrophys. J. 562, 1045 – 1057, doi:10.1086/323844, 2001.

Low B.C., Hundhausen A.J., The velocity field of a coronal mass ejection - The event of September 1, 1980. J. Geophys. Res. 92, 2221 – 2230, 1987.

Maričić D., Vršnak B., Stanger A.L. & Veronig A., Solar Phys. 225, 337, 2004.

Plunkett S.P., Brueckner G.E., Dere K.P., Howard R.A., Koomen M.J., Korendyke C.M., Michels D.J., Moses J.D., Moulton N.E., Paswaters S.E., St. Cyr, O.C., Socker D.G., Wang D., Simnett G.M., Bedford D.K., Biesecker D.A., Eyles C.J., Tappin S.J., Schwenn R., Lamy P.L., Llebaria A., The Relationship of Green-Line Transients to White-Light Coronal Mass

Ejections. Solar Phys. 175, 699 – 718, doi:10.1023/A:1004981125702, 1997.

Plunkett S.P., Vourlidas A., Šimberova S., Karlicky M., Kotrč P., Heinzel P., Kupryakov Y.A., Guo W.P., Wu S.T., Simultaneous SOHO and Ground-Based Observations of a Large Eruptive Prominence and Coronal Mass Ejection. Solar Phys. 194, 371 – 391, 2000.

Schmahl E., Hildner E., Coronal mass-ejections-kinematics of the 19 December 1973 event. Solar Phys. 55**,** 473 – 490, 1977.

Srivastava N., Schwenn R., Inhester B., Martin S.F., Hanaoka Y., Factors Related to the Origin of a Gradual Coronal Mass Ejection Associated with an Eruptive Prominence on 1998 June 21-22. Astrophys. J. 534, 468 – 481. doi:10.1086/308749, 2000.

Wood B.E., Karovska M., Chen J., Brueckner G.E., Cook J.W., Howard R.A, Comparison of Two Coronal Mass Ejections Observed by EIT and LASCO with a Model of an Erupting Magnetic Flux Rope. Astrophys. J. 512, 484 – 495. doi:10.1086/306758, 1999.

Hinode EUV Spectroscopic Observations of Coronal Oscillations

Y. Taroyan

Department of Applied Mathematics, University of She_eld, She_eld, S3 7RH, UK
(e-mail: y.taroyan@sheffield.ac.uk)

Abstract: Waves offer a unique opportunity to understand the properties of the solar coronal plasma. Hinode/EIS observations are analyzed to detect wave and oscillatory motions in the solar corona. The EIS observations are carried out in a sit-and-stare spectroscopy mode using a selection of EUV lines. Hinode/XRT images are concurrently taken. Two examples of oscillations in active regions are presented. The evolution of the intensities, Doppler shifts and widths is analised. The Hinode/XRT images suggest that both events occurred along loop-like structures. The first event is interpreted as a slow sausage (acoustic) type wave with a period of 1.2 mHz. The second example is associated with a transverse, most likely, kink type wave with a period of 3 mHz. EUV line ratios are used to determine the value of the coronal magnetic field.

Key words: Techniques: spectroscopic – Sun: corona – Sun: oscillations – Line: profiles – Magnetohydrodynamics (MHD)

1. INTRODUCTION

Magnetohydrodynamic (MHD) waves are important both energetically and as a di-agnostic tool in solar atmospheric research. Determining the physical parameters of the solar coronal plasma is important for understanding such fundamental processes as the heating of the coronal plasma and acceleration of the solar wind. In the past decade, new-generation satellites such as SoHO and TRACE have provided evi-dence of various types of MHD waves. Solar coronal structures support both prop-agating and standing MHD waves. Propagating slow magnetoacoustic waves have been detected in coronal plumes (Ofman et al. 1997, 1999) and near the footpoints of coronal loops (Berghmans & Clette 1999; De Moortel et al. 2000). Williams et al. (2001) have studied fast magnetoacoustic waves propagating along a loop. Among the standing, fast MHD waves observed in coronal loops are the global kink (Aschwanden et al. 1999; Nakariakov et al. 1999) and sausage-mode oscillations (Nakariakov et al. 2003). Oscillations interpreted as standing, slow magnetoacoustic waves have been studied in hot (T > 6 MK) loops with the SUMER spectrometer on board the SoHO satellite (Wang et al. 2002).

The Hinode satellite, launched in 2006, offers new opportunities for studying the Sun's atmosphere. The mission is equipped with several instruments that complement one another. The present letter reports the detection of magnetoacoustic oscillations by the EUV Imaging Spectrometer (EIS). Two examples are presented. The first event occurred on 2007 February 19 and the second on 2007 February 21. The EIS observations were carried out in a sit-and-stare spectroscopy mode using a selection of 17 different EUV lines. Both events are best seen in the strong Fe xii 195 Å line. Concurrent Hinode/XRT images show the location of the EIS slit on the solar disc. The images suggest that, in both cases, the oscillations occur in loop-like structures at different locations.

We discuss the nature and the origin of these oscillatory motions.

2. OBSERVATIONS

The EUV imaging-spectrometer Hinode/EIS has two CCDs each covering a 40 Å wavelength range: 170-210 Å and 250-290 Å. The wavelength response of EIS has two peaks at around 195 Å and 271 Å corresponding to the two CCDs. The EIS has both narrow (1'' and 2'' wide) slits, and wider (40'' and 266'') imaging slots, all with up to 512'' in the solar Y direction. It is able to make slit observations of active regions in ten seconds and of the quiet Sun in between thirty and sixty seconds, and of flares in approximately one second. The spectral resolution can be less than 1 km s $^{-1}$ for the Doppler shift. More details of the Hinode/EIS characteristics are given by Culhane *et al.* (2007) and Kosugi *et al.* (2007). Below, two examples of oscillations are presented.

2.1 February 19, 2007

The 2007, February 19 observations are sit-and-stare observations in which a 1'' wide EIS slit with a window height of 512'' is used. The observations began at 21:06 UT and lasted for about an hour. The location of the slit is marked by a vertical line in the XRT image (Figure 1) and in the EIS 40'' slot images taken after 22:10 UT (Figure 2). The exposure time was around 30 seconds and the total number of exposures 110. The centre of the slit has average coordinates solar X=6'', solar Y=35''. Standard procedures for EIS data reduction were applied to include calibrating the data and creating error arrays, applying Gaussian fitting to each line profile and correcting for the slit tilt and orbital variation. The resulting intensities and Doppler shifts were measured in DN (data number) and in km s $^{-1}$. The Doppler shift has an error of less than 1 km s $^{-1}$.

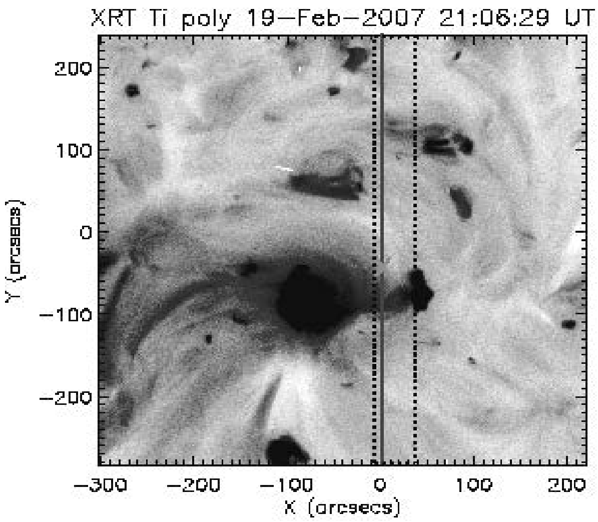

Figure 1. An XRT image of the solar disc taken February 19, 2007. The dotted rectangle shows the region of interest in which EIS imaging/spectroscopic observations were carried out. The 1'' EIS slit is marked by a vertical line. The cross indicates the location of the pixels that registered the oscillations starting at 21:06 UT.

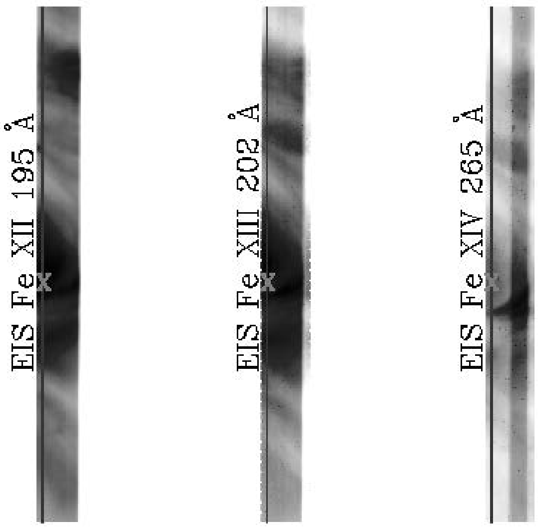

Figure 2. EIS 40'' slot observations lasting from 22:10 to 22:35 UT. Each image covers a 40'' x 512'' rectangular area that is marked by a dotted line in Figure 1. The 1'' EIS slit is marked by a vertical line. The cross indicates the location of the pixels that show oscilla-tions.

Oscillatory behavior was detected between pixels 230 and 234. These pixels are marked in the XRT and EIS images (Figs. 1 and 2). In order to verify that the os- cillations are not an instrumental artefact, the Doppler-shift time series along the entire slit is examined (Figs. 3). Except for the narrow horizontal stripe, no significant wave power was found elsewhere along the slit. An average of the intensity and the Doppler shift taken over these pixels for Fe xii 195 Å, Fe x 184.7 Å, and Fe xiii 202 Å is plotted in Figure 4. The oscillations show up both in the intensity and in the Doppler shift, which appear to be phase-shifted by a quarter period as shown by the sinusoidal fit. The maximum amplitude for the Doppler shift is about 4 km s^{-1}.

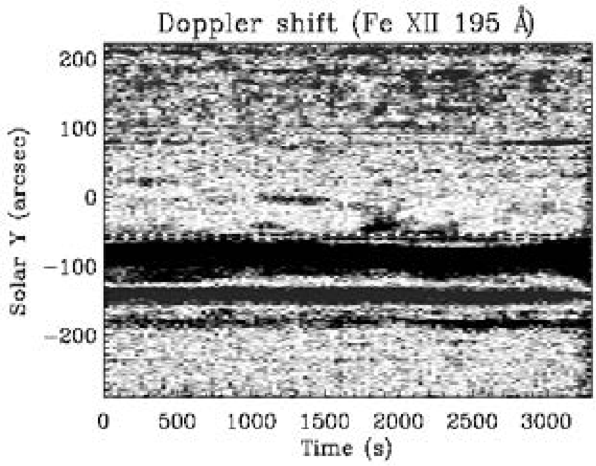

Figure 3. Doppler-shift time series along the 1'' EIS slit for the observations starting at 21:06 UT on 2007 February 19. Positive and negative Doppler shifts are represented by red and blue colours, respectively. The selected line is Fe xii 195 Å. The exposure time is 30 seconds and the total number of exposures 110. The narrow stripe between the horizontal dashed lines marks the pixels with high oscillation power and corresponds to the cross in Figures 1 and 2.

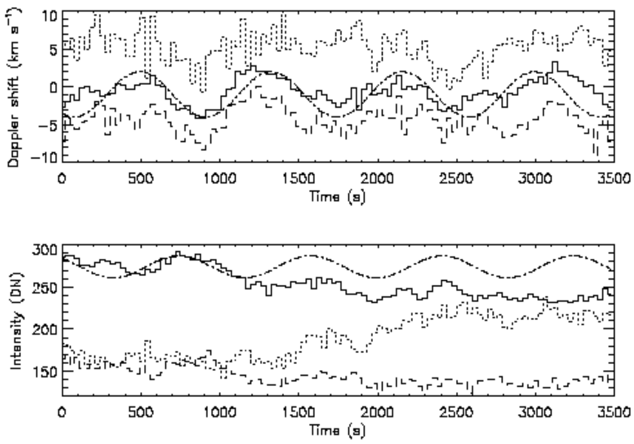

Figure 4.The Doppler shift and intensity time series averaged over five pixels between the dashed lines in Figure 3. The solid, dotted, and dashed curves correspond to Fe xii 195 Å, Fe x 184.7 Å, and Fe xiii 202 Å, respectively. The quarter-period phase shifted dashed-dotted curves represent sinusoidal fits to the Doppler shift and intensity oscillations.

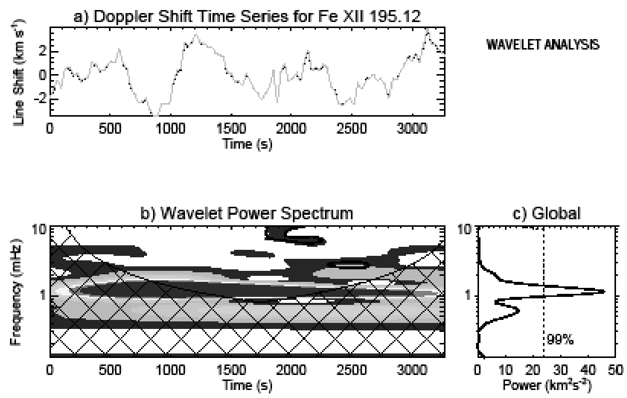

Figure 5. Wavelet analysis for the Fe xii 195 Å Doppler-shift time series shown in Figure 3. The top panel (a) shows the Doppler-shift time series with the subtracted mean value. The bottom left panel (b) displays the wavelet power spectrum. The red colour represents high power, and the blue colour corresponds to low power. The bottom right panel (c) is the global wavelet spectrum. In the global wavelet diagram, the dotted lines indicate a 99% significance level.

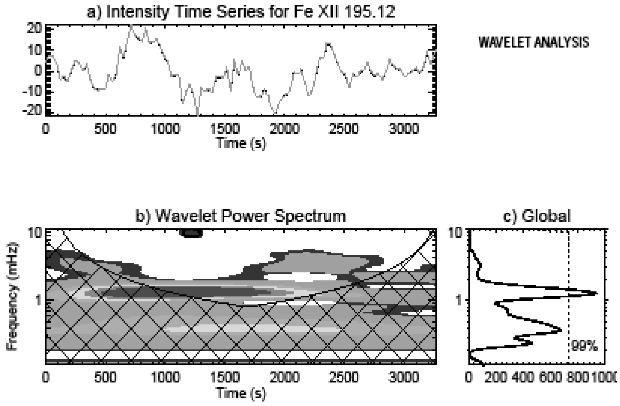

Figure 6. The same as in Figure 5 but applied to the Fe xii 195 Å intensity time series. A linear fit has been subtracted from the original time series to remove the background trend.

We also applied wavelet analysis, and details of the procedure are given by Torrence & Compo (1998). A randomization method was implemented to estimate the significance level of the peaks in the wavelet spectrum. The top panel in Fig. 5 shows the evolutions of the Doppler shift in spectral pixels averaged over 5’’ in solar Y. The mean value has been subtracted.

The bottom left panel shows the wavelet spectrum and the right panel shows the global wavelet spectrum, which is the sum of the wavelet power over time at each oscillation period. Cross-hatched regions indicate the cone of influence where edge effects become strong.

Due to the limited temporal resolution, only frequencies less than 10 mHz are considered. The wavelet for the Doppler shift (Figure 5) shows strong power at 1.2 mHz for almost the entire duration of the observations. The corresponding power in the global wavelet has a significance level above 99 %. In Figure 6 a similar wavelet analysis procedure is applied to the intensity. A linear fit was subtracted from the time series to remove the background trend. The peak at 1.3 mHz is above the 99 % significance level. The peak for the intensity has a slightly higher frequency that could be due to the phase shifts it may suffer as predicted by Taroyan & Bradshaw (2008). The XRT and EIS images (Figures 1 and 2) suggest that the oscillations correspond to a footpoint region of a loop where the slit crosses the loop. According to linear MHD wave theory, intensity and Doppler shift oscillations are usually associated with an acoustic longitudinal wave. From the analysis of the XRT image, longitudinal motions at the marked location should have a line-of-sight component resulting in the observed Doppler shift. The XRT movie associated with the EIS observations shows that the oscillations are preceded by a small microflare near the footpoint, which would heat the plasma and trigger the oscillations. Such events have been observed by SUMER in high-temperature lines (Wang *et al.* 2003, 2005). The microflare brightening starts at 20:30 UT and ends at 21:00 UT, i.e., around the time when the oscillation starts. The details and the for-ward modelling of microflare-triggered oscillations are discussed by Taroyan *et al.* (2005, 2007). The intensity increase seen in lower temperature lines (*e.g.*, Fe viii and the decrease in higher temperature lines (*e.g.*, Fe xii, Fe xiii, Ca xiii) conforms with the cooling scenario following a transient heat deposition. Fundamental mode standing sausage waves have so far been detected only in hot (T > 6 MK) loops (Wang *et al.* 2002). The presented example could be the first proof of the existence of such oscillations in cooler loops. The rather slow damping is more obvious in the intensity than in the Doppler shift oscillations and requires further theoretical investigation. The quarter-period phase shift seen between the intensity and Doppler shift oscillations in Figure 4 and their relative amplitudes also conform well with a standing-wave scenario (Taroyan & Bradshaw 2008).

2.2 February 21, 2007

The 2007, February 21 observations are again sit-and-stare observations with the 1’’ x 512’’ EIS slit. The exposure time is 50 seconds and the total number of exposures is 70. The observations started at 02:18 UT and lasted about an hour. The observations were carried out in 17 different lines as in the previous case. During the observations, the centre of the slit had average coordinates solar X =348’’’, solar Y =91’’.

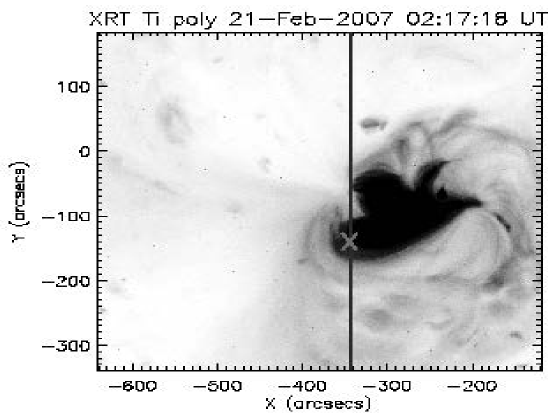

Figure 7 Oscillating coronal loops observed by XRT on the solar disc. The 1’’ EIS slit is marked by a vertical line. The cross indicates the location of the pixels that show oscilla-tions starting at 02:18 UT 2007 February 21.

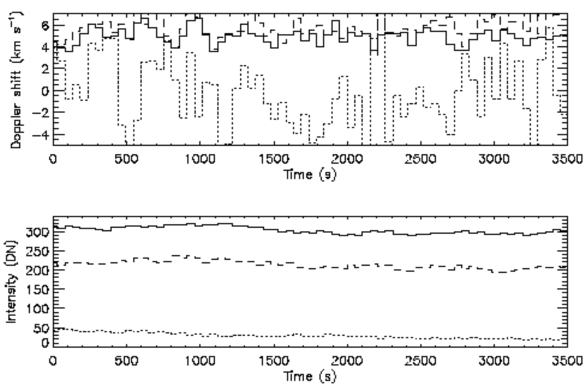

Figure 8 Intensity (DN) and Doppler-shift (km/s) time series for Fe xii 195 Å Fe viii 185 Å and Fe xiii 202 Å are represented by the solid, dotted, and dashed curves. The observations start at 02:18 UT 2007 February 21. An average over 5 adjacent pixels is taken along the slit. The exposure time is 50 seconds and the total number of exposures 70.

The XRT image shows the position of the slit (Figure 7). The standard procedure for data reduction was applied. The Doppler shift has an error of less than 0.6 km s -1 due to the longer exposure time. Oscillatory behavior was detected between pixels 200 and 204. An average of the Doppler shift and intensity was taken over these pixels for Fe xii 195.12 Å, Fe viii 185 Å, Fe xiii 202 Å, and plotted in Figure 8. A damped oscillation with maximum amplitude of 1.5 km s -1 can be seen in the Doppler shift. The intensity in all three lines remains almost constant and does not exhibit any oscillatory behavior. Similar to the previous case, no significant wave power is found elsewhere along the slit.

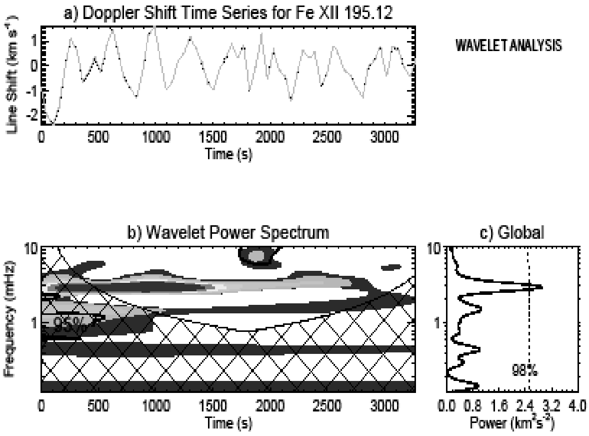

Figure 9 Wavelet analysis for the Fe xii 195 Å Doppler-shift time series shown in Figure 7. The top panel (a) shows the Doppler-shift time series with the subtracted mean value. The bottom left panel (b) displays the wavelet power spectrum. The red colour represents high power, and the blue colour corresponds to low power. The bottom right panel (c) is the global wavelet spectrum. In the global wavelet diagram, the dotted lines indicate 98% significance level.

The wavelet for the Doppler shift (Figure 9) show strong oscillations at 3 mHz that gradually decay. The corresponding power in the global wavelet has a significance level above 98 %. The XRT snapshot indicates that the pixels showing oscillations correspond to a near apex region of a loop where the slit crosses the loop. There is no evidence of an offset microflare or an intensity explosion with a subsequent decrease. Also the high frequency and the absence of intensity oscillations do not favor any interpretation in terms of a slow mode. The XRT image suggests that transverse motions at the marked location should have a line-of-sight component resulting in the observed Doppler shift. Doppler-shift oscillations without accompanying intensity oscillations would indicate the presence of either a torsional Alfven´ wave or a magnetoacoustic kink wave. However, a more plausible explanation is the kink wave since the sum of the torsional motions taken along the slit would most likely cancel out the oscillations seen in the Doppler shift (or, at least, the oscillations would not be in-phase in different pixels). Usually the excitation of transverse kink oscillations is associated with flares and erupting prominences. The present ex-ample seems to have a different origin that we currently do not understand. On the other hand, the five-minute period is similar to the periods of previously reported kink oscillations observed by TRACE (Aschwanden et al. 1999; Nakariakov et al. 1999). Kink oscillations have a broad range of damping times (Aschwanden et al. 2002). The present example is characterized by rather weak damping.

Estimates of coronal magnetic fields are one important application of wave studies. In the case of fundamental mode fast kink oscillations, the magnetic field strength is given by the formula

$$B_0 = 7.9x10^{-13} \frac{n_i^{1/2} d \sqrt{1 + n_e / n_i}}{P}$$

where n_e and n_i are the external and internal number densities measured in m $^{-3}$, d is the loop length measured in m, and P the oscillation period (Nakariakov & Ofman 2001). The XRT image suggests that the loop length is between 0.8 - 1.2x10^8 m, assuming that the loop has a semicircular shape. We also assume that the measured period of 300 s represents the period of the fundamental mode as the most natural and easiest to excite. The density is measured using the ratio between the Fe xii 186.88 and Fe xii 195.12 line intensities. The derived value of the density varies between 4 x10^{14} m $^{-3}$ and 8 x10^{14} m $^{-3}$. The resulting magnetic field strength of the oscillating loop is B_0 = 10.6 G.

3. SUMMARY

The present letter reports on the first detection of coronal oscillations by Hinode/EIS. The observations were carried out in a sit-and-stare 1’’ spectroscopy mode. The intensity and Doppler-shift time series were analysed to interpret the nature of the oscillations. The concurrent XRT images show the location of the oscillations on the solar disc. The first example (2007 February 19) consists of both intensity and Doppler-shift oscillations. These are interpreted as longitudinal sausage waves along a loop that is excited by a footprint microflare. The second event (2007 February 21) has no intensity component in the oscillations. It is most likely a kink type transverse wave. TRACE observations suggest that kink oscillations are usually triggered by flares and prominence eruptions. No such events are seen in the present example, and the source of the oscillations currently remains unknown. Finally, we note that there are other examples that have not been included in this Letter. A more comprehensive analysis including modelling aspects will be presented in a full forthcoming study.

REFERENCES

Aschwanden M. J., De Pontieu, Schrijver B., C. J., & Title, A. M., Solar Phys. 206, 99, 2002

Aschwanden M. J., Fletcher L., Schrijver, C. J., & Alexander D., ApJ, 520, 880, 1999

Berghmans D., & Clette, F. 1999, Sol. Phys., 186, 207

Culhane J. L., Harra L. K., James A. M., *et al.*, Solar Phys., 243, 19, 2007

De Moortel, I., Ireland, J., & Walsh, R. W. 2000, A&A, 355, L23

Kosugi T., Matsuzaki K., Sakao T. *et al.*, Solar Phys., 243, 3, 2007

Nakariakov V. M., Ofman L., DeLuca E. E., Roberts B., & Davila, J. M., Science, 285, 862, 1999

Nakariakov V. M., Ofman L., , A&A, 372, L53, 2001

Nakariakov V. M., Melnikov V. F., & Reznikova, V. E., A&A, 412, L7, 2003
Ofman L., Rokoli M., Poletto G., Noci C., & Kohl J. L. ApJ, 491, L111, 1997
Ofman L., Nakariakov V. M., & DeForest C. E., ApJ, 514, 441, 1999
Taroyan Y. & Bradshaw S. J. A&A (in press), 2008
Taroyan Y., Erdelyi´ R., Doyle J. G., Bradshaw S. J. A&A, 438 713, 2005
Taroyan Y., Erdelyi´ R., Wang T. J., Bradshaw S. J. ApJ 659 L173, 2007
Torrence C., & Compo G.P. 1998, Bull. Meteor. Soc., 79, 61.
Wang, T. J., Solanki, S. K., Curdt, W., et al., ApJ, 574, L101, 2002
Wang T. J., Solanki S. K., Curdt W., *et al.*, A&A, 406, 1105, 2003
Wang T. J., Solanki S. K., Innes D. E., *et al.*, A&A, 435, 753, 2005
Williams D. R., Phillips K. J. H., Rudawy P., et al. MNRAS, 326, 428, 2001

On the Relation of the Forbush Decreases Detected by ASEC Monitors During the 23rd Solar Activity Cycle with ICME Parameters

N. Bostanjyan and A. Chilingarian

Cosmic Ray Division, Alikhanyan Physics Institute, Alikhanyan Brothers 2, Yerevan 375036, Armenia
(e-mail: nikolai@yerphi.am)

Abstract: To improve the physical understanding of the Forbush decreases (FD) and to explore the Space Weather drivers, we need to measure as much geospace parameter as possible, including the changing fluxes of secondary cosmic rays. At the Aragats Space Environmental Center (ASEC) neutral and charged fluxes of secondary cosmic rays are routinely measured. Each species has different most probable energy of primary "parent" proton/nuclei. Therefore, the energy range of the Galactic Cosmic Rays can be estimated (GCR) using data of the ASEC monitor affected by Interplanetary Coronal Mass Ejection (ICME). We presented relations of the magnitude of FD observed in different secondary particle fluxes to the most probable energy of the primary protons. The FD magnitude measured at ASEC during the 23rd solar activity cycle ranges from about 1.5% to 20% in the secondary neutron flux, 1-15%, in the charged low-energy particle flux and 0.7-6% in the >5 GeV muon flux. We investigate the correlations between the magnitude of FD with the size, speed, density and magnetic field of the ICME. We demonstrate that the attenuation of the GCR flux incident on the Earth's atmosphere due to passing of the ICME is dependent on the speed and size of the ICME and the magnetic field strength.

1. INTRODUCTION

The Forbush decreases are the attenuations of the flux of the Galactic Cosmic Rays (GCR) measured by particle detectors on the Earth, on other planets' surfaces and in the interplanetary space before, during and after passage of the Interplanetary Coronal Mass Ejection (ICME). FD takes place in the course of a few hours; over the following several days the GCR intensity returns to pre-FD value.

Using cosmic-ray and magneto-metric measurements Scott Forbush established in 1930s the correlation of worldwide decreases in cosmic-ray intensity with Geomagnetic Storms (GMS, Forbush, 1937). Later he formulated a common geocentric cause for both effects (westward-flowing equatorial ring current as cause of FD, 1939). In 1954 it was recognized that FDs were not produced by the geomagnetic field variations (Simpson, 1954). He claimed on the existence of common mechanism which produces both the accelerating process for cosmic-radiation particles and, indirectly, the geomagnetic disturbances. Examining the relationships among solar activity, GMS, and cosmic-ray intensity, Philip Morrison in 1956 claimed that sporadic emission of clouds of magnetized plasma (now named ICMEs) can modulate the cosmic-ray intensity in interplanetary space and produce terrestrial geomagnetic storms (see Van Allen, 1985 for details).

After establishing that the origin of the non-recurrent FDs are ICMEs and recurrent FDs are caused by the co-rotation of high speed solar wind streams, numerous theoretical and experimental papers were devoted to the possible mechanisms of FD. One of the most intriguing problems was the magnitude of FD. In the paper (L.F. Burlaga and G. Chang., 1988.) authors concluded that relatively large decreases in the cosmic ray intensity are associated with magnetic clouds that are preceded by shocks, whereas only small decreases in CR intensity are associated with magnetic clouds that are not preceded by shocks. Cane, (2000) also pointed that 80% of FD with magnitude greater than 4% (in secondary neutron flux) are connected with passage of shock and ejecta. She also claimed that there should be at least 2 different mechanisms of FD corresponding to the interaction of the GCR with shock and ejecta.

In this paper we made an attempt to research the dependence of the FD magnitude not only on the CME launch helio-coordinates, or existence of the fast shock, but also on the energy of the primary cosmic rays, ICME speed, and ICME density and magnetic field.

In ASEC, (Chilingarian et al., 2003, 2005) we measure neutral and charged fluxes by particle detectors located at 3 different altitudes. Each species has a different most probable energy of primary "parent" proton/nuclei. As we can see from Figure 1, these energies range from 7 (mode of distribution of primary protons generated neutrons) to 40 GeV (the same for muons with energies greater than 5 GeV). New particle detectors now starting to operate in ASEC will prolong this maximal energy up to 200 GeV. Therefore, from the ASEC monitor data we can estimate the GCR energy range affected by ICME and reconstruct actual spectra of the GCRs incident on terrestrial atmosphere, thus revealing the energy-dependant pattern of the ICME modulation effects. Recently analog techniques were developed for the study of the GCR energy and the FD recovery time (Usoskin et al., 2008), with the difference that data was taken from world-wide networks of Neutron Monitors and 3 ground level muon telescopes. Measurements of all the secondary fluxes at one and the same location are preferable due to effects of the longitudinal dependence of the FD magnitudes (Haurwitz et al., 1965).

Also we can introduce several parameters enumerating the "FD-efficiency" of IMCE, for instance, correlation coefficients between time series of different species of secondary cosmic rays. For small FDs the correlation between neutrons and 5 GeV muons is small or moderate. Neutrons are correspondent to lowest energy of primary protons having access to Aragats ~ 7GeV, muons are correspondent to primary protons of most probable energies ~ 40 GeV, see Figure 1. We expected that large FDs will influence primary protons of much greater energies comparing with small ones, therefore correlations between fluxes of secondary neutrons and 5 GeV muons will be much greater for large FDs.

Another parameter possibly sensitive to ICME modulation strength is the power index of dependence of FD magnitude (percent of flux decrease) on energy of primary protons. Proceeding from a variety of particle detectors at ASEC we can reliably estimate the energy dependence of the attenuation of primary particle flux.

In the second section we present the selection criteria of the FD events detected by ASEC particle detectors. In the third section the comparison of the ASEC data with muon data from Moscow engineering-physics institute detectors is performed. The forth section is devoted to correlations of FD magnitude with ICME various parameters.

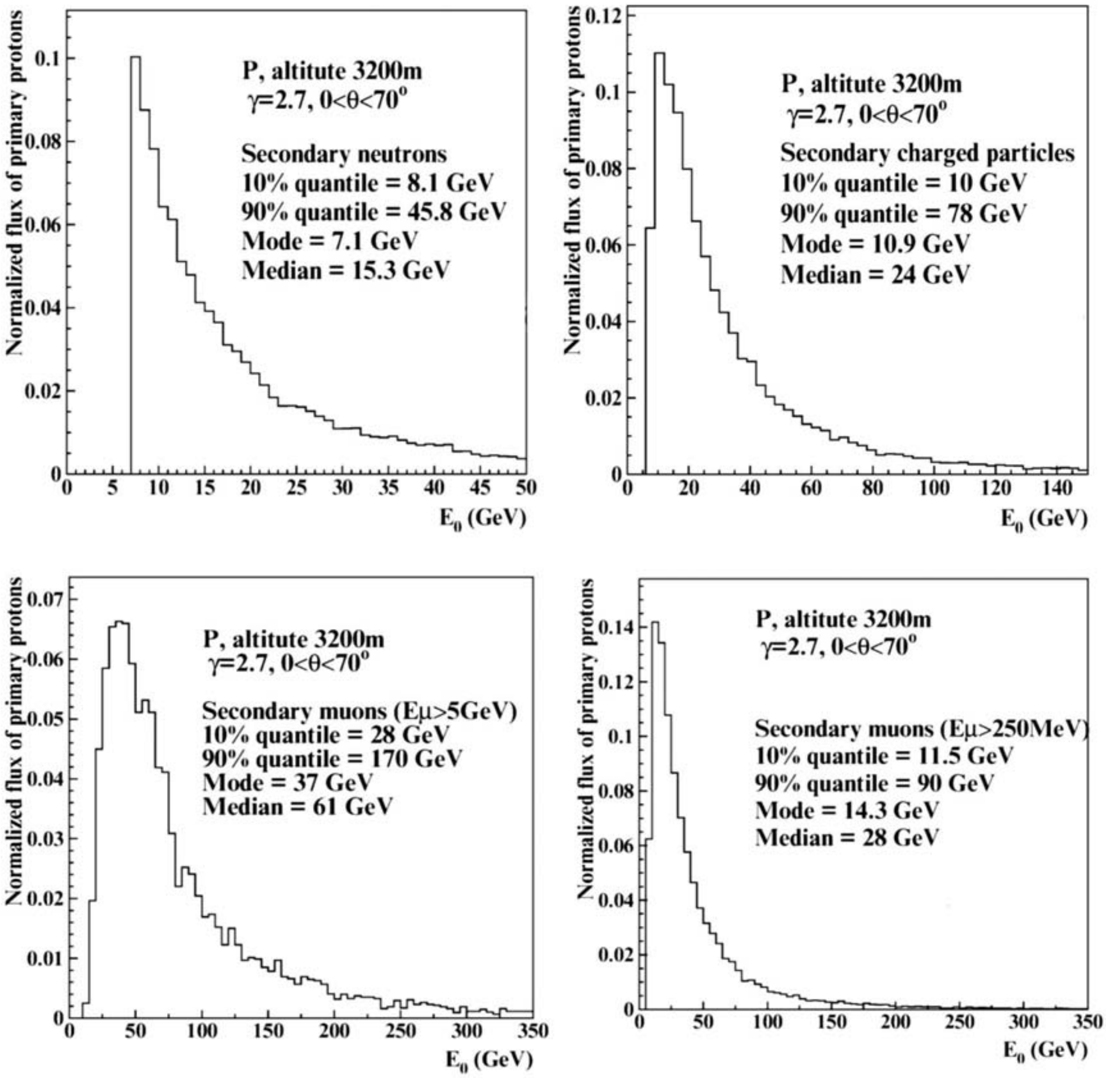

Figure 1. Energy distribution of the GCR protons initiated various secondary particles at Aragats, 3200 m altitude. The characteristic of the distributions (quintiles, mode, median) helps to estimate most probable energy of each of secondary particle species; the detection efficiency equals to the ratio of primary protons to detected particles.

Table 1 Relative decreases of neutrons, low energy charged particles and high energy muons with energies greater than 5 GeV during FD and the corresponding ICME parameters.

	Relative decrease of neutrons (%)	Relative decrease of charge component (%)	Relative decrease of muons >5GeV	Correlation coefficient between 1 minute time series of neutrons and muons >5GeV	Power index of the fit of FD magnitude vs primary energy	Maximum speed of solar wind km/s (by ACE, SOHO)
2002.09.07	3.6	2.6	1	0.64	-0.99	570
2003.10.29	20	15	6	0.97	-0.89	>1000
2003.11.20	3.8	2.8	1	-	-	730
2004.01.22	7.5	4	1.3	0.88	-1.26	690
2004.07.27	10	7	3	0.97	-0.88	1000
2004.11.09	6	2.5	1.2	0.45	-1.11	800
2005.01.17	5.1	3.6	1	0.65	-1.21	800
2005.05.15	6.7	4	1.4	0.7	-1.13	875
2005.09.11	10	5.5	1.7	0.93	-1.28	1000
2006.12.14	4.7	1.7	0.7	0.84	-1.4	900

2. SELECTION OF THE FD EVENTS DETECTED BY ASEC

In Table 1 we present selected FD events detected by the ASEC particle detectors during 2002-2006 and introduce indices reflecting the "modulation strength" of the corresponding ICMEs. We select data from 3 ASEC monitors covering a large range (7-40 GeV, columns 2-4) of the primary proton energies. Correlation coefficients are calculated at FD attenuation phase by 1-minute time series for intervals of 5-10 hours (by 300 – 600 points), column 5. In column 6 we post the index of the fitted power function dependence of FD magnitude on the primary energy. The power function fit was done for 3 points correspondent to FD magnitude in fluxes of neutrons, low energy charge particles and muons with energies above 5 GeV, as it is demonstrated in the figure 3. In the last seventh column the maximal solar speed from 1-min data measured by instruments SWEPAM, ACE and SOHO is posted.

In Figure 2 we can see the relative decreases in different secondary fluxes (neutrons, low energy charged particles, muon with energies greater than 5 GeV) for selected FD events. As it is expected, the relative decrease of definite species of secondary cosmic rays is inversely proportional to the most probable energy of primary generating this species. The most pronounced FD is observed on November 20, 2003 in neutron flux (~20%) and lowest - in >5 GeV muon flux (~6%).

The correlation matrix of the largest detected FD of cycle #23 on October 29, 2003 is posted in Table 2. We can see very large correlation coefficients between the neutrons and >5 GeV muon fluxes (most probable energies of primary protons ~7 and ~40 GeV, respectively). ICME having originated the FD on October 29, 2003 was so huge that it equally influenced the GCR flux at least till energies up to 40 GeV. In the scatter plot of the FD magnitude and the correlation coefficient between neutron and > 5GeV muon fluxes (Figure 3) we can notice a trend, showing growing correlation coefficients for FDs with large magnitudes.

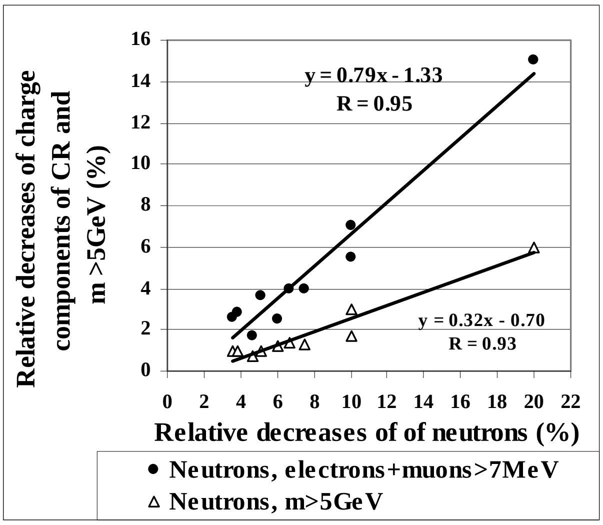

Figure 2 Relative decreases of the charged CR compared with neutron

Another possible parameter characterizing the FD strength is the functional dependence of the relative magnitude on the most probable primary energy. In Figure 4 the dependence of the FD magnitude (for events of 29 Oct. 2003 and 27 July, 2004) of the different secondary cosmic ray species (neutrons, charged particles and muons with energies greater than >5 GeV) was approximated by the power function. We can see that quality of fit is very high and we can use the power index of the dependence as a parameter to characterize the FD strength. In the Figure 5 we post the scatter plot of spectral indices calculated for the FDs from Table 1 vs magnitude of FD in charged component (we use only events in which all the 3 mentioned fluxes were observed. Although scattering of points is rather large, obviously larger FDs are correspondent to the biggest indices (weaker dependence of FD magnitude on the primary energy).

Table 2 Correlation matrix of time series of different secondary fluxes measured by ASEC on 29 October 2003

Type of facility	ANM	NANM	SNT Thr0	SNT Thr 1	SNT Thr 2	SNT Thr 3	SNT Thr 4	Muons > 5Gev
ANM	1							
NANM	1.00	1						
SNT Thr 0	0.99	0.99	1					
SNT Thr 1	0.99	0.99	1.00	1				
SNT Thr 2	0.99	0.99	0.99	1.00	1			
SNT Thr 3	0.98	0.98	0.99	0. 99	0.99	1		
SNT Thr 4	0.98	0.98	0.99	0.99	0.99	0.99	1	
Muons > 5Gev	0.97	0.97	0.97	0.97	0.97	0.96	0.95	1

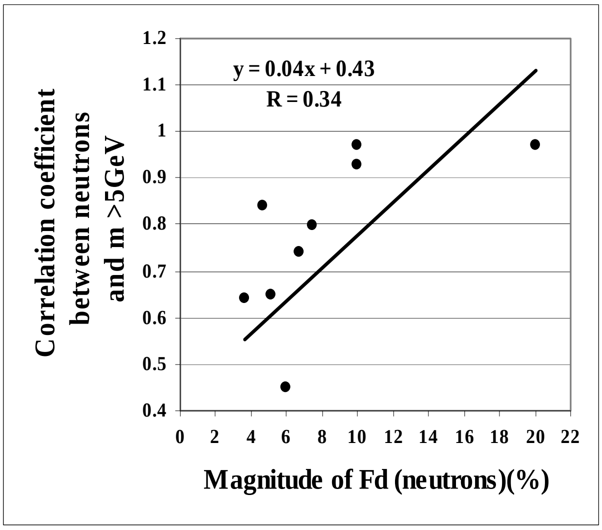

Figure 3. Dependence of FD magnitude (neutrons) and correlation coefficient between Neutron Monitors and Aragats Multichannel Muon Monitor (>5 GeV muons) time series

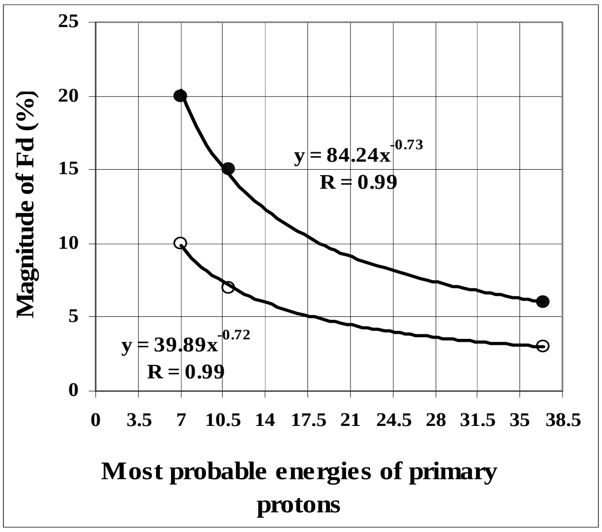

Figure 4 Dependence of the magnitude of Forbush decrease on the primary energy.

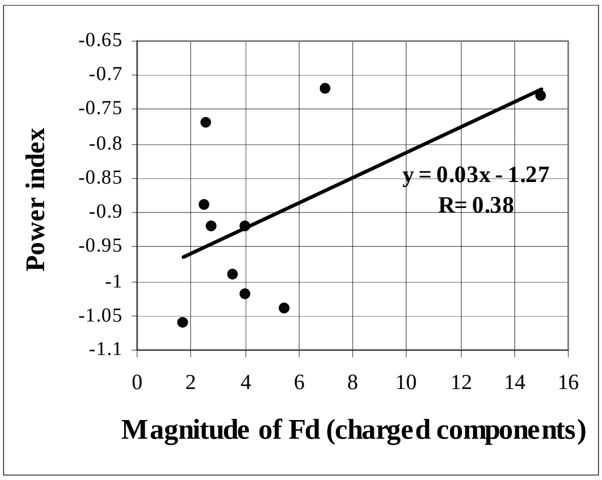

Figure 5 Dependence of the FD magnitude (in charged secondary flux) and the value of the power index.

3. JOINT ANALYSIS OF FD WITH THE MOSCOW ENGINEERING-PHISICS INSTITUTE MUON DETECTOR DATA

Muon rate variations during some of the FDs of the 23rd solar cycle were registered by muon detectors DECOR, TEMP and URAGAN operating in the experimental complex NEVOD (MEPhI, Moscow, Barbashina et al., 2007). MEPhI data can path the gap between low energy charged particles and high energy muons (> 5 GeV) measured by ASEC. In Table 3 and Figure 6 we present the data on a FD, which occurred on May 15, 2005. Because MEPhI group publish data corresponding to median energies of primary flux, we also present ASEC data accordingly. In Figure 6 we see good agreement for data obtained by detectors located at different latitudes and altitudes. It is evident that FD magnitude in the high energy muon flux measured on the Earth's surface is global characteristic, approximately the same for different detector locations.

Table 3 Magnitudes of FD detected on May 15, 2005 by MEPhI and ASEC

	Median energies of primary (GeV)	Magnitude of FD (%)
Moscow NM	10	7.3
ANM	15	6.7
Charged ANI	24	3.8
URAGAN	23	3.3
TEMP	28	2.8
DÉCOR	50	2.2
AMMM	60	1.34

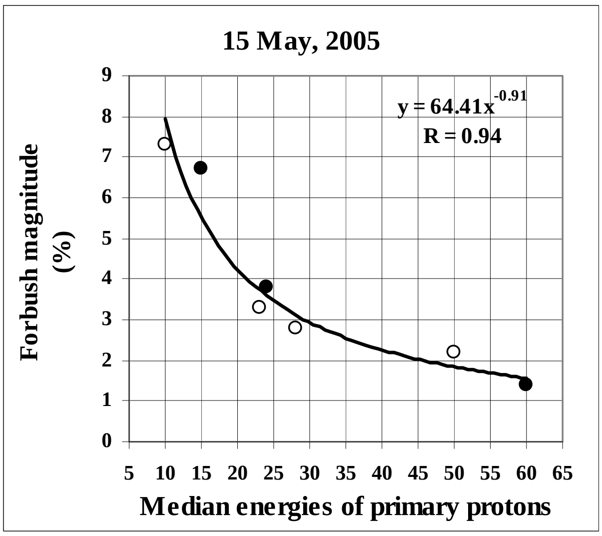

Figure 6 Observation of the FD from 15 May 2005 by MEPhI (for ASEC monitors we use medians of primary proton energy distributions). Open symbols – MEPHi data, close symbols – ASEC data.

4. RELATION OF THE FD MAGNITUDE TO THE ICME PARAMETERS

The attenuation of the GCR flux due to approaching ICME is dependent on its speed, size, the field strength, and the orientation as well as on the pre-shock conditions of the Interplanetary Magnetic Field (IMF). Most of these parameters are rather difficult to measure and interpret; therefore, the explanation of the mechanisms of FD mechanisms still lacks many details. For instance, it is rather difficult to estimate the spatial elongation of the ICME. The standard technique of measuring ICME thickness is based on the detection of the region with low proton temperature in solar wind passing ACE and SOHO spacecraft and simultaneously – the mean speed of solar wind (V_{sw}, see Richardson & Cane, 1995; Gopalswamy, 2006). However, this method is not applicable for the multiple colliding ICMEs; disturbances of IMF by previous ICMEs; nonlinear interactions of ICME and magnetosphere, etc.

The method we use is similar to the described one, with the difference that the time of ICME passage is estimated by the duration of FD decreasing phase (from the start of count rate decrease until maximal decrease). Both methods meet difficulties to distinguish successive ICMEs, as an example let's consider the FD occurred at ~18:00 on November 7, 2004: the solar wind speed enhanced by ~200 km/sec and the neutron count rate started to decrease. However, patterns of both count rate and solar wind changes are rather complicated, showing several peaks and dips. Therefore, estimation of the size of the ICME is not a simple arithmetic and for reliable estimation we need "clear" events involving a single ICME.

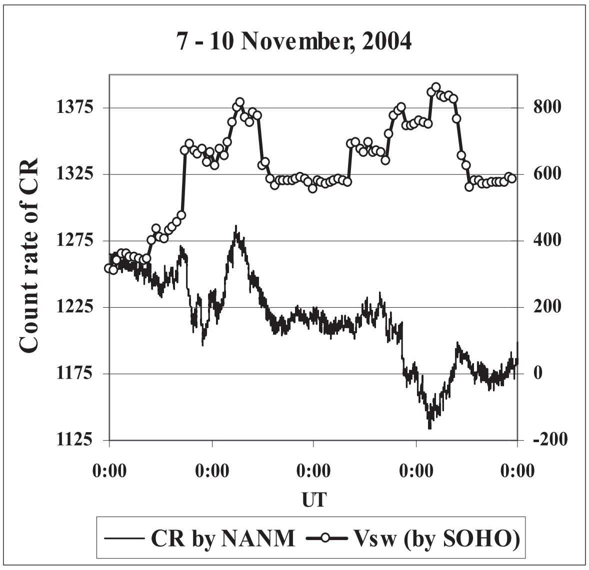

Figure 7 Several successive ICMEs and geomagnetic storm prevents reliable estimation of the ICME size.

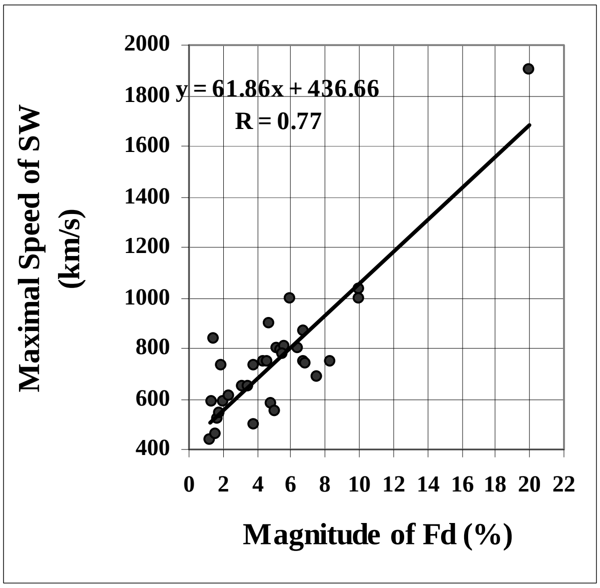

Figure 8 Dependence of the magnitude of the Forbush decrease on the maximal solar wind speed.

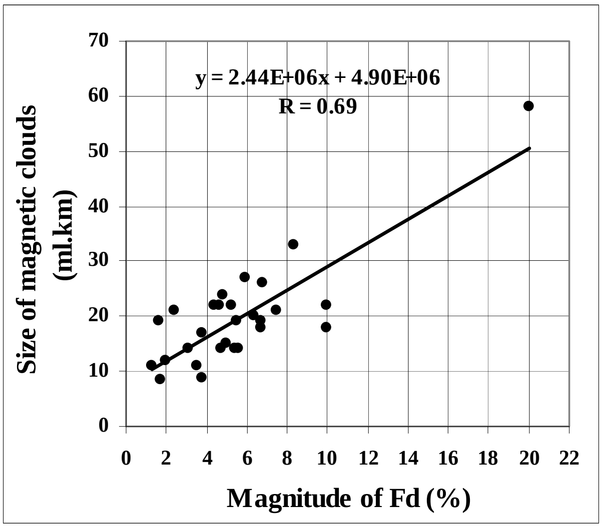

Fig. 9. Dependence of the magnitude of Forbush decrease on the value of solar wind speed jump, for 32 events.

The selected standalone ICMEs that generated FDs and allowing estimation of the sizes of ICME are posted in the Table 4. The helio-coordinates of the CME are posted in first column, the date in the second. In the third column we posted the FD magnitude in neutron flux. In columns 3-6 are posted the ICME parameters as measured by ACE spacecraft facilities. Maximal speed of Solar Wind (Vsw) and density of solar wind protons are estimated by data from instrument SWEPAM of ACE spacecraft; B-total values are from MAG facility of ACE. The same procedure was applied to all ICMEs that unleash FD to calculate sizes of ICME; the estimated duration of the FD decreasing phase is posted in the seventh column and corresponding calculated size of IMCE – in the eighth. Data from Table 4 was used to investigate correlations between magnitude of FD and ICME parameters. As we can see in Figure 8 and 9 there is a pronounced dependence between the FD magnitude and ICME speed and size. The dependence of the FD magnitude on the ICME magnetic field is much weaker (Figure 10). However, if we exclude the FDs accompanied by strong geomagnetic storms (the depression of CR intensity is someway masked by the reduced cutoff rigidity leading to CR flux enhancement) the discrepancy of points on scatter plot reduces. In Figure 11 we post the same events as in Figure 10, excluding events occurred on May 5, 1998, March 31, 2001, and November 20, 2005. The correlation between FD magnitude and change (jump) of total magnetic field measured by MAG facility of ACE spacecraft are highly enlarged. And we did not observe any significant correlation between FD magnitude and Solar Wind density (Figure 12).

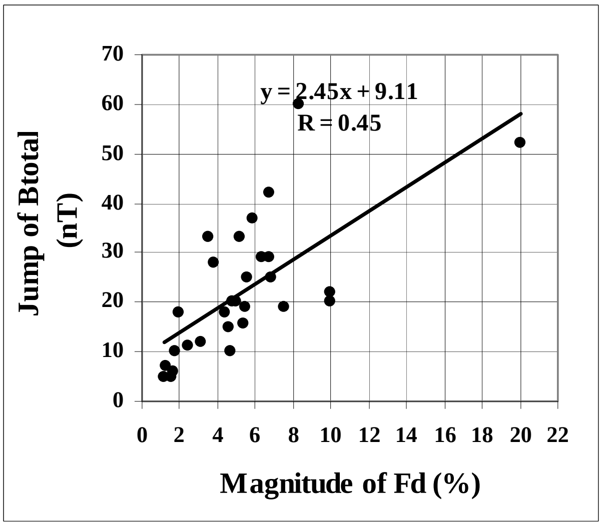

Figure 11 Dependence of the estimated ICME linear size on the FD magnitude for 28 events.

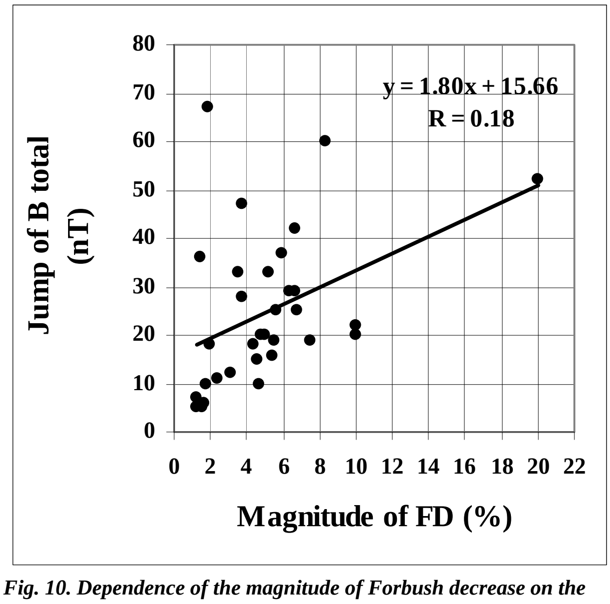

Fig. 10. Dependence of the magnitude of Forbush decrease on the value of solar wind speed jump for Oulu NM. (The magnitude of FD is larger for Oulu compared with Aragats).

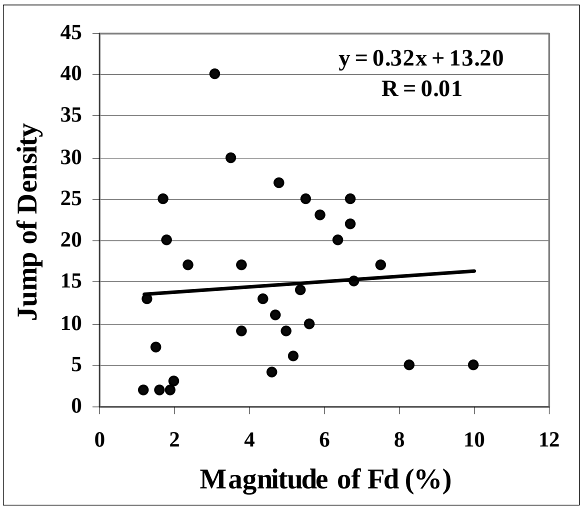

Fig.12 Dependence of the magnitude of Forbush decrease on the density of solar wind (SW density corresponds to the ICME sheath regionl

Table 3 "Standalone" ICMEs that generates FD

The Solar Source of CME	Years, Months, Days	Relative decrease of neutrons (%)	Maximum speed of SW km/s (by ACE, SOHO)	Jump of density of SW	Jump of B_{total} (nT) By ACE	Durations of decrease phase (hour)	L –size of clouds, associated with decrease phase of FD
?	2000.11.26	1.2	435	5	5	?	*
?	2000.11.06	1.3	590	2	7	5	1.1E+07
S15,W15	1998.05.04	1.5	835	13	36	?	*
?	2000.08.10	1.6	460	7	5	12	1.9E+07
N07,W56	2000.02.11	1.7	520	2	6	5	8.4E+06
N14,W12	2001.03.31	1.9	730	25	67	?	*
S07,E89	2003.06.17	1.8	540	2	10	?	*
S17,W40	2000.02.12	2	590	20	18	6	1.2E+07
N20,E70	1999.09.15	2.4	615	3	11	10	2.1E+07
N16,W18	2001.10.21	3.1	650	17	12	7	1.4E+07
N26,W10	2001.08.17	3.8	500	30	28	7	8.8E+06
N00,E18	2003.11.20	3.8	730	17	47	7	1.7E+07
N10,E08	2004.11.7	3.9	650	40	33	5	1.1E+07
N17,W31	2001.04.28	4.4	750	9	18	9	2.2E+07
S21,E31	2001.04.08	4.6	750	13	15	8.5	2.2E+07
S06,W24	2006.12.14	4.7	900	4	10	4.5	1.4E+07
N09,W28	2002.09.7	4.8	580	11	20	13	2.4E+07
S23,E17	2001.10.11	5	550	27	20	8	1.5E+07
N15,W05	2005.01.17	5.2	800	40	33	8.5	2.2E+07
N19,W85	2001.04.04	5.4	790	6	15.5	5.5	1.4E+07
N18,E09	1998.09.24	5.6	810	14	25	6.5	1.40E+07
N20, E18	2000.06.08	5.5	780	10	19	7	1.9E+07
N22,W07	2000.07.15	5.9	1000	25	37	7.5	2.7E+07
N08,W28	2004.11.9	6.4	800	23	29	7	2.0E+07
N12,E12	2005.05.15	6.7	870	20	42	6	1.8E+07
S18,E27	2001.04.11	6.7	750	25	29	7.5	1.9E+07
S16,W12	2001.09.25	6.8	740	22	25	11	2.6E+07
S23,W09	2004.01.22	7.5	690	15	19	9	2.1E+07
N06,W18	2001.11.06	9.4	790	30	60	13	3.3E+07
N04,W30	2004.07.27	10	1035	5	22	5	1.8E+07
S01,E70	2005.09.11	10	1000	5	20	6	2.2E+07
S16,E04	2003.10.29	20	1900**	?	52	11.5	5.8E+07

5. CONCLUSION

We perform a statistical study of FD decreases detected by the ASEC particle detectors during 23rd solar activity cycle. We present relations of the measured magnitude of FD in different secondary particle fluxes to the most probable energy of the primary protons of GCR that initiated these fluxes. The FD magnitude measured in ASEC during the 23rd solar activity cycle ranges from about 1.5% to 20% in the secondary neutron flux, 1-15% in the charged low-energy particle flux and 0.6-6% in the >5 GeV muon flux. We introduce two indices to enumerate the ICME "modulation strength", namely:

- the correlation coefficient of time series of two secondary CR species (neutrons and muons with energies greater than 5 GeV), corresponding to the highest and lowest primary proton energies;
- the power index of the estimated power dependence of the FD magnitude on the most probable energy of primary protons.

Both indices demonstrate apparent positive trend, proving obvious fact that if FD magnitude is large, both low and high energy primaries will be affected by ICME. However, rather large scattering pointed that proposed indices should be calculated by subsamples of events, after applying more specific selection criteria.

Neutron Monitor data was only used for analysis of characteristics of single ICMEs causing Forbush decreases. The modulation strength of the ICMEs is highly correlated with the speed and size of ICMEs, but not with solar wind density. The correlation with ICME magnetic field can be significantly enlarged if we exclude events accompanied with strong geomagnetic storms.

ACKNOWLEDGEMENT

This work was partly supported by ISTC A1554 grant and INTAS 8777 grant. Authors thank N. Gopalswamy and G. Karapetyan for useful discussions and the ASEC staff for providing continuous operation of the particle detectors during the 23rd solar activity cycle.

REFERENCES

Barbashina N.S., Dmitrieva A.N., Borog V.V. Investigation of Forbush effects in muon flux measured in integral and hodoscopic modes. Proc. 30th Intern.Cosmic Ray Conf., 1, 315–318, 2007.

L.F. Burlaga and G. Chang., J. Gephys. Res., 93, 2511-2518, 1988.

Cane H.V. Coronal Mass Ejections and Forbush Decreases. Space Science Reviews 93, 55-77, 2000.

Chilingarian A.A., Avagyan K., et al., J.Phys. G:Nucl.Part.Phys. 29, 939-951, 2003

Chilingarian A.A., Arakelyan K., et al., NIM, A543, 483-496, 2005

Forbush S.F. On the effects in cosmic-ray intensity observed during the recent magnetic storm, Phys. Rev. 51:1108-09, 1937.

Forbush S.F. World-wide changes in cosmic-ray intensity, Rev. Mod. Phys. 11:168-72, 1939.

Gopalswamy N. Properties of interplanetary coronal mass ejections. Space Science Reviews, 2007

Haurwitz M.W., Yoshida S., and Akasofu S.I. (1965), Interplanetary Magnetic Field Asymmetries and their Effects on Polar Cap Absorption Effects and Forbush Decreases, J.Geophys.Res 70, 2977-2988.

Richardson I. G. and Cane H. V. Regions of Abnormally Low Temperature as Signatures of Ejecta in the Solar Wind and Their Solar Sycle Dependece. Proc. 24th ICRC,4., 868.,1995.

Simpson J.A., Cosmic-Radiation Intensity-Time Variations and Their Origin, Phys. Rev. 94, 426 – 440, 1954.

Usoskin I.G., Braun I., Gladisheva O.G., et al., Forbush decrease of cosmic rays Energy dependence of recovery phase, J.Geophys.Res., 113, A07102, doi:10.1029/2007JA012955, 2008.

Van Allen J.A., Scott Ellsworth Forbush, biographical memoirs, http://books.nap.edu/html/biomems/sforbush.html, 1985

Cosmic Ray Intensity Increases Detected by ASEC Monitors During the 23rd Solar Activity Cycle in Correlation with Geomagnetic Storms

N. Bostanjyan and A. Chilingarian

Cosmic Ray Division, Alikhanyan Physics Institute, Alikhanyan Brothers 2, Yerevan 375036, Armenia
(e-mail: nikolai@yerphi.am)

Abstract: Interplanetary Coronal Mass Ejections (ICMEs) dominate the intense Geomagnetic Storm (GMS) occurrences and simultaneously they are correlated with the variations of the spectra of particles, ranging from the isothermal solar wind ions to GeV energy protons and fully stripped nuclei. The aim of this paper is to get more insight in the correlations of ICME parameters with geospace parameters, including the Dst index and the secondary Cosmic Ray (CR) flux. Our observations of the GMS occurred during the 23rd solar activity cycle demonstrates that the count rate increase during GMS occurs coherently (or up to one hour in advance) with Dst changes.

We show that the ratio between the increases of neutron and charged fluxes is approximately constant in a large range of the GMS severity (-470 - 20 nT). The neutron flux always undergoes larger changes comparing with the charged component. The difference in peak amplitude can be explained by the lower energy of the primary particles initiated neutrons comparing with primaries generated electrons and muons reaching Earth's surface. Also we illustrate that the main driver of GMS is southward B_z component of magnetic field of ICME. Thus, the information on the flux changes for different secondary particles helps to "test" the models of Interplanetary Magnetic Field (IMF) and the magnetosphere for understanding of the level of disturbance and the specific mechanisms leading to cutoff rigidity reduction.

1. INTRODUCTION

Huge magnetized plasma clouds and shocks initiated by Coronal Mass Ejections (CME) travel in the interplanetary space with mean velocities up to 2500 km/sec (the so called Interplanetary Coronal Mass Ejection (ICME), are known as major drivers of severe space weather conditions when arriving at the Earth. On their way to the Earth ICMEs also "modulate" the flux of Galactic Cosmic Rays (GCRs) introducing anisotropy and changing energy (rigidity) spectra (Dvornikov et al., 1988) of the previously isotropic population of protons and stripped nuclei accelerated in the numerous galactic sources. Changes in the rather stable flux of GCR are detected by space-born spectrometers (rigidities up to ~1GV) and by world-wide networks of particle detectors (rigidities up to ~100GV) located at different latitudes, longitudes and altitudes.

The magnetic field found in some ICMEs known as magnetic clouds usually has a well-formed flux-rope structure (see Koskinen & Huttunen, 2006 and references therein). The cross-section of the magnetic "rope", a twisted bundle of magnetic fields, connecting the Earth's magnetosphere directly to the Sun, was observed by the THEMIS satellites on May 20, 2007 (see NASA science, 20.03.08). This can explain the "collisionless" transport of Solar Cosmic Rays (SCR) via "highways" inside the magnetic system connected Sun with ICME (see Valtonen, 2007 and references therein for details).

The ICME is a major modulating agent, interacting with GCR, and introducing anisotropy in their flux. The anisotropy of GCR manifested itself as peaks and deeps in time series of secondary cosmic rays, detected by surface particle detectors.

Therefore, measurements of secondary fluxes can be used for "probing" ICMEs, providing highly cost-effective information on the key characteristics of these interplanetary disturbances. The size and magnetic field strength of ICMEs are correlated with the ICME modulation effects on the energy spectra and direction of GCRs. At the same time the presence of strong and long-duration southward magnetic field component in the sheath region of ICMEs is the primary requirement for their geoeffectiveness (Valtonen, 2007 and references therein). Thus, strong magnet field of the ICMEs is the modulation agent for both the GCR and the driver of GMS.

Although there is no one-to-one dependence between the variations of the GCR and the strength of GMS (see Kudela & Brenkus, 2004) and there exist other drivers of storms and modulation agents of GCRs, the large B_z value associated with approaching ICMEs is a best known diagnostics of GMS strength. Therefore, appropriate observations of the variations of the primary and secondary cosmic rays can be a proxy of B_z value available long before IMCEs reach the L1 libration point where B_z is measured directly (see e.g., Kudela & Storini, 2006).

The Solar and Heliospheric Observatory (SOHO) - detected relativistic electrons by its Comprehensive Suprathermal and Energetic Particle Analyzer (COSTEP, R. Müller-Mellin et. al., 1995) instrument. Enhancements in the electron flux also can point to an approaching ICME. The modulation effects posed by ICMEs on the particles of higher energies, not measurable by space-born facilities due to very weak fluxes, are detected by the world-wide networks of Neutron Monitors (NM) that respond to GCRs with rigidities 1 - 14 GV and Muon Telescopes (MT) that respond to GCR rigidities 2-100 GV well before the onset of a major geomagnetic storm (Belov et al., 2003, Munakata et al., 2000).

In addition, analysis of the correlations of the changes of cosmic ray fluxes in large energy range with geomagnetic effects makes it possible to check the development of the current system models on different stages of the geomagnetic storm (Belov et al., 2005, Kudela et al, 2008).

GMS usually lead to the increase of intensity of secondary CR flux. In contrast to the modulation effects caused by other solar transient events (Forbush decreases, Ground Level Enhancements) the GMS modulation effect is more pronounced at middle latitudes and not at high latitudes. The variety of particle detectors of the Aragats Space Environmental Center (ASEC, Chilingarian et al., 2003, 2005), allows us to extend the maximal energies from hundreds of MeV accessible to space-born facilities up to tens of GeV.

The aim of this paper is to get more insight into the correlations of IMCE parameters with geospace parameters, including changing intensities of the particle fluxes measured at the Earth's surface.

2. SELECTION OF THE PARTICLE EVENTS RELATED TO THE ICME-INDUCED GEOMAGNETIC EFFECTS.

Selection of the particle events related to geomagnetic storms was made by correlation analysis of the cosmic ray fluxes measured by the particle detectors operating at ASEC, the intensity of geomagnetic storm measured by magnetometers located at middle latitudes and summarized as Dst index at the World Data Center for Geomagnetism, Kyoto, (http://swdcdb.kugi.kyoto-u.ac.jp/) and B_z measurements in transient magnetic structures at their passage of the ACE spacecraft (http://www.srl.caltech.edu/ACE/ASC/level2/lvl2DATA_MAG.html) . The typical pattern of the inter-correlation of CR intensity, Dst index and B_z is apparent in Figure 1. On 20 November, 2003 a very large increase of CR intensity was detected by Aragats Neutron Monitor (~7.5%) after a small Forbush decrease (Fd). As we can see in Figure 1 the Dst index was decreasing reaching a record value -472 nT, the severest GMS of cycle 23 (Gopalswamy et al., 2005). The correlation coefficient (R) between the 1-hour time series of the Dst index and the neutron flux is -0.91 for the time span between 14:00 UT on November 20 and 05:00 UT on November 21. Better anti-correlation (R = - 0.96) is achieved with a one-hour shifted Dst time-series taken from 15:00 UT on November 20 to 06:00 UT on November 21). We also present in Figure 1 the most "geoeffective" ICME characteristic - B_z. Magnetic field of the ICME and geospace parameters (Dst and neutron flux, measured at the Earth surface) are well correlated; and the ICME magnetic field influenced both the cosmic ray flux and unleashed geomagnetic storm. The Bz minimum (-48 nT) the CR intensity maximum and the Dst minimum occur at 16:30 UT, 19:00 UT, and 20:00 UT, respectively. The maximal "delayed" correlation (~2.5 hours) between the CR intensity and B_z reaches – 0.7.

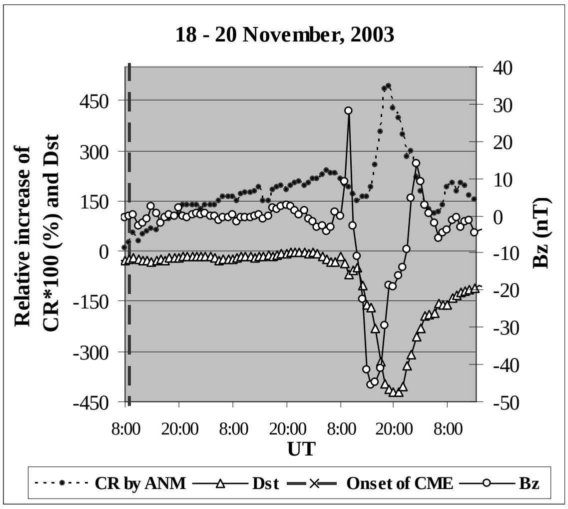

Figure 1 Coherent changes of the neutron flux intensity, Dst index and Bz; note the pronounced peak in the neutron flux. CR intensity is multiplied by 100.

Coherent changes of CR intensity and Dst index pointed on the effective decrease of the strength of the geomagnetic field, because of its coupling with the ICME magnetic field. As we mentioned in the introduction, such effects are triggered by ICMEs with strong southward magnetic fields. Decrease of cutoff rigidity will allow primary protons and nuclei (with energies lower than usual) enter the atmosphere and generate particle cascades reaching the Earth's surface, thus increasing the count rate of particle detectors. However, not all secondary fluxes will enhance. In Figure 2, the energy distributions of the primary protons, which generated neutrons and low and high energy muons are depicted. Primary protons of energies immediate continuing the ones corresponding to the cutoff can generate secondary neutrons, oppositely the ≥ 5 GeV muons can be generated only by primary protons with energies ≥15 GeV (see also Wang & Wang, 2006a). Therefore, the flux of high energy muons detected by the Aragats Multichannel Muon Monitor (AMMM) during 20 – 21 November, as we can see in Figure 3, stay unchanged during the severe disturbance of the magnetosphere.

The decrease of the cutoff rigidity cannot influence the ≥ 5 GeV muon flux because the primary protons have much more energy than that corresponding to the rigidity cutoff.

In Figure 4 we can see another kind of neutron intensity enhancement not correlated with sudden commencement of geomagnetic storm. On May 15, 2005, after the large Fd, we detect 4.3% enhancement of Aragats Neutron Monitor (ANM) count rate, but the delay of the flux maximum compared with the observed minimum of Dst was approximately 3 hours. Furthermore, the 5 GeV muons also demonstrate the peak apparent in the Figure 5, thus the interplanetary magnetic field (IMF) or/and system of magnetospheric currents was highly disturbed to enable additional portion of the high energy primary protons to enter the atmosphere.

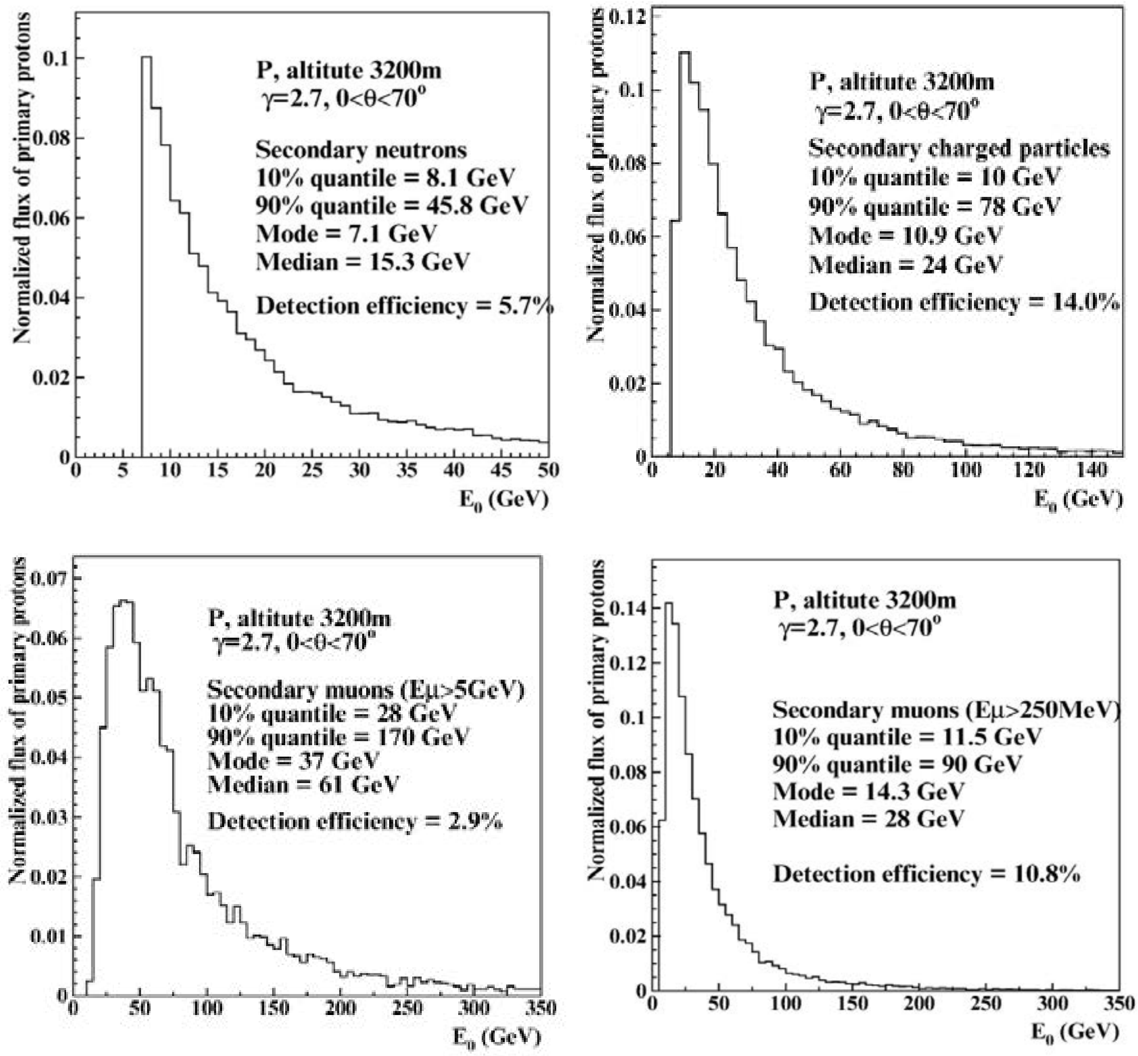

Figure 2 Energy distribution of the GCR protons initiated various secondary particles at Aragats, 3200 m altitude. The characteristic of the distributions (quintiles, mode, median) helps to estimate most probable energy of each of secondary particle species; the detection efficiency equals to the ratio of primary protons to detected particles.

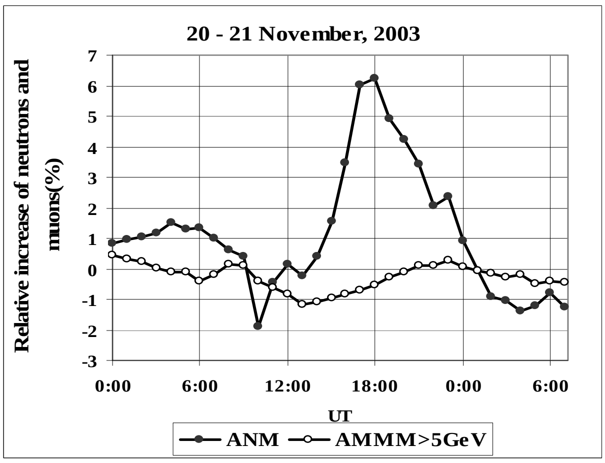

Figure 3. Changes of the hour time series of Aragats Neutron Monitor (ANM) and Aragats Multichannel Muon Monitor (AMMM); no peak is detected in the >5 GeV muon flux.

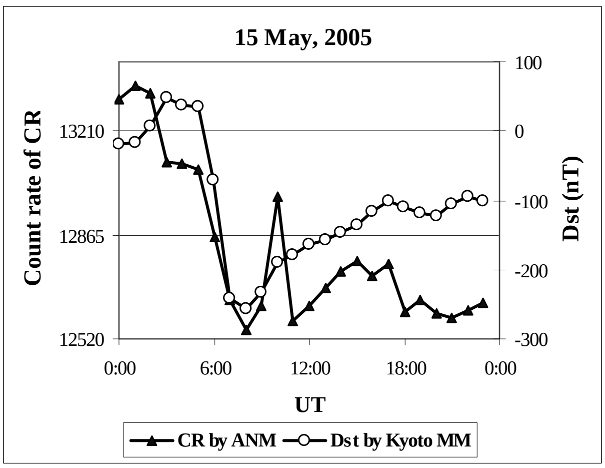

Figure 4. Hourly time series of Aragats Neutron Monitor count rate and the Dst index; Uncorrelated changes.

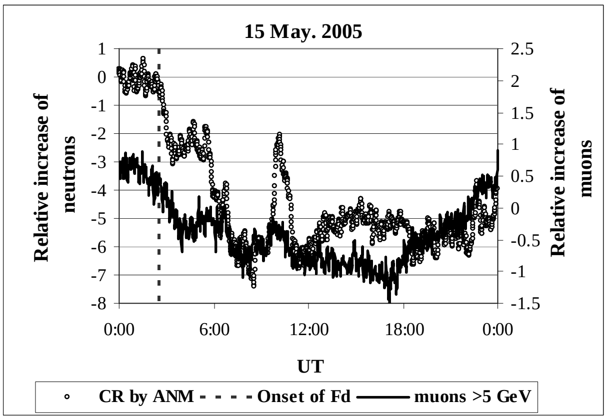

Figure 5 Time series of count rates of neutrons and > 5 GeV muons demonstrate coherent peaks at a overall decrease of the cosmic ray intensity.

Table 1 Characteristics of enhancements of the neutral and charged fluxes during GMS and the corresponding ICME and IMF parameters as well as heliocoordinates of the CME launch.

Date	Heliocoo-rdinates of CME	Increase of neutron count rate (%)	Increase of charged CR count rate (%)	Dst (nT)	Bz (nT)	Delay times between Dst and B_z minimums (hours)	Max. speed of ICME (km/s)	Jump of Solar WindV_{sw} (km/s)
2003.06.17	N20,E70	0.5	*	-21	-11	3	515	0
1999.09.15	S07,E89	1.36	*	-22	-12	1	615	105
1998.09.24	N18,E14 or S20,E22	1.2	*	-27	-9.4	5	520	70
1998.03.10	S24,W67	0.97	*	-28	-12	4.5	350	20
2000.08.10	?	1.1	*	-29	-11	3.2	460	100
2003.06.17	?	1.4	0.68	-38	-12	2	535	0
2004.11.09	N09, W17	1.6	0.65	-66	-14.8	2	695	118
1998.03.21	?	2.6	*	-76	-23	2.3	600	180
2004.11.07	N08,E15	1.9	*	-80	-20	3	688	214
2000.08.11	N22W71	1.4	*	-81	-20	6	440	0
2003.06.18	S07,E80	4	*	-107	-22	3.5	556	100
2002.09.07	N09,W28	2.3	1	-112	-25	2.5	570	180
1998.08.06	S19,E78	2.3	*	-115	-21	3	430	60
1999.10.22	?	2.6	*	-128	-21	3	690	195
1998.05.04	S15,W15	3.1	*	-143	-26	2	860	380
1998.09.25	N18,E09	3.5	*	-166	-36	2.5	830	400
1999.09.23	N21,W76	3.7	*	-191	-38	3.2	600	245
2000.08.12	N11,W11	3.7	*	-205	-40	2.5	670	250
2005.08.24	?	3.64	1.4	-216	-51	1.5	750	200
2003.10.30	S15,W02	4.1	1.7	-283	-36	2.5	>1000**	
2003.10.29	S16,E08	5.6	2	-320	-41	5	>1000**	
2004.11.08	N10,E08	5.9	2.2	-413	-48.5	4	814	340
2001.03.31	N20,W19	6	*	-415	-48	2.3	770	330
2003.11.20	N00,E18	7.5	3	-455	-49	4	770	325

* no ASEC data available

** On October 29 and 30, 2003 the ACE solar wind detector was put in stand-by mode and SOHO detector was saturated.

Examining all cases of coherent changes of count rate and Dst index we selected 24 GMS events (for 8 of which we also have time series of low and high energy muons). Characteristics of these events are listed in Table 1; events are arranged in ascending order of GMS severity measured by Dst index.

Characteristics of the CME are from Master Data Table of Major Geomagnetic Storms (1996-2005) **http://cdaw.gsfc.nasa.gov/geomag_cdaw/Data_master_table.html**; increase of the neutral and charged cosmic ray species is measured during GMS by ASEC particle detectors; Dst index is taken from the World Data Center for Geomagnetism, Kyoto, **(http://swdcdb.kugi.kyoto-u.ac.jp/)**; B_z is measured in transient magnetic structures at their passage of the ACE spacecraft **(http://www.srl.caltech.edu/ACE/ASC/level2/lvl2DATA_MAG.html)**; maximal speed of Solar Wind (V_{sw}) and jump of the V_{sw} is estimated by data from facilities of ACE spacecraft. We calculated the delay time of Dst minimum relative to B_z minimum and the average time of this delay is equal to ~3 hours.

3. CORRELATIONS BETWEEN LEVEL OF INCREASE OF CR INTENSITY AND SEVERITY OF GMS

In Table 1 we present the parameters of disturbed IMF: southward component of magnetic field B_z and change of the Solar Wind speed (Vsw) at the Magnetic cloud/Shock transition measured by SOHO and ACE spacecrafts. Coherently changing geophysical parameters measured by the surface magnetometers and networks of particle detectors also are listed in the table. Clearly, the common driver of all changes is the ICME and the most geoeffective parameters of the ICME are the strength and direction of the magnetic field, its size and velocity.

In Figure 6 we can see that the CR increase (both neutrons and low energy charged particles) and GMS severity are well correlated for the GMS events of the 23rd cycle (correlation coefficients are 0.97 and 0.95, respectively for the neutrons and charged components).

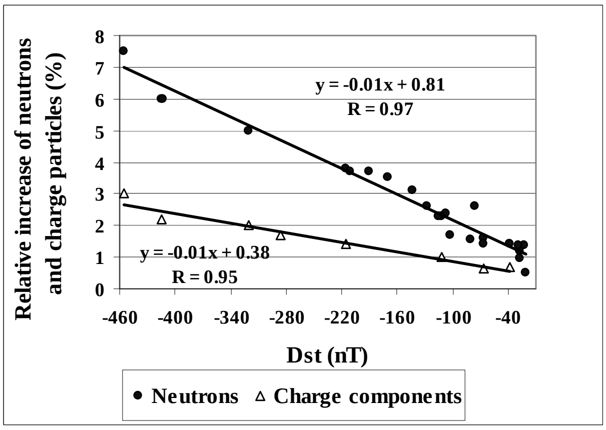

Figure 6. Relation between relative increase of charged and neutral components during the GMS and the corresponding values of Dst index.

A similar relation could be obtained between the Bz, measured at ACE and the particle flux enhancement measured by the ASEC monitors (see Figure 7). It is evident that both the cosmic ray intensity changes and the strength of the geomagnetic storm are determined by the one and the same ICME parameter, namely B_z.

As we can see from Figures 6 and 7, the increases of the flux of different CR species are highly correlated, and the increase of neutrons is always greater compared with the increase of low energy charged particles. The difference in peak amplitudes can be explained by the fact that lower-energy primary particles produce neutrons compared with the primaries that generate electrons and muons reaching the Earth's surface (see Figure 2). Detailed information on the distributions of primaries is given in (Chilingarian & Zazyan, 2008).

It has been demonstrated that ~ 70% of all front side high speed halo CMEs are geoeffective (Gopalswamy et al., 2007, Wang and Wang, 2006b). Therefore, halo CMEs provide a warning of the imminent danger tens hours before CMEs reaching 1 AU and unleashing geomagnetic storms.

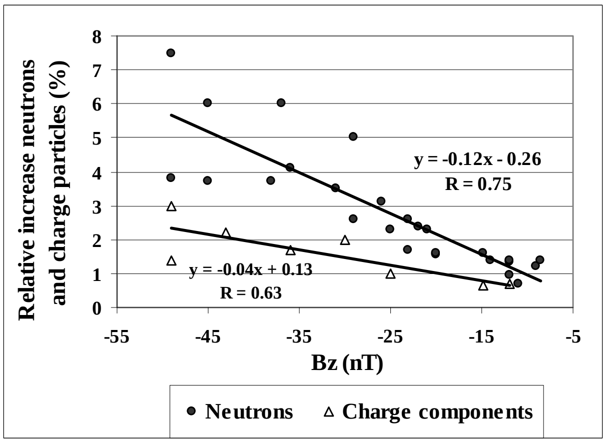

Figure 7. Relation between the relative increase of cosmic ray intensity (neutrons and charge components) and B_z.

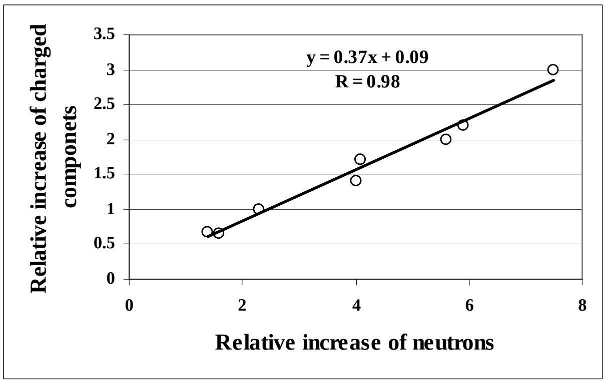

Figure 8. Relation between the relative increases of neutral and charged components of secondary CRs during GMS.

By measuring the magnitude of the southward magnetic field at 1 AU (or at the libration point L1) it is possible also to forecast the strength of the expected geomagnetic storm, see Figure 1.

Using the ICME parameters measured by ACE spacecraft, several groups are providing short term forecasts of the strength of the expected geomagnetic storm (see for instance Li et al., 2008). Information on the changing cosmic ray fluxes also can be very useful, especially when space-born facilities are put in the standby mode due to abundant cosmic ray fluxes and when ground based data are on line.

Besides the B_z, the Solar Wind speed is also used for forecasting the severity of upcoming GMS. In Figures 9 and 10 we present dependence of the peak increase of secondary cosmic ray flux on the Solar Wind speed and on the "jump" in the solar wind speed at the shock transition. As it was previously mentioned (see for instance Kane, 2006) the linear correlation of solar wind parameters with CR flux relative increase is weaker compared to the B_z dependence.

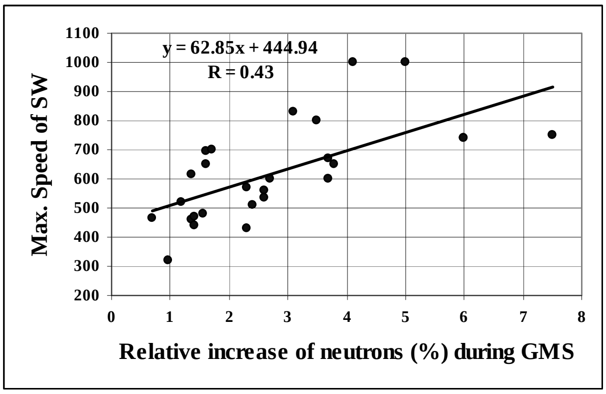

Figure 9. Dependence of the maximal value of solar Wind speed (V_{sw}) on the relative increase of the CR count rate for events listed in Table 1

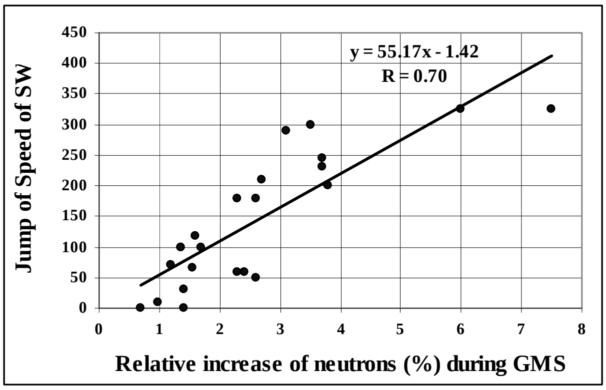

Figure 10. Dependence of the solar wind speed "jump" on the relative increase of the CR count rate.

From Figures 9 and 10 we can conclude that the changes of cosmic ray fluxes (we use it as proxy to the GMS severity) better correlate with the changes of the solar wind speed (jump) at L1 point, than with the maximal speed of the solar wind.

In Table 2 we combine 24 events in 5 groups according to the GMS severity, as proposed by Loewe and Prolss, 1997; the values posted in the columns of Table 2 are group averages of Geospace parameters. It is interesting to note that the quadratic function describes the data very precisely, see Figure 11 (it contradiction to the common view that the SW speed poorly correlates with Dst, see for instance discussion in Kane, 2006). This contradiction points on the limitations of the linear correlation analysis and on the rather strong influence of grouping of the GMS data.

Table 2 Relative increase of the neutron monitor count rate during GMS

Category of Storm (nT)	Dst (nT)	Bz (nT)	Relative increase of neutrons (%)	Jump of Vsw (km/s)
Weak (-30 – 50)	-28	-11	1.0	52
Moderate (-50 - -100)	-76	-20	1.9	128
Strong (-100 – 200)	-121	-27	3.1	215
Severe (-200 - -350)	-200	-33	4.0	250
Great <-350	-428	-48	6.5	330

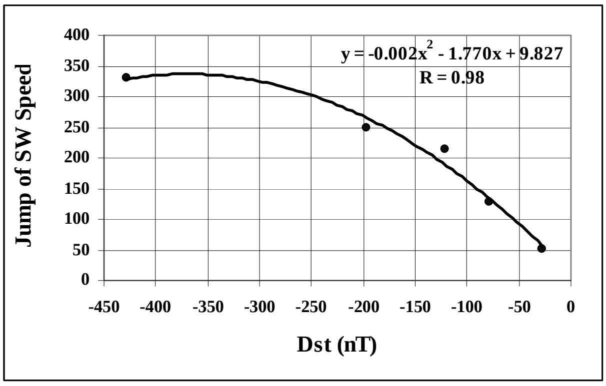

Figure 11. The same dependence as in Figure 10, with the data from Table 2 grouped in 5 GMS categories

4. ICME ARRIVAL AT 1 AU AND COSMIC RAY INTENSITY CHANGES

The time series of the cosmic ray intensities are closely related to the magnetic properties and the structure of the approaching ICME (Bieber and Evenson, 1998). Using the model of the inclined cylinder to represent a large-scale loop structure draped from the sun by CME, Kuwabara, Munakata et al., (2004) derived the tree-dimensional geometry of the cosmic-ray depleted region behind the shock. GMS events of the 23rd solar cycle give several examples of the various patterns of ICME interactions with magnetosphere (see discussion in Wang, 2007). If we accept the inclined cylinder geometry with slow rotation of the magnetic field, different patterns of the secondary flux enhancement should arise. If the Bz is southward just at the arrival of the ICME, the cosmic ray flux will show a peak coinciding in time (or tens of minutes later) with the abrupt change of the solar wind speed and Bz measured by ACE (see Figure 12). The change of the effective cutoff rigidity due to the reduction of the geomagnetic field lasting several hours, allows the lower energy primary GCRs enter the atmosphere and generate particle cascades detected by the particle monitors located at the Earth's surface. After the passage of the ICME, the disturbed geomagnetic field is recovered and again prevents the low energy particle from entering the atmosphere. Furthermore, the overall disturbance of the IMF leads to an overall depletion of the cosmic ray intensity (the so called Forbush decrease), starting just after the end of the geomagnetic storm (see Figure 12).

If the magnetic field at the arrival of the ICME isn't oriented southward we detect first Forbush decrease followed after several hours by increase of CR intensity, see Figure 13.

In Figure 13 we can see that on November 20, 2003, the B_z becomes southward only 5 hours after the interaction of the ICME with the magnetosphere. At the same time we detect start of the CR flux intensity increase.

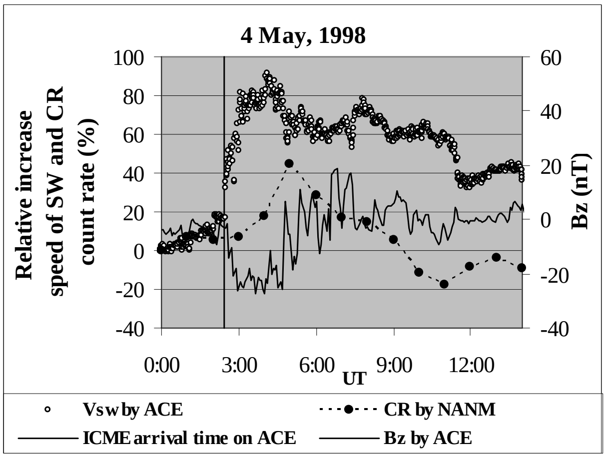

Figure 12. The ICME arrives to 1 AU with southward oriented Bz component of the magnetic field. Observed Cosmic Ray intensity enhancement followed by a Forbush decrease

If the magnetic field at the arrival of the ICME isn't oriented southward we detect first Forbush decrease followed after several hours by increase of CR intensity, see Figure 13.

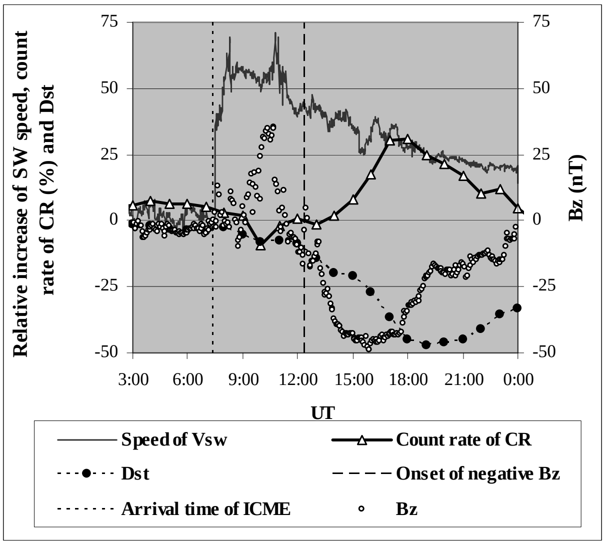

Figure 13 The Bz at the arrival of the ICME isn't oriented southward we detect first Forbush decrease followed after several hours by the intensity increase of CR (when Bz component of magnetic field comes to be southward)

5. CONCLUSION

Severe geomagnetic storms are known to be triggered by prolonged periods of negative Bz (when the later reconnects with the terrestrial magnetic field), thus the Dst index can be predicted from the solar wind and interplanetary magnetic field conditions. Cosmic Ray flux also change due to approaching ICMEs. Therefore, the changing fluxes of secondary cosmic rays measured at the Earth's surface can be used as proxies of ICME parameters when measurements at L1 Lagrange point are not feasible due to severe radiation storms.

Information on the simultaneous detection of GMS in neutral and charged fluxes gives clues on the disturbance of the IMF and the magnetosphere. The ratio between increases of neutral and charged fluxes is approximately constant in a large diapason of GMS severity and neutral flux always undergoes larger changes as compared to the charged component.

The linear correlation of solar wind parameters with CR flux relative increase is much weaker as compared to the B_z dependence.

The maximal enhancement of the neutron flux during the GMS was ~7.5% and the low energy charged particles ~3% during the 23rd solar cycle.

The relative time of successive changes of CR flux intensity increases (due to geomagnetic storm) and intensity decreases (Forbush decreases) can be used for the determination of the ICME structure.

ACKNOWLEDGEMENT

This work was partly supported by ISTC A1554 grant and INTAS 8777 grant. The authors thank Gopaswamy N. and Karapetyan G. for the useful discussions and the ASEC staff for providing continuous operation of the particle detectors during the 23rd solar activity cycle.

REFERENCES

ACE News, ACE News #86 – Nov 14, Real-time Solar Wind Data from ACE make Accurate Forecasts of Magnetic Storms a Reality, 2004

Belov, A.V., Bieber, J.W., Eroshenko, E.A. et al., Cosmic ray anisotropy before and during the passage of major solar wind disturbances, *Adv. Space Res.*, ***31***, 919-924, 2003

Belov A., Baisultanova L. Eroshenko E., et al. Magnetospheric effects in cosmic rays during the unique magnetic storm on November 2003, *J.Geophys. Res.*, *110*, A09S20, 2003

Bieber J.W., Evenson P. CME geometry in relation to cosmic ray anisotropy, *Geophys. Res. Lett.*, ***25***, 2955-2958, 1998

Kuwabara T., Munakata K., Yasue S., et al., Geometry of an interplanetary CME on October 29, 2003 deduced from cosmic rays, *Geophys. Res. Lett.*, ***31***, L19803, 2004

Chilingarian A., Arakelyan, Avakyan, K., et al., Correlated measurements of secondary cosmic ray fluxes by the Aragats Space – Environmental Center monitors, *Nucl. Instrum. Methods Phys. Res.*, ***A543***, 483-496, 2005

Dvornikov V.M., Sdobnov V.E., Sergeev A.V., Anomal variations of the Cosmic Rays in the rigidity interval 2-

4 GV, *Rep. AN USSR. Ser. Phys. 52, 12.* 2435–2437(in Russian), 1988

Gold R. E., Krimigis S. M., et al., Electron, proton, and alpha monitor on the Advanced Composition Explorer Spacecraft. *Space Sci. Rev., **86**,* 54, 1998

Gopalswamy N., Yashiro S., and Akiyama S., Geoeffectiveness of halo coronal mass ejections" *Journal of geophysical research **112,*** A06112, doi:10.1029/2006JA012149, 2007

Koskinen H.E.J., Huttunen K.M.J., Space Weather:From Solar Eruptions to Magnetospheric Storms, in Solar Eruptions and Energetic Particles, *Geophysical Monograths Series*, ***165***, 375-385, 2006

Kudela K., Brenkus R., Cosmic ray decreases and geomagnetic activity: list of events 1982–2002. *Journal of Atmospheric and Solar-Terrestrial Physics,* ***66***, 1121 – 1126, 2004

Kudela, K. and Storini, M., Possible tools for space weather issues from cosmic ray continuous records. *Advances in Space Research, **37***, 1443-1449, 2006

Kudela K., Buchık R., PBobık P., (2008), On transmissivity of low energy cosmic rays in disturbed magnetosphere, *Advances in Space Research, 42*, 1300–1306,.

Leerungnavarat K. , Ruffolo D., Bieber J. W., (2003) Loss Cone Precursors to Forbush Decreases and Advance Warning of Space Weather Effects, *The Astrophysical Journal*, ***593***, 587–596.

Li, X., Kap Soo Oh, and Temerin M., Prediction of the AL index using solar wind parameters, *J. Geophys. Res., Vol. 112*, A06224, doi:10.1029/2006JA011918, 2007

Loewe and Prolss, Classification and mean behavior of magnetic storms, *J. Geophys. Res.*, ***102,*** 209, 1997

Munakata K., Bieber J.W., Yasue S., et al., Precursors of geomagnetic storms observed by the muon detector network, *J. Geophys. Res. 105***,** 27457-27468, 2000

Valtonen E., Geoeffective Coronal Mass Ejections and Energetic Particles, in Solar Eruptions and Energetic particle, edited by Gopalswami N., Mewaldt R, Torsti J., *AGU, Washington, DC, 335*, 344, 2007

Zazyan M., Chilingarian A., to be published in Proceedings of FORGES-2008 workshop, Nor Amberd, Armenia, 2008

II. Characteristics of The Ground-Based Networks of Particle Detectors; Experimental Methods of Measuring Count Rates and Energies of Secondary Cosmic Rays; Efficiency of Detecting Various Species of Secondary Cosmic Rays. Networks Monitoring Main Geophysical Parameters.

Calculations of the Sensitivity of the Particle Detectors of ASEC and SEVAN Networks to Galactic and Solar Cosmic Rays

M. Zazyan, A. Chilingarian

Cosmic Ray Division, Alikhanyan Physics Institute, 2 Alikhanian Brothers st., 0036, Yerevan, Armenia, chili@aragats.am

Abstract: Primary cosmic rays interact with the Earth’s atmosphere producing atmospheric showers, thus giving rise to the fluxes of secondary particles. Particle detectors of the Aragats Space Environmental Center (ASEC) and Space Environmental Viewing and Analysis Network (SEVAN) continuously measure neutral and charged fluxes of elementary particles, incident on the Earth’s surface. Using CORSIKA code, we have calculated response of ASEC detectors to galactic and solar cosmic rays. The main result of the paper is the estimation of the most probable energy of primary proton generating different secondary fluxes detected on the Earth’s surface by a variety of instruments. Results of the paper are applicable to recover the solar proton flux from the surface observations of the Ground Level Enhancements (GLE). In addition, the determination of the most probable energies of the primary proton will help to study energy dependence of solar transient events (Forbush decreases, geomagnetic storms).

1. INTRODUCTION

Timely and reliable information on the state of radiation environments in the interplanetary space is of great importance when considering planned manned flights to the Moon and Mars and overall enhancement of space activity of our civilization. For reliable and timely forecast, we need adequate models of the major solar energetic events in progress. The information on the highest energy solar cosmic rays, available from surface based particle detectors can be used to test such models and to obtain thorough knowledge on the particle acceleration in flares and by fast shock blasts.

Neutron monitors and muon detectors are measuring count rates of secondary cosmic rays produced by the interactions of primary cosmic rays with the Earth’s atmosphere. The information about primary particle type and energy is mostly smeared during its multiple interactions in the atmosphere. To recover the primary particles fluxes, incident on the Earth’s atmosphere, it is necessary to know the relationship between observed count rates of the detectors and the primary particles fluxes, i.e. the most probable primary energy initiating the secondary fluxes detected by neutron monitors and muon telescopes. This relationship can hardly be determined experimentally or analytically, but can be carried out through the modeling process. Of course, the reliability of results depends on the validity of model assumptions and the quality of the simulations.

Several Monte Carlo codes were implemented to simulate the propagation of particles and nuclei through the Earth's atmosphere. One of the first successful attempts in developing simulation code was the work of Debrunner and co-authours (Debrunner and Brunberg, 1968; Fluckiger, 1977; Raubenheimer and Flückiger, 1977). Shibata (Shibata, 1994) performed extensive calculations to investigate transport of primary neutrons. Several authors (Clem and Dorman, 2000; Poirier and D’Andrea, 2002; Bieber et al, 2004) adopted the Monte Carlo particle transport code FLUKA (Fasso et al, 2005) to couple the observed count rate of the detectors with the flux of cosmic rays at the top of atmosphere. Recently, CORSIKA (Heck and Knapp, 1998) & FLUKA were used to calculate cosmic ray induced ionization in the atmosphere (Usoskin and Kovaltsov, 2006) and production of the 7Be in the atmosphere (Usoskin and Kovaltsov, 2008). A new simulation code called ATMOCOSMICS (Desorgher, 2005) based on GEANT4 (Agostinelli et al, 2003) was recently developed by the Bern University cosmic ray group.

Our modeling procedure includes the simulation of primary particle propagation through the Earth’s atmosphere using CORSIKA package. CORSIKA was originally designed for the simulation of extensive air showers with energy above 1014eV in the context of the KASCADE experiment (Antoni et al, 2003). CORSIKA code, however, is also widely used for many other experiments by the cosmic ray physics community. It is already successfully used for the interpretation of the data of low energy experiments (Lopate, 2001; Falcone et al, 2003; Alania et al, 2003; Moser, 2005; Karpov, 2005; Braun et al, 2005).

We used CORSIKA code to simulate ground level particle fluxes in order to determine responses of ASEC monitors (Chilingarian et al., 2003, 2005) to galactic and solar cosmic rays (GCR and SCR). Various particle detectors are monitoring different species of secondary cosmic rays. ASEC monitors register low energy charged particles (with energies > 7 MeV), muons with energies >250 MeV, high energy muons (>5GeV) and neutrons. For the analysis of Ground Level Enhancements (GLE) it is convenient to relate each detector to the particular (most probable) energy of the primary particle. Of course there cannot be established one-to-one relations of primary energies and count rates of different secondary particles. However, we can outline subsamples of primary energy spectra giving rise to the corresponding particles detected at the Earth’s surface. Analyzing these subsamples (energy spectra of primary particles), obtained by simulation of cascade passage through atmosphere and particle detector, we can define representative energy related to various ASEC monitors (Zazyan and Chilingarian, 2005a.). Based on the most probable energies, determined for each of the ASEC and SEVAN detectors and measuring count rate enhancements it will be possible to estimate the energy spectra of Solar protons initiating GLE at Aragats. A variety of particle detectors at Aragats allow estimating energy spectra at energies from 7 up to 50 GeV (if any).

Another important problem is the energy dependence of transient solar events caused by Interplanetary Coronal Mass Ejections (ICMEs). Flux of GCR is changing (modulated) by disturbed Interplanetary Magnetic Field (IMF) and geomagnetic field. The intensity of the neutron flux measured on the Earth's surface can be depleted up to 20 percents at a time scale of several hours. Different secondary particle fluxes undergo different changes dependent on the energy of originated primary particles.

The research of energy dependence of Forbush decreases (Fd) and Geomagnetic Storms (GMS), using the method of most probable energy of primaries which have generated secondary fluxes registered by various particle detectors located in one-and-the-same place, is more effective than the method of using detectors located at different places (see for instance Usoskin et al, 2008).

Aragats group is initiating a world-wide network of particle detectors measuring simultaneously 3 components of secondary cosmic rays. It gives definite advantages in solar physics and Space Weather research and determination of the most probable energies for different secondary particles located at various sites are of upmost importance (see, for instance, Chilingarian & Reymers, 2008, and Chilingarian et al., 2009).

The paper is organized in the following way:

- in the second section the ASEC monitors are briefly described;
- the third section is devoted to the simulation, including CORSIKA options used in the simulations, validation of simulations, determination of the energy spectra of primary protons generating different secondary fluxes and illustration of the robustness of the simulation results relative to the change of strong interaction model;
- in the forth section the possibility to study the solar modulation effects is demonstrated;
- in the fifth section we investigate the disturbances of the Earth's magnetic field during the magnetic storms;
- the sixth section is devoted to the estimation of the power index of GLE N69 on January 20, 2005;
- the seventh section describes the most probable energies of the primary protons having initiated secondaries detected by the new particle detector network named SEVAN.

2. ASEC PARTICLE DETECTORS

Particle detectors of the Aragats Space Environmental Center (ASEC, Chilingarian et al., 2003, 2005,) are located on the slope of Mount Aragats and in Yerevan, Armenia; geographic coordinates: 40°30'N, 44°10'E, altitudes - 3200m, 2000m and 1000m a.s.l. Various ASEC detectors, measuring fluxes of various secondary cosmic rays, are sensitive to different energetic populations of primary cosmic rays. Two neutron monitors (18NM-64) operating at the Nor-Amberd and Aragats research stations detect secondary neutrons. The Nor-Amberd muon multidirectional monitor (NAMMM) detects low energy charged particles and muons. The threshold energy of the detected muons is estimated to be 350 MeV. The Aragats Multidirectional Muon Monitor (AMMM) registers high energy muon flux (threshold energy - 5 GeV). The Aragats Solar Neutron Telescope (ASNT) measures neutrons and charged particles. ASNT is a part of the world-wide network coordinated by the Solar-Terrestrial Laboratory of the Nagoya University. Another monitoring system based on the scintillation detectors of the Extensive Air Shower (EAS) surface arrays, MAKET-ANI (Chilingarian et al., 2007a) and GAMMA (Garyaka et al., 2002), detects low energy charged particles. The particle detectors of the new world-wide networked named SEVAN (Chilingarian & Reymers 2008, Chilingarian et al., 2008) are in operation on the slope of Mount Aragats at altitudes 3200, 2000, 1700 and 1000 meter and in Bulgaria and Croatia at altitudes 2925 m. and 130 m. respectively. SEVAN detectors also measure low energy charged particles, neutral particles (gammas and neutrons), muons (>250 MeV) and high energy muons. NAMMM and ASNT measuring channels are equipped with Amplitude-to-Digital (ADC) convertors and microcontroller based advanced electronics. Data Acquisition (DAQ) electronics and flexible software triggers allows to register not only the count rates of the detector channels, but also histograms of energy releases; correlations of the charged and neutral fluxes and many other physical phenomena. Details of the detector operation can be found in (Chilingarian et al., 2007b and Arakelyan et al., 2009)

3. SIMULATIONS

3.1. CORSIKA package options used in simulation

Atmospheric shower production and propagation through the atmosphere has been performed using CORSIKA package with the following options:

- primary cosmic ray particles: protons, helium nuclei;
- zenith angles of incidence $0 < \theta < 70°$.
- geomagnetic field corresponding to the location of Aragats Bx=25.5μT, Bz=41.2μT.
- low energy thresholds for secondary particles:
  for hadrons: 50 MeV.
  for muons : 10 MeV
  for electromagnetic particles: 3MeV;
- interactions of the low energy primary protons (E0 < 80 GeV) was modeled by : GHEISHA2002 (Fesefeldt, 1985) and FLUKA2006 (Fasso et al, 2005);
- interactions of the high energy primary protons (E0 > 80 GeV) - by: QGSJET01 (Kalmykov et al.,1997);
- CORSIKA version: 6.720
- observation levels: Aragats – 3200m above sea level

Nor-Amberd –2000m above sea level
Yerevan – 1000m above sea level

- flat atmosphere model, where the density of the air decreases with the height, is used.

3.2. Validation of simulation results

Most important stage of any simulation is the validation of simulation results. Any model performs a reduction of a sophisticated physical process. Due to many simplifications, we cannot expect that results of simulations will exactly coincide with measurements. Nonetheless, the basic features of simulated phenomenon should coincide within definite limits with measurements. To validate CORSIKA simulation, we choose count rates of ASEC particle detectors and muon spectra measured at mountain altitude.

3.2.1. Count rates of ASEC particle detectors

The threshold energies for the incident particles correspond to the cutoff rigidity of the location – 7.0 GV. All secondary particles are followed until they are below the threshold energies or reach the Earth surface.

The total number of particles entering the atmosphere within the solid angle ΔΩ during the time interval Δt has been estimated according to the equation:

$$N_{ot} = I(>E)\ \Delta\Omega\ \ \Delta t, \qquad (1)$$

where I(>E) is the integral energy spectrum.

The input spectra for the simulation were selected to follow the observed proton and helium spectra of CAPRICE98 balloon-borne experiment (Boezio et al, 2003). We have transformed the CAPRICE98 kinetic energy spectra into the total energy spectra, which can be represented by

$$I(E_0) = 1.1{\cdot}10^4{\cdot}E_0^{-2.69} \text{ particles } (m^2{\cdot}GeV{\cdot}sr{\cdot}s)^{-1} \qquad (2)$$

for protons in the energy range 6.5 GeV to100 GeV and

$$I(E_0) = 7.07{\cdot}103{\cdot}E_0^{-2.73} \text{ particles } (m^2{\cdot}GeV{\cdot}sr{\cdot}s)^{-1} \ (3)$$

for helium nuclei in the energy range 13.5 GeV to 200 GeV . E0 is the energy of primary particle. The simulated ground level particles were stored and used to estimate ASEC monitors count rates. Due to high efficiency of the 5 cm thick plastic scintillators to register charged particles (see for instance Chilingarian et al., 2007a) with energy greater than 7 MeV we assume 100% efficiency of detectors measuring fluxes of muons and electrons on the Earth's surface and in the underground hall. To calculate Aragats and Nor-Amberd neutron monitors count rates we used NM-64 neutron monitor detection efficiency as a function of rigidity from the report of (Clem and Dorman, 2000). As far as neutron monitor responds mostly to neutrons and protons, only these secondary particles are taken into account.

The mean count rates with the statistical errors calculated from 5 independent simulated samples for primary protons and helium nuclei are presented in Tables 1 and 2. For comparison, experimentally measured count rates of ASEC monitors on a quiet day (minimal solar modulation) are presented as well (given errors are statistical ones). Of course, the experimental values are changing with the phase of solar cycle and other solar modulation effects, but one can conclude that there is a reasonable agreement (5 – 15%) between the simulated and the measured count rates of ASEC monitors.

Table 1. The ASEC monitors' count rates at Aragats level (3200m a.s.l) due to secondary galactic cosmic rays (cts/m² min)

	Neutrons, protons	Low energy charged particles	Muons (>350 MeV)	Muons (>5GeV)
Simulated	2,919±33	23,378±214	12,479±92	3,223±239
Experimental	3,218±22	24,985±320	-	3,688±35

Table 2. ASEC monitors' count rates at Nor-Amberd level (2000m a.s.l) due to secondary galactic cosmic rays (cts/m2 min)

	Neutrons, protons	Low energy charged particles	Muons (>350 MeV)	Muons (>5GeV)
Simulated	1,196±19	15,320±138	9,997±89	2,839±20
Experimental	1,325±12	14,540±130	9,600±150	-

3.2.2. Differential muon flux

Muon measurements (Kocharyan et.al., 1958) at Mt. Aragats can be used to check modeling of atmospheric cascade. Experimental results were obtained during the low solar activity period, 1953 - 1956. The spectrometer accepted particles in the near vertical direction (0°<θ<20°). Muons with energies E>2GeV were detected.

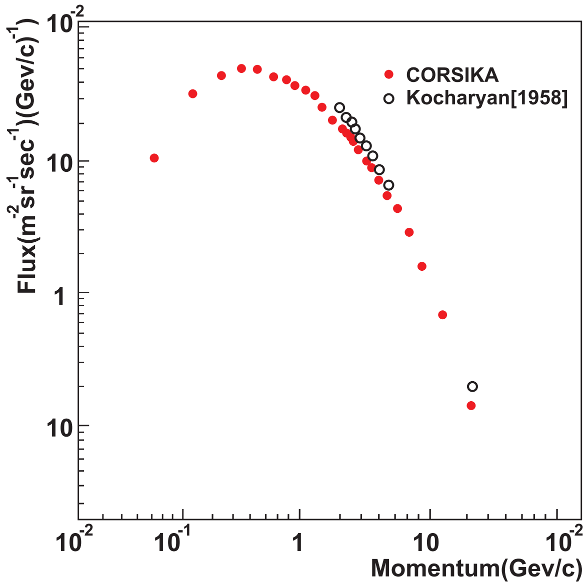

Figure 1. Experimental (Mt. Aragats, 3200, Kocharyan et al., 1958) and simulated (CORSIKA) near-vertical muon spectra.

The corresponding muon flux was computed with CORSIKA for the mixture of primary protons (87%) and helium nuclei (13%). One can see in Figure 1 that the experimentally measured flux is a little higher than the simulated one, perhaps, because of the missing heavier nuclei or because no adequate primary particles spectra were used in the simulation. Nonetheless, agreement of both curves is apparent

3.3. Primary energies responsible for different secondary fluxes

To relate each ASEC detector to the primary proton energy the fluxes of secondary cosmic rays were computed on three observation levels. The number of generated showers was 300000 for each simulation. Parameters of primary protons (energy, angle of incidence, number of secondaries, etc.), producing certain secondary flux (low energy charged particles, muons with energies greater than 250 MeV, high energy muons with energies greater than 5 GeV and neutrons) were stored. In this way the energy spectra of protons (subsamples of overall energy spectra) responsible for generation of different secondary fluxes were obtained. Partial energy spectra obtained in this way depend on the power-law index used in simulation and on the observation level and geographic coordinates. In this study simulations were performed for four spectral indexes γ=2.7 (galactic cosmic rays) and 4, 5, 6 (solar cosmic rays) and 3 observation levels. The comparison of the spectra of GCR and SCR generating high energy muons at Aragats are presented in Figure 2.

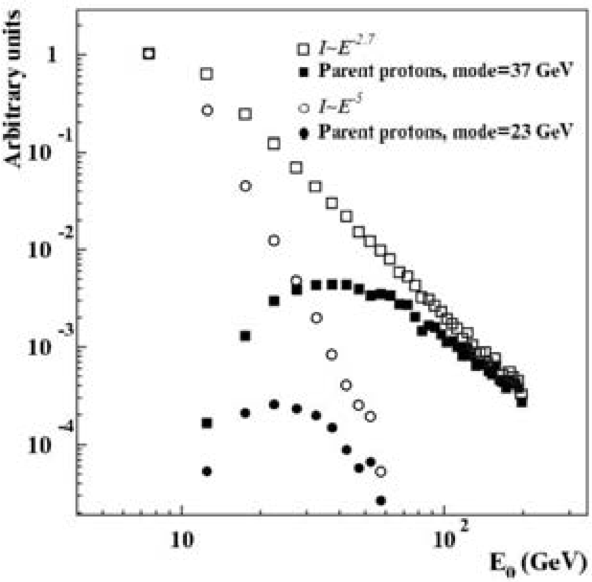

Figure 2. Energy spectra of primary protons and protons responsible for the flux of secondary high energy muons obtained by QGSJET01 + GHEISHA2002 at Aragats level for two cases - GCR and SCR.

It is possible to describe the energy spectra by different characteristics, for instance, by 10% quantile (1st decile cut), 90% quantile (9th decile cut), median and mode of distributions (see Figure 3, where the statistical distributions of the primary protons are posted for the secondary charged particles detected on Aragats level).

In Figure 4 we posted efficiencies of the primary proton incident on the Earth's atmosphere to yield neutron and muon (with energy greater than 5 GeV) being registered by the appropriate detectors located at Aragts geographical coordinates (the probability that primary particle will generate a secondary particle reaching observation level).
As an optimal characteristic describing the energy spectra we chose the mode, because it represents the most probable energy of primary particle. This characteristic is stable, as we will see in the next sections, against change of the model (both strong interaction and primary spectra), robust against random fluctuations and robust against occasional very large energies encountered in simulations (outliers).

3.4. Comparison of two codes: FLUKA and GHEISHA

Another check of simulation is its robustness relative to alternative strong interaction model. The energy interval in simulation was 7 GeV – 350 GeV. Because of the steep primary energy spectrum the low energy interval (below 80 GeV) is more important for our analysis. To check the robustness of the obtained statistical parameters of the primary distributions against the change of strong interaction model the comparison of the results obtained by 2 low energy codes (FLUKA and GHEISHA) was performed. The outputs from both codes are in good agreement (see Figure 5).

4. SOLAR MODULATION OF GALACTIC COSMIC RAYS

Fluxes of the elementary particles on the Earth's surface are highly dependent on the energy spectra of primary protons and nuclei. Highly isotropic flux of GCR can be described by power law, $dN/dE_0 \sim E_0\gamma$, with a rather stable power index, $\gamma \sim -2.7$. However, GCR fluxes with energies up to few tens of GeV are modulated by the solar wind. During the active sun years, the strong solar wind blows out from solar system significant fraction of the low energy protons and nuclei. Therefore, an energy spectrum of lowest energy range is changing and should be described by another functional dependence.
The primary particle generator in CORSIKA uses power law spectra. For the accurate description of the gradually softening shape of proton spectrum the original CORSIKA has to be extended by parameterization of the solar modulation. For our analysis we just tried to roughly reproduce low energy curvature and model the deficit of lower energy protons at year of active sun approximating primary proton spectrum by a *broken power law* with γ= -2, in the energy range 7 GeV < E_0 < 15GeV and γ = -2.7 for E_0 > 15GeV.

As we can see in Table 3 the influence of changing energy spectra is apparent and most probable energies of primary protons are shifted to the right. Effect is energy dependent and at highest energies almost no noticeable.

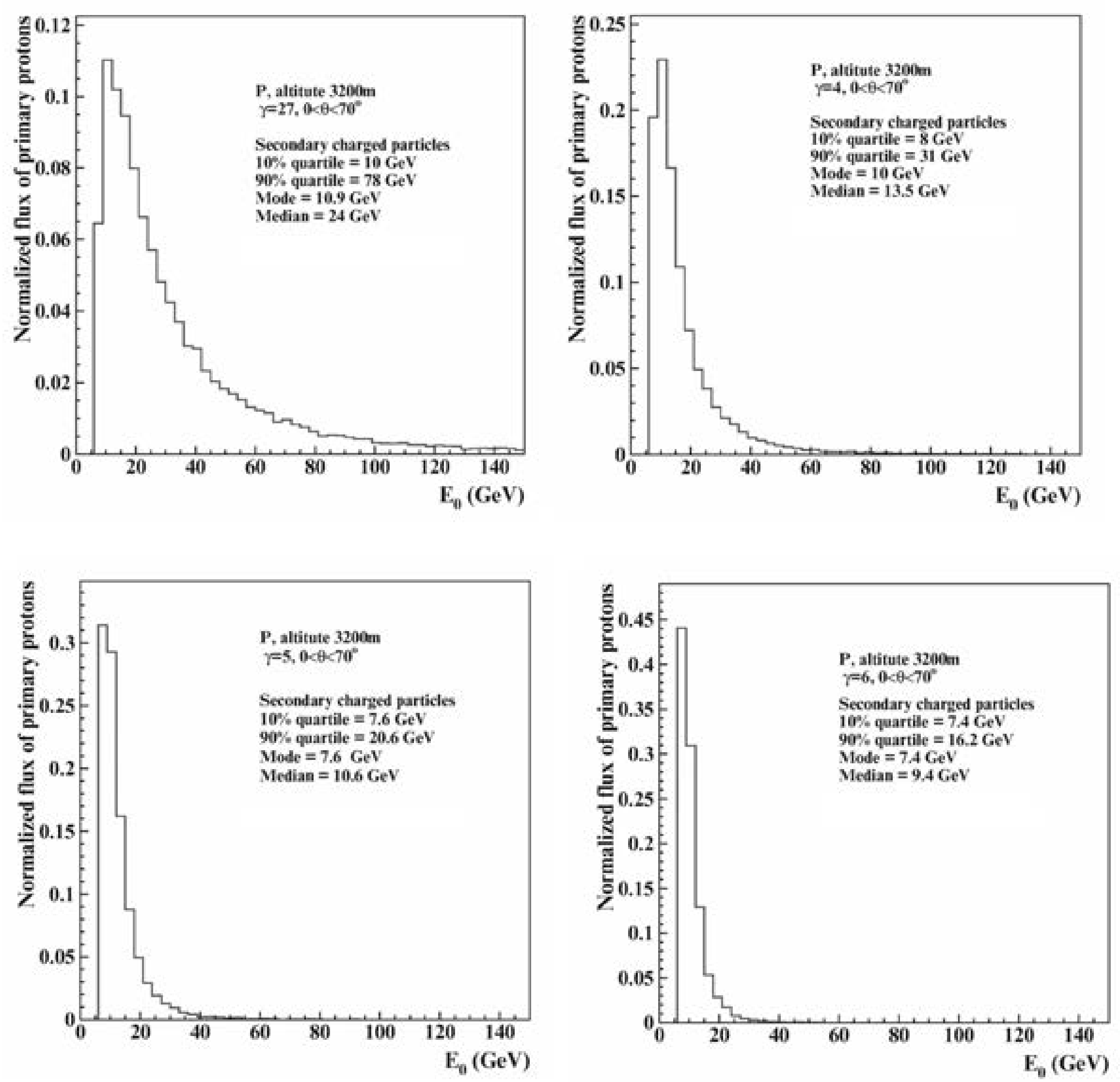

Figure 3. Energy distributions of primary protons responsible for the secondary charged particles flux obtained by QGSJET01 + GHEISHA2002 at Aragats level for four spectral indexes.

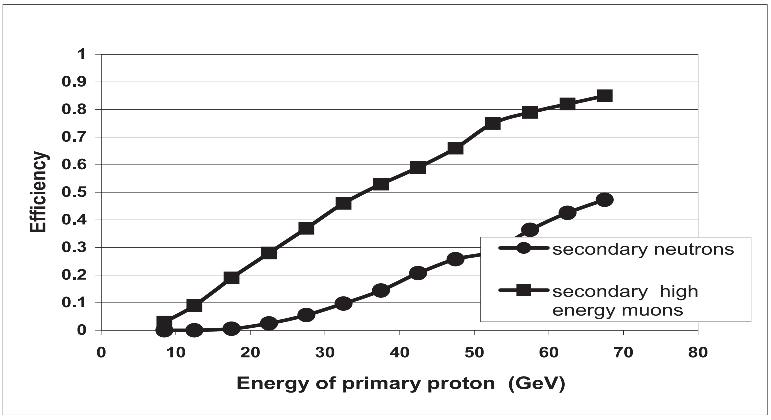

Figure 4. Efficiency of primary proton incident the Earth's atmosphere to yield secondary neutrons and high energy muons at Aragats level, calculated with CORSIKA code.

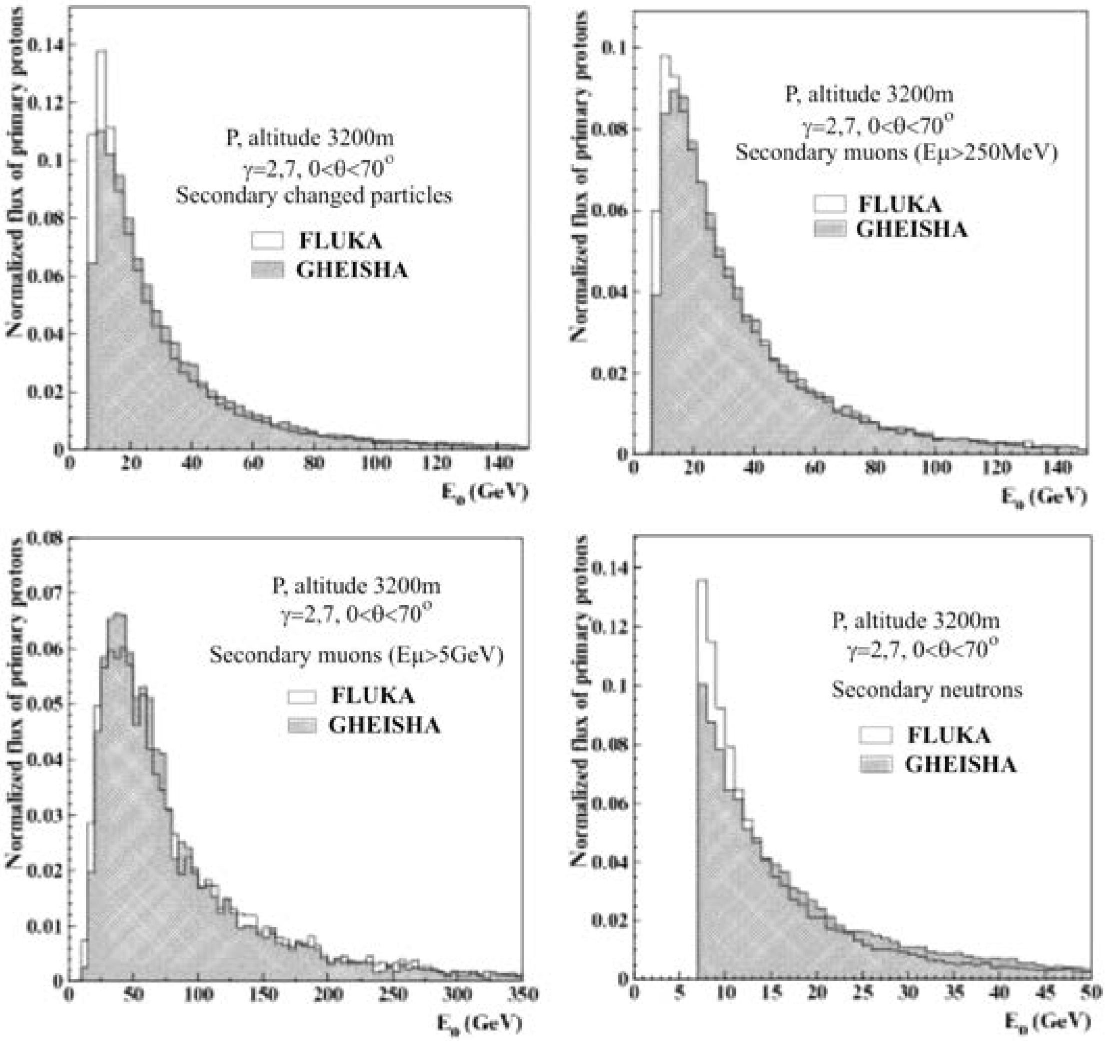

Figure 5. Comparison of energy distributions of primary protons responsible for different secondary fluxes obtained by GHEISHA and FLUKA codes at Aragats level.

Table 3. The most probable energy of GCR primary protons producing secondary fluxes at Aragats level for 2 phases of the solar activity

Secondary Flux	γ=2.7	γ=2 for 7GeV<E_0<15GeV and γ=2.7 for E_0>15GeV
Charged particles	10.5 ± 0.2 GeV	13.4 ± 0.3 GeV
Muons (E>250 MeV)	14.0 ± 0.2 GeV	15.2 ± 0.4 GeV
Muons (E>5 GeV)	36.2 ± 0.7 GeV	37.7 ± 1.3 GeV
neutrons	7.1 ± 0.04 GeV	8.1 ± 0.2 GeV

5. VARIATIONS OF COSMIC RAYS CAUSED BY CUTOFF RIGIDITY CHANGES DURING GEOMAGNETIC STORM.

Disturbances of the Earth's magnetic field during the magnetic storms can cause changes of effective cutoff rigidity. These changes may be sufficiently large to change essentially cosmic ray intensity measured by ground-based detectors. We have studied the CR intensity dependences on cutoff rigidity. The count rates for the ASEC monitors for the four different values of rigidity cutoff are calculated. The relative increases of count rate $\Delta N_{cnts}/N_{cnts}$ due to the decreases of rigidity cutoff are presented in Table 4. One can see that the neutron flux is much more influenced by the cutoff rigidity decrease than the charged particle flux.

Table 4. The simulated increase $\Delta N_{cnts}/N_{cnts}$ in the 5-minute count rates of ASEC monitors due to the changes of rigidity cut-off.

Rc decreases	neutrons, protons	low energy charged particles	muons (>350MeV)
from 7.56 to 7.00GV	3.1%	0.74%	0.43%
from 7.56 to 6.50GV	6.0%	1.34%	0.74%
from 7.56 to 6.00GV	9.2%	1.93%	1.00%

The relative increases of the measured count rates for two geomagnetic storms detected by ASEC monitors are presented in Table 5. The experimental increases are estimated above pre-event background, calculated by one-hour data prior shock arrival. The comparison of simulated and experimental increases in count rates shows that the November 20, 2003 event could be associated with the cut-off rigidity changes of ~1GV. This is in a good agreement with the cut-off rigidity variation (~1.2 GV for Aragats station) calculated by (Belov, Baisultanova et al., 2005) using global survey method.

Table 5. The experimental increases $\Delta N_{cnts}/N_{cnts}$ (5-minute count rates)

event	neutrons, protons	low energy charged particles	muons (>350MeV)
November 20, 2003	6.2%	0.8%	0.5%
September 7, 2002	2%	0.5%	0%

From Tables 4 and 5 one can conclude as well that the decrease of cut-off rigidity on September 7, 2002 is less than 0.5GV.

6. ESTIMATION OF THE POWER INDEX OF GLE N 69 ON JANUARY 20, 2005

A traditional method for determining energy spectra is to employ GLE observations from the world-wide network of neutron monitors with different cutoff rigidities. An example of such model is the NM-BANGLE model which couples primary solar cosmic rays at the top of the Earth's atmosphere with the secondary ones detected at ground level by the world-wide network of neutron monitors, characterized by the rigidity range from 0.5 until 12 GeV (Plainaki et al, 2008). However, the usage of the model function separable in energy and anisotropy for the GLE fitting can introduce a bias in the recovered spectra (see discussion in Abassi et al., 2008) and it is difficult to follow the time-history of spectral indices. ASEC monitors access wide range of primary energies and allow recovering of the energy spectra by the particle data measured at one and the same location. Sure, only from ASEC data we cannot measure the anisotropy of the event; however, the observations from the growing SEVAN network (Chilingarian et al., 2008) along with existent particle detector networks will allow accessing also information of the anisotropy of the GLE event.

The largest GLE of the space era was detected by particle detectors worldwide on 20 January 2005 (Bieber et al, 2005, Buetikofer et al., 2006). All Aragats particle detectors registered significant intensity increases. The most important result was obtained with the Aragats Multichannel Muon Monitor (AMMM), establishing flux of >20 GeV muons at 7:01-7:03 UT, 20 January 2005 (Bostanjyan et al, 2007, Chilingarian, 2009). In addition neutron monitors located at Aragats detected significant enhancement of neutron intensity, several minutes later at ~7:15 UT.

The analysis presented in this paper is based on the Aragats and Nor-Amberd neutron monitors count rates. These two neutron monitors are located on different altitudes, but at the same geographical coordinates.

The idea to deduce the spectra of solar flare protons using two neutron monitors located close by at the same vertical cutoff rigidity, but at different altitudes above sea level was proposed by J.A. Lockwood et al. (2002). Using Mt. Washington and Durham neutron monitors' count rates, coupled with the knowledge of the proton specific yield functions, they have derived the rigidity spectra, AR-γ, for selected solar flare events since 1960.

Our method is based on the modeling of the responses of Aragats and Nor-Amberd neutrons monitors to solar proton flux ((Zazyan, Chilingarian, 2005b). We use some trial spectrum of solar protons for CORSIKA simulation. Based on data from ACE, SAMPEX and GOES11 spacecraft (ACE News #87) the intensity of protons with kinetic energy Ek<1GeV was found to be

$$I(E_k) \sim 4.07\times10^5\ E_k^{-2.15}\ \text{part}/(\text{m}^2\cdot\text{sr}\cdot\text{s}\cdot\text{GeV}) \qquad (4)$$

Taking indo account that ground-based instruments observed much softer spectra and assuming that there is a knee around ~1GeV, a trial spectrum at higher energy was adopted in the form:

$$I(E_k) \sim 4.07\times10^5\ E_k^{-\gamma}\ \text{part}/(\text{m}^2\cdot\text{sr}\cdot\text{s}\cdot\text{GeV})$$

The total number of solar protons of kinetic energy corresponding to rigidity cut-off of the location was calculated according to equation (1) for different spectral indexes. Particle fluxes at ground level were simulated, and the count rates were determined for Aragats and Nor-Amberd neutron monitors.

The expected increases in the count rates, calculated for possible spectral indices, as well as detected increases of Aragats and Nor-Amberd neutron monitors are presented in Table 6. We conclude that the spectral index $\gamma \sim 6$.

Table 6. Simulated and experimental count rate relativeincreases of the Aragats and Nor-Amberd neutron monitors at 7:15UT on 20 January 2005

γ	Aragats NM	Nor-Amberd NM
4	105%	88%
5	10.5%	8.5%
6	1.4%	1.1%
7	0.15%	0.12%
Exp.	1.52%	1.23%

However, we realize that the results of simulation depends also on the value of the second spectral parameter, the constant A in the power-law energy spectrum $I(E_k)=AE_k^{-\gamma}$. To avoid this dependence, we consider the ratio of count rate increases of two monitors:

$$R(\text{ArNM/NANM}) = (\Delta N/N)_{ArNM}/(\Delta N/N)_{NANM}, \quad (6)$$

which is a function on spectral index only.

The ratios of the count rate relative increases for Aragats and Nor-Amberd neutron monitors simulated for different spectral indexes and the calculated from measured count rates are presented in Table 7.

Table 7. Simulated and experimental ratios of count rate relative increases of Aragats and Nor-Amberd neutron monitors at 7:15UT

	R(ArNM/NANM)
4	1.19±0.02
5	1.26±0.05
6	1.29±0.07
7	1.30±0.14
Exp.	1.24

From the comparison of the computed and observed ratios we estimate that at 7:15 the spectral index of the primary solar proton flux was equal or greater than 5. Thus, based on our analysis (see Tables 6 and 7) we conclude that $\gamma \sim 6$ is a reasonable choice for the spectral index at the time 7:15 UT.

Table 8. The range of most probable energies (in GeV) of primary protons producing secondary fluxes at different SEVAN sites

	GCR (γ=2.7)				SCR (γ=4,5,6)			
Station	Charged particles	Muons (E>250MeV)	Muons (E>5 GeV)	neutrons	Charged particles	Muons (E>250 MeV)	Muons (E>5 GeV)	neutrons
Yerevan (Armenia)	14.6	18.4	38.4	7.1	8.2 - 1.2	10 - 11.6	21.2 -31.9	7.1
Nor-Amberd (Armenia)	13.1	14.9	41.2	7.1	7.6 - 10.6	9.7 - 11.3	20.5 - 31.3	7.1
Aragats (Armenia)	10.9	14.3	37	7.1	7.4 - 10	7.6 - 10.6	21.2 - 27	7.1
Mussala (Bulgaria)	10.6	13.3	-	7.4	6.6 - 7.4	7.1 - 9.5	-	7.6 - 9.4
Zagreb (Croatia)	17.4	17.3	-	7.6	9.4 - 12.9	9.1 - 13.4	-	5.1 - 5.7
Lomnisky Stit (Slovakia)	11.5	14.5	-	4.1	4.1 -6.5	5.2 - 8.3	-	4
Delhi (India)	18.1	18.1	-	16.5	14.2 -15.1	14.3 - 15.3	-	14.3- 14.4

7. SEVAN PARTICLE DETECTOR NETWORK

Networks of particle detectors on the Earth's surface are an important element of planetary Space Weather warning services. The big advantage of ground based particle detectors upon space-based facilities is their consistency, 24-hour coverage, and multi-year operation. In contrast, the planned life of the satellites and spacecraft is only a few years, the same solar blast that they should alert can destroy them, and space-born facilities instead of sending warnings are usually set in the stand-by mode.

The SEVAN multi-particle detectors (Chilingarian & Reymers, 2008, Chilingarian et al., 2009) will probe different populations of primary cosmic rays. The basic detector of the SEVAN network measure fluxes of neutrons and gammas, of low energy charged particles and high-energy muons. The rich information obtained from the SEVAN network located mostly at low and middle latitudes will allow estimating the energy spectra of the highest energy SCR. The SEVAN network will be sensitive to very weak fluxes of SCR above 10 GeV, a very poorly explored region of the highest energy. To understand the sensitivity of the new type of particle detectors to high-energy solar ions we calculate most probable energies of primary protons to which the SEVAN basic units, located at different latitudes, longitudes and altitudes are sensitive (see Table 8). Construction of the SEVAN network started in the framework of the International Heliophysical Year and United Nations Basic Space Science (UNBSS) program focusing on deployment of arrays of small inexpensive instruments around the world. The Cosmic Ray Division of the Alikhanyan Physics Institute donates scintillators, photomultipliers, and Data Acquisition electronics to donor countries. Six SEVAN detectors starting from 2008 are monitoring cosmic ray fluxes at research high mountain stations in Armenia and Bulgaria, at the Yerevan CRD headquarters and at Zagreb observatory (supported by European Office of Aerospace Research and Development).

8. SUMMARY

Based on the detailed analysis of distributions obtained for different observation levels and different spectral indexes of initial energy (γ=2.7,4,5,6) the range of the most probable energy of primary protons producing different secondary fluxes were calculated. These results can be used for recovering of the solar proton flux from the GLE and to investigate energy dependence of the transient solar events (Forbush decreases, geomagnetic storms) in energy range from 4 to 50 GeV.

Results of the simulations were validated in 2 ways: by comparing the experimentally measured count rates of the neutron monitors located on the slope of Mount Aragats and by comparing simulated and experimentally measured muon energy spectra. We also check the robustness of simulation results relative to strong interaction model and the adequateness of treatment of the solar modulation effects. In this way, we demonstrate that CORSIKA code allows relating the primary cosmic ray flux on the top of the atmosphere to observed ground level fluxes.

In addition, we recommend using as most probable energy not the median of the distribution of the "parent protons", but the mode of the same distribution.

ACKNOWLEDGEMENTS

We thank the staff of Cosmic Ray Division for the operation of ASEC monitors.

This work was supported by the Armenian government grants and by ISTC grant A1554.

REFERENCES

Abassi R., Ackermann M., Adams J., et al. Solar Energetic particle spectrum on 2006 December 13 determined by IceTop. ApJ Letters, 689, L65-68, 2008

Agostinelli, S., Allison, J., Amako, K. GEANT4 — a simulation toolkit. Nucl. Instr. Meth. A 506, 250-303, 2003

ACE News #87 - Feb 23, 2005. “Space Weather Aspects of the January 20, 2005 Solar Energetic Particle Event”.
www.srl.caltech.edu/ACE/ACENews/ACENews87.html

Alania, M., Jedrzejczak, K., Swarzinsky, J. et al. Directional Variation of 5 GeV Muon Flux Observed in the Underground Muon Telescope. Proc.28th International Cosmic Ray Conference, 3573-3575, 2003

Antoni, T. et al.- KASCADE Collaboration, The cosmic-ray experiment KASCADE. Nucl. Instr. Meth. A 513, 490-510, 2003

Arakelyan K., Abovyan A., Avetisyan A., Chilingarian A., Chilingaryan S., Danielyan V., Pokhsraryan D. New electronics for the Aragats Space-Environmental Center (ASEC) particle detectors, J. Adv. Space Res., in press

Belov, A., Baisultanova, L., Eroshenko, E., Mavromichalaki, H., Yanke, V., Pchelkin, V., Plainaki, C., and Mariatos, G. Magnetospheric effects in cosmic rays during the unique magnetic storm on November 2003. J. Geophys. Res., 110, A09S20, doi:10.1029/2005J A011067, 2005

Bieber, J.W., Clem, J.M., Duldig, M.L. et al. Latitude survey observations of neutron monitor multiplicity. J. Geophys. Res., 109, A12106, 2004

Bieber, J., Clem, J., Evenson, P., Pyle, R., et al. Largest GLE in Half a Century: Neutron Monitor Observations of the January 20, 2005 Event, Proc. 29th International Cosmic Ray Conference (Pune), 1, 237-240, 2005.

Boezio, M., Bonvicini, V. , Schiavon, P., Vacchi, A., and Zampa, N. The cosmic-ray proton and helium spectra measured with the CAPRICE98 balloon experiment. Astropart. Phys. 19, 583-604, 2003

Bostanjyan, N.K. et al. On the production of highest energy solar protons at 20 January 2005, J. Adv. Space Res. 39, 1456-1459, 2007

Braun, I., Engler, J., Horandel, J.R., and Milke, J. Solar modulation of cosmic rays in the energy range from 10 to 20 GeV. Proc. 29th International Cosmic Ray Conference, 2, 135-138, 2005

Buetikofer, R., Flueckiger, E.O., Moser, M.R., and Desorgher, L. The extreme cosmic ray ground level enhancement of January 20, 2005, Proc. 2nd International Symposium on Solar Extreme Events, Nor-Amberd, Armenia, 1, 214-217, 2006

Chilingarian, A. Avakyan K. Babayan V., et al. Aragats space-environmental centre: status and SEP forecasting possibilities. J. Phys. G: Nucl. Part. Phys. 29, 939–951, 2003

Chilingarian, A., Arakelyan, K., Avakyan, K. et al. Correlated measurements of secondary cosmic ray fluxes by the Aragats Space-Environmental Center monitors. NIM, A 543, 483-292, 2005

Chilingarian A.A., Hovsepyan G.G., Melkymyan L.G., et al Study of Extensive Air Showers and Primary Energy Spectra by MAKET-ANI Detector on Mountain Aragats. Astroparticle Physics 28, pp.58-71, 2007a

Chilingarian A., Melkumyan L., Hovsepyan G., et al. The Response Function of the Aragats Solar Neutron Telescope, Nucl. Instr. and Meth. A574, 255-263, 2007b

Chilingarian A. and Reymers A. Investigations of the response of hybrid particle detectors for the Space Environmental Viewing and Analysis Network (SEVAN). Ann. Geophys., 26, 249-257, 2008

Chilingarian A. Statistical study of the detection of solar protons of highest energies at 20 January 2005. J. Adv. Space Res.,43,702-707,1009

Chilingarian A., Hovsepyan G., Arakelyan K., et al., Space environmental viewing and analysis network (SEVAN). Earth, Moon, and Planets, v.104, p.195, 2009. DOI: 10.1007/s11038-008-9288-1

Clem, J.M. and Dorman, L.I., 2000, “Neutron monitor response functions” Space Sci. Rev., 93, 335

Debrunner, H. and Brunberg, E., 1968, Monte Carlo calculation of nucleonic cascade in the atmosphere. Can. J. Phys. 46, 1069

Desorgher L., 2005, PLANETOCOSMICS Software User Manual, http://cosray.unibe.ch/~laurent/planetocosmics

Fasso, A., Ferrari, A., Ranft, J., and Sala, P.R., 2005, FLUKA: a multi-particle transport code. CERN Yellow Report, INFN/TC_05/11

Falcone, A., Atkins, R., Benbow, W., Berley, D. et al., 2003, Observation of GeV Solar Energetic Particles from the 1997 November 6 Event Using Milagrito. The Astrophysical Journal, 588:557-565

Fesefeldt, H., 1985, GHEISHA The Simulation of Hadronic Showers 149 RWTH/PITHA 85/02

Fluckiger, E., 1977, Theoretical spectra of cosmic ray neutrons in the atmosphere for the energy range 50 MeV E 100 GeV. Proc. 15th International Cosmic Ray Conference, Plovdiv, 4, 144

Garyaka A.P., Martirosov R.M, et al., The Cosmic Ray Energy Spectrum Around the Knee Measured with the GAMMA Array at Mt. Aragats, J. Phys. G: Nucl. Part. 28, pp. 231-2328, 2002

Heck, D., and Knapp, J., A Monte Carlo Code to Simulate Extensive Air Showers, 1998, Forschungszentrum Karlsryhe, FZKA Report 6019

Kalmykov N.N., Ostapchenko, S.S. and Pavlov, A.I., Quark-gluon-string model and EAS simulation problems at ultra-high energies, Nucl. Phys. B (Proc. Suppl.) 52B 17 (1997)

Karpov, S.N., Karpova, Z.M., and Chernyaev, A.B., 2005, Multiplicity, Yeald and Response Functions for Baksan EAS-arrays and Muon Detector in Comparison with similar functions of Neutron Monitors. Proc. 29th International Cosmic Ray Conference, Pune, 261-264.

Kocharyan N.M., Sahakyan G.S., Kirakosyan Z.A., Energy spectra and nuclear interactions of cosmic ray particles, JETF, 35, 1335, 1958

J.A. Lockwood, H. Debrunner, E.O. Flukiger and J.M. Ryan. “Solar proton rigidity spectra from 1 to 10 GV of selected flare event since 1960.” Solar Physics, 208 (1) , pp 113-140 (2002)

Lopate, C., 2001, Climax neutron monitor response to incident iron ions: An application to the 29 September 1989 ground level event, Proc. 27th International Cosmic Ray Conference, Hamburg, 8, 3398

Moser M.R., 2005, Applications of CORSIKA at low energy experiments. VIHKOS CORSIKA School.
www-ik.fzk.de/corsika/corsika-school/talks/8_applic2/moser_neutrons.pdf/

Plainaki C., Mavromichalaki H., Belov A., Eroshenko E. and Yanke V. Modeling the solar cosmic ray event of 13 December 2006 using ground level neutron monitor data. doi:10.1016/j.asr.2008.07.011

Poirier, J. and D'Andrea, C. , 2002, Ground level muons in coincidence with the solar flare of April 15. J. Geophys. Res., Space Physics, 107(A11) 1376-1384.

Raubenheimer, B., and Fluckiger, E., 1977, Response function of a modified NM64 neutron monitor. Proc. 15th International Cosmic Ray Conference, Plovdiv, 4, 151

Shibata, S., 1994, Propagation of solar neutrons through the atmosphere of the Earth. J. Geophys. Res., 99, A4, 6651.

Usoskin, I. G., Braun, I., Gladysheva O. G., et al., Forbush decreases of cosmic rays: Energy dependence of the recovery phaseJ. of Geophys. Res., 113, A07102, doi:10.1029/2007JA012955, 2008

Usoskin, I. G., and Kovaltsov. G.A. Cosmic ray induced ionization in the atmosphere: Full modeling and practical applications, J. Geophys. Res., 111, D21206, doi:10.1029/2006JD007150, 2006

Usoskin, I. G., and Kovaltsov G.A. Production of cosmogenic 7Be isotope in the atmosphere: Full 3-D modeling. J. Geophys. Res., 113, D12107, doi:10.1029/2007JD009725., 2008

Zazyan, M.Z., Chilingarian, A.A. Modeling of the Aragats Space Environmental Center Monitors Response to Galactic and Solar Cosmic Rays. 2nd Int. Symp. on Solar Extreme Events, Fundamental Science and Applied Aspects, Nor-Amberd, Armenia, 197-199, 2005a

Zazyan, M.Z., Chilingarian, A.A.. On the Possibility to Deduce Solar Proton Energy Spectrum of the 20 January 2005 GLE using Aragats and Nor-Amber Neutron Monitors Data. 2nd Int. Symp. on Solar Extreme Events, Fundamental Science and Applied Aspects, Nor-Amberd, Armenia, 200-202,2005b

SPhERA: Solar Cosmic Ray Monitor and Surveyor in the Heliosphere

P. Spillantini

INFN Branch and Physics Department of the Firenze University,
Via Sansone 1, I-50019 Sesto Fiorentino, Firenze, Italy
Tel. +39-055-4572261, +39-335-395941, Fax +39-055-4572367
(e-mail: spillantini@fi.infn.it)

On behalf of the SPhERA collaboration[1]

Abstract: The scientific objective of the SPhERA experiment is the observation of the energetic portion of the Solar Cosmic Rays (SCRs), registering for each of them its nature, kinetic energy and arrival direction. The envisaged energy ranges from a few ten MeV/nucleon up to more than 400 MeV/nucleon. It concerns Solar Energetic Particles (SEPs) penetrating about 2 mm of equivalent aluminium (20 MeV), up to the highest energies occurring in the most violent solar events foreseen on the basis of the last 5 decades of solar activity. The measurement of the arrival direction will cover the whole solid angle and will be continuous in time on the whole period of duration of the mission in order to acquire the information in correspondence of the different solar event typology during a large fraction of the 11-year solar cycle.

The observation will provide for the first time a complete description of the SCR distribution in energy, direction and time on an energy range quite important for the knowledge of the interplanetary environment and is a basic input for planning an adequate protection of the astronauts from the interplanetary ionizing radiation in future interplanetary flights. This protection will necessarily be a massive and complex system either on board of a future interplanetary spaceship or on the surface of Moon or Mars or on Space Bases, so that the basic knowledge needed for its design is an urgent item that must be considered from the very beginning of any manned mission project. The information until now available gathered by all past, present and planned interplanetary probes is neither sufficient nor appropriate, and a dedicated experiment is mandatory.

Keywords: space weather, energetic solar cosmic rays, direction measurement.

---

[1] M. Casolino[a], G.Castellini[b], A.Galper[c], M.Martinov[d], D.Naumov[e], P.Papini[f], W.Pecorella[g], P.G.Picozza[a], F.Rossitto[h], P.Spillantini[f], F.Taccetti[f].
[a]INFN and Dept. of Physics, University of Rome Tor Vergata, Italy.
[b]Instituto di Fisica Applicata N.Carrara, CNR, Via Madonna del Piano, Sesto Fiorentino, Italy
[c]Moscow Engineering Physics Institute, Kashirskoe Chosse, Moscow, Russia
[d]Lavochkin Association, Leningradskoe Chosse, Moscow, Russia
[e]Joint Institute of Nuclear Researches, Dubna, Moscow region, Russia
[f]INFN and Dept. of Physics, University of Firenze, via Sansone 1, 50019 Sesto Fiorentino, Italy
[g]Telespazio, via Tiburtina, Rome, Italy
[h]Moon Base Intiative, ‘Solidarietà e Sviluppo’ association, Via Ombrone 3, 00198 Rome, Italy

1. INTRODUCTION

The present work discusses the SCR monitor and surveyor SPhERA (Solar Phenomena Explorer for Radiation Assessment) to be operated outside the terrestrial magnetic field, in the region of space between the orbits of the Earth and Mars. It is the elaboration of the project presented at the COSPAR2004 in Paris (Spillantini, 2004), following the recommendations of the two studies supported by ESA in 2003-2004, i.e. the ESA Topical Team on 'Shielding from the cosmic radiation for interplanetary missions: active and passive methods' (ESA 2004, ESA 2005, Spillantini et al. 2007) and the industrial study 'Radiation Exposure and Mission Strategies for Interplanetary Manned Missions (REMSIM)' (Alenia-aerospazio 2004, Cougnet et al. 2005). It has been submitted in 2007 to the Italian Space Agency (ASI) in response to the call for missions of opportunity (Picozza, 2007). The SPhERA acronym wants to put in evidence the concept of the instrument, conceived as a telescope registering SCR's arriving from any direction in the whole solid angle, as a sphere does.

2. NEED OF MEASURING THE DIRECTION OF ARRIVAL OF THE HIGH ENERGY SCR

The arrival directions of SCR's were measured by different instruments on board of numerous spacecraft sent in deep space or operating far away from the influence of the terrestrial magnetic field. At energies exceeding a few ten MeV/nucleon the collected information is poor and scant (Casolino 1999). Only a few of the instruments were equipped for supplying the angular distributions with the correlated information on the energy and on the evolution in time, and with a sufficient granularity. Sometimes they accurately describe a single solar event, but are scarcely useful for a general description of the angular distribution as a function of the energy in correspondence of the different solar event typologies, and of its temporal evolution. However, as stated in the above quoted ESA studies, an exhaustive information is needed for protecting health and lives of astronauts operating outside the protection of the terrestrial magnetic field, either inside a spaceship or in a spacesuit during a spacewalks or on the Moon or Mars surface.

The retrieval of the arrival direction of the high energy SCRs from the data collected in all the previous missions is a duty of the cosmic ray community; however the systematic measurements of a dedicated instrument are surely needed for finalizing the distribution of passive materials in the spaceships and shelters, as well in providing active systems of protection.

3. THE SPHERA INSTRUMENT

3.1 General scheme of the instrument

The minimum requirements to the instrument should be:

- identify the protons and measure their instantaneous flux, since they are accountable for most of the dose released in the encountered materials;
- measure the energy of the protons up to about 400 MeV, i.e. up to an energy at which the total flux of a possible extremely intense solar event is still enough high to be dangerous to the astronaut's health (figure 1);
- measure event by event the direction of the incoming particles, in order to construct the instantaneous angular distributions in the suitable coordinates and scales;
- accept the particles in the whole solid angle, possibly without dead sectors in the ecliptic plane.

An added requirement could be that of:

- identifying a rapid increase of the electron flux, allowing to alarm the environmental space of the soon arrival of the much more dangerous protons (figure 2).

The 'minimal' instrument that can satisfy the above requirements can be based on three well known techniques of the particle physics: the measurement of the time of flight (ToF) between scintillation counters; the registration of the charge released in the crossed detectors; the measurement of the position by a system of microstrip silicon detectors.

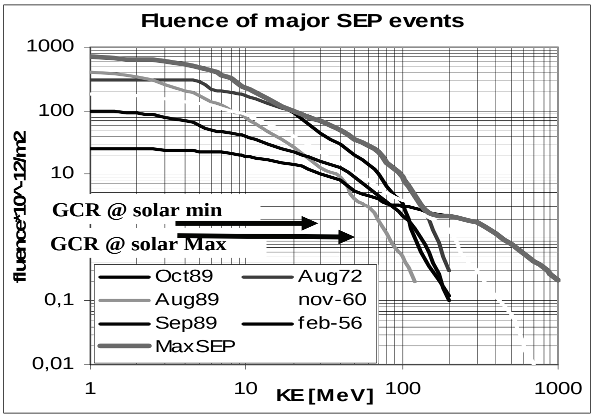

Figure 1. Fluence of the maximum possible SEP event (MaxSEP, thick green line) as a function of the energy obtained as convolution of the Feb56, Aug72 and Oct89 events. The fluence in one year of the GCR's (about constant with energy in the considered range) is also indicated in correspondence of the minimum (maximum) solar activity of the ≈11 years solar cycle.

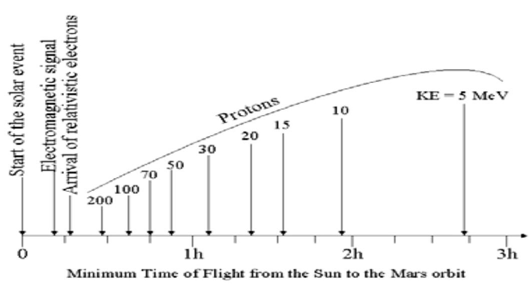

Figure 2. Minimum ToF from the Sun to the Mars orbit. The Minimum ToF from the Sun to the Earth orbit is about 1.5 times shorter

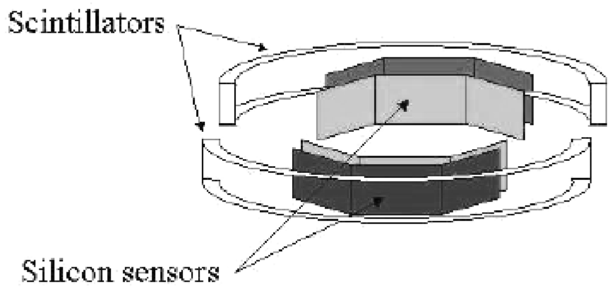

Figure 3. – Conceptual scheme of the SPHERA detector.

A bidirectional telescope as indicated in fig.3 can accomplish this job in a wide portion of a plane (> ¾, i.e. >270°) accepting about ±30° in zenith. Combining three such telescopes, one for each perpendicular plane (figure 4), the whole solid angle could be sufficiently well covered.

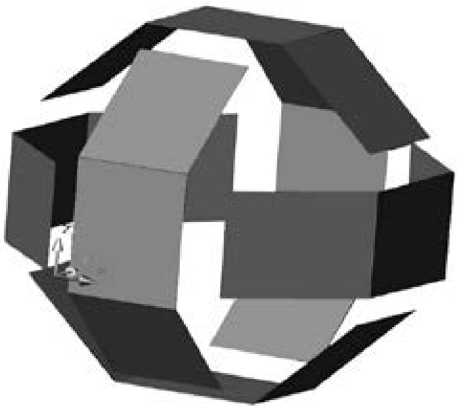

Figure 4. The quasi-spherical structure resulting with the arrangement of three bi-directional telescopes. For sake of simplicity only the silicon sensors are shown, as they are the innermost part of the instrument.

3.2 – Dimensioning of the instrument

The geometrical dimensions of the instrument must compromise between the need of a sufficient rate for registering the overall stability of the system during the period of quietness of the Sun and the high counting rate during the most intense solar events. Therefore the overall geometrical acceptance must be of the order of a few cm^2sr, and the time needed for triggering and registering the event of the order of a few microsecond, what allows for a dynamics of $\approx 10^5$ in the counting rate.

Obviously the dead time of the silicon strip readout and the time for measuring the ToF increase at the increasing of the rate, and cannot cope with the most intense solar events. This fact does not affect the result of the measurement provided that few ten events per second could be fully registered. A few thousand events can be collected in few minutes, what is sufficient for constructing an overall angular distribution with a granularity of a few degrees, enough for following events that evolve in times longer than several minutes.

The dimensions of the sensors can be pushed down to a few cm, the limit being given by the resolution of the ToF, which measures the proton energy. The energy resolution for different ToF resolutions on a flight length of 10 cm is reported in fig. 5.

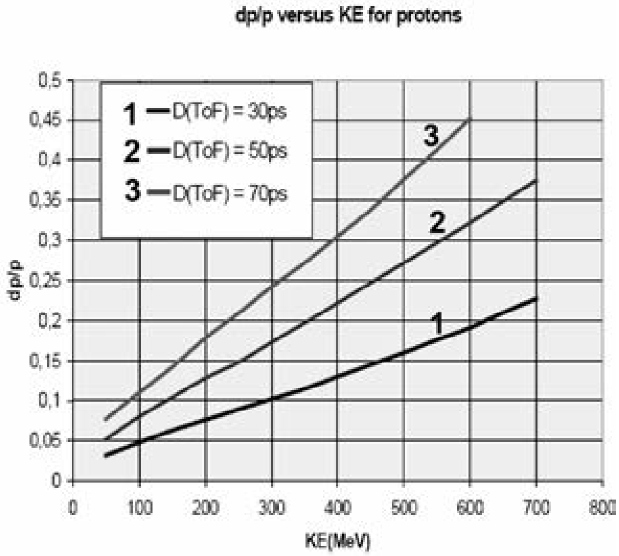

Figure 5. Momuntum resolution as a function of the ToF for different ToF resolutions on 10 cm flight length.

The time resolution of the electronics developed for the PAMELA experiment was stable between 35 and 42 ps (Russo,2006). Taking in consideration the very small dimensions of the ToF scintillators, it can be foreseen a not much worse ToF resolution. It means that the ToF base of 10 cm can be assumed as a basic dimensioning.

Two approaches are possible. In the first one the light released in the scintillators is conducted by light-pipes to optical PM's, sticking out from the volume defined by the sensor, as represented in figure 6.

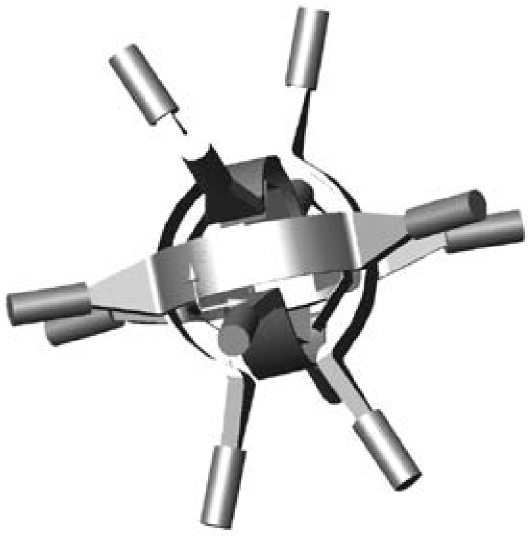

Figure 6. The six structures of the three telescopes connected one to the other, constituting one robust self-supporting mechanical system.

An alternative solution is that of gluing to the sides of the scintillators a number of Silicon PM (SiPM) for multiplying and reading out the released light. This solution is much more compact, allowing maintaining the overall dimensions inscribed in a sphere of about 10cm diameter, and also minimizing the obscured angles. However it requires specific R&D work for assuring that the resolution of the ToF system is not affected and the quantity of light released in the scintillator is adequately measured. This added work should be afforded only in case that it would be necessary for the arrangement of the instrument in the spacecraft. Therefore in this report only the first solution, with light pipes and optical PM's, will be considered.

3.3 - The mechanical structure

The total volume occupied by the SPhERA instrument (sensors, PM's and front-end electronics) mainly depends from the shape of the light-pipes bringing the light to the PM's and from the dimensions and location of the PM's themselves. They occupy small angular sectors in the plane of each telescope, leaving free a large fraction (more than 300 degrees) of the total 360 degrees on the telescope plane.

Each one of the three telescopes is constituted by two mechanically independent identical structures, and does not obstruct the FoV of the other two telescopes. The six structures of the three telescopes can be connected one to the other for constituting a robust self-supporting mechanical system. With this arrangement and using the most compact available PM's the total encumbrance of the detector system can be inscribed in a sphere of about 30cm diameter. This configuration is assumed as a basic solution for the instrument.

The needs of the spacecraft and of the other instruments could require a different arrangement, with the light-pipes and the PM's much less sticking out from the volume defined by the sensors. In this case they could obstruct more the FoV angles and affect the light collection efficiency in some angular region, and accurate evaluations must be conducted for the real arrangement.

3.4. – The electronics and the onboard data treatment.

The trigger is constructed by the coincidence of the OR's of the two PM's of each of the two counters of the same telescope. It starts the conversion and readout of all the signals from the PM's and from the microstrip front-end electronics. All the digitised signals are transferred to the On Board Data Handling (OBDH) unit for the subsequent elaboration. A simplified electronics layout of the instrument in shown in figure 7.

The basic solution for the front-end electronics (FEE) of the silicon sensors is the highly performance and low consumption electronics used for the PAMELA tracker (Straulino, 2006). Different solutions are under consideration for extending the linearity and supplying auxiliary signals to be used in the trigger logic and in the online data treatment. The digital electronic and electric power distribution were studied for a previous version of the instrument by LABEN industry, as an extrapolation of the PAMELA system (LABEN, 2002). The data handling unit included the CPU module with 1553B command interface, the telecommands and telemetry standard LABEN module, an interface and pipeline temporary buffer, an ECC solid state mass memory module of 2 GByte capability and the power supply module, for a total power consumption of 15 W, a total mass of 2350 g and a 20 x 20 x 20 cm^3 encumbrance volume. These figures resulted from standard LABEN space electronics modules, assuring performances close to the functional needs. As the LABEN study was based on space qualified component technologies available in 1999, the mass and consumption parameters can be considered as upper limits for the final data handling unit. A more detailed study and a more specific approach towards the different electronics modules can optimise power, mass and encumbrance budgets, by using customized modules.

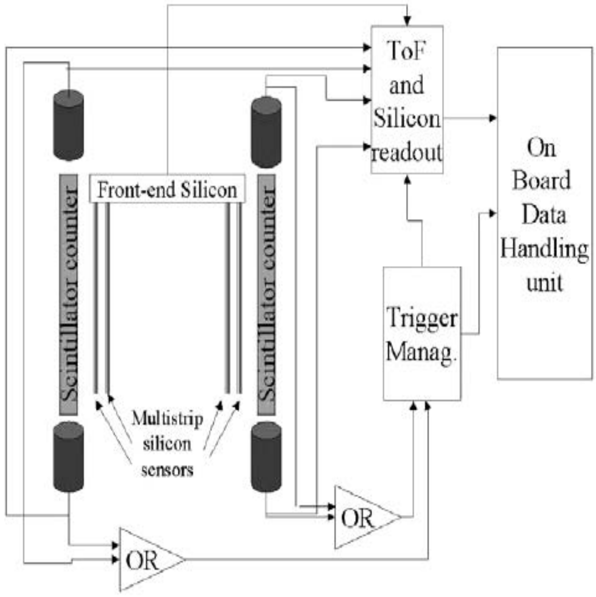

Figure 7. Electronic layout of the SPHERA instrument

4. RATES, DATA HANDLING AND TELEMETRY

When the Sun is quiet the instrument mainly registers GCR's, whose rate, for each one of the three telescopes, ranges from 6.0 particles per second in the period of minimum solar activity down to 4.4 particles per second at maximum solar activity. Since the GCR flux is stable and isotropic, these events can be used for automatically on-board self-calibrating and monitoring the instrument, sending to Earth only a few events for control purposes.

In correspondence of solar phenomena the rate can increase by several orders of magnitudes, up to about 10^5 useful triggers per second. The information will be registered and handled on board according to criteria depending from the effective instantaneous rate. If it is very high, exceeding several hundred useful triggers per second, the dead times of the readout electronics of the signal amplitudes, the ToF and the angle measurements will increase, allowing to register and handle only a sample of events, with very few raw events stored to be sent to Earth for control purposes.

The signal amplitude, ToF and tracking information are handled on board for updating the content of matrices giving the angular distribution at several energies for the different particles: protons, electrons, some light elements and someone of the lightest isotopes. The matrices content is memorized on board at regular time intervals (typically a few times per hour), that could depend from other needs of the spacecraft or from the general telemetry budget. The telemetry will send to Earth, besides the basic housekeeping information, a few raw events, the trigger rates of the telescopes as a function of the time, and the content of the matrices.

If the matrix granularity is chosen to be 3÷4 degrees in both the orthogonal angles and for ten energy intervals each matrix accounts for 10^2 kbyte. Considering about ten matrices stored 6÷10 times per hour, the total daily rate amounts to about 200 Mbyte/day, to be sent to Earth in the period (typically a few days) of the most intense solar events. The on board mass memory of the OBDH unit is enough to buffer the produced data for several days.

5. RESOURCES (MASS, POWER, …) AND INTERFACES (MECHANICAL, THERMAL ELECTRICAL, …).

The resources needed for the above described instrument are summarized in table 1.

Table 1. - Distribution of weight and power for SPhERA instrument

System	Mass (kg)	Power (W)
Scintillator counter system (trigger + ToF)	1.0	2.0
Silicon detector System (Si + F.E.E.)	0.5	1.0
Readout and digitisation system	0.5	1.0
Mechanics and Cables	1.0	-
On Board Data Handling	<2.4	<15
Total	<5.4	<19

The instrument consists of two parts: the detector, constituted by the sensors, the PM's and the FEE of the silicon sensors, and the other part consisting of one or more boxes for trigger and ToF electronics, the readout and digitisation electronics, the data handling and the power supply.

The detector must be located outside of the spacecraft in order to have as much as possible wide Field of View (FoV) in any direction. It is not important in what side it will be mounted provided that its FoV will not be significantly obstructed by the spacecraft structure, the solar panels and the other instruments.

The box(es) for the digital electronics and the data handling can be located everywhere, also at some distance from the detector.

The thermal interfaces can be studied when the detector configuration will be frozen. They should not constitute a major problem because the whole detector can be covered by a thin MLI shielding, without prejudice of its performance, and the sensors can maintain their characteristics on a wide temperature range.

The OBDH acts also as a slow control unit for the whole instrument and will automatically manage the failure detection, isolation and recovering. The electrical and data interfaces are standard and do not need special requirements.

6. THE SPHERA MISSION

For accepting particles from the whole solid angle the SPhERA instrument should be as far away as possible from any supporting structure and from the boxes for the power supplies, the data treatment and the communications. In particular the accommodation should be such that does not obstruct sectors of the ecliptic plane larger that a few degrees. If this is not possible, the obscured solid angle given by these parts must be covered by a suitable rotation of the spacecraft, such that the whole solid angle could be scanned in a few minutes.

The Russian Lavochkin Association industry, participating to the mission proposal, offered to accept the SPhERA instrument on board of one of its future spacecrafts that should operate far away from the terrestrial magnetic field: (1) LunaGlob in orbit around the Moon; (2) Fobos-Grunt, mission for delivery of soil samples from Phobos; (3) small spacecraft (MKA-FKI program) for studying plasma dynamics and turbulence. All these missions have the status of federal projects.

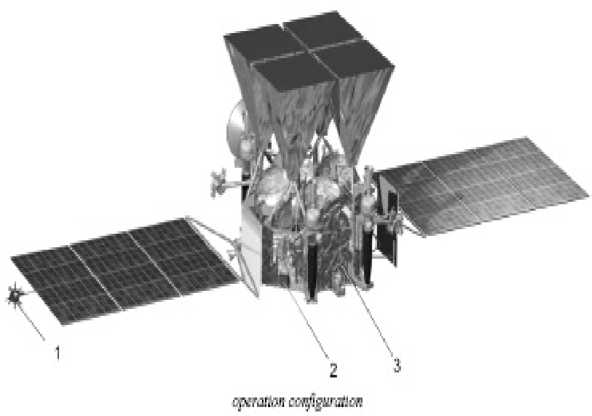

Figure 8. Integration di SPhERA on board of the "Luna-Glob" Orbiter SPhERA detector; 2. SPhERA Data Handling Unit; 3. "Luna-Glob" Orbiter)

In the Lavochkin study for the LunaGlob lunar orbiter (Polishuk, 2007) the SPhERA instrument was proposed to be installed at the outer side of the external solar panel in order to assure an optimal FoV, with the other boxes integrated in the structure of the spacecraft, as shown in figure 8.

7. SPHERA APPLICATIONS AND BY-PRODUCTS

5.1. Alarming capability

Very important it is the capability of the SPhERA instrument of detecting online the increase of the counting rate of relativistic particles (i.e. with a minimum ToF), due to the arrival of high fluxes of electrons. The rate increasing allows to alarm the environing space of the soon arrival, in ten or more minutes and from a determined direction, of the much more dangerous proton component (15 minutes for 100 MeV protons at the Earth orbit), allowing to take the needed counter measurements, such as switching off the power supply to sensible devices, the immediate re-entry of astronauts operating in EVA or outside shelters, etc.. In particular it must be reminded that the outer walls of the manned spaceships cold not absorb protons with energy higher than 40-50 MeV, and that a large portion of solar events, specially the most intense and energetic, cannot be forecast, so that an onboard alarming system is of overwhelming importance.

5.2. Moon (and Mars) exploration

For what concerns the future exploration of Moon (and Mars) a SPhERA-like instrument can contribute to the knowledge of the most penetrating solar ionizing radiation in the surrounding region of space, and therefore to the understanding of the history of these celestial bodies. In particular for Mars, the continuous monitoring of the energetic tail of SCR's can contribute to the understanding of its effects on the dynamics and escape of the Mars atmosphere on its external layers as well in the layers where the solar wind cannot penetrate. It must be reminded that the penetration inside the Mars ground of the most energetic solar particles (>20cm) can be correlated to the depth at which a possible primordial life can be survived and can develop.

5.3. Forecasting the CME events

A promising method, named method of relativistic particles trajectories, was developed by Petukhov I. and Petukhov S. (2008) for the prediction of the occurrence of large-scale interplanetary disturbances at Earth orbit and the corresponding geomagnetic storms: the energetic GCR's encounter the front of the disturbance and are scattered back to the Earth orbit well before, up to 20 hours, the appearance of the storm. Since SPhERA can measure the direction of the scattered particles, a rate variation should appear on one or few bins of the angular distribution on the top of the bulk of the stable and isotropic distribution of the registered GCR's. It would be a powerful means for forecasting the most dangerous phenomenon threatening the health and safety of manned space flight. This argument requires a more deep quantitative understanding and realistic evaluations.

5.4 Dosimeter for spacecrafts

The SPhERA instrument can be regarded as a radiation 'super-dosimeter' operating in real-time. The development of a compact and light system for identifying event by event the nature of the arriving particle, its energy and its arrival direction opens the possibility of constructing dosimeters measuring the radiation event by event and supplying the fluxes separately for type of particle as a function of the energy and of the direction, and their temporal evolution. The key point is the identification of the particle by its energy loss in the sensors, the measure of its energy by a precise determination of the ToF between two or more scintillators and the measurement of its arrival direction by solid state detectors, i.e. just the techniques developed for SPhERA, the whole supplied with its specific software. The geometry can be 4π as for SPhERA, but also reduced in acceptance according to the needs, resources and encumbrance. It must also recalled on this subject that the readout of the scintillators and the ToF measurement could be based on the technical solution mentioned in sub-section 3.2, i.e. by amplifying and registering the collected light by SiPM's. Also if this development is not presently foreseen in the framework of SPhERA program, it is in any case worthwhile to be conducted as it will allow to realize radiation monitors with innovative performance, very compact and requiring low voltage power supplies. Adding the suitable passive absorbers they can be easily specialized for the detection of gammas and neutrons.

REFERENCES

Alenia-aerospazio, Space Division, "REMSIM-Final Report", report to ESA ALS-RMS-VRP-001, 15 September 2004

Casolino M., Rossi L., Spillantini P., "Study of magnetic radiation shielding of spacecrafts in interplanetary flights", Report under the ESA appointment n. 034/99/Spillantini, Dec.1999

Cougnet C. et al., "Radiation Exposure and Mission Strategies for Interplanetary Manned Missions (REMSIM)", Final report, ESA, 2005.

ESA Topical Team on "Shielding from the cosmic radiation for interplanetary missions: active and passive methods", 35th COSPAR Scientific Assembly, Paris, July 2004

ESA sp-1281 report on "Topical Teams in the Life and Physical Sciences: toward New Research Application in Space", pagg.184-199, October 2005

LABEN, "CREAM: architectural and electronic feasibility study", report TL 17931, January 2002

Petukhin I. and Petukhin S. "Dynamics of the GCR intensity in presence of solar wind disturbances". 21th ECRS, Kosice, Slovakia, 9-12 September 2008

Polishuk G.M. "O vozmozhnosti realizazii italyanskovo eksperimenta po issledovaniyu vspushechnovo izlucheniya na bortu rossiiskkkii KA". Federal Space Agency of Russian Federation and Lavochkin Association, letter prot. N. 87/3394, 24.10.2007

Picozza P.G., Rossitto F., Pecorella W. "SPhERA, Mission Proposal". Doc. N. PG/PS/822/07, 31.10.2007

Russo S., Barbarino G., Campana D. et al. "Technical features of the Time-of flight system for the PAMELA experiment in space". Nucl. Instrum. and Methods A572, p. 495, 2007

Spillantini P., Casolino M., Papini P., Taccetti F., "Solar Cosmic Ray surveyor and monitor for Earth-Mars missions", 35th COSPAR Scientific Assembly, Paris, July 2004

Spillantini P., Casolino M., Durante M., Mueller-Mellin R., Reitz G., Rossi L., Shurshakov V., Sorbi M., “Shielding from the cosmic radiation for interplanetary missions: active and passive methods”, Radiation Measurements 42, pp.14-23, 2007.

Straulino S., Adriani O., Bonechi l:, et al. “Spatial Resolution of Double-Sided Silicon Microstrip Detectors for the Pamela Apparatus”. Nucl. Instrum. and Methods A556, p.100, 2006.

Handling of Experimental and Slow Control Data for Large Scale Cosmic Ray Detection Networks

S.Chilingarian[1], A. Chilingarian[2], W. Eppler[1] and A. Kopmann[1]

[1].Institut fuer Prozessdatenverarbeitung und Elektronik, Forschungszentrum Karlsruhe, Hermann-von-Helmholtz-Platz 1, 76344 Eggenstein-Leopoldshafen, Germany;
[2]. Cosmic Ray Division, Alikhanyan Physics Institute, Alikhanyan Brothers 2, Yerevan 375036, Armenia
(e-mail: Suren.Chilingarian@ipe.fzk.de)

Abstract: Storage and handling of experimental data is one of the most important aspects while planning data acquisition and control systems for long-term experiments. The appropriate and easily extensible metadata is extremely important for real-time management of the detector setups and for future processing of the collected data. Even more important is to have well defined annotations of experimental data for automation of data processing and, hence, for automate detection of cosmic weather disturbances and alert generation. However, wrong organization of metadata could lead to enormous augmentation of the stored data and will significantly slow down all subsystems including data acquisition and data analysis parts.

For Aragats Space Environmental Center (ASEC) and Space Environmental Viewing and Analysis Network (SEVAN) we have developed hybrid XML based data format. The metadata information is separated from experimental/control data and encoded in XML format. It consists of 3 main components: Global Detector Description containing information on installation location, responsible persons, running software, etc. Detector Geometry which is describing the detector component parts as well as their positions and dimensions and, finally, multiple Data Layouts sections defining experimental and control data structure. The experimental data collected by each of the detectors are divided into one or more independent data sets. Each data set is represented as a sequence of data vectors associated with the acquisition time (time series) and one or more Data Layout records in the detector description. For compatibility reasons the data vectors are encoded using space-delimited ASCII strings. These ASCII strings are enclosed in the XML structure providing basic information about the data and referencing appropriate Data Layout section in the metadata. To handle data exploration and export the Advanced Data Extraction Infrastructure (ADEI) is developed at Forschungszentrum Karlsruhe. The primary targets are the slow control systems of Test Facility for Fusion Magnets (TOSKA) and Karlsruhe Tritium Neutrino (KATRIN) experiment. However, ADEI have a modular architecture and is able to handle any data which could be represented as time series including intensity measurements of incident cosmic ray fluxes. The data visualization is implemented using dynamic web interface. To achieve acceptable performance the time series are aggregated over few predefined time slices and stored in temporary caching database. This approach allows to visualize time series over long periods (years) within hundreds of milliseconds. Then, it is possible to navigate trough the data and quickly zoom into the intervals of interest. Extensible export subsystem is able to provide data in multiple formats including CSV, Excel, ROOT, and TDMS. In order to facilitate integration with various development environments ADEI is implementing a set of web services which are providing functions to browse address space and query most recent data as well as data for the required historical interval.

1. INTRODUCTION

Galactic Cosmic Rays (GCR, mostly protons and heavier nuclei) may be accelerated in our Galaxy by supernova explosions, in jets ejected from black holes or by other exotic stellar sources. After traveling millions of light years in our Galaxy they arrive in the solar system as a steady flux. On the other side, our Sun is a very variable object which changes radiation and particle flux intensities on many orders of magnitude within a few minutes. Because of the Sun's closeness the effects of changing fluxes have a major influence on the Earth including climate, safety and other issues (see for example Carslaw et al, 2002). Hybrid particle monitors at Aragats Space Environmental Center (ASEC Chilingarian et al, 2003) measure both charged and neutral components of secondary cosmic rays and provide a good coverage of different species of secondary cosmic rays with different energy thresholds. A multivariate correlation analysis of the detected fluxes of charged and neutral particles is used for analysis of geo-effective events, i.e.Ground Level Enhancements, Forbush decreases, Geomagnetic Storms and for reconstruction of the energy spectra of SCR (see Chilingarian, 2005).The particle monitors are located in the two research stations on the slopes of Aragats Mountain at altitudes 2000 and 3200 meters above sea level and are connected with the data analysis center in Yerevan by means of a wide-range radio network. The Cosmic Ray Division of Yerevan Physics Institute (CRD) has started an ongoing process of establishing a world-wide network of detectors operating at different latitudes, longitudes and altitudes. The Advanced Data Acquisition System (see ADAS, Chilingarian S., 2006, Chilingaryan S., 2009) is used to collect data and provide slow control capabilities to all detectors run by CRD. It is designed having in mind the distributed nature of GCR detection networks often consisting of multiple detectors located in hardly accessible places. The data acquisition network is constructed of multiple uniform components communicating using web services. These components are able to operate completely autonomous for long periods of time. Self-describing XML files are used for information storage and exchange. The developed format is extensible and could be easily adapted to different kinds of cosmic ray monitoring detectors.

The big amount of data is recorded during the life time of detector. The users need to examine collected data checking the integrity and validity of measurements as well as export it to various formats supported by end-user applications, like ROOT, Origin, Matlab, etc. The Advanced Data Extraction Infrastructure (ADEI) has been developed at Forschungszentrum Karlsruhe to provide these capabilities. ADEI is inspired by *Google-Maps* interface and implemented using Asynchronous JavaScript and XML (AJAX, see Brett McLaughlin, 2000) approach. The navigation through the data is feasible using mouse only. Single or multiple time series are plotted using the data from currently selected time interval. Then, the plot could be dragged and zoomed over time and value axes. Detailed information is provided about the graphics around mouse pointer. The region of plot may be selected and exported in one of supported formats including CSV, Excel, ROOT, and TDMS. The users on slow network connections may request data compression as well.

ADEI uses highly modular architecture. The data access is handled through the abstract interface implemented by dedicated drivers. Multiple drivers are provided. ADEI supports multiple relational databases, RRD files (see RRD tool team, 2009), ROOT trees (see the ROOT Team, 2009), and ADAS data format. The data received from the drivers is preprocessed using pluggable filters and distributed to the AJAX web frontend and other client applications using web service interface. Caching technology is used to provide fast access to the data collected over long periods.

Both ADAS and ADEI are licensed under GNU General Public License and uses only free open source technologies. ADAS has been operating at ASEC since November 2006. ADEI is currently implemented at slow control systems of Karlsruhe Tritium Neutrino (KATRIN see KATRIN Collaboration, 2005) experiment and Test Facility for Fusion Magnets (TOSKA). There is also experimental implementation providing access to the data collected by ASEC and SEVAN monitors.

The next section of article will provide details of XML data format used at ASEC. The third section describes features of ADEI web frontend. In the forth section more details on ADEI architecture are presented.

2. ADAS DATA FORMAT

The ADAS data consists of two components:

1. Collected data along with several properties characterizing the data (including the data timestamp, data quality, etc).
2. The detector description providing detailed information on the detector and collected data.

The detector description consists of three main components: *Global Detector Description*, *Detector Geometry* and *Logical Data Layout*. The *Global Detector Description* provides metadata describing the detector in general (detector name, its type, information on participation in various international detector networks, like Neutron Monitor network (see Morall et al, 2000) contact information of maintaining organization, geographical location). The *Detector Geometry* describes the detector component parts as well as their positions and dimensions. The multiple *Data Layout* sections indicate the physical meaning and acceptable value ranges of the data. The first two components are preliminary filled during the detector setup. The *Data Layout* is automatically generated by the ADAS software. However, additional properties still can be specified manually during the setup stage.

The data collected by each of the detectors are divided into one or more independent data sets. Each data set is represented as a sequence of data vectors associated with the acquisition time (time series) and one or more *Data Layout* records in the detector description. The multiple layouts are considered for handling cases when the structure of the data set had been changed during the detector operation. For compatibility reasons the data vectors are encoded using space-delimited ASCII strings. These ASCII strings are enclosed in the XML structure providing basic information about the data and referencing appropriate *Data Layout* section in the detector description. Example:

<Data installation="installationid" layout="layoutid"> <Time>2006-02-25T16:50:00.0000000+04:00</Time> <Duration>PT30.0000000S</Duration> <Quality>100.00</Quality> <Value>1846 2760 1956 1848 1763 </Value> </Data>

This example illustrates the representation of a single data element in the ADAS format. The *installation* and *layout* attributes reference the appropriate layout in the detector description. The *Time* and *Duration* elements are indicating the start and duration of the data integration time slice (both the timestamp and duration are encoded using rules defined by *ISO-8601* specification (see ISO, 2004). Special conditions encountered during the data acquisition are described using *Quality* element. Usually, this element indicates hardware failures resulting in partly or completely inaccurate data. The *Value* element holds a data vector in the space delimited ASCII representation.

The storage subsystem downloads the data from all URCS servers and stores it in the MySQL database. For each data set a separate table is created and for each attribute and element (*installation*, *layout*, *Time*, *Duration*, *Quality*) an individual column is used. All values are represented by individual columns as well. Such mapping allows an easy and fast access to the data, while the original XML form could be easily recovered. The description is not transported together with the collected data but available upon request from the URCS servers. However, the collected data and detector description is reconciled in a single document while exchanging data with collaborating groups.

Using the described approach the legacy application can easily extract ASCII strings from the data set and use them in the old fashion. The new applications consider the XML description in order to extract the appropriate data subset automatically.

3. ADEI WEB INTERFACE

The main view of ADEI web frontend is represented on Figure 1. The screenshot is taken using real system running at slow control system of Karlsruhe Tritium Neutrino (KATRIN [9]) experiment. Numeric labels from 1 to 12 are used to reference interface elements in the description below.

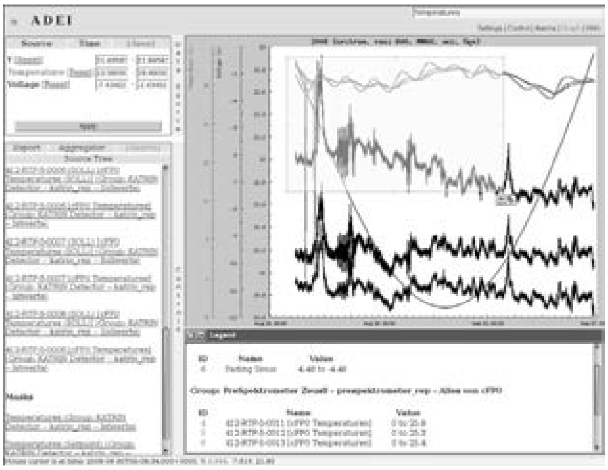

Figure 1. The screenshot of ADEI Web Frontend. The data from KATRIN slow control system is rendered in the plot. The data outage is indicated using a small line on top of the plot (see 5). Legend contains description of displayed graphics. The selected part of plot may be zoomed or exported using buttons 3 and 4. Axes controls and results of search are located in the left sidebar.

The main window (*label 1*) contains plot depicting measurements of 7 sensors over two week period from August 26, 2008 to September 07, 2008. The registrations of sensors were sampled into the database approximately ten times in a second what gives about 12 millions of data records over two week interval. To handle such an amount of data, ADEI aggregates data and produces approximately few thousand data points which are, then, used to plot a graph.

The overall aggregation and plotting performance is near to real-time. ADEI intensively uses caching techniques to accelerate data aggregation (see details below in sections 4.3, 4.4). The actual performance highly depends on the computational power of server hardware and its I/O throughput. However, on the most of up to date systems the complete time of plot generation does not exceed 500 milliseconds.

ADEI supports multiple value-axes on a single plot. The amount of supported axes is only limited by the size of browser window (any single axis needs approximately 75 pixels). The axes information is normally provided by the data source and can be overridden in ADEI configuration. The color encoding is used to show correspondence between axes and graphics on the plot: few primary colors are used to represent axes and their undertones are used for each of the graphics. In the presented example, totally three axes are used. One is used for a single voltage sensor, another for three temperature sensors, and a last one depicts three remaining sensors for which axis information is not available.

The rest of section describes ADEI user interface and its subsystems.

3.1. Data navigation

The subarea of plot can be selected using mouse pointer while holding left button (*label 2*). After selection is made it still can be fine tuned: resized or positioned using mouse or keyboard arrows. The buttons in the right-bottom part are used to export data within selected time interval (*label 3*) or to zoom into the selection (*label 4*). Additional functional buttons can be implemented using custom plugins. For example, ADEI installation at KATRIN uses a special button to search for experiment runs within selected time interval. If runs are found the run list along with descriptions is displayed in the sidebar (*label 7*). Version designed for FZK weather tower provides an extra button to mark selected data as invalid.

The data navigation is following *Google-maps* standards. The current plot on display can be zoomed in and out by scrolling mouse wheel. The default action is to zoom along time axis at the position of mouse pointer. However, the key modifiers may be used to zoom over value axis or zoom in the center of the plot. The adjustments of plot position on the time and value axes are achievable by scrolling mouse over the correspondent axis. The support for dragging plots along axes is included in development branch. The double click on considered axis will restore it into the automatic mode and all available data will be displayed.

The time series on display are selected and adjusted using several methods:

1. The *Source* tab of the upper sidebar (*label 6*) contains a selectable list of channel groups. These groups are provided by data source or/and set in the ADEI configuration. It is possible to plot a whole set of channels from the selected group or any single item from it.
2. The *Source Tree* tab of the bottom sidebar (*label 7*) contains hierarchical tree of all time series available in the system. It is possible to select and plot any desired subset of them.
3. Fast switching between the data channels and channel groups on display is possible by scrolling mouse wheel while holding the correspondent modifier key.

ADEI supports navigation history. Forward and Back buttons of the browser could be used to go back and forth in the history. The URL in the navigation bar is always precisely describing current position, selected time series, and all configured properties. This URL could be sent to the colleagues over e-mail and exactly the same plot will be displayed on their PC.

3.2. Plot interaction

A status bar (*label 10*) is used to provide status and contextual messages to the user. Currently performed actions, their completion status, contextual help, emerging error messages are reported using status bar. On mouse movement the position of mouse pointer along all axes is reported as well. An example could be seen on the provided screenshot. The color coding is used to help with association of axes. On a key presses the help message describing effects of this key when used as modifier while scrolling mouse wheel, dragging its pointer or pressing button is displayed.

In order to simplify analysis of complex plots with big amount of curves, ADEI provides possibility to investigate graphics passing in the specified area of the plot. A legend window (*label 10*) is popped up when the left mouse button is clicked. It contains a list of all graphics on the plot which are passing near position where mouse was clicked. The short name, description, and a range of values possessed in the neighborhood are presented on the legend. Current development branch allows selecting subset of channels from the legend. These channels may be removed from the plot or displayed solely. The color coding is used to associate graphics on the plot with information in the legend.

3.3. Search capabilities

ADEI includes an extensible search engine. It supports pluggable search modules and is able to search for channels, channel groups, channel values, and time intervals.

The channel search is very flexible. The channel names and descriptions are searched for single and multiple words, exact phrases, and regular expressions. The words are matched in three different ways:

- The words should match exactly
- The matched word need to start from the search term but may have arbitrary suffix
- The matched word needs to contain the searched term
- The search is case-insensitive and all these types of matching can be mixed in a single search query.

The value search finds a set of time intervals where the values of the given channel are above/below the specified threshold. The two modes are supported: search for time intervals where any value from the interval is above/below the specified threshold and search for time intervals where at least some of the values are above/below the threshold. The data cache is used to accelerate searches over big amounts of data and, therefore, precision of found intervals depends on the caching configuration. The current version of ADEI only supports searches on a single data channel.

The interval search allows users to quickly position time axes. The search module supports strings like *January 2005* or *January - March, 2006* and upon submitting of search request the time axis are set accordingly.

The search input (*label 11*) is located in the right-top corner of browser window. Upon search completion, the bottom sidebar (*label 7*) is opened and results are reported in the *Search* tab. The example presented on screenshot displays results of searching for temperature sensors in the KATRIN slow control database.

3.4. Missing and invalid data

Often due to the sensor failures, power outages, and other problems in the control and data acquisition systems, the collected information includes periods when no data was recorded or existing recordings are invalid. Normally, operators should be able to quickly locate problematic intervals and investigate them. However, using aggregating plots over lasting time intervals it is rather difficult to notice outages of short duration. On the yearly surveys the day data is represented by a few points only. It makes impossible to visualize problematic intervals shorter than a quantity of hours and in the same time appropriately plot the valid data.

In order to handle such situations, ADEI includes a quality indication line on a top of the data plot (just below a plot title). On the screenshot it is possible to see a tiny line indicating short period when the data was not recorded due to restart of the slow control system (see *label 5*).

3.5. Data export

ADEI supports multiple export formats. The current version includes support for CSV (Comma Separated Values), Microsoft Excel, ROOT (an analysis framework for high energy physics see the ROOT Team, 2009), and TDMS (Technical Data Management Streaming see National Instruments, 2009). The separator and decimal points used in CSV output are specified in the ADEI configuration to support users with different locale settings.

Additional formats may be implemented in two ways. The ADEI support custom export plugins. Alternatively, it is possible to filter exported data using system scripts. For example, to generate ROOT output, the data in CSV format is piped to standard input of a simple ROOT application which converts it to ROOT format and prints to standard output. The same mechanism could be used to compress output before returning it to the client application. The chains of filters are supported. This allows producing of archived ROOT files.

To limit amount of exported data, a data resampling may be requested by user. When switched on, the export subsystem will skip some of the data records to produce data at frequency lesser than the specified rate.

The properties of export subsystem are configured in the *Export* tab of sidebar (*label 7*). Export button extracts all data currently on display. A part of data may be exported using area selection (*label 3*).

3.6. ADEI wiki

In the big systems with large number of data channels and long data collection intervals it is rather difficult for new users to find important data. It is extremely helpful to have a descriptive listing of important channel groups along with links to the actual plots. The multiple small previews collected at one page may provide indispensable information about current system status.

This functionality is provided by Wiki engine included in ADEI web interface. Besides standard Wiki syntax it includes few ADEI-specific extensions:

1. *[preview]* - generates a preview plot. The channel group, time interval, image size, aggregation mode, and other standard properties may be specified. The preview is linked and upon a click will switch to the plotting view and display appropriate graph.
2. [grouplist] - generates linked previews for all channel groups available in the system.
3. [channels_by_name] - includes alphabetical listing of all channels in the system. Upon a click the selected channel will be plotted.
4. *[channels_by_group]* - includes hierarchical listing of all channels in the system. The selected channel will be plotted upon a click as well.

The example Wiki is depicted on Figure 2. It includes previews of three groups for last 24 hours and alphabetical list of data channels below.

***Figure 2.** Screenshot of ADEI Wiki designed for KATRIN slow control system. The page displaying activity for last 24 hours is open. Previews are depicting status of three KATRIN subsystems. According to the third preview the temperature database is currently offline. The alphabetical list of sensors follows previews.*

4. ARCHITECTURE

ADEI is designed to deal with the data sampled at high rates and stored for long periods of time. ADEI implementtation at TOSKA deals with the data continuously sampled at 10 Hz. The weather tower at Forschungszentrum Karlsruhe has an archive of measurements since beginning of 20th century. Processing such amounts of data requires enormous computational power. However, the interactive tools should operate in near real-time and extract important information from the data. To achieve this goal ADEI continuously monitors incoming data, performs preprocessing and caches important information in a MySQL database.

The simplified diagram of ADEI architecture is presented on Figure 3. The main logic of ADEI system is contained in a backend which is implemented purely in PHP programming language. The backend incorporates a Data Access Layer (DAL), a caching daemon, and ADEI library. DAL hides details of underlying data sources providing other components with a uniform way of data access. The caching daemon is continuously running on the backend server and polls the data sources for a new data. When the new data is registered it piped through series of filters which check the data quality, apply correction coefficients and drop invalid records. Then, the data is aggregated and the resulting information is stored in the caching database. The ADEI PHP library implements several classes which are using the caching database and DAL to provide stored data in various forms: binary, textual, graphical.

Communication with the web frontend and other client applications is maintained using web services. HTTP protocol is used for data exchange, XML and JSON - for data encoding. The libraries are provided to simplify ADEI integration in the projects using ROOT analysis framework and control systems based on National Instruments LabVIEW.
The rest of the section gives details on the system architecture. The first subsection presents data organization. DAL is described in the second subsection. The third and forth sections contain details on data processing and cache. Web services are briefly reviewed in the fifth section. And the last section is devoted to the frontend.

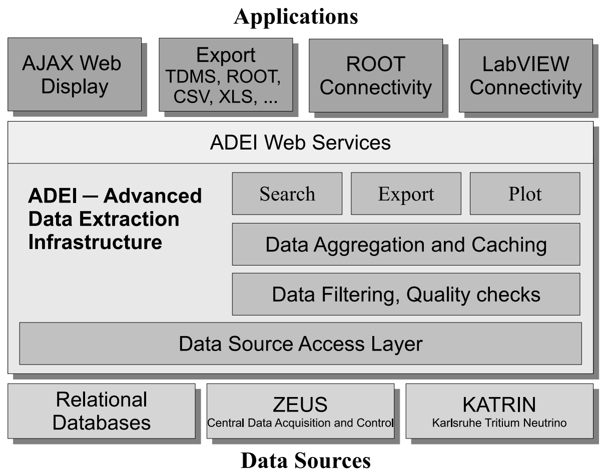

***Figure 3.** Architecture of Advanced Data Extraction Infrastructure. Data Source Access Layer unifies access to the time series stored in different formats. After data filtering and quality checks the data is aggregated and stored in intermediate caching database. Access to the data is provided by ADEI library and web services are used to communicate with client applications.offline. The alphabetical list of sensors follows previews.*

4.1. Data structure

The data access is organized hierarchically. The top level of hierarchy is a data source and ADEI may underline one or more data sources. The data provided by the data source is divided into the *LogGroups*. All channels of such *LogGroup* are synchronized by time (i.e. records have coincident timestamps). Multiple *LogGroups* are bounded together to produce another structural level. All together there are four levels of hierarchy. For example, in the case of relational database the data source describes a database server. The properties needed to connect including database type, server IP address, port, authorization information, timeouts, and so on are given in the data source setup within ADEI configuration. Databases form the next level of hierarchy. *LogGroups* are mapped to the tables or views. One of the table columns is expected to contain timing information and the rest provide data. The databases and tables as well as column mappings are given in the ADEI configuration using regular expressions.

Besides standard data sources ADEI supports virtual groups which are used to group together items from multiple data sources. Such groups contain no data, but only a record in the ADEI configuration describing which channels should be actually accessed.

4.2. Data access layer

DAL defines an abstract interface and includes number of dedicated drivers implementing this interface and providing access to the data. The current version includes drivers to access data stored in:

1. ASEC and SEVAN native data format (see section 2)
2. Relational databases accessible using PDO or ODBC modules of PHP. Most of popular databases including MySQL, PostgreSQL, Oracle, and Microsoft SQL server are supported.
3. ZEUS (The Central Data Acquisition and Control System (see Lefhalm et al, 2005) control system
4. RRD (Round Robin Database Tool (see RRD tool team, 2009) data format
5. ROOT files (see the ROOT Team, 2009).

The driver design is rather simple. Abstract interface defines only four required methods:

1. *GetGroupInfo* - provides the list of available *LogGroups*. For each of the groups information about data availability is returned: timestamps of the first and last records.
2. *GetItemList* - returns list of all items containing in the specified *LogGroup*. Upon the extended request the information on channel axes and value limits may be returned.
3. *HaveData* - returns information on the data availability in the specified interval.
4. *GetRawData* - returns the stored data from the specified *LogGroup* within the specified interval.
5. The optional methods may provide support for non-standard timestamps, information on axes and plotting preferences for each of the channels, a list of important time intervals, etc.

4.3. Data processing

The data returned by *GetRawData* is piped through the chain of filters. The filters are configured for each data source individually. They are implemented using simple PHP classes which provide a single function accepting data vectors along with associated timestamps. The function may accept or reject current supplied vector and/or correct some of the values. The information about configured filters is supplied to the *GetRawData* function which is allowed to consider this information and perform part of the filtering, hence, improving performance. The currently implemented filters include:

1. Filter resampling the source data in order to reduce data rate.
2. Filter dropping vectors with values outside of allowed range or replacing them with defaults.
3. Filter correcting the values using configured formula.

For each *LogGroup* the filtered data is aggregated over intervals of few different sizes. For each size, called a Cache Level, the new time series are constructed and stored in caching database (MySQL is used in the current version). Five new time series are generated for each original data channel and contain the following properties of the original channel aggregated over the intervals of the specified size.

1. Number of records
2. Longest period without valid data records
3. Average value
4. Minimum value
5. Maximum values

The interval sizes are selected in the way what for an arbitrary data request it is possible to find appropriate cache level providing between 1000 and 10000 data records within the demanded time interval. Such an amount of points fulfills most of plotting demands and in the same time the plots could be generated relatively fast. In order to optimize performance of cache generation, the previous cache level is used to construct cache of the higher level.

4.4. Cache usage

The generated cache is used by plotting and value search modules of ADEI library. The plot module first selects the maximal cache level providing enough points to generate a plot of the specified size. Then, the aggregated values are extracted from the correspondent caching table and one of the supported algorithms is used to convert extracted values into the graphic points. The following algorithms are available:

1. Just the average values are used
2. Sum of all values (average multiplied by number of records)
3. Both minimal and maximal values are used to display extremums

Finally, the points are plotted using JpGraph library (see Aditus Consulting, 2009). The search module checks supplied condition using highest cache level first. If criteria are met it follows down the cache chain to refine results. The real data is never examined and, therefore, minimal cache level limits search precision.

4.5. ADEI Web Service Interface

Simple web service interface is used by ADEI backend to communicate with the web frontend and other client applications. Plain HTTP protocol is used for data exchange. The request properties are encoded using GET and POST variables. The information is returned using XML or JSON encoding.

Each service is provided by standalone PHP script which decodes properties from the GET/POST variables, queries ADEI library for the requested data, and encodes in into the XML/JSON. There is a quantity of standard properties accepted by the services. The *db_server*, *db_name*, *db_group*, and *db_mask* are used to specify the data source, *LogGroup*, and the list of channels. The *experiment* and *window* are defining the time interval. The *xslt* property specifies XSLT stylesheet which is used to convert standard XML output into the format required by the client application, HTML for example. Other properties are specific to the request.

The following services are implemented and used by the web frontend:

1. *list* service provides various meta information about data sources. Depending on the supplied *target* property, it returns list of the configured data sources, *LogGroups* within the data source, channels in the *LogGroup*, etc.
2. *getimage* service renders data plot and returns PNG image. The *frame_height* and *frame_width* properties define the dimensions of image. The *aggregator* property specifies algorithm which would be used to convert aggregated properties into the graphic points. The *show_gaps* sets the mode of the missing data indicator (see section 3.4). The *precision* property is used to decrease plot details and, hence, reduce rendering time.
3. *getdata* service returns the data in the format specified by the *format* property. To reduce an amount of the returned data the *resample* property may be used.
4. *legend* service generates a list of channels which have values in the range specified by the *y* property at the timestamp specified by the *x* property.
5. *search* service accepts a search string and returns the list of found items. The *search_modules* and *search_threshold* properties alter default configuration of search engine.

The following request is used to get all channels from the first group of sensors in the slow control system of KATRIN prespectrometer. The *target* property specifies what the channel list should be returned. The *db_server*, *db_name*, and *db_group* specify the required *LogGroup*. The *db_server* refers the data source of KATRIN experiment. It uses ZEUS control system and multiple databases, specified by *db_name* property, for various subsystems. http://adei.org/services/?service=list

target=items

db $_s erver = katrindb_n ame = prespecdb_g roup = 0$

Below is shown response to this request. The default XML encoding is used. The *value* attribute specifies channel position in the group and the *name* - short channel name, the KATRIN part number in this specific case. <?xml version="1.0" encoding="UTF-8"?> <result> <Value value="0" name="412-RPV-3-0005"/> <Value value="1" name="412-RTP-5-0011"/> ... <result>

4.6. Fronted

ADEI frontend is implemented using AJAX approach. The pages are rarely reloaded, required information is obtained from the ADEI services using XMLHTTPRequest object, and JavaScript is used to update content of the page (see McLaughlin et al, 2000, W3C, 2008). The data plots are generated by the backend and delivered to frontend as PNG images.

The open source JavaScript libraries are widely used to implement advanced features.

1. *Prototype* framework is used to transparently support multiple browsers (see Prototype Core Team, 2009).
2. *dhtmlHistory* is providing navigation history and bookmarking support in AJAX context (see Dillard et al, 2007).
3. *DHTMLX* components are providing menu and source tree objects (see DHTMLX, 2009).
4. *ImageCropper* is modified and used to select subregions of plot (see Spurr et al, 2006).
5. *YUI Compressor* is used to compress JavaScript code (see Yahoo, 2009).
6. The frontend was tested and reported to work in following browsers:
7. Mozilla Seamonkey 1.1.7 (Linux, amd64)
8. Mozilla Firefox 3.0.3 (Linux, x86)
9. Mozilla Firefox 2.0.0.11 (Linux, x86)
10. Safari 3.0.4 (MacOS 10.4.11, PowerPC G4)
11. Safari 3.1 (WinXP, x86)
12. Arora 0.4 (Linux, amd64)
13. Opera 9.23 (Linux, x86)
14. Konqueror 4.2 (Linux, amd64)
15. Google Chrome 0.3.154.9 (WinXP, x86)
16. Internet Explorer 6.0 SP1 (Win2000, x86)
17. Internet Explorer 7.0 (WinXP, x86)

REFERENCES

Carslaw K. S., Harrison R. G., Kirkby J., Cosmic rays, clouds, and climate, Sci. 289 1732–1737, 2002.

Chilingarian A., Avakyan K., Babayan V., et al., Aragats space- environmental center: Status and sep forecasting possibilities, J. of Phys.G 29 939–951, 2003

Chilingarian A., Arakelyan K., Avakyan K., et al., Correlated measure- ments of secondary cosmic ray fluxes by the aragats space-environmental center monitors, Nucl. Inst. Meth. A543 483–496, 2005.

Chilingaryan S., Universal data exchange solution for modern distributed data acquisition systems and its implementation for cosmic ray monitor networks, Ph.D. thesis, 2006. URL http://dside.dyndns.org/cv/phd4.pdf

Chilingaryan S., Chilingarian A., Danielyan V., Eppler W., Advanced data acquisition system for sevan, Advances In Space Research 43 717–720, 2009.

Brett McLaughlin, Mastering ajax, URL http://www.ibm.com/developerworks/web/library/wa-ajaxintro1.html, 2000

RRD tool team, Round robin database tool URL http://oss.oetiker.ch/rrdtool, 2009.

The ROOT Team, Root: A data analysis framework URL http://root.cern.ch, 2009.

KATRIN Collaboration, Katrin design report 2004, Tech. rep.,Forschungszentrum Karlsruhe, URL http://www-ik.fzk.de/~katrin/publications/documents/DesignReport 2004-12Jan2005.pdf, 2005

Morall H., Belov A., Clem J. M., Design and co-0rdination of multi-station international neutron monitor networks, Space Sci. Rev. 93285–303.19, 2000.

ISO, International standard iso 8601 URL http://www.iso.org, 2004.

National Instruments, Ni tdm data model, URL http://zone.ni.com/devzone/cda/tut/p/id/3727, 2009

Lefhalm C., Krieger V., A full featured monitoring, control and data management system for liquid metal coolant loops, in: Proc. of 14th IEEE-NPSS Real Time Conference, p. 132. 2005.

Aditus Consulting, Jpgraph - php graph creating library URL http://www.aditus.nu/jpgraph/, 2009.

W3C, The xmlhttprequest object, 2008.

URL http://www.w3.org/TR/XMLHttpRequest/

Prototype Core Team, Prototype javascript framework, 2009.

URL http://www.prototypejs.org/

Dillard B., Neuberg B., Really simple history (rsh): Ajax history and bookmarking library URL http://code.google.com/p/reallysimplehistory, 2007.

DHTMLX, Dhtml extensions - professional ajax components for ad-vanced web ui. URL http://www.dhtmlx.com/, 2009.

D. Spurr, Javascript image cropper ui, using prototype and script.aculo.us,URLhttp://www.defusion.org.uk/code/javascript-image-cropper-ui-using-prototype-scriptaculous/, 2006.

Yahoo, Yahoo! ui library: Yui compressor URL http://developer.yahoo.com/yui/compressor/, 2009.

Estimation of the Energy Threshold of NAMMM, ASNT and SEVAN Particle Detectors

B. Mailyan

Cosmic Ray Division, Alikhanyan Physics Institute, Alikhanyan Brothers 2, Yerevan 375036, Armenia
(e-mail: bagrat_mailyan@yerphi.am)

Abstract: After the major modernization of the data acquisition electronics of the Aragats Space Environmental Center (ASEC) particle detectors the calculations of the barometric coefficients of all the ASEC particle monitors were performed at the beginning of the 24th solar activity cycle. The time periods of minimal disturbances of the interplanetary magnetic field (IMF) were selected to avoid biases due to transient solar events. The barometric coefficients of different particle detectors measuring various secondary cosmic ray fluxes located at altitudes of 1000 m, 2000 and 3200 m. a.s.l. are calculated and compared. The barometric coefficients for the several Neutron Monitors of recently established Eurasian data base (NMDB) and SEVAN particle detector networks were also calculated. The latitude and altitude dependencies of the barometric coefficients were investigated, as well as the dependence of coefficients on the most probable energy of the primary protons generated definite species of the secondary fluxes.

1. INTRODUCTION

High energy particles, accelerated on the Sun (Solar Cosmic Rays – SCR) are superimposed on the Galactic Cosmic Ray (GCR) background. Cosmic Rays have the most direct impact on humans in space, on space-based electronics and on other important technological assets. The other source of the variability of cosmic ray flux are huge magnetized clouds (Coronal mass ejections – CMEs), emitted by the sun and traveling in the Interplanetary Space (IP). This gigantic plasma clouds with “frozen” magnetic field disturb the Interplanetary Magnetic Field (IMF). The SCRs arrive at the Earth in the time from 10 minutes till many hours due to particle energy dependent diffusion. The intensity of radiation in the near-Earth environment can boost thousand times in a few minutes posing serious hazard to space operations and over-polar flights. Therefore, continuous monitoring of the particle fluxes is of crucial importance for alerting on radiation hazard. Because only highest energy cosmic rays can generate particle cascades reaching the Earth surface (and triggered Ground Level Enhancements – GLE), the information of upcoming abundant low and middle energy cosmic rays can be ascribed from the enhancements of the time series of count rays of surface particle monitors. On the other hand the same time series contain information on the disturbances of the IP magnetic field and may prove useful for the forecasting of the severity of geomagnetic storm unleashed by at the arrival of ICME. The size and magnetic field of IP CMEs (ICMEs) are correlated with the modulation effects the ICME poses on the ambient population of the galactic cosmic rays during its propagation up to 1 AU. On the way to the Earth (15 – 50 hours) the magnetic cloud and shock modulate the GCR flux, changing its intensity and making it anisotropic. The strength of these modulation effects correlate with geomagnetic indices of the storm unleashed on the arrival of the ICME to the magnetosphere.

Space-borne spectrometers measure the time series of the changing fluxes with excellent energy and charge resolution. Surface detectors measure time series of secondary particles born in cascades originated in the atmosphere by primary ions and solar neutrons. Networks of the particle detectors located on the Earth surface can detect these modulation effects, predict the upcoming geomagnetic storms hours before the ICME arrival at the magnetometers on ACE and SOHO. The half-hour lead time (time span ICME travels from space stations to magnetosphere) provided by the particle detectors located at the space stations ACE and SOHO 1,5 million kilometers from the Earth is a bit short to take effective mitigation actions and protect satellites and surface industries from harm of major geomagnetic storms.

To establish reliable and timely forecasting service we need to measure, simulate and compare:

- time series of neutrons, the low energy charged component (mostly electrons and muons) and the high energy muons;
- the correlations between changing fluxes of various secondary particles; and
- direction of the detected solar cosmic rays.

Surface monitors located at the Aragats Space Environmental Center (ASEC) at 2000 and 3200 m altitudes (40˚25′N, 44˚15′E; Vertical cut-off rigidity in 2007: 7.1 GV) detect charged and neutral components of the secondary cosmic rays with different energy thresholds and various angles of incidence.

2. ESTIMATION OF THE THRESHOLD ENERGY OF NAMMM

The Nor Amberd multidirectional muon monitor (see Chilingarian for the ASEC team, 2005) (NAMMM, see Figure 1) is operated by Cosmic Ray Division (CRD) at the Nor Amberd research station of the Alikhanyan Physics Institute.

NAMMM is located on the slope of the mountain Aragats at 2000 m above sea level. Geographical coordinates are 40°22'N, 44°15'E.

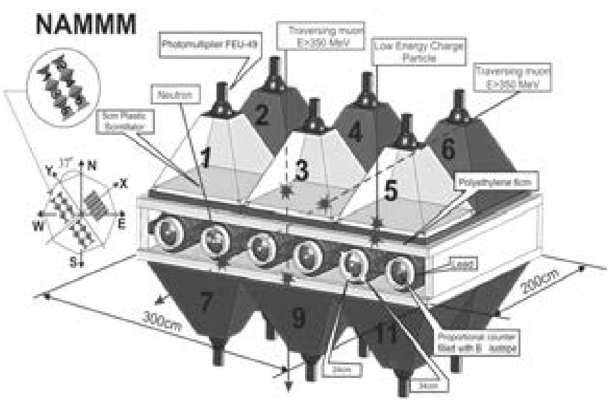

Figure 1. Nor Amberd Multidirectional Muon Monitor (NAMMM).

The monitor consists of two layers of plastic scintillators above and below two of the three sections of the Nor Amberd Neutron Monitor 18 NM64. The lead (Pb) filter of NM absorbs electrons and low energy muons. The distance between layers is approximately 1 m. Each layer consists of six detectors, each having the area of 0.81 m^2. The data acquisition system of the NAMMM can register all coincidences of detector signals from upper and lower layers, thus, enabling measurements of the arrival of the muons from different directions.

In Figure 2 the blue curve demonstrates the angular frequency histogram of muons incident the upper layer of detector. In the same Figure the analogical frequency histogram of muons traversing the scintillator in the lower layer just below the upper one is denoted in red.

An example of such an event is depicted in Figure 1.

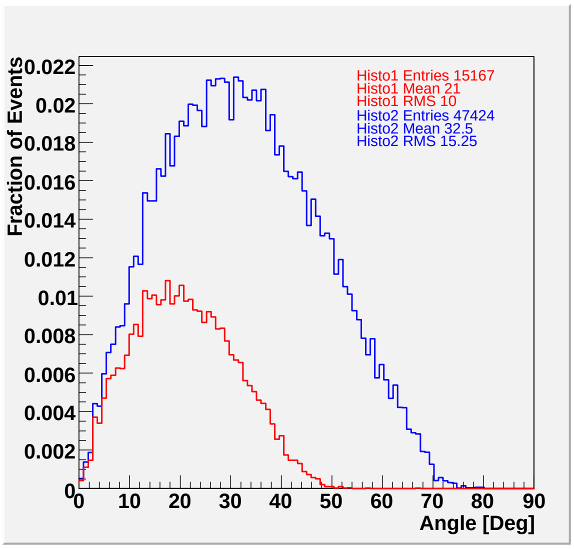

Figure 2. Angular frequency histograms of muons registered by upper detector of NAMMM (in blue), and – by coincidence of upper and lower detectors(in red).

NAMMM is a hybrid detector measuring neutral and charged CR fluxes. The upper layer of the detector measures low energy charged particles, mostly electrons and muons. The energy threshold of the upper scintillators is determined by the sensitivity of photomultiplier PM and data acquisition electronics (DAQ) and is equal to about 7 MeV.

The neutron monitor measures secondary neutrons of the cosmic ray flux. The lower layer of the NAMMM scintillators is sensitive to high energy muons because low energy muons and electrons are absorbed by the 10 cm lead filter.

Detecting Ground Level Enhancements by different monitors, sensitive to various energetic populations of the primary solar particles, it will be possible to reconstruct energy spectra of GLE and determine the spectral index. The large energy spectral index of the SCRs at highest energies ($\gamma \geq -5$, hard spectra; usually SCR spectra is very steep at GeV energies: $\gamma \leq -7$) is a very good indicator of upcoming abundant SCR protons and ions with energies >50 MeV, extremely dangerous for the astronauts and high over-polar flights, as well as for satellite electronics.

This is the way it is important to know the energy threshold of the lower layer of NAMMM. From the known threshold energy of the secondary muons detected by the NAMMM we'll reconstruct the most probable energy of the primary solar protons giving rise to the GLE. Along with similar data from the neutron monitor and the upper layer of the NAMMM we will have enough information to calculate the spectral index of the GLE in progress and warn space operators if estimated value of index is greater than –5.

We estimate the threshold energy using 3 different methods:

- by calculation of ionization losses of muons in lead;
- by computer simulation of particle cascade development in atmosphere and response of monitor to the secondary cascade particles;
- by comparing simulated spectrum and experimentally measured detector count rate.

3. CALCULATION OF ENERGY LOSSES OF MUONS IN LEAD

Moderately relativistic charged particles ($\beta\gamma < 1000$) other than electrons lose energy in matter primarily by ionization and atomic excitation. The mean rate of energy loss is given by the Bethe-Bloch equation,

$$-\frac{dE}{dx} = Kz^2 \frac{Z}{A}\frac{1}{\beta^2}\left[\frac{1}{2}\ln\frac{2m_e c^2\beta^2\gamma^2}{I} - \beta^2 - \frac{\delta}{2}\right],$$

β=v/c, $\gamma = (1-\beta^2)^{-1/2}$, $K = 4\pi N_A r_e^2 m_e c^2$.

Here K = 0.307075 MeV cm^2, z is the charge of incident particle, Z-atomic number of absorber, A - atomic mass of absorber in g mol^{-1}, $m_e c^2$-the rest energy of electron, $I = 16Z^{0.9}$ is the mean excitation energy. δ is the density effect correction to ionization energy loss. In our calculations we will not take into account this effect.

By integrating equation (1) we can obtain total energy release of muon before reaching the lower scintillator, which coincides with energy threshold of NAMMM.

The right hand part of Bethe-Bloch equation contains quantities, which are not dependent on path length x explicitly. That's why we cannot integrate Eq. (1) on x directly and find function E(x). But since the right hand part of equation (1) depends on β, which determines explicitly kinetic energy E, the inverse function *dx/dE* can be immediately integrated:

$$R = -\int_{E_f}^{E_{in}} \frac{dE}{dE/dx} \qquad (2)$$

Here R represents integral path (or simply path length) of the particle. E_{in} is the initial energy of muon and E_f is its final energy.

Using muon kinetic energy $E = Mc^2/(1-\beta^2) - Mc^2$, we find $dE = M\,v\,dv/(1-\beta^2)^{3/2}$. Substituting the found dE and dE/dx from Eq (1) into (2) and neglecting δ we will obtain the following expression:

$$R = C\int_{\beta^2_f}^{\beta^2_{in}} \frac{\beta^2 d\beta^2}{(1-\beta^2)^{3/2}(\ln\frac{k\beta^2}{1-\beta^2}-\beta^2)}, \qquad (3)$$

$$C = \frac{A}{(Kz^2Z)}Mc^2, \quad k = \frac{2m_e c^2}{I}.$$

Here *C* and *k* are constants. From this expression we can get the threshold energy of NAMMM. *R* is the path length in g/cm^2. If we want to get value in cm-s, we should divide *R* on the density of absorber. Path length is fixed by the geometry of detector and by angle of incidence. There is about 10 cm of lead between the upper and bottom layers of NAMMM. For Pb the numerical values of the constants C and *k* come to *C*=430 g/cm^2 and *k*=1200. But we should take into account that scintillators register particles with energies >7MeV. Thus we need to know the energy of incident muon, which can penetrate through 10 cm of lead and still have residual energy equal to 7 MeV. We have calculated integral in equation (3) numerically by using Simpson's method (see McCracen & Dorn, 1977). In this method integration results in calculating of sum by using following extrapolating formula:

$$I=\int_a^b f(x)dx = \frac{h}{3}(y_0+4y_1+2y_2+4y_3+2y_4+\ldots+2y_{n-2}+4y_{n-1}+y_n), \qquad (4)$$

where y_i are values of function f(x) in discrete points x_i: $y_i=f(x_i)$, i=0,1,…,n; $h=x_{i+1}-x_i$

In Simpson's method error of calculation is minimal for n = 50…100. Relative error is less than 0.01%. We have calculated integral in (3) for n=50 and 100 for various values of β_{in} and fixed β_f corresponding to 7MeV. Thus we found the value of β_{in} for equation (3) at R=10 cm. The found β_{in}^2 = 0.87 gives for this case the value of E_{thresh}=188 MeV. The value of integral (4) in this case was equal to 0.266. These calculations have been performed using standard Mathematica 5.0 program.

4. ESTIMATION OF THE ENERGY THRESHOLD OF NAMMM USING COMPUTER SIMULATION

The second method of energy threshold estimation is based on the computer simulation of passing primary particles through the Earth's atmosphere and NAMMM. The simulations are performed using GEANT 3 package. We simulate particle cascade development in the atmosphere and response of NAMMM to the secondary cascade particles. Thus we have the energy spectrum of secondary particles at 2000m above sea level.
In Figure 3 we can see the frequency histogram of energies of muons registered by the lower detector of NAMMM (we put a limit on the maximal energy of 500MeV); secondary muons usually have energy above 200 MeV. This picture can be easily obtained from the Browser of Root package (see ROOT user's guide 5.14, http://root.cern.ch/).

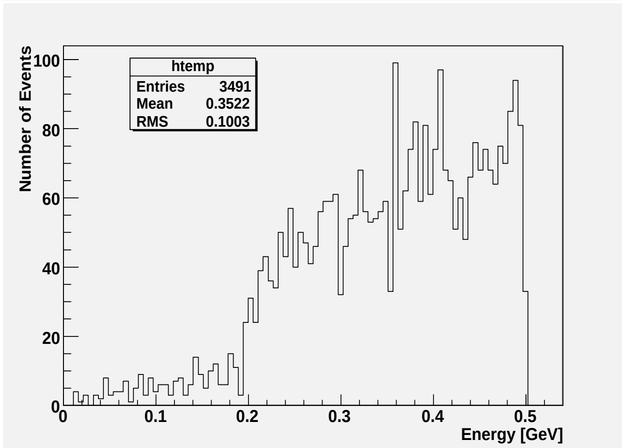

Figure 3. Events registered by the lower layer of NAMMM with energies<500MeV

Fitting of muon spectrum function was performed by the power function. The result is shown in Figure 4.

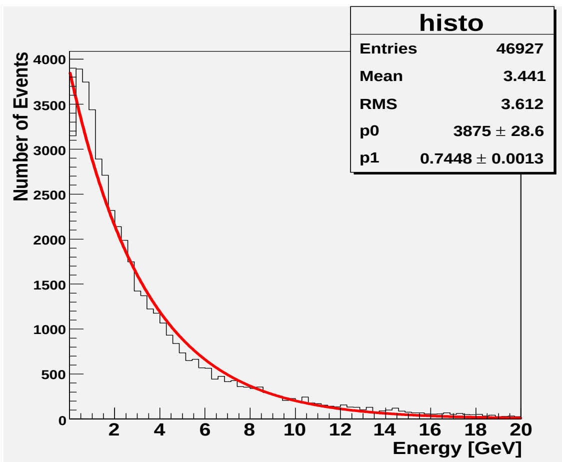

Figure 4. Fitting the spectrum of muons at 2000m above sea level

To obtain the energy threshold of NAMMM, we should calculate the lower limit of the following integral

$$\int_{E_{tresh}}^{20} p0\cdot p1^E\,dE = \tfrac{2}{7}N \qquad (5)$$

Note, that before we tried to fit the spectrum by power function $E^{-\gamma}$, but results were worse than in the case of b^E, i.e. fit function didn't correspond to the histogram and a considerable part of the histogram points were far from fit function curve.

Here p0=3875 and p1=0.7448 are parameters of the fit, N is the count rate per 5 min, which coincides with the histogram entries in Figure 4. We multiply count rate by 2/7 since there are 7 histogram bins in the range of 2GeV energy. The value of the integral (5) equals to the area of histogram. And the area of this histogram is equal to the number of bins in the histogram.

According to simulated data count rate of NAMMM is equal to N=44176 for 5 minutes (simulations were performed for 5 min. to provide more statistics) and the energy threshold is correspondingly equal to 140MeV.

The underlying cause of such a small value is the bad fit, especially in the region up to 2 GeV.

5. EXPERIMENTAL DATA FROM NAMMM

Now let's compare experimental and simulated data. Data of NAMMM from September 15 to 30 of 2006 were used, according to which the lower detectors of NAMMM have registered in average 8700 particles per minute per $0.81m^2$ (each detector surface area is 0.81 m^2). When placing this value in equation 5 instead of N we will get for the threshold energy the value E = 200MeV. This value obtained from experiment is higher than the modeled value of 140MeV. Such a discrepancy is apparently due to 16cm polyethylene layer not taken into consideration in the model. Due to this layer some particles with relatively low energy (about 190 MeV) can't traverse through these two layers of scintillators and the energy threshold will be higher. The difference between the experimental and simulated results should be about 60 MeV.

Muons passing the upper layer should have enough energy to reach the bottom scintillator layer. And here can be used the approximate formula for ionization loses of relativistic particles in the light matter (A/Z=2). According to that formula, mean rate of energy loses in light matter for relativistic particles are 2 MeV/cm. So we will get 16 MeV for the upper polyethylene layer.

Energy loses in the lower polyethylene layer are calculated using Bethe-Bloch equation as described above. Here approximate formula can't be used, because muons already passed 8cm polyethylene and 10cm lead and they may have small energies. Consequently energy loses could be much higher. In case of polyethylene, constants are C=600 g/cm^2 and K=21000 correspondingly. And the energy loss in the bottom detector is about 44MeV.

So 60MeV should be added to the result of the first method. The energy threshold will be 248 MeV.

Besides we have not taken into account the low energy particles incident upon the sides of NAMMM, which may be registered in the lower detector. Due to that the energy threshold is smaller.

6. ESTIMATION OF THE ENERGY THRESHOLD OF SEVAN PARTICLE DETECTOR

The basic detecting unit of the SEVAN network (see Chilingarian & Reymers, 2008) (see Fig. 5) is assembled from standard slabs of 50×50×5 cm^3 plastic scintillators. Between 2 identical assemblies of

100×100×5 cm^3 scintillators (four standard slabs) are located two 100×100×5 cm^3 lead absorbers and a thick

50×50×25 cm3 scintillator assembly (5 standard slabs). A scintillator light capture cone and Photo Multiplier Tube (PMT) are located on the top and bottom, as well as in the intermediate layers of the detector. The detailed detector charts with all the sizes are available from crd.yerphi.am.

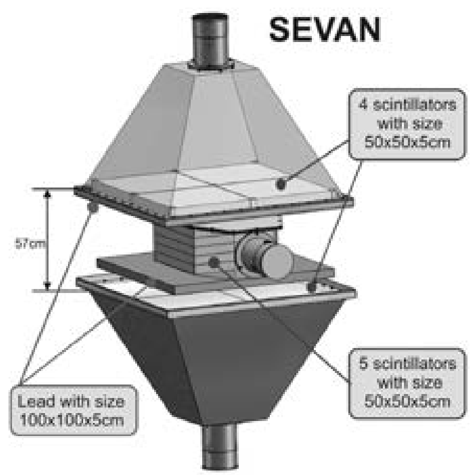

Figure 5. The basic detecting unit of the SEVAN network

Incoming neutral particles undergo nuclear reactions in the thick 25-cm plastic scintillator and produce protons and other charged particles. In the upper 5-cm thick scintillator charged particles are registered very effectively; however, for the nuclear interactions of neutral particles there is not enough substance. When a neutral particle traverses the top thin (5 cm) scintillator, usually no signal is produced. The absence of the signal in the upper scintillators, coinciding with the signal in the middle scintillator, points to neutral particle detection. The coincidence of signals from the top and bottom scintillators indicates the traversal of high energy muons. Lead absorbers improve the efficiency of the neutral flux detection and filtered low energy charged particles. If we denote by "1" the signal from the scintillator and by "0" the absence of the signal, the following combinations of the 3-layered detector output are possible:

- 111 – traversal of high energy muon;
- 011 and 010 – traversal of the neutral particle;
- 100 – traversal of low energy charged particle stopped in the scintillator or in the first lead absorber.
- 110 – traversal of higher energy charged particle stopped in the second lead absorber.
- 001 – registration of the inclined charged particles.

The efficiency of the charged particle detection by all 3 layers of the SEVAN detector is about 95%; the neutron detection efficiency in the middle "thick" scintillator reaches 30% at 200 MeV, the efficiency of the -quanta detection reaches 60% at the same energies.

The lead absorbers filter low energy electrons and gammas. Figure 6 shows the result of simulation - histogram of events registered by the lower layer of SEVAN monitor with energies lower than 500 MeV. As one can see, the lower layer is sensitive to the high energy muon flux with the threshold energy approximately 250MeV. Using equation (1) we have confirmed this result by analytical calculations of ionization loses in lead and scintillator. The result of calculations is in a good agreement with simulated one and equal to about 245MeV.

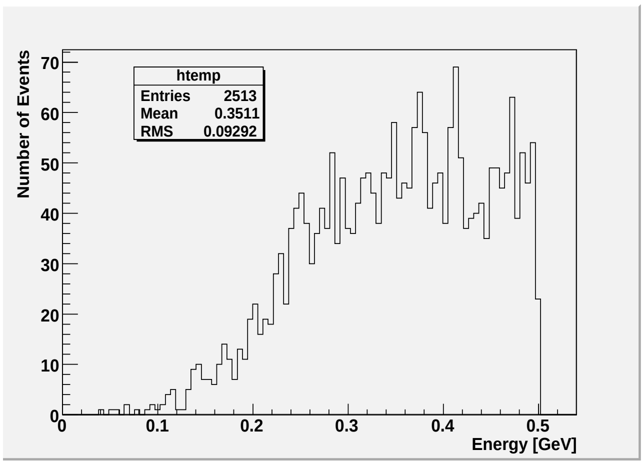

Figure 6. The energy threshold of basic detecting unit of the SEVAN network according simulation

7. PASSAGE OF THE LOW ENERGY ELECTRONS THROUGH THE ROOF OF MAKET BUILDING

Low energy electrons should have enough energy to pass through the roof of the building and material of the scintillator's housing and still have residual energy 7 MeV to be registered in the upper detector of SEVAN monitor. The roof of the detector consists of 0.6 mm iron and 3 cm of wood. The housing of detector is made of 2 mm aluminium tin plate.

Ionization loses in iron, wood of the roof and aluminum of scintillator's housing are equal to about 7.6 MeV (6 MeV loses are due to the wood). So electron should have 14.6 MeV energy to pass the roof, detector's housing and be registered in upper scintillator. But we have to take into account also the radiation loses, which are significant for electrons. Radiation loses are proportional to the energy of particle and can be given by the following expression.

$$E = E_0 \exp(-x/X_0) \qquad (6)$$

Here E_0 is the initial energy of particle, x is the path length in g/cm^2 and X_0 depends on material of absorber.

Thus we should find out the minimal energy of electron which loses energy by ionization and radiation and has residual energy 7 MeV. After considering the radiation loses, the value of 15.97 MeV is obtained.

It's worth mentioning that wooden roof is not solid bridged, there are many gaps (~ 70% of surface) above SEVAN detector and lower energy particles can penetrate and be registered by the upper detector of SEVAN monitor. If we exclude 3 cm of wood from the calculations we'll get 9.59 MeV for the threshold energy.

Estimation of the threshold energy for electrons detected by upper layer of SEVAN monitor is especially important for investigations of cosmic ray intensity changes during thunderstorms. SEVAN monitor and Aragats Solar Neutron Telescope (ASNT) (see Chilingarian & Melkumyan, 2007) are unique instruments to investigate this, yet unsolved phenomena. The SEVAN monitor and ASNT both located in the same building (under the same roof) on mountain Aragats where thunderstorms are usual in May - June. The energy threshold for the upper layer of ASNT is the same as for SEVAN. But for the lower layer of 60 cm scintillators the threshold is bigger due to upper layer of 5 cm scintillating detectors. Distance between these two layers of the detectors is 1 m. The upper detectors absorb low energy electrons and the threshold is bigger approximately by 10 MeV for lower detectors. After taking into account radiation loses the energy threshold of ASNT lower detectors for electrons is 29.3 MeV. However there is also possibility to enter the volume of detector avoiding passing the 5 cm scintillator (particles can hit the sides of 60 cm thick volume of detector under zenith angles greater than 30°). If we take into account the gaps in the wooden roof and assume that electron doesn't pass through the wood, but traverses the 5 cm scintillator, we will get 21.5 MeV for the threshold energy.

Therefore the upper layers of both SEVAN and ASNT are sensitive to lower energy electrons and muons starting from ~9.6 MeV.

8. CONCLUSION

We have estimated the threshold energies of NAMMM and SEVAN particle detectors.

For NAMMM we found three different estimations for the threshold energy:

- 187 MeV from Bethe-Bloch equation
- 140 MeV from simulated data
- 200 MeV from superimposing simulated and experimental data

To obtain more precise value of threshold energy in our simulations and calculations we should take into account polyethylene layer of 16 cm, which gives increase in the calculated energy threshold by 60 MeV.

In case of SEVAN we had a good agreement between analytical calculations and simulation.

The analytically calculated values and results obtained from simulation and experiment are about 250 MeV for both detectors.

These values of threshold energy should be used for simulation of primary particles corresponding to secondaries detected by ASEC monitors.

REFERENCES

Chilingarian A. for the ASEC team, Correlated Measurements of Secondary Cosmic Ray Fluxes by the Aragats Space- Environmental Center Monitors, NIM-A, 543, 483-496, 2005

McCracen D.D. and Dorn W.S., Numerical Methods and FORTRAN Programming, by (translation into Russian “Мир”), 1977

ROOT user’s guide 5.14, http://root.cern.ch/

Chilingarian A. and Reymers A., Investigations of the response of hybrid particle detectors for the Space Environmental Viewing and Analysis Network (SEVAN), Ann. Geophys., 26, 249.257, 2008

Chilingarian A., Melkumyan L., Hovsepyan G., Reymers A., The response function of the Aragats Solar Neutron Telescope, Nuclear Instruments and Methods in Physics Research A 574, 255-263, 2007

Investigation of Daily Variations of Cosmic Ray Fluxes Measured by ASEC Monitors

A. Chilingarian, B. Mailyan

Cosmic Ray Division, Alikhanyan Physics Institute, Alikhanyan Brothers 2, Yerevan 375036, Armenia
(e-mail: bagrat_mailyan@yerphi.am)

Abstract: We have performed a study of daily variations of secondary Cosmic Rays (CR) using data on charged and neutral CR fluxes measured by particle detectors of Aragats Space Environmental Center data (ASEC), which continuously register different species of secondary CR with different threshold energies and incident angles. Data at the beginning of 24-th solar activity cycle are used to avoid biases due to solar transient events and to establish benchmark for the monitoring of solar activity in new started solar cycle.

After eliminating changes associated with atmospheric pressure variations, solar diurnal variations are clearly seen in muon and neutron fluxes. Magnitude of daily variations of neutrons correspondent to the lowest energy primary protons is comparable to the magnitude of variations of charged secondary CR. Diurnal variations of neutron flux are higher for the high latitudes comparing with middle latitudes and for low energy muons comparing with higher energy muons. Time of maximum for high latitude neutron monitors is comparable with those for middle latitude monitors. Amplitude of variation is 0.24% and phase is about 14:00 and 14:30 local time, for Aragats and Nor Amberd neutron monitors respectively.

1. INTRODUCTION

After the discovery of Cosmic Rays (CR) and after starting particle flux monitoring at different locations worldwide there were discovered different types of periodic variations of CR intensity. Some of them were connected with galactic rotation (Compton & Getting, 1935); others with co-rotation of the CRs with Interplanetary Magnetic Field (IMF), attached to the sun (Parker, 1964). The first effect becomes apparent as periodicity in sidereal time; the second – as periodicity in local (solar) time, i.e. as diurnal variations. This paper presents the calculations of daily variations of secondary particle fluxes measured by particle detectors of Aragats Space Environmental Center (ASEC) and by particle detectors of particle detector networks SEVAN (Chilingarian et al., 2009) and NMDB, - a European project to develop data base of minute count rates of several Eurasian neutron monitors.

The diurnal variations are the result of complex phenomena involving IMF, magnetosphere and in addition dependent on the latitude, longitude and altitude of detector location on the earth. The diurnal CR variations comprise an important tool for understanding basic physics of the heliosphere and Earth's magnetosphere. Low energy galactic CRs (GCR, with energies below few tens of GeV) are moving mostly along lines of IMF and their intensity should peak at time of best connections of solar magnetic field (brought to 1 AU by solar wind) with magnetosphere (flux transfer events).

Diurnal variations can be characterized by the maximal value (amplitude) and phase (time of the maximal amplitude). Different species of the secondary CR undergo different diurnal variations. It is overall understanding that more the most probable primary energy of the monitored CR specie (neutron, electron, muon ,etc…) – less should be the amplitude of diurnal variation. Therefore the third parameter characterizing the diurnal variations at definite location and time is, so called, upper limited rigidity, i.e., the threshold rigidity not influenced by the solar, interplanetary, and geomagnetic disturbances.

CR flux can be decomposed into radial and tangential components. Solar wind convective outflow in radial direction compensates galactic CR flux. CR flux in tangential direction generates variations with maximum believed to happen at 18:00 local time (Krymsky, 1964; Mourzin, 1970; Forman and Gleeson, 1975; Bieber et al., 1983). However, as the Earth's magnetic field bends the flux in tangential direction we expect that the maximum of intensity occurs few hours earlier (Dorman, 1970). Amplitude of daily variation detected by ground-based detector reported to be less than 0.5 % (Thompson, 1938) at latitudes ranging from 54.7 N to 40 S degrees.

The atmospheric effects also influence the daily variation of the count rate of particle detectors. However, the effects of temperature, humidity, electric field, and gravity are negligible as compared to the effect of pressure; and the correction for the pressure are necessary (Pomernatz and Duggal, 1971). The long term daily variations of the atmospheric pressure are also periodic and can introduce bias in the obtained results if not treated properly. Hadronic component of CR are believed not to be influenced strongly by the temperature gradient in the atmosphere. On the other hand, variations of temperature gradient cause changes in count rates of secondary muons. According to Dorman, (1975) atmospheric temperature effects of muons are in order of 0.1-0.2%.

There is a variety of papers concerning the dependence of amplitude of daily variation on geomagnetic activity. Agrawal et al., (1995) have shown that during the periods with low Ap geomagnetic index, amplitudes of diurnal variation are significantly smaller compared to the periods before and after. Kumar et al., (1993) found that distribution of amplitudes and times of maximums for geomagnetically quit days are very narrow as compared to the all days. Thus, they concluded that quit days are better suited for the CR daily variation studies. Both groups have used middle latitude Deep River neutron monitor data, located at latitude of 46°06', north and longitude 77°30', west.

Several papers investigate the dependence of daily changes on the phase of the solar activity cycle. It was found that the upper limiting rigidity varies with solar cycle. Begum (1974) has studied the variation of the upper limiting rigidity from 1965-1971. Neutron data from five mid-latitude stations and muon data of 2 stations have been used. They show that the limiting rigidity varies from minimum value of about 35 GV in 1965 to a maximum of about 125 GV in 1970. At solar minimum in 1965, the annual mean diurnal variations were very small. Agarwal and Mishra, (2008) showed that diurnal amplitude significantly decreases and the time of maximum shifts to the earlier hours during the solar activity minimum years for high and middle latitude neutron monitors.

Another group of papers presented the dependence of daily changes on solar transient events.

El-Borie et al., (1996) observed large solar diurnal amplitudes associated with high values of solar wind speed, plasma temperature, and value of the IMF Bz component.

Duldig and Humble, (1990), have analyzed enhanced cosmic ray diurnal variations in Mawson and Hobart neutron monitor and underground muon data. At the near solar activity minimum year 1987 the mean amplitude of the diurnal variation for underground muon detectors with median energy of response of about 170 GV was 0.03% and 0.05% for Mawson and Hobart detectors respectively. For neutron data, the amplitude was 0.2% and 0.21% for Mt.Wellington and Mawson neutron monitors. They also claim that it is necessary to derive free space amplitudes outside the geomagnetic field. Then it will be possible to connect obtained parameters with IMF, solar wind and plasma data.

Using the data of neutron monitor network from 1965-2003, Belov et al. (2006) have derived diurnal variations for disturbed and quit days by the Global Survey Method. They found that anisotropy in disturbed days has bigger amplitude and differs by the phase from the anisotropy in quit days, but these differences are less than those in solar wind parameters or in geomagnetic activity indices. Their main conclusion is that properties and long term behavior of CR anisotropy are mainly determined by the long term periodical changes on the Sun and in the heliosphere and not by particular disturbances in the solar wind.

Munakata et al., (1995) based on the data of surface and underground muon monitors, claim that during periods when magnetic polarity of Sun is positive the maximums of daily variations significantly shift toward earlier hours. In the recent paper by Kudela et al., (2008) using data of Lominsky Stit, Oulu and Climax neutron monitors no clear difference in the dependence of daily variations on the daily average IMF value, solar wind velocity and geomagnetic indices were observed. Badruddin, (2006) found that enhanced diurnal anisotropy is a precursor to smaller (< 5%) amplitude Forbush decrease.

Thus, we see that the detailed investigation of the diurnal variation can comprise a basis of scientific data to be used in wide context of solar-terrestrial connections.

The goal of the presented paper is to calculate phase, amplitude for the ASEC monitors at minimum of solar activity year. These data will be used for physical analysis of ASEC particle detector data as 24th solar activity cycle proceed.

The paper is organized as follows: in the second section brief description of the ASEC monitors is made; in the third section the used data and methods of characterizing diurnal variation are described; in the forth section daily variations detected by ASEC monitors are presented and discussed.

2. ASEC PARTICLE DETECTORS

Particle detectors of the Aragats Space Environmental Center (ASEC, Chilingarian et al., 2003, 2005,) are located on the slopes of mountain Aragats and in CRD headquarters in Yerevan, Armenia; geographic coordinates: 40°30'N, 44°10'E, altitudes - 3200m, 2000m and 1000m. Various ASEC detectors, measuring fluxes of various secondary cosmic rays, are sensitive to different energetic populations of primary cosmic rays. Two neutron monitors (18NM-64), operating at Nor-Amberd and at Aragats research stations, detect secondary neutrons. The Nor-Amberd muon multidirectional monitor (NAMMM) detects low energy charged particles and muons. The threshold energy of the detected muons is estimated to be 250 MeV. The Aragats Multidirectional Muon Monitor (AMMM) registers high energy muon flux (threshold energy - 5 GeV). The Aragats Solar Neutron Telescope (ASNT) measures neutrons and charged particles. ASNT is a part of a world-wide network coordinated by the Solar-Terrestrial Laboratory of the Nagoya University. Another monitoring system, based on the scintillation detectors of the Extensive Air Shower (EAS) surface arrays, MAKET-ANI and GAMMA (3200 m a.s.l.), detects low energy charged particles. The new world-wide particle detector networked, named SEVAN, is under construction now in Armenia, Bulgaria, Croatia and India (Chilingarian & Reymers 2008, Chilingarian et al., 2008). 3 SEVAN detectors are already operating in Armenia at altitudes 3200, 2000 and 1000 meters and 2 other monitors are working in Bulgaria and Croatia. SEVAN detectors also measure low energy charged particles, neutral particles (gammas and neutrons) and high energy muons. NAMMM and ASNT measuring channels are equipped with Amplitude-to-Digital (ADC) convertors and microcontroller based advanced electronics. Data Acquisition (DAQ) electronics and flexible software triggers allow to register not only the count rates of the detector channels, but also get histograms of energy releases; correlations of the charged and neutral fluxes; and many other physical phenomena. Details of detector operation can be found in (Chilingarian et al., 2007 and Arakelyan et al., 2009). A new type particle detector, which registers horizontal muons was recently installed at CRD headquarters (Chilingarian & Hovsepyan, 2009).

3. DATA AND METHODOLOGY

For daily variation studies, we use one-month time series taken from May 2008 until January, 2009. Data from the SEVAN Aragats (located at 3200m) is available from October 2008.We took data of the Yerevan SEVAN detector from January and February 2009. Data from SEVAN Bulgaria and SEVAN Croatia - from December 2008. One week data from July 2008 is used in case of horizontal muon detector; data on muons > 5GeV of AMMM - from December, 2006. Raw data were corrected by median filtering algorithm (Chilingarian & Hovhannisyan, 2009) to eliminate spikes and abrupt changes of mean, i.e. changes caused by errors of the data acquisition electronics.

In case of neutron data we performed the following operations. Filtered and pressure corrected (Chilingarian & Karapetyan, 2009) daily data were fitted by the harmonic approximation function for each day of selected period. In this way, we get distributions of amplitudes and phases of daily variation. The following approximation was used (Kudela et al., 2008):

$$f(ti) = A + B.\cos(\omega ti + \psi) \quad (1)$$

Here A is the daily average value of cosmic ray intensity, B is the amplitude of daily variation, ω is the angular frequency and ψ is the phase of daily variations. Phase is directly connected to local (solar) time. The quality of fit *d*, difference between experimental data and the fit is calculated according Kudela et al., (2008):

$$d^2 = \sum_{i=1}^{n} d_i^2 = \sum_{i=1}^{n} \left[Y_i - f(t_i) \right]^2 \quad (2)$$

Amplitudes and phases obtained by means of equation (1) and fit quality calculated by the equation (2) for ASEC and some other neutron monitors are presented in the Table1 in the section 4.

In case of SEVAN monitors we decided to present fitting of the monthly-averaged curves of daily variations, which were found to be more illustrative. Daily data were summed and presented in percents. Thereafter averaged daily curves were fitted by cosine function (1), the amplitude and phase of a curve were estimated and quality of the fit by equation (2) also was calculated.

4. DAILY VARIATIONS DETECTED BY ASEC AND NMDB MONITORS

a) *Daily variations of neutron data*

Recently new electronics was installed on all the ASEC particle detectors (Arakelyan et al., 2009) and barometric coefficients were recalculated (Chilingarian & Karapetyan, 2009). After appropriate filtering (Chilingarian & Hovhannisyan, 2009) the one- minute daily data were summed for all 18 channels of monitor. Then 1 minute time series were summed into hourly time series. Daily 1 hour time series from May 2008 were pressure corrected and fitted by equation (1). Days with abnormal values (for example negative amplitudes) were eliminated. Totally, three days were excluded from Moscow data and two days from NANM data.

In Figure 1 we present daily data typical for Nor Amberd Neutron Monitor (NANM). Data are pressure corrected and presented in percents, as 100% the average value of daily count rate is taken. As we can see the amplitude of variation is about 0.24% and phase is 3.307 in radians, which corresponds to 11:22 in UT or 15:22 in local time.

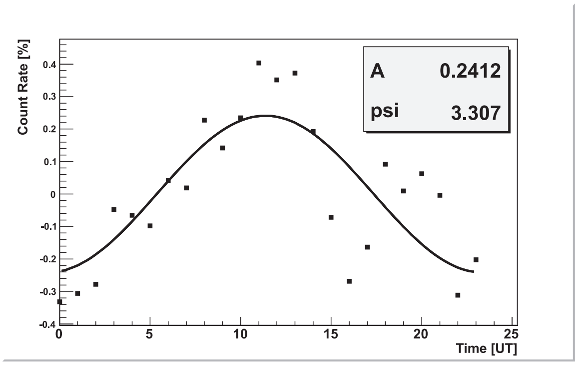

Figure 1. Daily variations according to NANM pressure corrected, hourly data fitted by cosine function

Several Eurasian neutron monitor groups join efforts to create an on-line data base of their data. The Neutron Monitor Data Base (NMDB) project (funded by European FP7 programme) contains time series of 12 neutron monitors located at high, middle and low latitudes. We compare daily waves of several monitors to investigate the latitude effects of diurnal variations. In Figure 2 Moscow, Alma-Ata and Nor Amberd neutron monitors' daily data from 11 May, 2008 are compared. Variations of the Moscow monitor are much bigger than of the two others'. Times of maximum are almost the same if we take into account that Alma-Ata local time is UT+7, Nor Amberd time is UT+4 and Moscow time is UT+3.

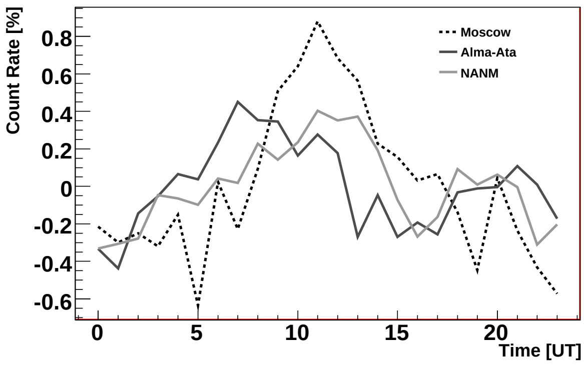

Figure 2. Comparison of Moscow, Alma-Ata and Nor Amberd neutron monitors' daily data

After fitting the 11 May, 2008 data of Moscow, Alma-Ata and Nor Amberd monitors the values of amplitudes – 0.47%, 0.20% and 0.24% were obtained respectively. Phases in local time for these monitors are 14:53, 15:25 and 15:21 accordingly.

In the Figure 3 we present the distributions of amplitudes and phases of diurnal variation of IZMIRAN (Moscow) and Nor Amberd neutron monitors, obtained by fitting with cosine function. The diurnal amplitude is significantly larger in Moscow NM (0.38). Moscow NM is more sensitive to low energy particles due to lower cutoff rigidity of the site.

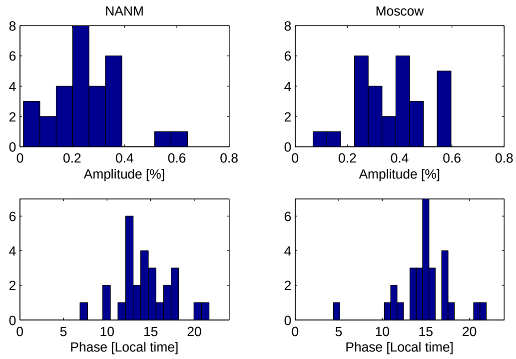

Figure 3. Comparison of Moscow and Nor Amberd neutron monitor data: distribution of amplitudes and phases of daily wave rom 1-31 of May, 2008.

Table 1. Daily variations of neutron data from NMDB

May 1-31, 2008	Median amplitude [%]	Median phase [Local time]	Median quality of the fit (2)	Most probable primary energies
NANM	0.24	14:34	0.67	7.1 GeV
ARNM	0.24	14:07	0.62	7.1 GeV
Alma-Ata NM	0.24	14:38	0.61	6.7 GeV
Moscow NM	0.38	14:49	0.91	2.46 GeV
Oulu NM	0.29	15:13	1.03	0.81 GeV

In Table 1 we present the parameters of the pressure corrected diurnal variations for 5 neutron monitors of NMDB project (data were taken from site nmdb.eu). Most probable energies of primary particles were obtained from computer simulation using CORSIKA code (Zazyan & Chilingarian, 2009). We expect that primary particle (mostly protons) bending is weaker at higher latitudes, consequently phases of diurnal variation were expected to be larger, i.e. local time of maximum is later for lower cutoff rigidity stations. At the same time amplitudes of variations should be bigger at high latitude stations, because of sensitiveness to lower energy primary CR. This statement is correct for 3 of 4 NMDB monitors. However, the amplitude of the Oulu monitor, being higher than calculated for Aragats monitors, is less comparing with IZMIRAN monitor. This discrepancy can give a hint to find some instrumental effects to check the quality of data.

The quality of the interpolation is rather high for all the monitors, i.e. diurnal variations are close to the sinusoidal and discrepancy between fitting curve and experimental data is small.

b) Daily variations of muon data

We also investigated daily variations of charged secondary particle fluxes corresponding to the primary GCR with different energies. Most probable energies of primary particles generating secondary charged particles reaching the Earth surface are higher, than energies of primaries corresponding to neutrons. For instance, most probable primary proton energies corresponding to muons with energies > 5GeV is 42 GeV. Consequently, charged secondary CR are not influenced by atmospheric pressure changes as much as neutrons. However, for muons besides pressure corrections the temperature corrections are essential; see for example Dorman, (1975). Unfortunately, due to the absence of appropriate temperature data we do not correct for changing gradient of temperature in atmosphere above detector.

In Figure 4 one can see the daily changes of Aragats Multichannel Muon Monitor data (AMMM). AMMM measures muons with energies higher than 5 GeV. The pattern of daily variations of 5 GeV muons is more complicated, than for neutrons. Existence of 2 minimums and maximum in between needs additional analysis for relevant interpretation. Apparently, AMMM data cannot be fitted by equation (1), more complicated function is required, for taking into account both solar and sidereal (Compton & Getting, 1935) periodicities. To describe daily variations of muons with energies > 5 GeV, data were fitted by sum cosines with 24 and 12 hour periods.

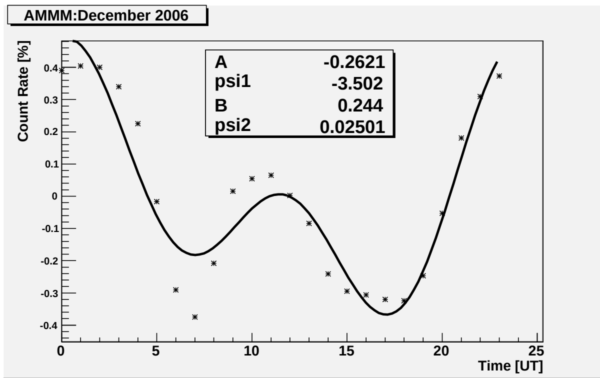

Figure 4. Daily variations of AMMM data fitted by sum of cosines

SEVAN monitor consists of three layers of plastic scintillating detectors and 5 cm thick lead filters up and below middle detector (see Figure 5). Upper and lower scintillators have a thickness of 5 cm, middle scintillator is 25 cm thick and sensitive to neutrons. Lead filters absorb low energy muons and lower detector is sensitive to muons with energies > 250MeV. SEVAN hybrid particle detectors allow us register fluxes of neutral particles, fluxes of high (>250MeV) and low (>7MeV) energy charged particles. Using different coincidences of the three layered detector it's possible to distinguish above mentioned components (Chilingarian and Reymers, 2008).

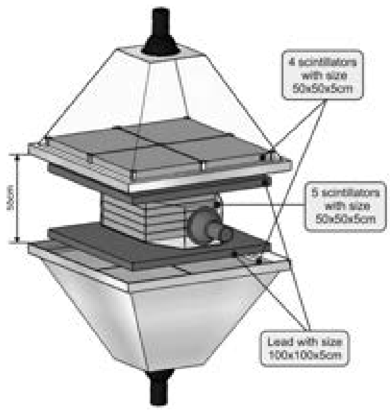

Figure 5. Basic detecting unit of SEVAN network

SEVAN monitors are already installed in Aragats (3200 m), Nor Amberd (2000 m), Yerevan (1000 m), Mt. Moussala (Bulgaria) and Zagreb (Croatia).The Figure 6 shows daily variations of the upper, lower and middle detectors of SEVAN monitors located at Nor Amberd. Aragats, Moussala and Zagreb. On the pictures geographical coordinates and altitudes of the monitors are also presented.

SEVAN Yerevan were not suitable for daily variation studies.

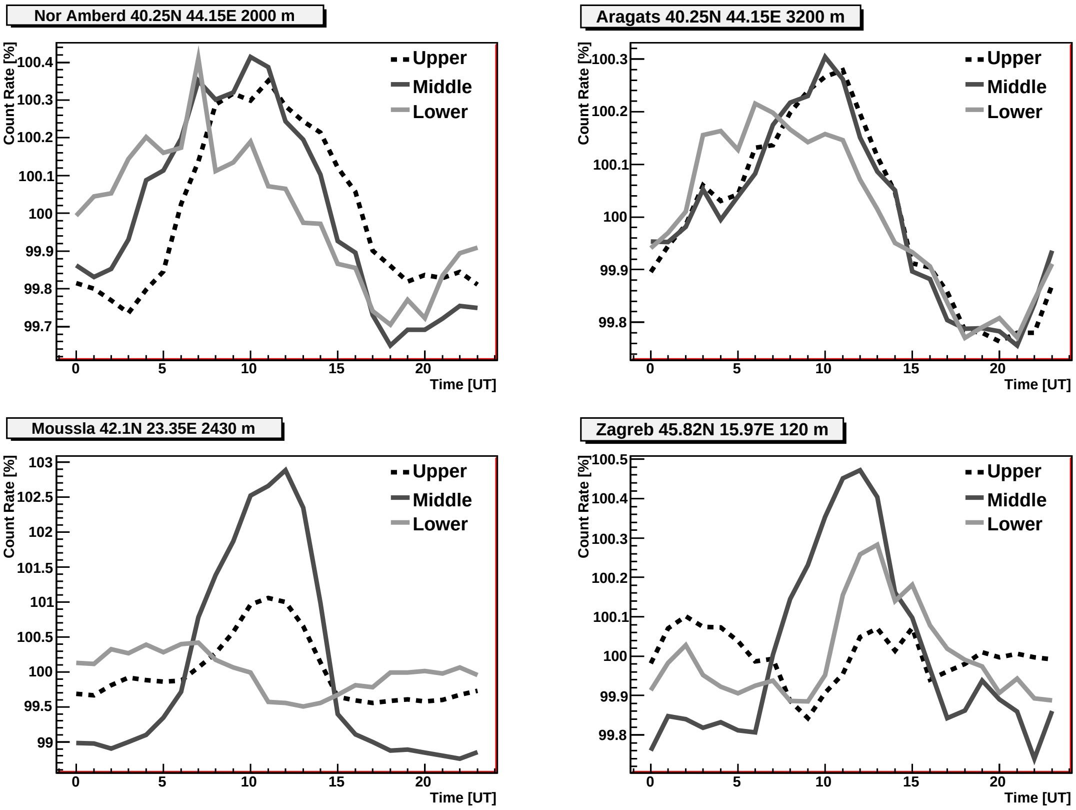

Figure 6. Daily variations of high, low energy charged fluxes and neutral fluxes according to SEVAN detectors located in Nor Amberd, Aragats, Moussala and Zagreb.
Month-averaged daily count rates, Nor Amberd May 2008, Aragats data – October 2008, Moussala and Zagreb December 2008- January 2009.

In Figure 6 we can see that detectors located at close geographic co-ordinates demonstrate similar patterns of the daily variations. By comparing Aragats and Balkanian monitors we can deduce that both the latitude and the longitude of site location influence diurnal wave pattern. However, very large amplitude of Moussala monitor's middle scintillator points on the possible defects in light proofing of middle detector. It is worth mentioning that Balkanian SEVAN monitors are working in a test mode yet.

In Table 2 we present the parameters of the best fit curves (1) for monitors presented in Figure 6. We do not fit curves with 2 peaks and without apparent peak. For Nor Amberd's SEVAN, as expected, the daily changes of lower energy fluxes are bigger than for higher energy fluxes. The magnitude of variations for the upper, middle and lower detectors are about 0.3%, 0.35% and 0.2% respectively. For local time the maximums are at 15:00 for the upper and middle detectors, and few hours earlier for the lower detector. Similar to SEVAN Nor Amberd, Aragats' upper and middle detectors also show maximum with magnitude about 0.3% at 15:00 LT, and lower detectors show variations approximately 0.2% at 11:00 LT. All in all, for these two monitors, secondary particles corresponding to higher energy primaries show smaller variations. Data of

Table 2. Daily variations of data of SEVAN monitors; Nor Amberd data from May, 2008, Aragats data from October, 2008, Moussala and Zagreb data are taken from December 2008-January, 2009.

SEVAN	Median amplitude [%]	Median phase [Local time]	Quality of the fit	Most probable primary energies
Nor Amberd				
upper detector	0.28	15:13	1.33	14.6 GV
middle detector	0.34	12:55	1.15	7.1 GV
lower detector	0.24	10:36	0.18	18.4 GV
Aragats				
upper detector	0.23	12:42	0.71	14.6 GV
middle detector	0.21	12:27	0.62	7.1 GV
lower detector	0.20	11:17	0.33	18.4 GV
Mousalla				
upper detector	0.55	11:58	2.31	
middle detector	1.80	12:33	8.16	
lower detector	No peaks			
Zagreb				
upper detector	Two peaks			
middle detector	0.28	12:39	1.35	
lower detector	0.12	14:43	0.51	

5. CONCLUSION

ASEC neutron monitors can register diurnal variations in large diapason of primary rigidities. It opens possibilities to follow the changes of parameters of daily wave (amplitude, phase, maximal limiting rigidity) during the start of the 24th solar activity cycle.

The magnitude of daily variations of neutrons correspondent to the lowest energy primary protons is comparable to the magnitude of variations of charged secondary CR.

Diurnal variations of neutron flux are higher for the high latitudes comparing with middle latitudes and for low energy muons comparing with higher energy muons. The time of maximum for high latitude neutron monitors is comparable with the time for middle latitude monitors. Amplitude of variation is 0.24% and phase is about 14:00 and 14:30 local time, for Aragats and Nor Amberd neutron monitors respectively.

Amplitudes of muon data are bigger or comparable with neutron data, except AMMM data (energy of primary protons higher than 42 GeV), which have more complicated shape of variations and lower amplitude. First data available from SEVAN network demonstrate that charged component variations are comparable with neutron variation and that diurnal variations are sensitive to longitude of site location.

ACKNOWLEDGMENT

Authors are grateful to the staff of Aragats and Nor Amberd research stations for the uninterruptable operation of ASEC monitors. The work was supported by the grant RA610 and ISTC grant A-1554. The part of research leading to these results has received funding from the European Community's Seventh Framework Programme (FP/2007-2013) under grant agreement no 213007.

We thank SEVAN groups of Bulgaria and Croatia for cooperation.

REFERENCES

.Abovyan S., Arakelyan K., Chilingarian A., Danielyan V., Pokhsraryan D., Electronics for the Space Environmental Viewing and Analysis Network (SEVAN), 2009

Agarwal R. and Mishra R., Modulation of cosmic rays at different cutoff rigidity, Brazilian Journal of Physics, vol. 38, no. 1, March, 2008

Agrawal P. et al., Study of cosmic ray daily variations during quiet periods at neutron monitor energies, Proc. 24th ICRC, p.932-934, 1995

Badruddin, Transient perturbations and their effects in the heliosphere, the geo-magnetosphere, and the Earth's atmosphere: Space Weather Perspective, J.Astrophys. Astr., vol. 27, pp.209-217, 2006

Begum Q.M. The change in the upper limiting rigidity for the cosmic ray diurnal intensity variation from 1965-1971, J.Phys.A: Math., Nucl. Gen., Vol.7, No.6, 1974.

Belov A.V., Eroshenko E.A., Oleneva V.A., Yanke V.G, Mavromichalaki H., Long-term behavior of the cosmic ray anisotropy derived from the Worldwide Neutron Monitor Network Data, Proc. 20th ECRS-2006, (http://www.lip.pt/events/2006/ecrs/proc/ecrs06-s0-123.pdf)

Bieber J.W. et al., A unified theory of cosmic ray diurnal variations, Geophysical Research Letters, vol. 10, Sept. p. 920-923,1983

Chilingarian A., Avakyan K., Babayan V. et al., Aragats space-environmental centre: status and SEP forecasting possibilities. J. Phys. G: Nucl. Part. Phys. 29, 939–951, 2003

Chilingarian A., Arakelyan K., Avakyan K. et al. Correlated measurements of secondary cosmic ray fluxes by the Aragats Space-Environmental Center monitors. NIM, A 543, 483- 492, 2005

Chilingarian A., Melkumyan L., Hovsepyan G., Reymers A., The response function of the Aragats Solar Neutron Telescope, Nuclear Instruments and Methods in Physics Research A 574, 255-263, 2007

Chilingarian A. and Reymers A., Investigations of the response of hybrid particle detectors for the Space Environmental Viewing and Analysis Network (SEVAN), Ann. Geophys., 26, 249-257, 2008

Chilingarian A., Hovsepyan G., Arakelyan K., et al., Space Environmental Viewing and Analysis Network (SEVAN), Earth, Moon and Planets: Vol.104, Issue 1, (195), 2009

Chilingarian A., and Hovhanissyan A., Median Filtering Algorithms for Multichannel Detectors, 2009, ibid.

Chilingarian A., and Hovsepyan G., New type of particle detectors for the Space Weather research, 2009, ibid

Chilingarian A. and Karapetyan T., Calculation of the barometric coefficients for the particle detectors belonging to the world-wide networks at the start of the 24-th Solar Activity cycle, 2009, ibid

Compton, A. H. & Getting, I. A. An Apparent Effect of Galactic Rotation on the Intensity of Cosmic Rays. *Phys. Rev.* 47, 817−821, 1935

Dorman L.I., Problems and the main results of investigation of cosmic ray variations (modulation effects), Procedings of Russion Academy of science, physics series, 24, 234, 1970 (in Russian).

Dorman L.I., Variations of Galactic Cosmic Rays, Moscow University publishing house, 1975. (in Russian).

Dorman L.I. et al., Features of diurnal variations of cosmic rays in high speed streams of the solar wind. Geomagnetism and Aeronomy ,vol. 24, July-Aug., p. 546-551, 1984 (in Russian)

.Duldig M.L. and Humble J.E., Enhanced cosmic ray diurnal variations in Mawson and Hobart neutron monitor and underground data records, Astronomical Society of Australia, Proceedings, vol. 8, p. 268-273, 1990

El-Borie M.A. et al., Diurnal variations of cosmic rays during a solar magnetic cycle, Astron. Nachr. 317 4, 267-272, 1996

. Forman M.A and Gleeson L.J., Cosmic-ray streaming and anisotropies, Astrophysics and Space Science, vol. 32, p. 77-94, 1975

Krymsky G.F., Diffusion mechanism of the diurnal cosmic ray variation, Geomagn. And Aeronomy, 4, 977-986, 1964 (in Russian)

.Kudela K., Firoz K.A., Langer R, Kollar V., On diurnal variation of cosmic rays: statistical study of neutron monitor data including Lominsky Stit., 2008, in press

Kumar S. et al., Comparative study of diurnal anisotropy in CR intensity on quiet days and all days, Bull. Astr. Soc. India, 21,395-397, 1993

Lopez R.C. and Valdes-Galicia J.F., Variations in cosmic radiation intensity associated with the barometric effect, Geofisica Internacional, Vol. 39, Num. 1, pp. 135-137, 2000

.Mourzin V.S., Physics of Cosmic Rays, Moscow University publishing house, 1970 (in Russian)

.Munakata Y., Tatsuoka R. et al., Observation of the First-Three Harmonics of Cosmic-Ray Daily Intensity Variations and the Magnetic Polarity of the Heliosphere, Proc. 24th ICRC, p.615,1995

Parker E.N., Planet Space Sci., 12, 735, 1964.

Pomerantz M.A. and Duggal S., The Cosmic Ray Solar Diurnal Anisotropy, Space Science Reviews, Volume 12, Num. 1, pp. 75-130, 1971

Sokhoyan S. et al., Large Scale Cosmic Ray Anisotropy with Maket Ani, Proceedings of the International Cosmic Ray Workshop “Aragats 2007”, 87-92, 2008

Thompson J., Solar Diurnal Variation of Cosmic-Ray Intensity as a Function of Latitude, Phys. Rev. 54, p. 93-96, 1938

Zazyan M., Chilingaraian. A., Sensitivity of Aragats Space Environmental Center (ASEC) Particle Detectors to Primary Cosmic Rays, (2009), 2008

Prediction of Propagation Times of IMF Disturbances

B . Mailyan [1], C. Munteanu [2], A. Reymers [1], S. Haaland [3,4]

[1]*Alikhanyan Physics Institute, Alikhanyan Brothers, Yerevan 375036, Armenia*
[2]*Dept. of Physics, Al. I. Cuza University, Romania*
[3]*Dept. of Physics, University of Bergen, Norway*
[4] *Max-Planck Institute for Solar Systems, Lindau, Germany*

Abstract: We have performed a statistical analysis of the propagation of interplanetary magnetic field (IMF) disturbances from the Advanced Composition Explorer (ACE) spacecraft, located at the L1 libration point, to the Cluster spacecraft quartet, located near the Earth's magnetopause.

Observed propagation times of almost 200 events are compared with the predicted times. Four different methods for prediction of IMF disturbances propagation times were tested. It is shown that not only solar wind speed, but also the orientation of the IMF are important for predictions.

1. INTRODUCTION

Disturbances in the solar wind, in particular abrupt changes in the interplanetary magnetic field (IMF) direction often generate disturbances in the Earth's magnetosphere. At the Earth's dayside magnetopause, a southward directed IMF can reconnect with the geomagnetic field, and cause transfer of momentum and energy into the Earth's magnetosphere (see Dungey et al, 1961).

It has also been argued that sudden northward turnings may trigger magnetospheric substorms (see Sergeev, et al, 1986), (see Lyons, et al, 1996), (see Lyons, et al, 2003).

Knowledge about the IMF direction is important not only during the intervals with distinct disturbances, but for any time intervals. For example, the IMF orientation at the Earth's magnetopause direction is used for parameterization of the magnetic field models (see Tsyganenko, et al, 2002) and simulation models, (see Ogino, et al, 1994), (see Gombosi, et al, 2000).

In the recent years, IMF observations have often been obtained from the Advanced Composition Explorer (ACE) spacecraft solar wind monitor located at L1 libration point, 1.5 million km away from the Earth. The propagation time from ACE to the Earth's magnetopause is about 1 hour, depending on the solar wind speed. Using ACE measurements, combined with a propagation model, we can predict arrival times of IMF disturbances to the Earth.

Instead of simply diving the distance to the Earth by the solar wind velocity, it's possible to obtain more precise results. Earlier studies have shown that not only the solar wind speed, but also the IMF direction determines the propagation times (see Horbury, et al, 2001) (see Weimer, et al, 2002).

In the present work we use the dataset and methods presented in some detail by Mailyan et al. (see Mailyan, et al, 2008), where data from Cluster mission and ACE spacecraft were used to calculate IMF propagation times for almost 200 cases.

The paper is organized as follows:

- Data sources
- Methods for prediction the propagation times
- Results

2. DATA SOURCES

The main data sources of this study are the ACE solar wind monitor, and the Cluster quartet of spacecraft, located near the Earth's magnetopause.

We have used ACE magnetic field instrument (see Smith, et al, 1998) with 16-second resolution to identify IMF disturbances, and solar wind velocity from the SWEMAP instrument (see McComas, et al, 1998) with 64-second resolution. These data are available via the Coordinated Data Analysis Web (CDAWeb) facility (http://cdaweb.gsfc.nasa.gov/about.html).

Observations from the Cluster satellites have been used for the measurements of the IMF near the Earth's upstream magnetopause. The orbit of Cluster takes the spacecraft to the upstream solar wind during the months January - March every year. Thus, we have used the measurements from this period of time.

We have primarily used measurement from the magnetic field Experiment (FGM) (see Balogh, et al, 2001) Data from the Cluster Ion Spectrometry (CIS) Experiment (see Reme, et al, 2001) were checked to verify that Cluster was located in the solar wind. The Cluster data used are the official prime parameters with approximately 4-s time resolution, provided by the Cluster Science Data System (CSDS).

3. METHODS FOR PREDICTION THE PROPAGATION TIMES

To determine the exact propagation times of the IMF disturbances it is necessary to identify the same structure at two locations in space. We first identified the abrupt directional changes of IMF in Cluster measurements. Some of these events were also identified in the ACE measurements. Between 2001 and 2007, almost 200 events were identified.

Using four different models we calculated the propagation times. The predicted times were thereafter compared to observed exact propagation times.

The simplest model, so-called flat delay model, assumes that the solar wind and embedded IMF are convected with a constant velocity along the Sun-Earth line.

In other words, to calculate the IMF propagation time one needs to divide the distance between satellites by the solar wind velocity component along the Sun- Earth line.

$$t_{Flat} = \frac{\Delta x}{v_x} \quad (1)$$

The following figure describes this approach.

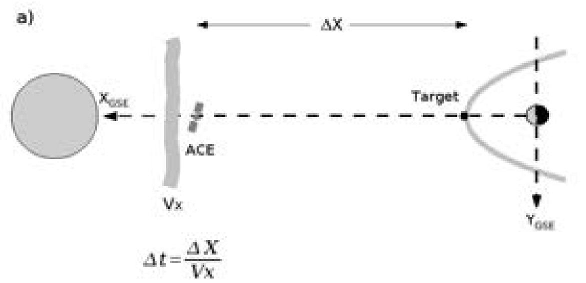

Figure 1. Description of flat delay model which assumes the propagation of plasma structure along Sun-Earth line with constant speed.

More precise predictions of the propagation times are possible if the IMF normal and positions of the spacecraft are taken into account. The figure below illustrates such models.

The propagation time of IMF disturbances can be

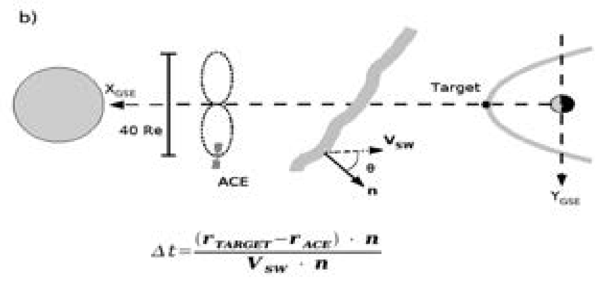

Figure 2. Illustration of models, which take into account the normal of IMF and actual solar wind velocity vector.

calculated from equation (2), where $\mathbf{r}_t$ is the vector of the target spacecraft position, in our case the Cluster's position vector, and $\mathbf{r}_m$ is the ACE spacecraft position vector. The vectors, $\mathbf{n}$ and $\mathbf{v}_{sw}$ are the boundary normal of the IMF discontinuity or phase plane and solar wind velocity vector, respectively.

$$t_d = \frac{(\mathbf{r_t} - \mathbf{r_m}) \cdot \mathbf{n}}{\mathbf{v_{sw}} \cdot \mathbf{n}} \quad (2)$$

The normals of solar wind discontinuity were calculated using the following methods:

- Cross product
- Minimum variance of the magnetic field(MVAB)
- Constrained minimum variance(MVAB-0)

The cross product method works only if the following conditions are realized; there is no plasma flow along the discontinuity $\langle \mathbf{v_{sw}} \rangle \cdot \mathbf{n}$ and no magnetic field along the normal $\langle \mathbf{B} \rangle \cdot \mathbf{n}$ (tangential discontinuity-TD). If these conditions are satisfied, the IMF normal is given by the following.

$$\mathbf{n_{Cross}} = \frac{\langle \mathbf{B_u} \rangle \times \langle \mathbf{B_d} \rangle}{\left| \langle \mathbf{B_u} \rangle \times \langle \mathbf{B_d} \rangle \right|} \quad (3)$$

$\langle \mathbf{B}_u \rangle$, $\langle \mathbf{B}_d \rangle$ are the averages of the magnetic field vector upstream and downstream of the discontinuity respectively. In our study we have calculated $\langle \mathbf{B}_u \rangle$ and $\langle \mathbf{B}_d \rangle$ from 10 sample averages before and after the center of the discontinuity.

In the MVAB method (see Sonnerup, et al, 1998) one tries to find the a priori unknown direction in which the magnetic field has minimum variance. Mathematically this can be done by constructing a covariance matrix from magnetic field measurements and finding the eigenvectors and eigenvalues of the matrix. The eigenvector corresponding to the smallest eigenvalue is the normal of the IMF phase plane.

The MVAB-0 (see Weimer, et al, 2003) method differs from the MVAB by an additional assumption that there is no magnetic field component along normal direction.

In our calculations we have used a 7 minute interval centered around the magnetic field discontinuity to calculate the covariance matrix. The choice of 7 minutes was found to be a good compromise which ensures sufficient data points around the discontinuity.

4. RESULTS

During the period 2001-2007, 198 cases with abrupt changes of IMF which could be recognized at both ACE and Cluster were identified. For each event, solar wind velocities measured at ACE, magnetic field measurements from both spacecraft, and the position of ACE relative to Cluster were recorded. Thereafter we calculated the propagation times using four methods and estimated the difference between predicted and observed times. In figure 3, distributions of timing errors for each of the four tested models are presented. The horizontal axes indicate the time differences $dt = t_{model} - t_{observed}$ for each method, and the vertical axes, common to all panels in that row, show the relative distribution within that dt range.

5. CONCLUSION

The results show that taking into account the IMF direction and the relative positions of the spacecraft give more precise results for most events.

The best predictions of IMF disturbances arrival times at the Earth's magnetopause are obtained if the orientation of the IMF phase plane is determined from the constrained minimum variance method (MVAB-0). Despite this fact, the MVAB-0 method is much more complex and in many cases the flat delay method may be "good enough".

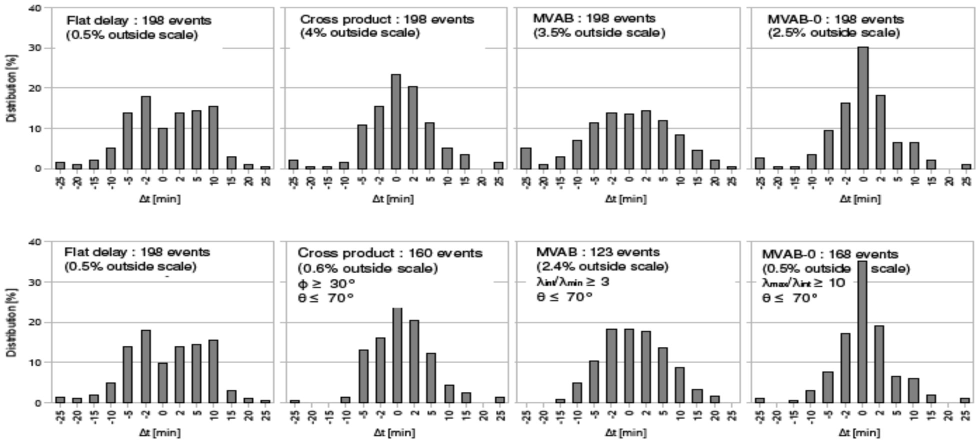

Figure 3. Distributions of time differences between predicted and observed propagation times.

REFERENCES

Dungey J. R.: Interplanetary magnetic field and the auroral zones, Phys. Rev. Lett**,** 6, 47, 1961

Sergeev V. A., Dmitrieva, N. P., and Barkova, E. S.: Triggering of substorm expansion by the IMF directional discontinuities: Time delay analysis, Planet. Space Sci., 34, 1109–1118, doi:10.1016/0032-0633(86)90023-1, 1986

Lyons, L. R.: Substorms: Fundamental observational features, distinction from other disturbances, and external triggering, J. Geophys.Res., 101, 13 011–13 026, doi:10.1029/95JA01987, 1996

Lyons, L. R., Liu, S., Ruohoniemi, J. M., Solovyev, S. I., and Samson,J. C.: Observations of dayside convection reduction leading to substorm onset, J. Geophys. Res. (Space Physics), 108, doi:10.1029/2002JA009670, 2003

Tsyganenko, N. A.: A model of the near magnetosphere with adawn-dusk asymmetry 1. Mathematical structure, J. Geophys.Res., 107, 12–1, doi:10.1029/2001JA000 219, 2002a

Tsyganenko, N. A.: A model of the near magnetosphere with a dawn-dusk asymmetry 2. Parameterization and fitting to observations,J. Geophys. Res., 107, 10–1, doi:10.1029/2001JA000220,2002b

Ogino, T., Walker, R. J., and Ashour-Abdalla, M.: A global magnetohydrodynamic simulation of the response of the magnetosphere to a northward turning of the interplanetary magnetic field, J. Geophys. Res., 99, 11 027–11 042, doi:10.1029/93JA03313, 1994

Gombosi, T. I., Dezeeuw, D. L., Groth, C. P. T., and Powell, K. G.: Magnetospheric Configuration for Parker-Spiral IMF Conditions: Results of A 3D AMRMHDSimulation, Adv. Space Res., 26, 139–149, 2000

Horbury, T. S., Burgess, D., Fr¨anz, M., and Owen, C. J.: Prediction of Earth arrival times of interplanetary southward magnetic field turnings, J. Geophys. Res., 106, 30 001–30 009, 2001a

Weimer, D. R., Ober, D. M., Maynard, N. C., Burke, W. J., Collier, M. R., McComas, D. J., Ness, N. F., and Smith, C. W.: Variable time delays in the propagation of the interplanetary magnetic field, J. Geophys. Res., 107, 29–1, doi:10.1029/2001JA009102,2002

Mailyan, B, Munteanu, C, Haaland, S : What is the best method to calculate the solar wind propagation delay?, Ann. Geophys., 26, 2383–2394, 2008

Smith, C. W., L'Heureux, J., Ness, N. F., Acuna, M. H., Burlaga, L. F., and Scheifele, J.: The ACE Magnetic Fields Experiment, Space Sci. Rev., 86, 613–632, 1998

McComas, D. J., Bame, S. J., Barker, P., Feldman, W. C., Phillips, J. L., Riley, P., and Griffee, J. W.: Solar Wind Electron Proton Alpha Monitor (SWEPAM) for the Advanced Composition Explorer,Space Sci. Rev., 86, 563–612, 1998

Balogh, A., Carr, C. M., Acuna, M. H., Dunlop, M. W., Beek, T. J.,Brown, P., Fornaco¸n, K. H., Georgescu, E., Glassmeier, K. H.,Harris, J., Musmann, G., Oddy, T., and Schwingenschuh, K.:The Cluster Magnetic Field Investigation: Overview of in-flightperformance and initial results, Ann. Geophys., 19, 1207–1217, 2001, http://www.ann-geophys.net/19/1207/2001/

Reme et al.: First multispacecraft ion measurements in and near the Earth's magnetosphere with the identical Cluster ion spectrometry (CIS) experiment, Ann. Geophys., 19, 1303–1354, 2001, http://www.ann-geophys.net/19/1303/2001/

Sonnerup, B. U. O. and Scheible, M.: Minimum and Maximum Variance Analysis, in: Analysis Methods for Multi-Spacecraft Data, edited by Paschmann, G. and Daly, P. W., ISSI SR-001, p. 1850, ESA Publications Division, 1998

Weimer, D. R., Ober, D. M., Maynard, N. C., Collier, M. R., McComas, D. J., Ness, N. F., Smith, C. W., and Watermann, J.: Predicting interplanetary magnetic field (IMF) propagation delay times using the minimum variance technique, J. Geophys. Res., 108, 16–1, doi:10.1029/2002JA009405, 2003

New Type of Particle Detectors for the Space Weather Research

A. Chilingarian, G.Hovsepyan

Cosmic Ray Division, Alikhanyan Physics Institute, Alikhanyan Brothers 2, Yerevan 375036, Armenia
(e-mail: hgg@.yerphi.am)

Abstract : We assemble and test two multilayered detector setups utilizing 1 m.sq. area and 1 cm thick plastic scintillators , equipped with light wave shifters. Detector setups were implemented for the secondary cosmic ray monitoring and for measurement of the muon flux. The detector layout is rather compact and allows stacking horizontally and vertically. Both detectors are interlayered by 1.5 cm thick lead plates to use as a calorimetric device for estimating energy of muons and neutrons, as well as for measuring electron, muon and neutron content of the Extensive Air Showers. The position of the spectra maximum correspondent to the minimal ionizing particle proves to be rather stable in time.

1. INTRODUCTION

The particle detectors operating at the Aragats Space Environmental Centre (ASEC, Chilingarian et al., 2003, 2005) measure neutral and charged particle fluxes sensitive to a wide primary energy range. The solar and galactic protons of energies from 7 – until 40 GeV entering terrestrial atmosphere generate secondary elementary particles that can reach and be registered by ASEC monitors (Zazyan & Chilingarian, 2008). This energy span is adequate for the research of the highest energy Solar Cosmic Rays (SCR) and for recovering SCR energy spectra (Chilinarian & Reimers, 2007). However, for the research of the energy dependence of the transient solar events (Forbush decreases and Geomagnetic storms) we need to expand energy interval up to several hundreds of GeV. In addition for the investigations of the solar cycle dynamics of the some daily wave parameters (upper limited rigidity) we need access to primary energies above 100 GeV (Begum, 1974). Another research project to measure sidereal anisotropy of Galactic Cosmic Rays (GCR) is now under consideration; the investigation of the TeV energy range will be essential for this problem.

A scintillation electromagnetic calorimeter is a universal detector for measuring energy of horizontal muons by the counting of the energy release (energy of electron-positron pairs born in lead filter). The accessed primary energies range will be enormously large, of course for a price of very weak flux at highest energies. It Table 1 we post the intensities and count rates of the near-horizontal muon flux and correspondent energy deposit in the ten-layer detector (Ivanov, 2008). As we can see in Table 1 the expected count rate of > 5 GeV muons (this energy is definitely higher than the threshold energy of detector) for 1-hour (~$1.3 \cdot 10^4$), is rather large and we can perform time-series analysis both for diurnal variation research and for observing precursors of upcoming geomagnetic storms. Furthermore, we can establish the upper threshold of the Solar Cosmic Ray (SCR) spectra for strongest radiation storms.

Table 1. Expected intensities of the horizontal muon flux and corresponding medians of energy releases in the calorimeter layers (zenith angles range 45° - 90°)

E_μ	$I_\mu\,(m^2 \cdot h \cdot sr)^{-1}$	Median of the energy deposits in scint. layers
≥ 550 MeV	$1.77\ 10^4$	1.9 MeV
≥ 5.0 GeV	$1.3\ 10^4$	2.4 MeV
≥ 50 GeV	$2.16\ 10^3$	2.7 MeV
≥ 500 GeV	$1.08\ 10^2$	4.2 MeV
≥ 1.0 TeV	14.4	5.6 MeV
≥ 2.0 TeV	2.52	8.2 MeV
≥ 5.0 TeV	0.36	17 MeV
≥ 10 TeV	$7.2\ 10^{-2}$	30 MeV

Horizontal Electromagnetic Calorimeter (HEC) consists of ten 1 m^2 area and 1cm thick plastic scintillators with fiber readout. Scintillators are interlayer by 1.5 cm. thick lead filters; with total thickness of 170 g/cm^2. The minimal ionizing particle (mip) energy to generate signal in 1 cm. scintillator is 2.1 MeV (Reymers, 2008) and minimal muon energy to traverse whole detector is 210 MeV.

HEC acceptance corresponds to zenith angle range of 45°- 90°, to reduce acceptence of detector down to 80°- 90°, we put additional scintillaor at distance of 8 m. from HEC. This additional scintillator also can select unidirectional muons by applying time-of-flight technique. For suppressing shower event we use as VETO (rejecting trigger) signal from the same tape detector placed horizontally above HEC. The PM signals are digitized by the LeCroy ADC2249 (http://www.LeCroy.com) with discrimination of 1 mV.

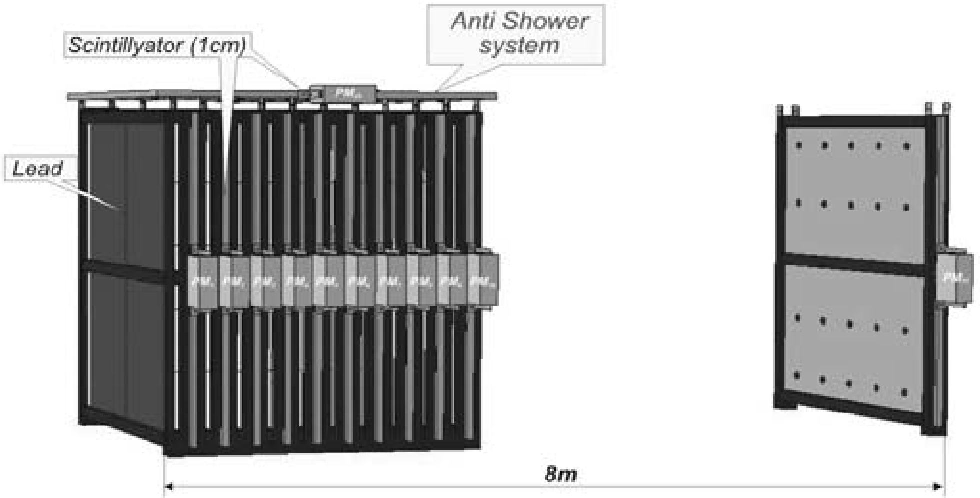

Figure 1. Setup of Horizontal Electromagnetic Calorimeter (HEC).

3. HEC TRIGGER SYSTEM

The HEC trigger system is built in the NIM standard; the data readout is in CAMAC standard.

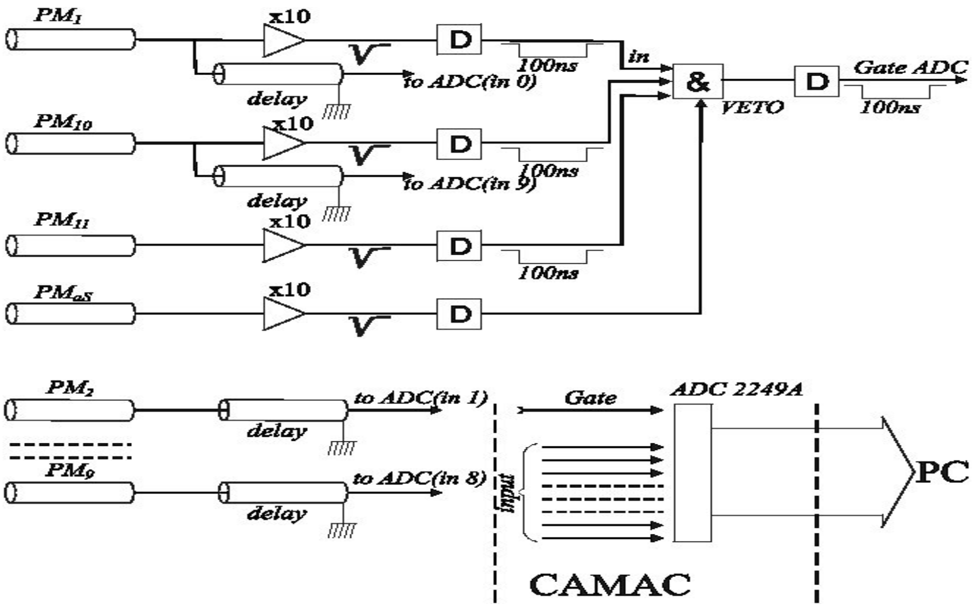

Figure 2. HEC Data Acquisition electronics

Data Acquisition (DAQ) electronics presented in Figure 2, within 20-30 ns opens the gates for data stream to linear ADC. The trigger is issued when signals from the first and the tenths scintillators coincide within gate of 100 nanoseconds. In parallel tenfold amplified signals from scintillators are fed to shaper-discriminators. If amplitude of signals is above 40 mV a NIM-standard signal with pulse width 100 nsec fed to coincidence module. The output of module after pulse forming opens the gate of LeCroy ADC2249A. After converting the Photomultiplier (PM) signal into code, ADC generates LAM signal and data is stored. The rate of double random coincidences at maximal frequency of 500 Hz will not exceed 1% of the count rate.

For the check of each of measuring channels during multiyear operation approximately once an hour the histograms of registered codes are stored for all 10 scintillators. The mode of the distribution (the histogram bin with maximal population) is used as a monitored stability parameter.

4. HEC SCINTILLATORS

We use for HEC *molded polystyrene* scintillation detectors designed and fabricated in the Institute for High Energy Physics (IHEP) in Protvino, the Russian Federation (Britvich,2002, Chubenko,2007) , see Figure 3.

Producer guarantees registration efficiency of a relativistic charged particle of 95% or better; high homogeneity of light collection (in the limits of +-12%) independent of the position of particle's trajectory (Ampilogov et al., 2007); stability for long time operation. RMSE of the mode of energy deposit distribution from single charged particles should be no worse than 2%.

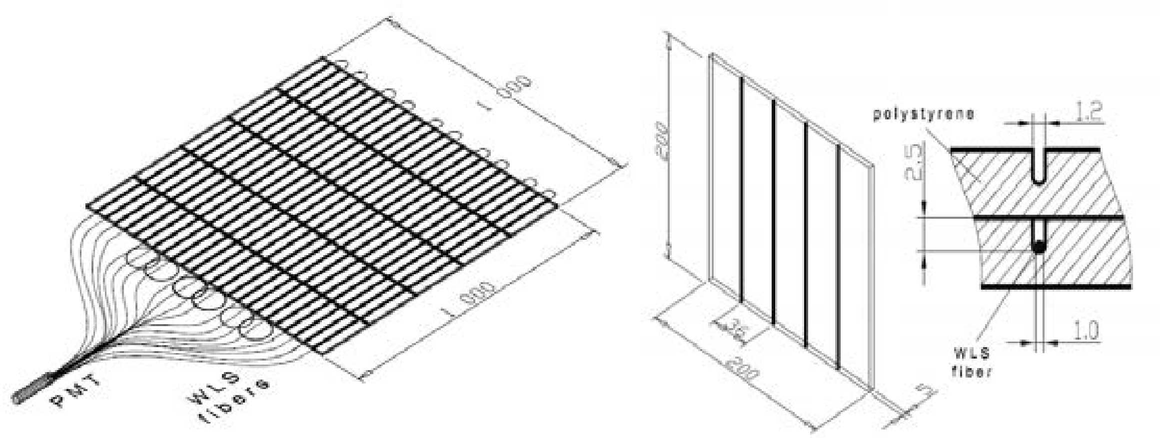

***Figure 3.** At the left: general view of the scintillator assembly; in the middle: the single molded polystyrene scintillation plate of the SC-301 type; at*

As an active medium are used molded polystyrene scintillation plates of the SC-301 type produced in IHEP; lateral sizes 20x20 cm^2, thickness 0.5 cm^2, light output about 60% of that of anthracene, maximum of luminescent spectrum around the wavelength 420 nm and the mean emission time t=2.3 ns (Britvich,2002). Scintillation plates are pressed without gaps in two layers, 25 plates per each. Each polystyrene plate has four lengthwise grooves 2.5 mm deep and 1.2 mm wide, pressed on its upper surface during the molding process. The grooves constitute channels for placement of wavelength shifting (WLS) fibers when the plates are pressed together. The fibers, which are of the Y11 type with double cladding (Catalog of KURARAY corporation LTD, 1997), 1.0-1.2 mm in diameter, are put inside the grooves which afterwards are coated with BC-600 type epoxy resin. The step distance between the grooves is 36 mm; total amount of the fibers in the whole assembly is 20. The fibers re-emit ultraviolet scintillation light in the 476 nm spectrum range and transmit them to a photomultiplier tube.

The method of the setting of WLS fibers inside the polystyrene scintillator is the following: each of the fibers, nearly double in the length as scintillation assembly is, is put in two adjacent grooves making a loop at the one side of assembly. At the other side, where a photomultiplier tube (PMT) is placed, the fibers are faked in the coils compensating the length differences of their stretched parts. (All the fibers have strictly the same length, which is necessary to achieve a time resolution of scintillation pulse registration of the order of some nanoseconds). Free ends of the fibers form a bundle impregnated with epoxy resin. After consolidation of the resin the edges of the fibers where cut, polished and placed opposite to the photo cathode of a FEU115M type PMT (http://www.melz.ct.ru/eng/elect). The maximum lateral cross-section of the fiber bundle cannot exceed the diameter of the active photo-cathode region (about 25 mm).

For checking the parameters of scintillators, a special test facility operates at ASEC. In Figure 4 we present the, so called, one-particle spectra from HEC channels.

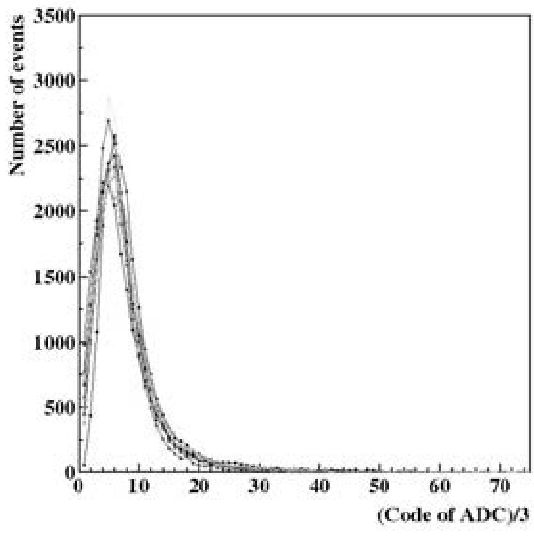

***Figure 4.** The histograms of the scintillators output codes (for simplicity codes are triple joined)*

The daily mean square deviation (MSD) of the 9 distribution modes is ~1%; and only for one channel ~2%. The distribution modes are in the range of 16-18 mV. Fourfold enhancement of the distribution mode upon the selected threshold value provides high efficiency of particle detection.

5. HEC TEST OPERATION

We illustrate the stability of the HEC operation by the data collecting during 2-week operation as seen in the Figure 5 and 6. The mean hourly count rate is ~1.99 •10^4 in good agreement with calculated value for >0.5 GeV muons in Table 1 (muons to reach HEC have to traverse several concrete walls therefore we can very roughly estimate the threshold energy of muons reaching HEC as 2-3 GeV). Relative error of minute data equals to ~6%; for 1-hour data 0.77%; The Poison values are ~5.5% and 0.7% respectively.

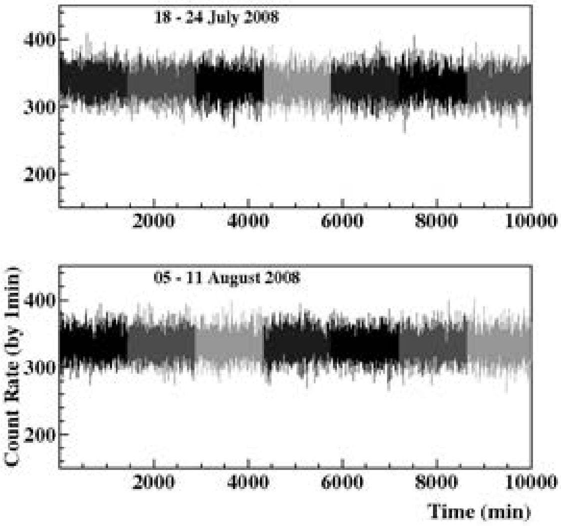

Figure 5. One-minute count rates; 2-week run. Average count rate equals to 333.2; MSD=18.9 (5.7%).

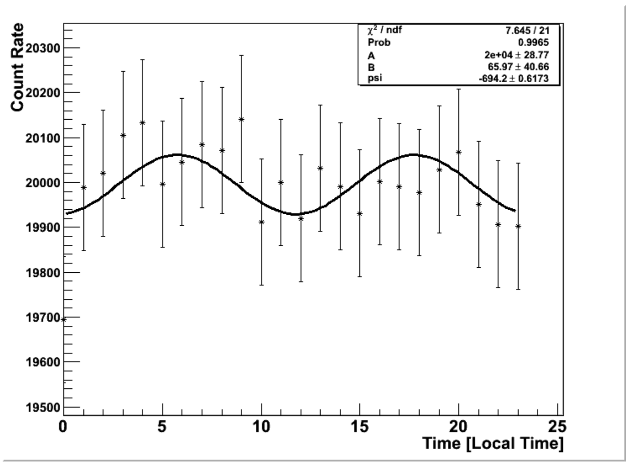

Figure 6. The daily variations of the HEC count rate; data averaged over 7 days from 18 until 24 July 2008.

6. ADVANCED MODULE FOR THE SEVAN PARTICLE DETECTOR NETWORK

To improve the efficiency of neutron detection and reduce γ-quanta contamination at CRD is under testing new module of SEVAN world-wide network of hybrid particle detectors (Chilingarian & Reymers, 2008, Chilingarian et al, 2009).

The prototype detector consists of 4 plastic scintillators interlayered by three 1.5 thick lead filters stacked vertically; total thickness of lead is 51 g/cm^2. MIP energy to be detected in one scintillator is 2.1 MeV and particle with energy greater than 65 MeV can intersect the detector. In Figures 7 and 8 we present the chart and picture of the detector.

Figure 8. 4-fold scintillator Detector assembly

DAQ electronics and trigger of SEVAN module are analogical to HEC (see Figure 2). As trigger of detector the signals from 2 middle scintillators was used, the coincidence of which opens the gate for pulse analyzer. The PM pulses within gate are converted to code and stored.

The characteristics of DAQ are the same as for HEC, with reduced random coincidences rate of 0.1% of trigger count rate.

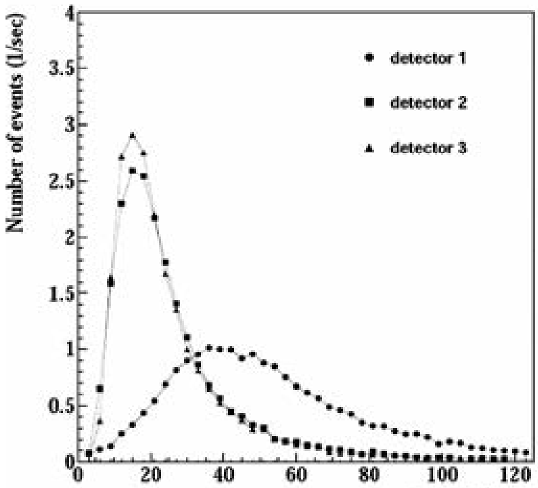

Figure 9. The PM code distributions for all 4 measuring channels

Figure 7. Chart of 4-fold Scintillator assembly

In figure 9 we present the "one particle" histograms of all 4 channels triggered by two middle ones. Due to high level of noise, we cannot trigger detector by the signal from one scintillator only. Therefore, we cannot test yet detector operation, as it will work in SEVAN network; instead of testing all 16 possible detector states (all 15 combinations of signal and absence of signal in 4 scintillators; sure, we did not consider 0000 combinations), chosen trigger allows only three combinations: 1111; 1110 and 0111.

Count rates of channels do not used for trigger are 5-10% less comparing with trigger ones. This difference is due to absorption of low energy particles in lead and due to finite efficiency of scintillators. Modes of all four distributions are equal to ~ 17 MeV and trigger frequency ~117 Hz.

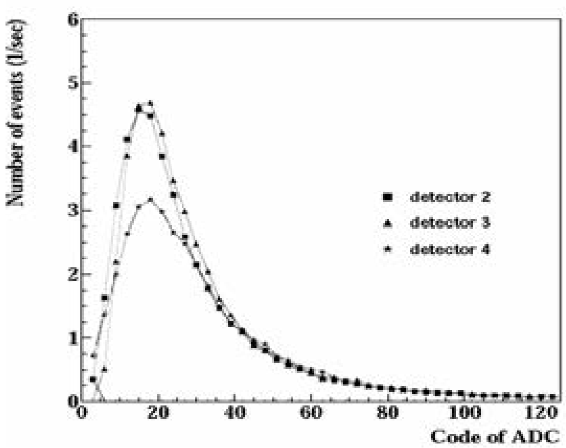

Figure 10. The nergy reease histogram in the detector layers when VETO signal comes from the upper scintillator

Introducing of VETO signal from the top scintillator will highly suppress charged particles registration. The probability that neutral particle will generate MIP in 1 cm scintillator is vanishingly small, on the other hand the efficiency of registration charged particle in the same scintillator is very high. The frequency of triggers was rather small - 7.95 Hz (6.7% of count rate without VETO signal) and frequency of the bottom detector was ~ 6.8 Hz.

The 10% difference can be explained by the absorption of particles in the lead filter and finite efficiency of scintillator. The modes of the distributions slightly shifted to 16.2, 17.6 and 18.6 mV (see Figure 10).

Alternative way to select neutral particle and simultaneously reject low-energy charged particles is to use for VETO signal from the bottom scintillator.

In Figure 11, we can see that trigger with "bottom" VETO is less "tight" comparing with upper VETO - 22.6 Hz (19.2% of case without VETO). Furthermore, the mode of the upper scintillator is shifted 2.5-3 times to the right. It can be explained by multiple traversal of detector (at 1000 m. altitude ~ 20% of traversals are multiple, i.e. >2 particles) and by the gamma-conversion in the detector body. Trigger by "firing" of 2 intermediate scintillators, with additional condition of absence of signal in the forth "bottom" scintillator requires a particle traversal with energy in the interval of (40 – 65 MeV).

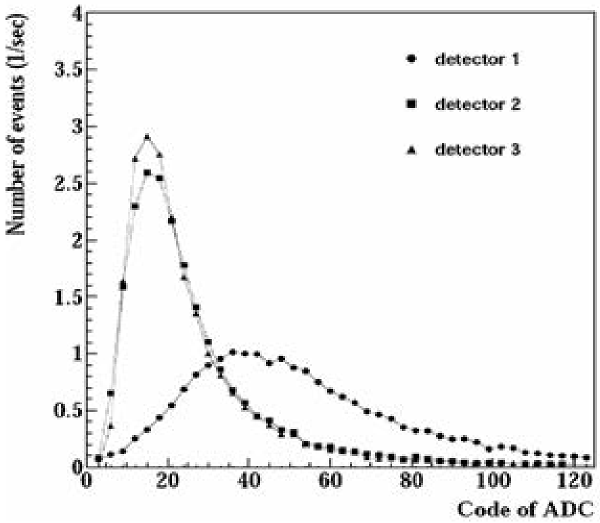

Figure 11. The energy release histogram in the detector layers when VETO signal comes from the bottom scintillator

Obtained characteristics of the 4-fold scintillator detector with 2 different VETOs, is in good agreement with the data obtained at Aragats (3200 m. altitude), if take into account altitude difference. Obtain frequencies will be compared with full simulation of the detector setup, underway now.

7. CONCLUSION

Test operation of the Horizontal Electromagnetic Calorimeter (HEC) with new type of scintillators allows to investigate its operational characteristics. The hourly count rates are rather stable, thus giving possibility to investigate transient solar events and overall solar-terrestrial connections in the energy range much higher comparing with the ones available from the existent networks of particle detectors measuring neutrons and muons of the secondary cosmic rays.

The 4-fold vertically stacked detector setup was assembled and investigated. Due to the high level of noise, only 2-fold coincidence trigger was implemented and corresponding possible configurations of signals from 4-layers were studied. Further work is required to determine characteristics of 4-fold scintillator setup, to investigate efficiency of detection of electrons, muons, gammas and neutrons and contaminations of selected events.

ACKNOWLEDGMENT

We thank the staff of the Cosmic Ray Division for contributing to the experiment.

We thank A.P.Soldatov and G.I.Britvich for cooperation and useful discussions. This work was supported by Armenian Government grants and ISTC grant A-1554.

REFERENCES

Begum Q.M., The change in the upper limiting rigidity for the cosmic ray diurnal intensity variation from 1965-1971, J.Phys.A: Math., Nucl. Gen., Vol.7, No.6, 1974

Chilingarian A., Avakyan K., Babayan V. et al., Aragats space-environmental centre: status and SEP forecasting possibilities. J. Phys. G: Nucl. Part. Phys. 29, 939–951, 2003

Chilingarian A., Arakelyan K., Avakyan K. et al., Correlated measurements of secondary cosmic ray fluxes by the Aragats Space-Environmental Center monitors. NIM, A543, 483- 492, 2005

Chilingarian A., Melkumyan L., Hovsepyan G., Reymers A., The response function of the Aragats Solar Neutron Telescope, Nuclear Instruments and Methods in Physics Research A 574, 255-263, 2007

Chilingarian A. and Reymers A., Investigations of the response of hybrid particle detectors for the Space Environmental Viewing and Analysis Network (SEVAN), Ann. Geophys., 26, 249-257, 2008

Chilingarian A., Hovsepyan G., Arakelyan K., et al. Space environmental viewing and analysis network (SEVAN). DOI: 10.1007/s11038-008-9288-1, 2009

Chilingarian A., Hovsepyan G., Arakelyan K., Chilingaryan S., Danielyan V., Avakyan K., Yeghikyan A., Reymers A., Tserunyan S., Space Environmental Viewing and Analysis Network (SEVAN), Earth, Moon and Planets, in press

LeCroy, http://www.LeCroy.com Etu ssilku tochno mojno ubrat' ! Vtexte address sita dan , 2008.

Arutunyan S.Kh., Chilingarian A., .Kokoulin R., On nonparametrical methods of suppresion of nuclear cascade background in measuring muon spectrum with pairmeter. Preprint ЕФИ-940(91) 86, Yerevan, 15p. (in Russian), 1986

Britvich G., Vasil'chenko V., Kirichenko V., et al., New polystyrene-based scintillator. Instrum. Exp. Tech., **v.**45 p. 664-676, 2002

A.P. Chubenko, A.L.Shepetov, G.I. Britvich et al. The new large-sized scintillation charged particles detector for extencive air shower experiments at Tien-Shan. Proc. 30-th ICRC, Merida, 2007

Catalog of KURARAY corporation LTD, Chuo-ku, Tokio, Japan, http://www.melz.ct.ru/eng/elect, 1997.

N.V.Ampilogov, M.B.Amelchakov, G.I.Britvich et al. Scintillation detector with fiberoptic readout system. Proceedings of Russian Academy of Science, series Physics, 71 p.580, 2007 (in Russian)

Calculation of the Barometric Coefficients for the Particle Detectors Belonging to the World-Wide Networks at the Start of the 24th Solar Activity Cycle

A. Chilingarian, T. Karapetyan

Cosmic Ray Division, Alikhanyan Physics Institute, Alikhanyan Brothers 2, Yerevan 375036, Armenia
(e-mail: ktigran79@ yerphi.am)

Abstract: After major modernization of the data acquisition electronics of the Aragats Space Environmental Center (ASEC) particle detectors the calculations of the barometric coefficients of all ASEC particle monitors were performed in the beginning of 24th solar activity cycle. The time periods of minimal disturbances of the interplanetary magnetic field (IMF) were selected to avoid biases due to transient solar events. The barometric coefficients of different particle detectors measuring various secondary cosmic ray fluxes located at altitudes of 1000 m, 2000 and 3200 m. a.s.l. are calculated and compared. The barometric coefficients for the several Neutron Monitors of recently established Eurasian data base (NMDB) and SEVAN particle detector networks also were calculated. The latitude and altitude dependencies of the barometric coefficients were investigated, as well as the dependence of coefficients on the most probable energy of the primary protons generated definite species of the secondary fluxes.

1. INTRODUCTION

Particle detectors of the Aragats Space Environmental Center (ASEC, Chilingarian et al., 2003, 2005,) are located on the slopes of mountain Aragats and in CRD headquarters in Yerevan, Armenia; geographic coordinates: 40°30'N, 44°10'E, altitudes - 3200m, 2000m and 1000m. a.s.l. Various ASEC detectors, measuring fluxes of diverse secondary cosmic rays, are sensitive to different energetic populations of primary cosmic rays. Two neutron monitors (18NM-64) operating at the Nor-Amberd and the Aragats research stations detect secondary neutrons. The Nor-Amberd muon multidirectional monitor (NAMMM) detects low energy charged particles and muons with energies above 350 MeV. The Aragats Multidirectional Muon Monitor (AMMM) registers high energy muon flux (threshold energy - 5 GeV). The Aragats Solar Neutron Telescope (ASNT) measures neutrons and charged particles. ASNT is a part of a world-wide network coordinated by the Solar-Terrestrial Laboratory of the Nagoya University. Another monitoring system, based on the scintillation detectors of the Extensive Air Shower (EAS) surface arrays, MAKET-ANI and GAMMA (3200 m a.s.l.), detects low energy charged particles. New world-wide particle detector networked, named SEVAN, operates now in Armenia, Bulgaria and Croatia (Chilingarian & Reymers 2008, Chilingarian et al., 2009). SEVAN detectors measure low energy charged particles, neutral particles (gammas and neutrons) and high energy muons. NAMMM and ASNT measuring channels are equipped with Amplitude-to-Digital (ADC) convertors and microcontroller based advanced electronics. Data Acquisition (DAQ) electronics and flexible software triggers allow not only to register the count rates of the detector channels, but also histograms of energy releases; correlations of the charged and neutral fluxes; and many other physical phenomena. Details of detector operation can be found in (Chilingarian et al., 2007 and Arakelyan et al., 2009).

ASEC detectors measure time series of secondary particles born in cascades originating in the atmosphere caused by primary protons and stripped nuclei. The networks of particle detectors can predict upcoming geomagnetic and radiation storms hours before the arrival of Interplanetary Coronal Mass Ejections (ICMEs) at the ACE and SOHO spacecraft. The less than one hour lead time (the time it takes for the ICME to travel from the spacecraft to the magnetosphere) provided by particle detectors located at ACE and SOHO at the libration point 1,5 million kilometers from the Earth is too brief to take effective mitigating actions to protect satellites and surface from the harm of major geomagnetic storms. For reliable and timely forecast we need adequate models of the major solar energetic events in progress. The information on the highest energy solar cosmic rays, available from surface based particle detectors can be used to test such models and to obtain overall knowledge on the particle acceleration in flares and by fast shock blasts; on transient modulation effects posed by sun activity on the Galactic Cosmic Ray (GCR) flux; on the interactions of solar wind with magnetosphere; on the dynamic of the magnetosphere and many others.

Cosmic Ray flux incident on the terrestrial atmosphere and measured elementary particles on the Earth surface comprise very different entities although genetically connected with each other. Primary particles interactions with atmospheric nuclei and different meteorological effects can hide genuine variations of the primary flux and prevent from understanding of dynamics of ongoing physical processes in solar-terrestrial chain.

For recovering the primary particles fluxes incident on the Earth's atmosphere it is necessary to know the relationship between observed count rates of the detectors and the primary particles fluxes, as well as the influence of the meteorological effects on the flux of secondary particles reaching the Earth surface. Dorman's theory of meteorological effects (Dorman, 2004) gives detailed classification of the effects; mentioned the barometric one as a major influencing particle fluxes (at least for highest energies – 10-100 GeV). Therefore, it is of greatest importance to accurately measure the barometric coefficients to “unfolding” the solar modulation effects. Besides this main goal there exists several independent research problems connected with barometric coefficient dynamics:

- rigidity dependence;
- solar cycle phase dependence;
- height dependence;
- detected particle type dependence

All these dependences can be investigated at ASEC and by SEVAN network due to different altitudes, various detected particle fluxes and planned long-term operation.

The main drivers of these dependences are changing according to solar cycle phase primary flux, type of secondary flux, and location of the detector. At minimum of solar activity, the GCR flux is enriched by abundant low energy (below 10 GeV) particles, blown out from solar system by intense solar wind at maximum of solar activity. Particle detectors located at high latitudes also are sensitive to lower primary energies compared with detectors located at middle low latitudes, because of lower rigidity cutoff. Detectors located at high altitudes are registering more cascade particles than sea level detectors due to attenuation of cascade in the atmosphere. Therefore, because pressure effects should be more pronounced for cascades initiated by particles of lower energies and at cascades containing more particles, following relation can be expected:

- Barometric coefficient absolute value for same secondary particle flux is greater for detectors located at high latitudes compared with low latitudes;
- Barometric coefficient absolute value for same secondary particle flux should be greater at minimum of solar activity compared with maximum;
- Barometric coefficient absolute value for same secondary particle flux should be greater for high altitudes compared with sea level location;
- Barometric coefficient absolute value should be greater for neutrons than for muons;
- Barometric coefficient absolute value should be inverse proportional to muon energy;
- Barometric coefficient absolute value should be inverse proportional to zenith angle of incident particle flux.
- Barometric coefficient absolute value should be lower for high multiplicities detected in Neutron Monitors and for greater dead times of DAQ electronics.

All mentioned dependences were investigated and discovered during the last 50 years by the networks of neutron monitors and muon detectors (see details in Dorman, 2004). Nonetheless, because of peculiarities of detection techniques, scarce statistics, highly different local meteorological conditions, cycle-to cycle variations of solar activities dependencies yet are more qualitative and additional investigations of dynamic and interrelations of barometric coefficients are needed. ASEC provides ideal platform for such research.

During more than 50-years operation Neutron Monitors (NM) network prove to be extremely effective in observing solar modulation effects. Several attempts were made to enlarge NM information contain: put additional channels without lead coverage, measure so called multiplicity (number of multiple counts), etc. The monitors are equipped with new electronics providing time integration of counts by three dead times. The first dead time equals to 400ns for collecting almost all secondary neutrons generated in the lead of NM. The second dead time is equal to the 0.25ms and the third one equal 1.25ms (as most of NM from world-wide network).

Physical analysis of the 3 time series from one and the same monitor and comparison of data from 2 monitors located at 2 altitudes will be presented in the report. Barometric coefficients of all 6 time series will be calculated and compared.

The paper is organized in the following way: the second chapter will explain the statistical techniques used for the barometric coefficient calculations; the third section will present the main results obtained for ASEC monitors at beginning of solar cycle 24; in discussion section we’ll compare our results with previously obtained data and will check consistency of obtained results with expectations.

2. REGRESSION METHODS USED FOR THE BAROMETRIC COEFFICIENT CALCULATION

Experimentally, the intensity I of any secondary cosmic ray component varies with a small change in the atmospheric pressure P (Dorman ,1974) as

$$\mathrm{dI} = -\mu \mathrm{dP} \quad (1)$$

where μ is the absorption coefficient for the secondary component under consideration. For

μ = constant, the equation (1) gives

$$I = I_0 e^{-\mu(P-P_0)} \quad (2)$$

Where P is pressure and P_0 is reference pressure, usually the average pressure at station. I and I_0 are counting rates at these pressures, β is barometric coefficient.

After simple transformation we readily get equation of linear regression:

$$Ln\frac{I}{I_0} = -\mu(P - P_O) \quad (3)$$

Empirically value of the barometric coefficient can be found by means of liner correlation between intensity of cosmic-rays I_i and data of atmospheric pressure P_i.

$$\beta = r \cdot \sigma_I / \sigma_p \quad (4)$$

Where r correlation coefficient:

$$r = \sum_{i=1}^{N} (I_i - I_0)(P_i - P_0) / \sigma_I \sigma_P N$$

$$\sigma_I^2 = \sum_{i=1}^{N} (I_i - I_0)^2 / N \; ;$$

$$\sigma_P^2 = \sum_{i=1}^{N} (P_i - P_0)^2 / N$$

$$I_0 = \sum_{i=1}^{N} I_i / N$$

$$P_0 = \sum_{i=1}^{N} P_i / N$$

The relative error of estimation β can be calculated as follows:

$$\frac{\Delta\beta}{\beta} = \pm \frac{1}{r} \sqrt{\frac{1 - r^2}{N - 3}}$$

Data for barometric coefficient calculation is selected at time periods when there were no disturbances of the Interplanetary Magnetic Field (IMF) and magnetosphere; and in addition there were significant changes in the atmospheric pressure. The least square method was used to obtain the regression coefficients. Large values of correlation coefficient prove correct selection of the reference data.

In Tables 1we summarize the calculated barometric coefficients of ASEC monitors. In the columns accordingly are posted the altitude; cut-off rigidity; barometric coefficient; goodness of fit – the correlation coefficient; minute count rate; relative error of count rate; "Poisson" estimate of relative error. Values posted in the last two columns should be very close to each other if the particle arrival can be described by the Poisson process. Any small deviation manifested the correlation between detector channels; any large correlation – failures in electronics or data acquisition software.

Aragats and Nor Amberd neutron monitors operate with 3 different dead times. The shortest dead time collected all secondary neutrons generated in lead by primary hadrons. As it was demonstrated in (Cilingarian & Oganissyan, 2009), secondary neutrons can be registered in neighboring channels of monitor. Therefore, due to this embedded correlation "Poisson" and measured relative errors for shortest dead time deviated from each other. When enlarging the dead time, the one-to-one relation between high energy hadron entering detector and detector count is established, inter-channel correlation vanished and Poisson and measured relative errors get equal.

The Aragats Multichannel Muon Monitor (AMMM) after changing data acquisition electronics, demonstrates large deviations of measured and Poisson relative errors. Therefore, electronics of AMMM is moved and under repair now.

In table 2 we present barometric coefficients for the SEVAN detectors located at Aragats and in Yerevan (Chilingarian and Reymers, 2008, Chilingarian et al., 2009). SEVAN detectors have 3 layers inter-layered with lead filters. Middle thick layer is sensitive to the neutral particles. Analyzing the outputs from each layer we can outline different species of the incident on detector particles. For instance combination (010 – signal only in middle scintillator) "selects" neutral particles. Probability that neutral particle give signal in upper 5 cm. thick scintillator less than 5%; and – the signal probability that neutron will give signal in middle 25 cm. thick scintillator is ~ 25%. The combination (111 signals in all scintillators) "selects: muons with energies greater than 250 MeV – the energy necessary to cross 10 cm. of lead.

In Table 3 we compare barometric coefficients of neutron monitors sending data to the Neutron Monitor Data Base (NMDB), a new European project to collect and present minute data from Eurasian detectors. The cutoff rigidities of selected monitors ranging from 0.81 to 7.1 GeV gave good representation of the network and, in addition, the Table provides some hints to compare monitor sensitivity to transient solar events and check of chamber failures. Different data reliability checks are of upmost importance when you have collected and compared data obtained from different detectors using various electronics and data acquisition software.

3. DISCUSSION

Large diapason of the barometric coefficient values, covering approximately one order of magnitude, from 0.08% for the >5 GeV muon flux till 0.73% for the neutron flux demonstrates unique sensitivity of ASEC detectors to primary rigidities from 7 to 50 GV.

ASEC neutron monitors simultaneously measure count rates corresponding to the 3 preselected dead times: 0.4 us, 250 us and 1250 us. This additional information will provide possibilities to access different primary energies. Indeed, from Figure 1 we can see that for both ANM and NANM larger dead times are correspondent to smaller barometric coefficients, i.e. to higher primary energies. As it was expected the absolute value of barometric coefficients increase with decreasing dead time, because of increasing sensitivity to lower energy primaries more influenced by pressure changes. In Figure 1 in addition have depicted barometric coefficient obtained from data of two proportional counters located in Nor Amberd without lead filters. As it was expected, these chambers are most influenced by atmospheric pressure, due to their sensitivity to the lowest energy atmospheric neutrons.

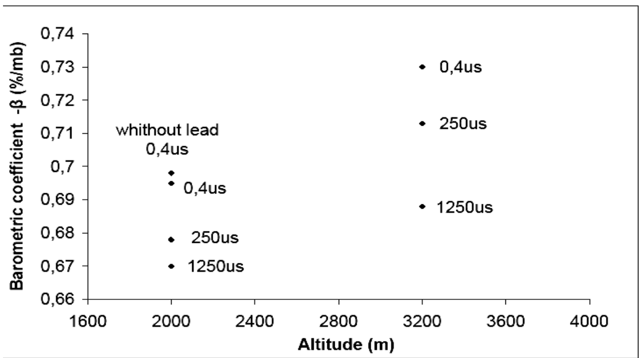

Figure1. Comparison of barometric coefficients different dead times ASEC neutron monitors.

In Table 3 and 4 you can also see barometric coefficients for neutron monitors of Izmiran (Moscow) and Oulu stations. Data were taken from Neutron Monitor Data Base (NMDB) in Kiel, Germany.

Table 1. Barometric coefficients, count rates and relative errors of ASEC monitors

Monitor	Altitude (m.)	Rc (Gv)	Barometric Coeff. %/mb	Correlation Coefficient	Count rate [min]	Relative error	$\frac{1}{\sqrt{N}}$
Aragats Neutron Monitor (18 NM 64) 0.4us	3200	7.1	-0.730±0.018	0.997	43954	0.007	0.0047
Aragats Neutron Monitor (18 NM 64) 250us	3200	7.1	-0.713±0.018	0.997	39654	0.006	0.0050
Aragats Neutron Monitor (18 NM 64) 1250us	3200	7.1	-0.688±0.018	0.996	35911	0.005	0.0052
Nor Amberd Neutron Monitor (18 NM 64) 0.4us	2000	7.1	-0.695±0.013	0.997	28508	0.009	0.0059
Nor Amberd Neutron Monitor (18 NM 64) 250us	2000	7.1	-0.678±0.012	0.997	24988	0.009	0.0063
Nor Amberd Neutron Monitor (18 NM 64) 1250us	2000	7.1	-0.670±0.021	0.995	22561	0.008	0.0066
Nor Amberd Neutron Monitor without lead (2 counters)	2000	7.1	-0.698±0.031	0.989	683	0.038	0.0383
Nor Amberd Multidirectional Muon Monitor(section 1) (upper layer) E>7 MeV	2000	7.1	-0.324±0.012	0.992	81557	0.004	0.0035
Nor Amberd Multidirectional Muon Monitor (section 1) (lower layer)E>250 Mev	2000	7.1	-0.223±0.013	0.987	44420	0.006	0.0047
Nor Amberd Multidirectional Muon Monitor(section 2) (upper layer) E>7 Mev	2000	7.1	-0.323±0.013	0.991	81548	0.004	0.0035
Nor Amberd Multidirectional Muon Monitor(section 2) (lower layer)E>250 Mev	2000	7.1	-0.225±0.013	0.987	44423	0.006	0.0047
Aragats Multichannel Muon Monitor Eμ >5 Gev	3200	7.1	-0.08±7.6E-05	0.924	267589	0.013	0.0019
Aragats Solar Neutron Telescope (5cm)	3200	7.1	-0.507±0.022	0.994	96721	0.003	0.0023
Aragats Solar Neutron Telescope (60cm)	3200	7.1	-0.427±0.017	0.994	175372	0.005	0.0035
Aragats SEVAN Upper detector	3200	7.1	-0.466±0.018	0.994	20768	0.005	0.0069
Aragats SEVAN Middle detector	3200	7.1	-0.406±0.012	0.996	6573	0.011	0.0123
Aragats SEVAN Lower detector	3200	7.1	-0.361±0.016	0.992	12481	0.008	0.0089
Nor Amberd SEVAN Upper detector	2000	7.1	-0.274±0.016	0.975	9100	0.011	0.0105
Nor Amberd SEVAN Middle detector	2000	7.1	-0.342±0.023	0.969	3988	0.015	0.0158
Nor Amberd SEVAN Lower detector	2000	7.1	-0.262±0.017	0.973	5103	0.014	0.0141
Yerevan SEVAN Upper detector	1000	7.1	-0.251±7.85E-05	0.994	14815	0.008	0.0082
Yerevan SEVAN Middle detector	1000	7.1	-0.238±0.014	0.981	3414	0.016	0.0171
Yerevan SEVAN Lower detector	1000	7.1	-0.190±0.025	0.903	9505	0.011	0.0102

Table 2 . Barometric coefficients, count rates and relative errors of SEVAN monitors

Monitor	Altitude (m)	Rc (Gv)	Barometric Coeff. %/mb	Correlation Coefficient	Count rate [min]	Relative error	$\frac{1}{\sqrt{N}}$
Aragats SEVAN Low Energy Charged Particles (Coincidence 100)	3200	7.1	-0.5±0.018	0.995	15389	0.007	0.0080
Aragats SEVAN High Energy Muons (Coincidence 111+ Coincidence 101)	3200	7.1	-.351±0.038	0.96	3868	0.014	0.0161
Aragats SEVAN Neutrons (Coincidence 010)	3200	7.1	-.511±0.018	0.995	1959	0.019	0.0225
Nor Amberd SEVAN Low Energy Charged Particles (Coincidence 100)	2000	7.1	-.281±0.022	0.957	5941	0.013	0.0129
Nor Amberd Sevan High Energy Muons (Coincidence 111+ Coincidence 101)	2000	7.1	-.242±0.022	0.952	1988	0.026	0.0224
Nor Amberd SEVAN Neutrons (Coincidence 010)	2000	7.1	-0.54±0.070	0.899	674	0.037	0.0385
Yerevan SEVAN Low Energy Charged Particles (Coincidence 100)	1000	7.1	-0.3±0.014	0.987	9446	0.010	0.0102
Yerevan SEVAN High Energy Muons (Coincidence 111+ Coincidence 101)	1000	7.1	-0.149±0.035	0.765	4714	0.015	0.0145
Yerevan SEVAN Neutrons (Coincidence 010)	1000	7.1	-0.4±0.039	0.943	425	0.048	0.0485

Table 3. Barometric coefficients, count rates and relative errors of Aragats (us=0.4), Izmiran(Moscow) and Oulu (Finland) neutron monitors, data from NMDB

Monitor	Altitude (m)	Rc (Gv)	Barometric Coeff. %/mb	Correlation Coefficient	Count rate [min]	Relative error	$\frac{1}{\sqrt{N}}$
Nor Amberd neutron monitor (18 NM 64) 0.4us	2000	7.1	-0.695±0.013	0.997	28508	0.009	0.0059
Aragats neutron monitor (18 NM 64) 0.4us	3200	7.1	-0.730±0.018	0.997	43954	0.007	0.0047
Izmiran (Moscow) neutron monitor (24 NM 64)	200	2.46	-0.74±5.11E-05	0.999	16054	0.012	0.0078
Oulu neutron monitor (9 NM 64)	0	0.81	-0.757±3.37E-05	0.999	5990	0.019	0.0129

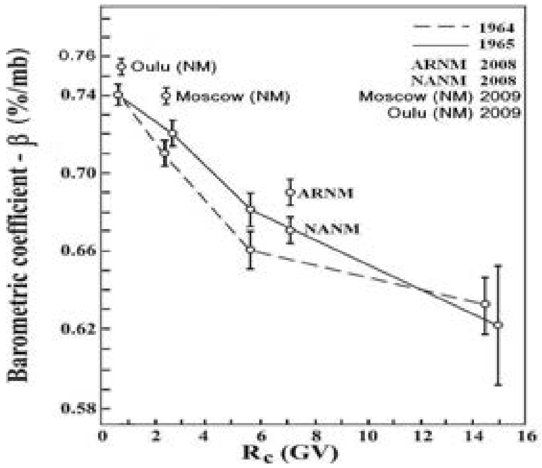

Figure2. Comparison of Aragats (ARNM), Nor Amberd (NANM), Izmiran (Moscow) and Oulu neutron monitors with barometric coefficients for neutron component calculated by L.Dorman.

In Figure 2 we compare barometric coefficients of Aragats (ARNM, 18 NM 64), Nor Amberd (NANM, 18 In In Figure 2 we compare barometric coefficients of Aragats (ARNM, 18 NM 64), Nor Amberd (NANM, 18 NM 64), NM 64), Izmiran (Moscow 24 NM 64) and Oulu (9 NM 64) neutron monitors with barometric coefficients for neutron monitors calculated by (Dorman et al., 1968) during minimum of solar activity in 1964-1965.

We use dead time equal to 1250 microseconds, value commonly used in the world-wide network of neutron monitors in 60-ths. All coefficients relate to solar activity minimum years (1965 and 2008) and are in good agreement with each other. Also it is apparent increase of the absolute value of barometric coefficients with decreasing of cutoff rigidity.

From ASEC muon channels we can see that absolute value of barometric coefficients is inversely proportional to the muon energy.

In addition, by SEVAN barometric coefficients we can illustrate that indeed measured fluxes “selected” by detector electronics are enriched by different species of cosmic rays. Of course we cannot measure “pure” flux of neutrons, due to contamination of gamma-quanta and muons. However, as we see from Table 2, events selected as “neutrons” demonstrate barometric coefficients approximately twice as events selected as muons. Just the same behavior we expect from the neutron and muon fluxes. SEVAN detector measure in addition different combinations of signals in detector layers; therefore we can pose problem of finding barometric coefficients of the “pure” fluxes, as it was described in (Quang et all., Proc. ASA 2 (5) September 1974).

The summary of ASEC barometric coefficients we present in Figures 3 and 4. From simulations (Zazyan & Chilingarian, 2008) we estimate the most probable energy for each detector.

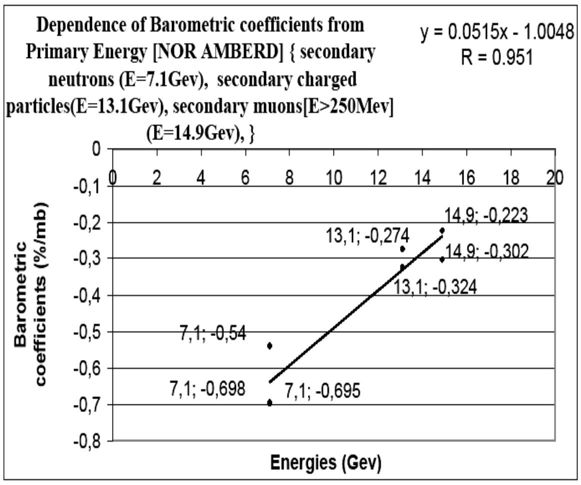

Figure 3. The dependence of barometric coefficient on the primary energy for Nor Amberd station detectors.

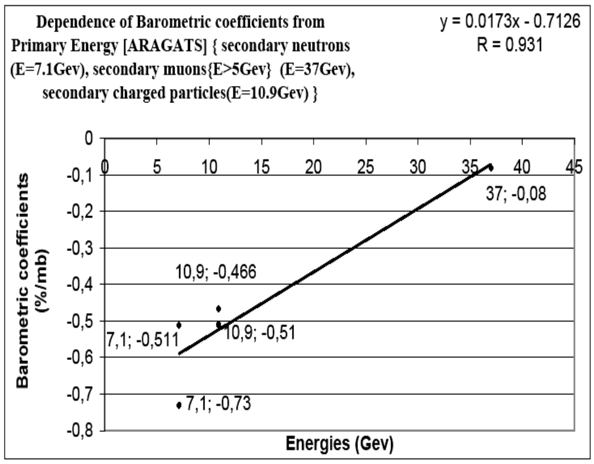

Figure 4. The dependence of barometric coefficient on the primary energy for Aragats station detectors.

As we can see in Figures 3 and 4, energy of primary particle to which detector is sensitive and barometric coefficient correlate rather well

4. CONCLUSION

1. Large diapason of the barometric coefficient values, covering approximately one order of magnitude, from 0.08% for the >5 GeV muon flux till 0.73% for the neutron flux demonstrates unique sensitivity of ASEC detectors to primary particles with rigidities from 7 to 50 GV.

2. Barometric coefficients of monitors belonging to the new particle detector network SEVAN demonstrate that 3 layers of monitors are sensitive to different species of the secondary cosmic rays, namely: low energy charged neutrons and high energy muons. It is independent check of the SEVAN, proving results obtained by simulations.

3. Preliminary analysis of the barometric coefficients calculated for ASEC monitors proves expectations about its energy and altitude dependence. Obtained coefficients are used for correcting ANM and NANM data to appear in the Neutron Monitor Data Base (NMDB) in Kiel, Germany, a European project to collect on-line data of neutron monitors. Data also is transferred to mirror site in USA and

will be transferred to new mirror sites of CRD site in Russia and Europe.

ACKNOWLEDGMENT

Authors are grateful to the staff of Aragats and Nor Amberd research stations for the uninterruptable operation of ASEC monitors. The work was supported by the grant RA610 and ISTC grantA-1554. The part of research leading to these results has received funding from the European Community's Seventh Framework Programme (FP/2007-2013) under grant agreement no 213007.

REFERENCES

Chilingarian A., Avakyan K., Babayan V. et al., Aragats space-environmental centre: status and SEP forecasting possibilities. J. Phys. G: Nucl. Part. Phys**.** 29, 9–951, 2003.

Chilingarian A., Arakelyan K., Avakyan K. et al. Correlated measurements of secondary cosmic ray fluxes by the Aragats Space-Environmental Center monitors. NIM, A543, 483- 492, 2005.

Chilingarian A., Melkumyan L., Hovsepyan G., Reymers A., The response function of the Aragats Solar Neutron Telescope, Nuclear Instruments and Methods in Physics Research A 574, 255-263, 2007.

Chilingarian A. and Reymers A., Investigations of the response of hybrid particle detectors for the Space Environmental Viewing and Analysis Network (SEVAN), Ann. Geophys., 26**,** 249-257, 2008.

Chilingarian A., Hovsepyan G., Arakelyan K., et al. Space environmental viewing and analysis network (SEVAN). Earth, Moon and Planets, 104, 195, 2009.

Chilingarian A., Hovhannisyan A. Calculation of Neutron Mulitplication Coefficients, private communication, 2009.

Dorman L.I. Cosmic Rays in the earth's atmosphere and underground, Kluver Academic Publishers, Dordrecht, Boston, London, 2004.

Dorman L.I., Rogava O.G., Shotashvili L.Kh. Planetary distribution of cosmic ray neutron component barometric coefficient during IQSY, Geomagnetizm and Aeronomy 8, 166-167, in Russian,1968.

Dorman L.I., Rogava O.G. and Shatashvili L. Kh. Planetary distribution of cosmic ray neutron component barometric coefficients during IQSY, Geomagnetism and Aeronomy, 8, No. 1, 166-167, 1968.

Dorman L.I., Cosmic Rays, Variations and Space Exploration. North-Holland, Amsterdam. 1974.

Rogelio Caballero López and José Fco. Valdés-Galicia. Variations in cosmic radiation intensity associated with the barometric effect. Geofisica Internacional Vol.39, Num. 1, pp. 135-137, 2000.

Quang T.T., Fenton A.G. and Fenton K.B.. Effect of the Muon Contribution on the Barometric Coefficient of Neutron Monitors, Proc. ASA 2 (5) September 1974

New electronics for the Aragats Space-Environmental Center (ASEC) Particle Detectors

K. Arakelyan [1], Abovyan [1], A. Avetisyan, A. Chilingarian [1], S. Chilingaryan [1,2], V. Danielyan [1], D. Pokhsraryan [1]

[1] *Cosmic Ray Division, Alikhanyan Physics Institute, Alikhanyan Brothers 2, Yerevan 375036, Armenia,*
[2]*Institut fuer Prozessdatenverarbeitung und Elektronik, Forschungszentrum Karlsruhe, Hermann-von-Helmholtz-Platz 1, 76344 Eggenstein-Leopoldshafen, Germany*

Abstract: The Data Acquisition (DAQ) system for the particle detectors operating at Aragats Space Environmental Center (ASEC) is very flexible and can be tuned by the software, it is design to meet rather severe requirements of multiyear stability and sophisticated operation in multi-channel multi-detector environment.

Devices having from 8 to 64 analog inputs, receive pulses from the scintillator detectors buffer amplifiers and from proportional counters. A newly designed readout is based on the concept of full software control of the detector parameters and maximum utilization of all detector data. Modern fast microcontrollers are used as the base element of the detector control system and physical information storage, analysis and retrieval. The Integrated Silicon Pressure Sensor and ATMEL 8-bit microcontroller is placed in a special pressure-tight box with a possibility of periodic calibration using a Hg standard barometer. The rate of pulses of ground-based particle monitors (not exceeding 10 KHz) allows for a new concept of the DAQ systems heavily using on-line analysis software to select all interesting physical events. The multi-channel DAQ unit consists of input discriminator-shapers with the programmable threshold, Digital-to-Analog Converters (DAC) for the threshold settings, simple logic, microcontroller and serial interface for connecting to the host computer.

Keywords— Data Acquisition electronics, Cosmic rays, Space weather, neutron monitors

1. INTRODUCTION

The standard requirements for the Data Acquisition Electronics (DAQ) system consist in reliable and consistent registration of the all electronic signals from particle detectors. During multiyear measurements the parameters of DAQ system should be continuously monitored to keep them stable. Electronics should not introduce loss of particle detection efficiency due to “dead times” and miscounts.

Additional options to DAQ design consist in physical requirement to measure as much as possible parameters of secondary Cosmic Rays (CRs) accepted by the Aragats Space Environmental Center (ASEC, Chilingarian et al., 2003, 2005). Following requirements was introduced to be fulfilled at the start of new 24th solar activity cycle:

A. The energy releases of particles in body of plastic scintillators provide additional information on the particle type and energy. DAQ electronics should be able to measure and store not only count the number of registered particle in the definite time span (usually 1 minute), i.e., time series of count rates, but also histograms of energy releases, i.e. amplitudes of the Photomultiplier (PM) signals. This amplitude is proportional to the amount of light reaching PM cathode. This light in turn is proportional to the energy release of particle in body of scintillator (you have to take into account also light attenuation, see Chilingarian et al, 2007b). For charged particles energy release (when properly calibrated) is proportional to the number of particles hitting the detector. And energy release is also good proxy of neutral particle energy when neutral particle generates nuclear cascades in the thick scintillator. Therefore, the time series of the histograms of the energy releases in plastic scintillators provide additional information (as we can see from the chapter 3) on the type of solar particles incident the terrestrial atmosphere. Information on the number of particles hitting array of plastic scintillators, along with relative timing can be used also for the reconstruction of the energy and angles of incidence of the very high energy Galactic Cosmic Rays (GCR).

B. Particle identification by registering of all logical combination of the signal occurrence in the multilayered particle detector systems; particle detectors of operating world-wide networks monitoring solar activity have very limited possibility of particle identification and energy estimation. New electronics combined with multilayered detectors interleaved by the lead filters enables much wider options for the identification of the particles. It became possible:

- to identify charged and neutral particles hitting detector;
- to identify primary solar particle hitting terrestrial atmosphere;
- to measure direction of the incident muons, which is good proxy of the incidence of the primary particle on the terrestrial atmosphere;
- to investigate very rare events of muon capture by lead nuclei;
- to measure burst spectra of cosmic rays;
- to measure spectra of horizontal muons, and many others…

C. In contrast to existing world-wide networks measuring only single component of secondary cosmic rays (muons or neutrons) ASEC intended to measure low energy charged component (mostly electrons and muons), neutrons and high energy muons. Correlations between changing fluxes of elementary particle measured at same location gives additional valuable information on transient solar events (Chilingarian & Reymers, 2007a). Therefore DAQ electronics should be designed to issue control signals and provide information readout and store from multiple remote detectors. Secondary cosmic rays are products of interactions of the primary high energy particle with terrestrial atmosphere; therefore fluxes of charged and neutral particles are correlated. Registration of the correlated time series, gives possibility not only detect peaks, deeps and other features connected with solar modulation effects, but also correlation matrices containing new interesting information on the nature of primary solar cosmic rays. Correlation matrices also are very useful for the continuous monitoring of trustworthiness of the detector channels and estimation of important parameters of detector, as, for instance, multiplication of neutrons in the sections of neutron monitor.

Mentioned tasks assigned to DAQ electronics are realized using integrated systems of Complex Programmable Logic Devices (CPLDs), microcontrollers and Field Programmable Gate Arrays (FPGA). Incorporation of the “intellectual” elements allows fulfilling rather complicated tasks mentioned in points 1-3 and, also, performing remote control and tuning of most crucial parameters of the detector. ASEC DAQ system is much more complicated comparing with ones often used in particle detectors of world-wide networks monitoring fluxes of cosmic ray. They usually use industrial 32 or less input cards, implementing simple pulse counting functions only. DAQ of Apatiti Neutron Monitor (NM) (Gvozdevsky et al., 2007) consists of 500 kHz frequency ADLINK PCI-7233H card with 32 inputs.

Dead time of card is 16 µsec. To feed NM signals to the card a shaper-discriminators are needed, as well as an on-line desktop computer. ASEC DAQ systems are fed by analog signals and output is read out from Ethernet port. Fast comparators and CPLDs reduce dead time down to 0.4 µsec. Total energy consumptions including DAQ electronics for 18 channels and build-in micro-PC did not exceed 100 wt. Therefore, accu-battery system powered by solar energy can be also used for feeding the detector, as usually is required for the CR experiments.

The paper is organized in the following way:

Electronics of the Aragats Neutron Telescope (ASNT) and Nor Amberd multidirectional Muon Monitor (NAMM); Electronics of Neutron Monitors; Electronics of Aragats Multichannel Muon Monitor (AMMM); Electronics of SEVAN detector; Description of the pressure sensor and it’s electronics.

2. ELECTRONICS OF ASNT AND NAMMM (SCINTILLATOR DETECTORS)

Functionally, the electronics of Aragats Solar Neutron Telescope (ASNT, see Figure 1) and Nor Amberd Multidirectional Muon Monitor (NAMMM, see Figure 2) consists of two parts: Data Acquisition (DAQ) and Detector Control System (DCS).

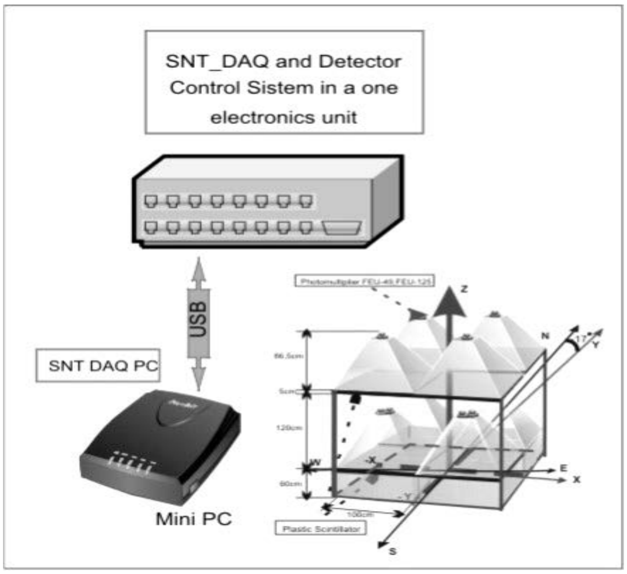

Figure 1. Layout of DAQ electronics of ASNT

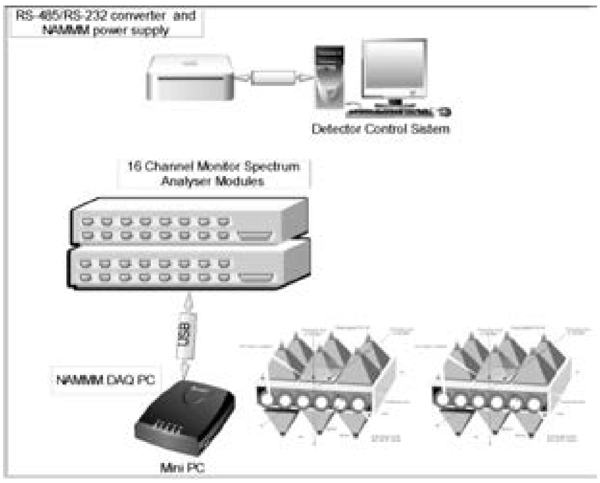

Figure 2. Layout of DAQ electronics of NAMMM

The DAQ chain comprises of Photomultipliers (PMT) FEU49 type, Buffer Preamplifier, Coaxial Cable, Logarithmic Analog-to-Digital Converter (LADC), 32-bit ARM Microcontroller board, USB/COM interfaces and the mini-PC. For the ASNT, all DAQ electronics, except of preamplifier is integrated into one 8-channel input unit, for the NAMMM in two 16-channel units, see Figure 3.

Figure 3. 16-channel electronics unit of NAMMM detector

The DAQ of both detectors are similar, except for the channel numbers, while the DCS is slightly different. The ASNT is a single setup that is why one electronics unit is used for its both subsystems. The NAMMM is only a part of a large experimental setup, consisting of two identical NAMMM detectors and 3 neutron monitors sections. That is why, for the NAMMM, the DCS for all mentioned detectors are integrated into a separate (from DAQ) DCS net as shown in Figure 4.

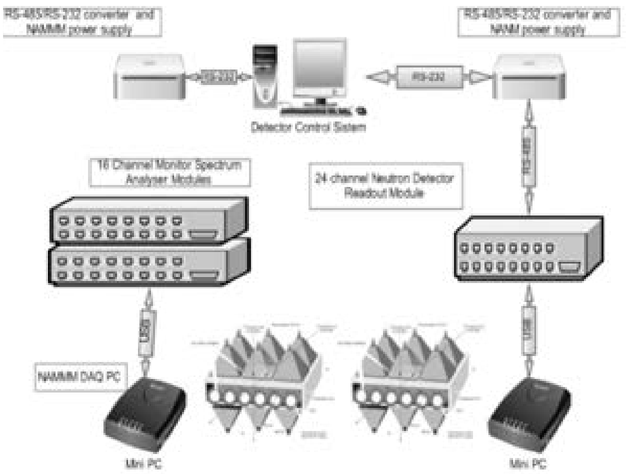

Figure 4. DAQ and DCS networks in Nor Amberd

The DCS of ASNT consists of: Programmable Local High Voltage Power Supply for PMT, RS-485 Local Net, Microcontroller and mini-PC. The same Microcontroller is shared by DAQ and DCS. The DCS of the Nor Amberd setup includes all Programmable Local High Voltage Power Supplies for Muon scintillator detectors PMTs and Neuton Monitor proportional chambers as well as discriminators thresholds of the Neutron Detector Readout Module (see description of the 24 Channel Neutron Detector Readout Module below).

As far as the frontend hardware is concerned, both DCS and DAQ subsystems are tightly integrated. The PMT, Preamplifier and HV Supply are places inside the metal screen case on the top of the scintillation detector. There are two connectors on the case: standard BNC for the main signal connecting cable and round multiple connector for RS-485 interface and unregulated +15V for powering the Preamplifier and HV Source.

The interface/power connections of the ASNT detector are divided into two daisy/chain lines, one line for the upper four detectors and the second one for the lower four. All electrical connections from the detectors come to the ASNT Electronics Unit; see Figure 5, containing both DAQ and DCS circuits.

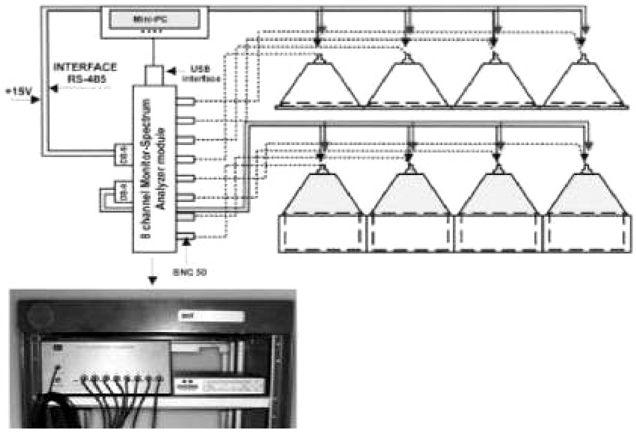

Figure 5. ASNT setup with electronics unit

The interface/power connections of the NAMMM detectors are divided into four daisy/chain lines, two to upper groups of 6 detectors and the two for lower groups.

Figure 6 shows the charts of the metal case of the PMT tube with the PMT and electronics boards inside. There are three connectors placed on the case, A and C for the system interconnections and B for the high voltage manual measurement.

The High Voltage Power Supply (Figure7) is based on a current fed push-pull topology DC/DC converter, working in a sinusoidal mode, to reduce the Electromagnetic Interferences (IMI) influence on the weak PMT output signal. To reduce the HV pulsations to sub-mvolt level, a two stage RC filter is used.

The HV Converter is powered by the switching regulator, controlled by the 8-bit ATMEL microcontroller chip. The microcontroller is integrated into the whole DCS by the RS-485 interface. The microcontroller receives the value of the HV setting from the RS-485 line and sends the measured value of HV to the line by request.

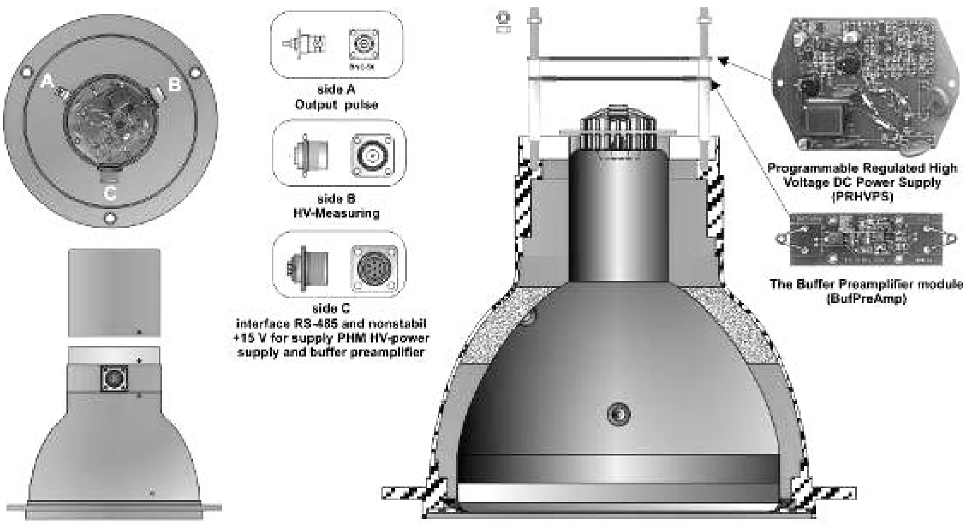

Figure 6. PM installation guide with housing, connectors and electronics

The necessary HV value, sent by command from DCS is stored in the microcontroller permanent memory, so at microcontroller restarts, caused by power spikes, watchdog reset, etc., the HV value is restored without additional setting.

The Figure 7 presents as well the Buffer Preamplifier schematics. It is powered from the same +15V unregulated line as the HV Power Supply through the local linear voltage regulator. The preamplifier is based on the wideband repeater chip LMH6559. Its purpose is to match impedances of the PMT anode load resistor and the 50 Ohm coaxial line. Along with a wide frequency band of preamplifier, another requirement is high dynamic range of output pulses. The polarity of pulses is negative, therefore initial working point of the repeater is chosen close to the upper saturation limit of the chip output voltage.

The rest of electronics is placed inside the ASNT Electronics Unit. The output pulses from the preamplifier are feed through coaxial cables and BNC connectors to the Logarithmic ADCs inputs.

3. LOGARITHMIC AMPLITUDE-TO-DIGITAL CONVERTOR

The principle of logarithmic ADC operation is based on the measurement of decay time of oscillation in the parallel RC tank. The oscillations are caused by current pulses in the parallel RLC tank with a well known Q-factor (Gadalov et al, 1973). We are aware of several realizations of this principle (Ctepanov, 1969, Silaev and Silantiev, 1981, Daryan et al, 1981). In all these cases the Photomultiplier Tube (PMT) of the scintillation detector, which can be considered as an almost perfect current source, was used as the generator of current pulses. The entire electronics of the logarithmic ADC was mounted inside the PMT case and the output signal was the sequence of standard pulses with ~1 MHz frequency and the quantity proportional to the logarithm of the area (charge) of the measured current pulse.

The advantage of this approach is the simplicity and the high noise tolerance provided by the complete shielding of the low-signal circuit in the PMT case.

Building large experimental setups with a large number of different particle detectors requires universal data processing schemes. Our overall strategy for cosmic ray research is to detect simultaneously with one and the same particle detectors both solar modulation effects and high energy galactic cosmic rays. This implies precise timing measurements (3-5 nanoseconds) and requires installation of the fast preamplifiers.

LADCs cannot provide necessary time precision. Since number of incident particles can reach 10^4 per 1 m^2 scintillator LADC can generate pulse sequences with duration 80-90 microseconds, respectively. It is possible to decrease the dead time value by increasing the tank resonance frequency. However, this frequency is limited by the 1.5 - 2 MHz value because if the duration of the input pulses exceeds the quarter of resonance frequency period, the proportionality of the number of output pulses to the logarithm of input signal is disrupted. To guarantee greater flexibility of experimental setup construction, we used another scheme of electronic circuit, see Figure7.

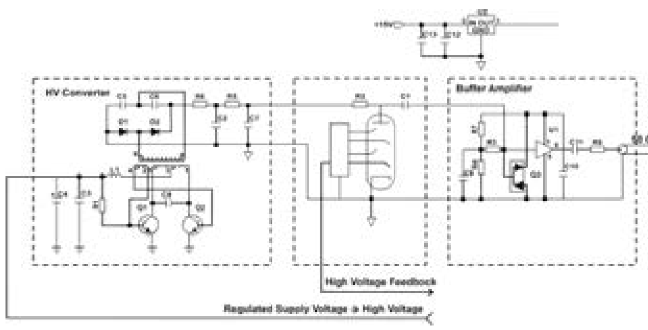

Figure 7. the pm output readout scheme

The voltage pulse from the PMT anode load resistor is amplified by the current by the buffer preamplifier with a +1 voltage gain. The amplifier with the output resistance of 50 Ohm sends the pulse signal, completely repeating the shape of PMT anode current pulse, through the impedance matched 50 Ohm coaxial transmission line to the counting room for further processing. Thus, the whole information about the event registered by the detector enters the laboratory practically without any losses. It can be subjected to various forms of processing, depending on the requirements of a particular physical experiment. The same output signal can simultaneously enter different electronic devices. For example, to undergo processing with short dead time, it can enter the discriminator with a fixed threshold and for the amplitude analysis to Analog-to-Digital Converter (ADC). Different types of ADC can be used simultaneously: inexpensive logarithmic ADC (LADC) with low amplitude resolution, similar to that described in the present paper, and the complex universal multi-channel amplitude analyzer.

The simplified schematic diagram of logarithmic LADC front-end is presented in Figure8.

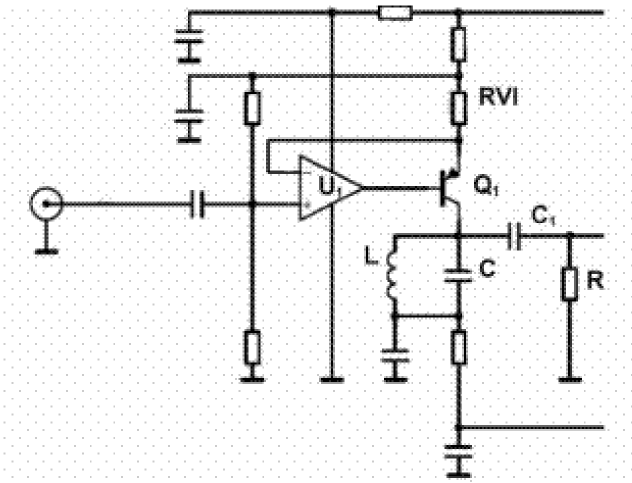

Figure 8. LADC_Frontend

The voltage-to-current converter is assembled on the elements U1, Q1, RVI, its conversion gain is

$$Gain_{vi} = \frac{1}{RVI} = 2\frac{mA}{V} \qquad (0.1)$$

This value is selected so that for the standard shape of PMT pulse, the peak voltage of the first half-wave on the oscillating LRC tank would be equal to the amplitude of the input pulse. Since the maximum amplitude of the input pulse is set in the preamplifier to the level of approximately 7V, the same amplitude is obtained at the entrance of Operational Amplifier (OA) – U_2. The greater maximal voltage values cause the limitation of oscillations amplitudes due to the sharp increase of the U_2 input current, whereas with the smaller values the dynamic range of converter decreases due to an increase in the portion of OA inherent noise, the Radio-Frequency Interferences (RFI) from the radio stations and other kinds of Electromagnetic Interferences (EMI).

As it was already mentioned, the oscillation amplitude on the RLC tank is proportional to the area of the pulse shape, if its duration is shorter, than one fourth of the tank resonance period, i.e.

$$V_0 = \frac{1}{C}\int I_{pulse}dt \qquad (0.2)$$

The current pulses from the Q1 collector cause oscillations damping in the LCR tank. The fact that R is connected to the tank through the capacitor C1 (not directly) is not relevant for the work of the circuit, since the C1 value is considerably higher than the C tank capacity. Figure 9 presents the input pulse and the damping oscillations it causes. These oscillations are further amplified by the two-stage amplifier-limiter on OA U2 and U3 (Figure 10).

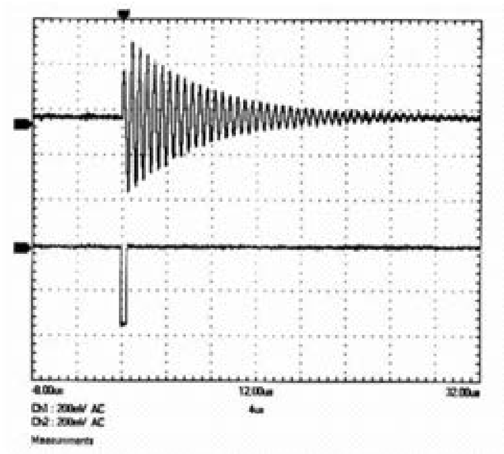

Figure 9. An input signal (lower) and damping oscillations

The amplifier-limiter consists of two identical non-inverting stages. The gain of each amplifier stage at 1.5 - 2 MHz operating frequency is equal to:

$$Gain_{amp} = 1 + \frac{R\_FB}{R_0} = 6.1 \qquad (0.3)$$

Respectively, the complete gain is equal to

$$Gain_{full} = Gain^2_{amp} = 37.21$$

The output signal from the amplifier enters the comparator U_4 non-inverting input.

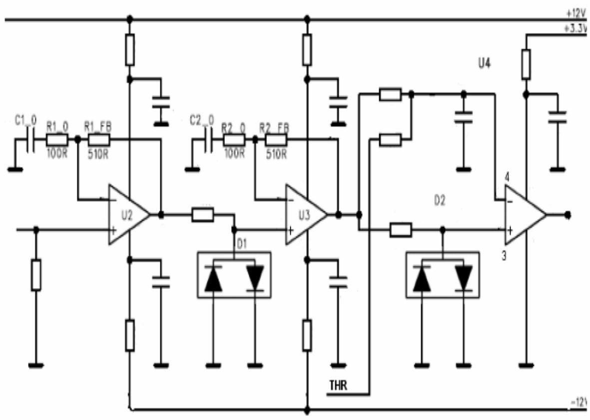

Figure 10. Amplifier-limiter

At large signal values operational amplifiers go saturated, limiting the magnitude of the half-waves of damping oscillations. An even larger level of limitation is provided by the diode limitersD_1, D_2. Since the threshold of the comparator is significantly lower than the limitation level, when the amplitude of oscillation decreases to the value close to the threshold, the amplifier returns to the linear work. It is very important to ensure that the operating point - the constant component of the input signal of comparator, returns to the initial level (which was before the excitation of the tank by the input pulse). In view of a certain asymmetry of levels of limitation, both of OA and of diodes, the capacitive coupling between the stages of the amplifier and the comparator can results in the displacement of operating point after large input signals, because of the recharge of coupling capacitors, which might require significant time for their discharge and operation point restoring. To avoid this, the DC connection is used between the stages of the amplifier and the comparator. At the same time, to decrease the influence of the possible temperature drift of input current of the U_2 and the bias voltages of U_2 and U_3, the DC gain of the amplifier is limited by means of capacitors C1_0 and C2_0 to the value of 1. Since even in this case the zero drift at the U_3 output can reach 20 Mv and more, the threshold of U_4 comparator is set relative to the DC output voltage of the amplifier U_3.

The shapes of signals in different points of amplifier are demonstrated in Figure 11. The output signal of the amplifier can be divided into 2 zones. In the zone I the amplifier works in the limitation mode, while in the zone II it works in the linear mode. To ensure the correct work of LADC, it is necessary to provide a threshold of comparator significantly lower than the limitation level, i.e., so that the comparison of the amplitude of oscillations with the threshold value would occur in the zone II, which actually occurs in our case. The threshold of the comparator is determined by the voltage entering from the output of the Digital-to-Analog Converter (DAC), signal THR1, and can be remotely programmed.

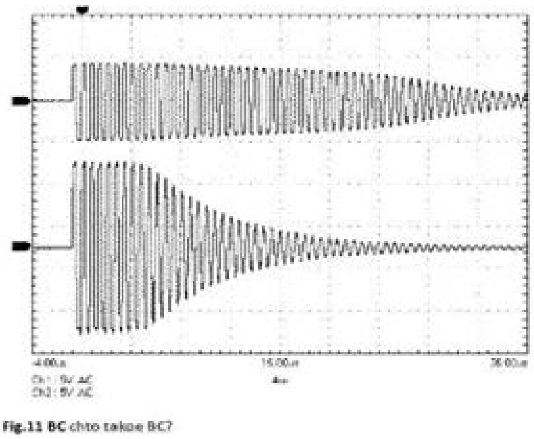

Figure 11. The output signal of the first stage of amplifier (lower) and input signal of comparator (upper)

While the amplitude of the oscillations entering the comparator U4: 3 exceed the threshold value of VU4: 4, each oscillation causes the generation of an output pulse of standard amplitude 3.3V, Figure12 CompOut. The comparator IC used has input hysteresis about 4mV, which ensures the pure form of the output signal.

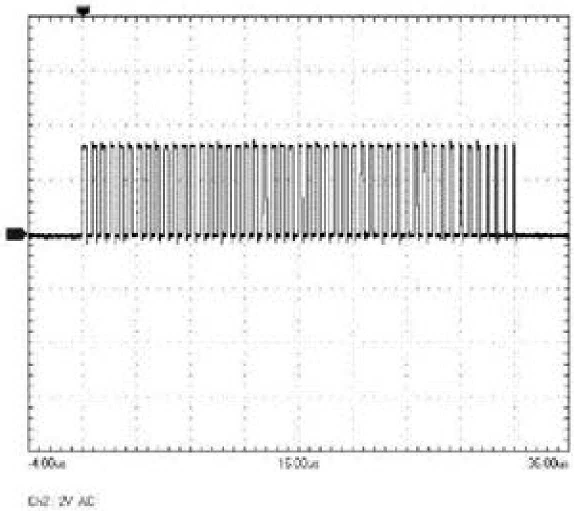

Figure 12. Comparator output signal

After the excitation of oscillations, their amplitude falls according to the law:

$$V = V_0 e^{-\frac{wt}{2Q}} \quad (0.4)$$

where V_0 is the initial amplitude of voltage, w the resonance frequency, Q - the quality factor of the tank. It is possible to rewrite the formula as

$$V = V_0 \cdot e^{-\frac{\pi N}{Q}} \quad (0.5)$$

from which

$$N = \mathrm{int}[\frac{Q}{\pi}\ln\frac{V_0}{V_{th}}], \text{ for } V_0 > V_{th} \quad (0.6)$$

where V_{th} – is the threshold voltage of comparator.

The (0.6) shows, that for providing the necessary conversion coefficient, it is necessary to have the stable Q-factor and a possibility to choose its value. In the previous versions of LADC the home-made induction coils with screw core from soft iron for the introduction of the necessary quantity of losses were used as L. The regulation of Q-factor was produced by the rotation of screw, which simultaneously changed the resonance frequency of the oscillatory tank. However, we implemented a different approach to guarantee the ease of fabrication, high reliability and stability.

A highly reliable industrial inductor with the high Q-factor initial value is used as L. The desired resulting Q-factor is hard set by shunting LC tank with a stable and precise resistor R. Since the resistance of resistor depends on the temperature and other destabilizing factors much less than losses in iron core, this solution allows to choose the necessary Q-factor, simply by selecting the resistance of R, and high stability of its value.

In our case the Q-factor is selected so that the change of the amplitude to 10 times, produce a change in the number of pulses of output sequence equal to 23. Respectively, (0.6) is changed into:

$$N_1 = \mathrm{int}[\frac{Q}{\pi}\ln\frac{V_0}{V_{th}}]$$

$$N_2 = \mathrm{int}[\frac{Q}{\pi}\ln 10 \cdot \frac{V_0}{V_{th}}]$$

where $N_2 = N_1 + 23$.

$$\frac{Q}{\pi} = \frac{23}{\ln 10} = 10$$

where $Q = 10 \cdot \pi = 31.415$

Hence, the required value of the tank Q-factor is approximately 31.

The total conversion factor is affected by the PMT pulse shape and amplitude, which, in turn, depends on the efficiencies of the scintillator, photo-collection, photoelectric cathode, on the PMT feedings voltage and so on. In the described device the controlled parameters are the feeding voltage of FEU and the threshold of LADC comparator. These parameters are remotely preset and they can be re-set in the process of the experiment. However, tuning of these two parameters is insufficient to guarantee the complete identity of the channels and, ideally, additional adjustments are required (PMT anode load, resonant frequency, Q factor). Since the absolute calibration of the entire chain from scintillator to the output sequence is completely stored for calibration and stability monitoring purposes in the off-line mode, we decided not to use in the hardware design such additional adjustment components as potentiometers and trimming capacitors, which significantly worsened the reliability and maintenance.

Structurally, all 8 LADC are located on one printed-circuit board. To simplify the installation and decrease the cost, the channels are not separated from each other by external screens; the problem of the channel interaction is solved as follows. First, the inductors of the oscillatory tanks of adjacent channels are chosen in a mutually perpendicular fashion, which sharply decreases the magnetic coupling. Secondly, by alternating the capacitances of contour capacitors, the resonance frequencies of adjacent channels are relatively shifted according to each-other approximately by 10-15%. In case of maximum amplitude values of input pulses, low oscillations can be observed in the adjacent channels. However, because of the sufficiently high values of the Q-factor, the oscillations increase gradually and up to the moment of the end of time gates (see below) they do not reach the lowest threshold level**.** The comparator threshold is set by the output signal of programmable DAC. One eight-channel DAC IC is used for threshold setting of all eight channels of the LADC board.

The output pulses of the comparator are taken to the IC of Complex Programmable Logic Device (CPLD) of the XILINX CoolRunner-II type that is used for identifying the event, counting the pulses of LADC outputs and sending the counters data to the microcontroller module.

All signals from the detectors, received during the specific interval of time, named gate, are considered as belonging to the same physical event. The gate value is set by CPLD and indicated as a logical signal GATE. The identification of the event and the corresponding trigger of the gate are initiated by the pulse, received in any of the 8-channels. The information about detectors which pulses where received during the gate interval is read out and stored at the end of the gate. Information is stored in the CPLD as a bite mask, named EVENT, in which one bit corresponds to the one input channel. The 1 in this bit means, that the pulse from the detector entered this channel during the gate period. The gate duration is fixed with the binary code (N_{gate}) hard soldered on the input pins GWIDTH0-GWIDTH3 of CPLD and is equal to

$$T_{Gate} = \frac{N_{Gate}+1}{12}\mu S \quad (0.7)$$

In our case N_{Gate} is selected as equal to 7 which corresponds to the gate duration of 0.666 microseconds (us). On the one hand, this value ensures time sufficiently large to register all pulses caused by one physical event, taking into account the spread of detector parameters, the lengths of coupling cables and so on. On the other, it reduces the probability of registering two different events as one to the negligibly low value.

In addition, the parasitic oscillations in the tanks, induced by the large amplitude pulses from the adjacent channels, mentioned above, do not manage to increase to the threshold values.

With the beginning of the time gate, the inputs of all eight counters in CPLD opened and counter start counting the pulses of the packets, entering from the LADC outputs. The signal DURATION, reporting to the microcontroller that the process of event registering goes on is also generated when the event starts. This signal is removed approximately in 1 microsecond after the longest pulse packet ends. After the signal ends, the inputs of all counters are closed and the microcontroller begins reading out the information accumulated in CPLD: EVENT bite and one bite of counter for each of eight channels.

After registering channel information, the microcontroller issues the RESET pulse on CPLD, indicating the end of event. Receiving this pulse, CPLD resets all counters and EVENT byte into the initial (zero) state. Thus, the system is ready to register the following event.

The total dead time of system consists of the count time of the longest pulse packet plus the information processing time of the microcontroller (see below) and is about 100us long for the worst case of the maximal input pulse amplitude. For signals, corresponding to the maximum of the so called “one-particle distribution” tuned for 5-th channel of spectrum, value of the dead time is about 20us.

The LADC module is designed in such a way that up to four LADC boards can be connected to one microcontroller, thus, forming the 32- channel DAC system. Figure 13 demonstrates such connection carried out with flat cables with 5 connectors on each. To simplify the construction, all connectors are fixed to the cable directly, without any over-twisting for the selection of the device number (practice standard for PC). Instead, each of four boards is identified by the address set on the board collected with the jumpers J10, J14.

The accepted scheme of jumper setting is as follows:

1 board (ASNT)– do not install,

2 boards (NAMMM) – do not install on the lower board, install both jumpers on the upper one,

4 boards- from bottom to top: 0,0; J10,0; 0, J14; J10, J14

The setting of the addresses serves both for the selection of internal information of CPLD (EVENT byte + 8 counters) and - for determination of the thresholds. In case of erroneous setting of the cross connections DAC is not programmed and the threshold values are set as equal to zero, which is easily detected by the continuous counting (the LED burn) along all channels, no matter whether the cables are plugged or not.

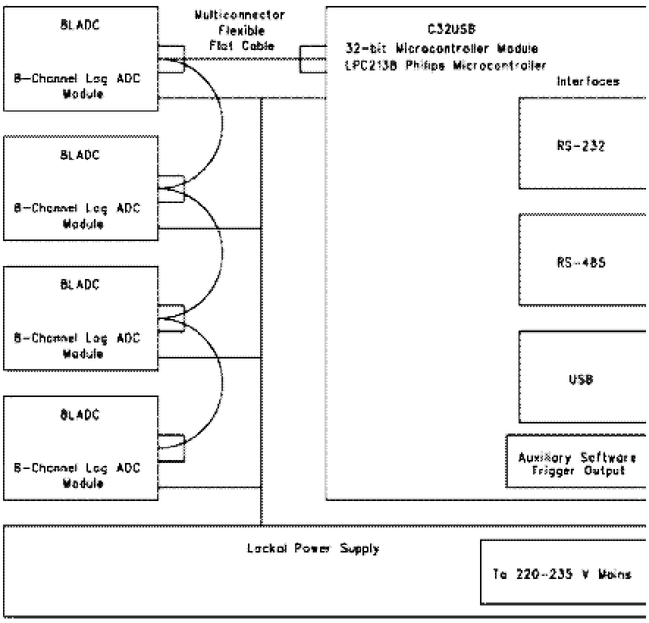

Figure 13. Assembling 4 ladc and microcontroller modules in one unit

When cascading, it is important to satisfy the following condition: the impulse arrival on the entrance of any of the LADC boards is considered as an event, whereas completion of longest of the pulse packets of all boards is viewed as the end of an event. Therefore, the CPLD outputs for the signals GATE and DURATION are programmed as outputs with the open collector and the logical inputs connected to it. This allows combining these signals as a wired OR.

The readout of information from CPLD of the 8LADC boards into the module of microcontroller C32USB is provided by the parallel code on the 8- bit bus. Eight 8-bit pulse counters of LADC and 8- bit EVENT register, total 9 registers, are addresses inside CPLD. To address them, it is necessary to have the 4-bit address, presented by the microcontroller at the lines SEL0-SEL3. The addresses from 0 to 7 are used to select each of 8 counters, while any address in range 8-15 selects one and the same register - the register of event mask (EVENT).

The C32USB module is based on the NXP company LPC2138 microcontroller of the ARM. It is designed as a multifunctional embedded data processing device for the initial on-line processing of data of arbitrary nature. The flexibility of the module application is provided by the possibility to work with any one of interfaces included in the system. The following interfaces are realized:

1. RS-232 for the connection to PC COM port. The rate of exchange is up to 115200 Baud. This port can be used also for the microcontroller IC firmware reprogramming.
2. USB 1- for connection to PC with virtual COM port driver. The exchange is provided through the UART micro-controller interface. The rate of exchange is up to 115200 Baud. This port can be used also for the microcontroller IC firmware reprogramming.
3. USB 2- for the high-speed exchange of information between PC and the microcontroller. Uses the parallel exchange of information between the USB interface IC and the microcontroller. The program access from the PC is provided with the driver of virtual COM port with the speed of exchange up to 115200 Baud and with DLL driver, which, in theory, can ensure the rate of exchange approaching the maximum speed, full USB2 - 10 MBaud.
4. RS-485. It is used for connecting the microcontroller to the local detector control system DCS network.

As the electronic devices, assembled on the basis of C32USB module can be used for the detector setups placed in distant places with difficult maintenance, it is very important to have WEB interface not only for the installation of the detector parameters (thresholds, the voltage of PMT supply), but also for the reprogramming of microcontroller itself. This possibility is necessary for the software modernization at changing conditions of physical experiments, i.e. for changing of so called “software triggers”, selecting data for different physical problems. Software triggers are altered by replacement of the consequences of coincidence and anti-coincidence, replacement of the conditions of the program-generated triggers and so on. Two of the realized interfaces make it possible to remote reprogramming the microcontroller by WEB interface.

The micro-controller software consists of system and problem-oriented parts. The system part includes initialization of I/O ports, watchdog and interval timers, interruption handlers and main input-output, local network managing, and other similar functions. The problem-oriented part, called Aragats Data Acquisition System (ADAS, see Chilingarian et al, 2008) includes pre-processing, storage and sending to the host PC data, collected from the detectors. In particular, the amplitude spectrum for each of the detectors is accumulated, coincidences and anti-coincidence are processed, the particle arrival directions statistics is accumulated, the program triggers are generated and so on. The software is written in the C language, using the free distributed GNUARM software. Some fragments of the code are written on the assembler to achieve the peak output.

As an example of the DAQ electronics and software operation we present in Figure 14 histograms of the energy releases in thin and thick scintillators of the ASNT. Maximums of both distributions correspond to the mean energy release in 5 and 60 cm. scintillators (see details in Chilingarian et al., 2007).

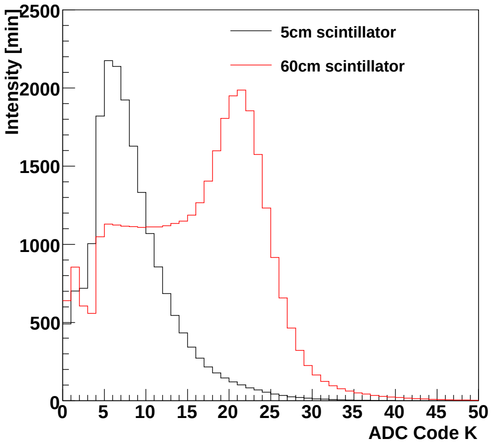

Figure 14. The histogram of the energy releases (pm amplitude spectra) as measured by the ASNT layers during a day.

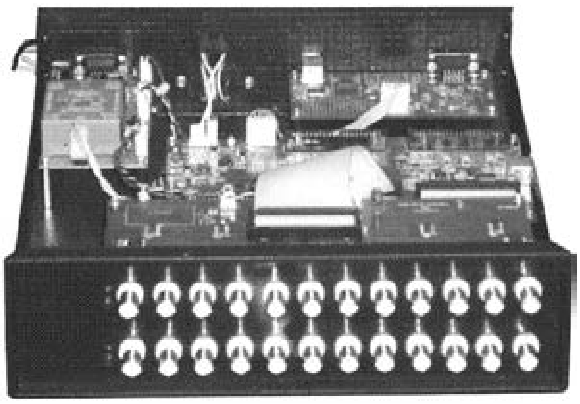

Figure 17. 24-Channel Neutron Monitor (NM) Readout Module

In Figure 16 we present the diagram of the NM readout electronics. In consists of:

1. Two Programmable Threshold 12-channell Discriminator/Counter boards.
2. Universal Multichannel Event Counter (UMEC) board.

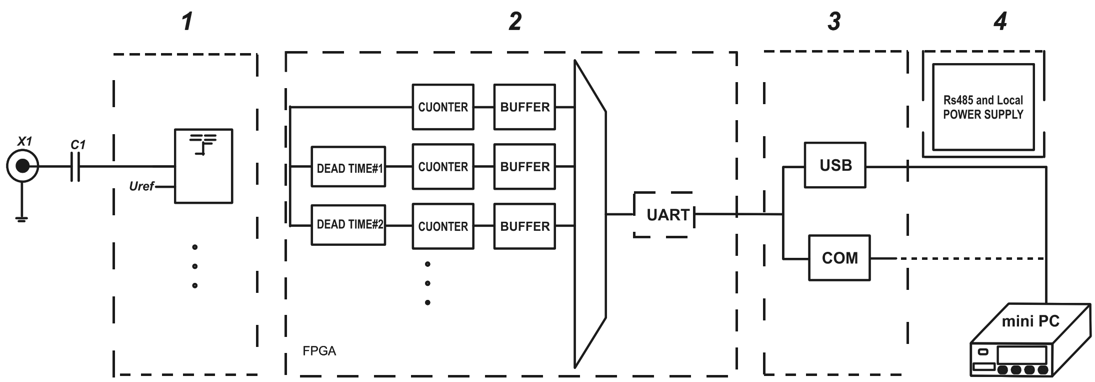

Figure 15. Functional diagram of the NM readout electronics

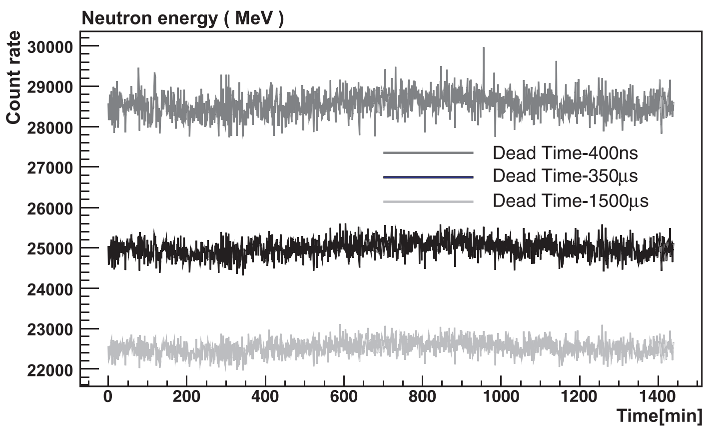

Figure 16. Tree time series from Aragats Neutron MonitoR

4. 24-CHANNEL NEUTRON MONITOR (NM) READOUT MODULE

The main function of the 24 Channel Readout Module is receiving and count of the 18-channel Neutron Monitor signals. It also has 6 auxiliary universal counter channels.

3. Universal Microcontroller Interface module (MultiIFC) board.
4. RS-485 and Local Power supply module.

Pulses from the detector preamplifier are discriminated and shaped in the unit 1. The discrimination threshold can be programmed in range 4mV-1000mV with 4mV step. Duration of the output TTL pulses is 400ns. The shaped pulse enters the input of Xilinx Spartan 3E FPGA (Field Programmable Gate) in the unit 2.

Inside module, the FPGA pulse is applied to three counters: to the first – directly, and to other two through programmable dead time circuits. The dead time values are preset to values of 250us (#2) and 1250us (#3) (see Figure 18). The last value coincides with one used for both Neutron Monitors at Aragats and Nor-Amberd during 23rd solar activity cycle (1996-2007).

Along with 18 programmable channels with 3 dead times (total 3x18 counters), the unit has 6 inputs for direct counting (without dead time circuits). The contents of all 60 (3*18 + 6) counters are downloaded each second in plane ASCII code to the PC through USB (or COM) interface. After downloading, all counters are instantly zeroed and start to count again.

Along with the main output connection, the unit has a RS-485 interface for connecting to the Detector Control Local Net of experimental setup for the on-line programming of the thresholds.

5. ELECTRONICS OF LARGE UNDERGRAOUND MUON DETECTOR

The Aragats Multichannel Muon Monitor was equipped with scalers (electrical pulse counters) based on the old discrete elements of soviet-times. The Pentiun-1 computers were used for data acquisition. To provide stable operation of the AMMM during 24th solar activity cycle (2008 – 2019) we have designed compact and reliable DAQ electronics based on FPGA Xilinx Spartan3E chips. Figure 18 demonstrates a single unit of new electronics. It is comprised from 2 boards containing 60 counters each, power supply, and ATNGW100 Network Gateway Kit equipped with AVR32 Digital Signal Processor (ATMEL AT32AP7000). The ATNGW100 is equipped with 32 MB SDRAM, 8 MB data flash and 2 GB SD flash memory (see Figure 19). The communication is feasible through two Ethernet ports, UART, USB, and JTAG. The external storage can be connected using SD and MMC card reader.

The FPGAs are programmed to realize 60 asynchrony counters to the serial port. In the preloaded LINUX system the serial ports are attached to /dev/ttyS1 и /dev/ttyS2. The system console port is attached to /dev/ttyS0. To provide access to third serial port we have recompiled a LINUX kernel. The port parameters are 8/n/1 115200 b/c. Each second the counters are transferred to ATNGW100 and are stored in hexadecimal format in 120 bite portions. Once a minute the data are archived to the /media directory which reside on the mounted flash card. If the flash card is not installed, the /media directory is mounted to the embedded flash memory. The time synchronization is performed by the NTP client installed on NGW. FTP server is configured to serve the data to data acquisition software. Remote control is enabled by means of SSH and Telnet servers.

The data transfer software twice a second read out serial ports buffers and integrate it up to 1 minute. Then 1- minute data are transferred to ATNGW100 in 120 bit portions and are stored in hexadecimal format. The number of blocks is checked and in the case if it's not equal to 60 (number of seconds in a minute) the minute count is proportionally scaled.

Figure 18. 120-channel fpga-based counter with under control of atngw100 network gateway kit

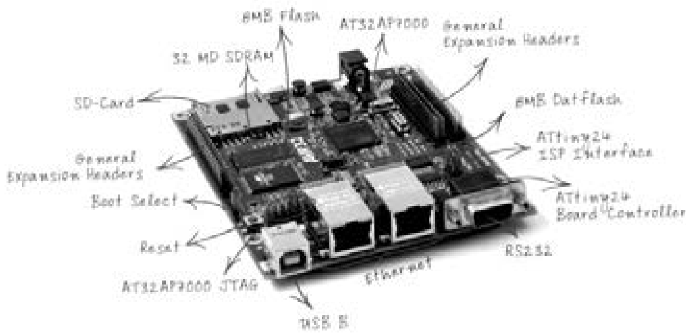

Figure 19. ATNGW100 network gateway kit

During exploitation the new DAQ electronics failed to fulfill requirements of stability and accuracy.

The a-synchronous counters discharge due to instability of FPGA clock lead to overflow and system often hangs. To overcome this difficulty the synchronous discharge was established; additional 20 nsec (2 ticks) time delay was introduced after discharge.

Distortions were detected due to noise in the connections of FPGA boards with ATNGW100. Several checks and consequent corrections were introduced in software as remedy.

6. SEVAN DAQ ELECTRONICS

A network of middle to low latitude particle detectors called SEVAN (Space Environmental Viewing and Analysis Network) (Chilingarian & Reymers, 2008) is planned in the framework of the International Heliophysical Year (IHY), to improve fundamental research of solar accelerators and space weather conditions. Besides the main DAQ function, the unit also acts as a master for the detector control Local Area Network (LAN) which is used for programming and monitoring high voltage values and for programming the ADC thresholds.

Data Acquisition electronics implementing registration of the charged and neutral fluxes of secondary cosmic rays consists of 8-Channel Discriminator/Counter Unit (8DCU) and 3 High Voltage supplies with presetting and automatic control, which are located in the corresponding PMT cases, see Figure 20.

8DCU parts are: The 8-channel Programmable Threshold Comparator and Counter board (8CNT)

Universal RS232/RS485 interface/power supply module - IFCC, Power transformer - 220V50Hz to 2x8V 0.5A + 2x15V 1.25A (Fig.20)

Figure 20. SEVAN DAQ module

The main features used in 8DCU are:

8 programmable threshold analog input,

Threshold programming range 4mV-1000mV with 4mV step,

Powered by AC 50-60Hz 220V, 30W

Maximal counting frequency – 60kHz,

LEDs to indicate the input pulses in each of 8channels, module power and programmable trigger condition, 8 input BNC connectors, 8CNT board is used as a standalone 8-channel counter (scalar) with a programmable threshold. For the threshold programming and the output data readout, it can communicate with the host PC (local network) through the IFCC module by any of RS-232 or RS-485 interface ports. The module counter and interface logic is based on the Atmel AVR Atmega88 (Atmel Corporation, 2008) 8-bit microcontroller. The same ATNGW100 Network Gateway Kit equipped with AVR32 Digital Signal Processor CPU (see previous section) is used as on-line PC for SEVAN modules.

DAQ software consists of the host PC program and the microcontroller program (firmware). The firmware for the DAQ and control is written in C language and stored in the microcontroller reprogrammable flash memory. Below is presented the functionality, implemented for the SEVAN detector setup. In this case the microcontroller operates both for the thresholds presetting and control and as a main DAQ controller, with listed below functions:

1. Counting of signals in each of 8 channels,
2. Counting of all types of coincidences of signals in channels 1-3.

The data collection time is set by the microcontroller firmware, so any other value can be chosen. The IFCC interface module has three connections: to the microcontroller, to the RS232 connector (DSUB9F) and RS485 connector (DSUB9M). The signals propagate from each of the mentioned connections to both of others. The power for the PMT High Voltage supplies (15V unregulated, 1.2Amax) is supplied from the 8DCU through the RS485 interface connector

7. PROGRAMMABLE REGULATED HIGH VOLTAGE DC POWER SUPPLY (PRHVPS)

The Programmable Regulated High Voltage DC Power Supply is designed to supply high voltage to different electrodes on photomultipliers and various elementary particle detectors (Figure 21).

Industrial DC-DC power supplies usually need for the remote control ADC-equipped cards (Pulse Power & Measurement Ltd, 2008). Our solution consists in high voltage power supply with build in controlled Via serial interface RS-485. Using the ATNGW100 Network Gateway Kit it is possible to remote tuning of the thresholds of discriminators and high voltage values for detector channels via Ethernet port.

The PRHVPS consists of:

- Current-driven, low-noise sine wave DC/DC converter, with up to 2 stage RC output ripple
- Pulse Width Modulated programmable DC regulator
- Local +5V linear voltage regulator
- Atmel microcontroller
- RS485 interface chip
- Optional temperature sensor

The Printed Circuit Board (PCB) can be assembled with various options for different output polarity, programmable voltage range, and so on.

Specific Features:

- Voltage programming in two hardware selectable ranges ± 900V to 2100V and ±1500 to 3000V in 2V steps
- Output voltage ripple less than 1mV
- Max. output current 1.2 mA for ± 900V to 2100V range; 0.8 mA for ±1500 to 3000V range
- Input voltage from +12V to +15V
- Absolute output voltage regulated to accuracy ±1V
- Optional temperature sensor
- RS-485 half-duplex 2-wire 9600 baud interface for programming and monitoring the output voltage

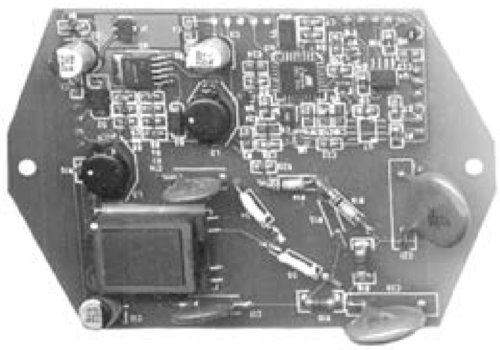

Figure 21. Programmable Regulated High Voltage DC Power Supply

8. CONCLUSION AND ACKNOWLEDGMENT

After one year operation of most components of the ASEC DAQ it proves reliability and multifunctional possibilities. Several papers are published based on the new physical results enabled by flexible and powerful DAQ system. System is still under extensive testing and tuning to be ready for uninterruptable operation during started in 2008 24th solar activity cycle. Work was supported by ISTC Grant A1554 and INTAS Grant 8777.

REFERENCES

Atmel Corporation, http://www.atmel.com/,2008

Chilingarian A.A., Avagyan K., Babayan V. et al. Aragats Space-Environmental Center: status and SEP forecasting possibilities. J.Phys. G:Nucl.Part.Phys. 29, pp. 939-952, 2003

Chilingarian A.A., Arakelyan K., Avagyan K., et al. Correlated measurements of secondary cosmic ray fluxes by the Aragats Space Environmental Center monitors. NIM, A543, pp. 483-496, 2005

Chilingarian A., Melkumyan L., Hovsepyan G., Reymers A.. The response function of the Aragats Solar Neutron Telescope, Nuclear Instruments and Methods in Physics Research. A 574, pp 255-263, 2007

Chilingarian A.A. and Reymers A. Investigations of the response of hybrid particle detectors for the Space Environmental Viewing and Analysis Network (SEVAN), Ann. Geophys., 26, pp. 249-257, 2008

Chilingaryan S., Chilingarian A., Danielyan V., Eppler W. The Aragats data acquisition system for highly distributed particle detecting networks. Journal of Physics: Conference Series 119 pp. 1-9, 2008 doi:10.1088/1742-6596/119/8/082001

Daryan A.V, Dolganov S.A., Khachatryan A.P., Preprint YerPhI 1485(2), 1997

Freescale semiconductor. 2008, http://www.freescale.com/

Gadalov A.N., Kaganovvv I.I., Silaev A.A. , Facilities and Techniques of Experiment N1, pp.39, 1973

B. B. Gvozdevsky, Yu. V. Balabin, E. V. Vashenyuk, L. I. Schur Neutron monitor multiplicity measurements during the 13.12.2006 GLE. in WEB site of conference SEE, 2007 ,http://cosray.phys.uoa.gr/SEE2007/, Athens, 2007, JASR, in press

Pulse Power & Measurement Ltd. 2008, http://www.ppmpower.co.uk/high_voltage_dc_dc_converters/

Silaev A.A., Silant'ev O.A., Facilities and Techniques of Experiment N1, pp.100, 1981.

Stepanov V.I., Facilities and Techniques of Experiment N3, pp.115, 1969

Atmospheric Pressure Measurements at the Aragats Space Environmental Center

K. Arakelyan

Cosmic Ray Division, Alikhanyan Physics Institute, Alikhanyan Brothers 2, Yerevan 375036, Armenia
(e-mail:karen @ yerphi.am)

1. INTRODUCTION

Cosmic Ray flux incident on the terrestrial atmosphere and measured elementary particles on the Earth surface comprise very different entities although genetically connected with each other. Primary particles interactions with atmospheric nuclei and different methodological effects can hide genuine variations of the primary flux and prevent from understanding of dynamics of ongoing physical processes in solar-terrestrial chain.

To recover the primary particles fluxes incident on the Earth's atmosphere it is necessary to know the relationship between observed count rates of the detectors and the primary particles fluxes, as well as the influence of the meteorological effects on the flux of secondary particles reaching the Earth surface. Dorman's theory of meteorological effects (Dorman, 2004) gives detailed classification of the effects; mentioned the barometric one as a major influencing particle fluxes (at least for highest energies – 10-100 GeV). Therefore, it is of greatest importance to accurately measure the atmospheric pressure to "unfold" the solar modulation effects. And, consequently, the precise sensors equipped with automatic readout systems are the essential part of each monitoring system.

The secondary component of the cosmic ray intensity is sensitive to variations in the atmospheric column density above the particle detectors. This leads to a change in absorption of the secondaries, and a consequent change in the counting rate. Local station pressure is a generally accepted measure for this column density. These pressure effects must be taken into account before the neutron monitor data can be used for cosmic ray studies. A period of high pressure is associated with more absorber above the detector and a lower detection rate results. The purpose of this investigation is to determine the relationship between barometric pressure and cosmic ray intensity.

The paper consists of description of the atmospheric pressure measuring device used at high altitude research stations of Yerevan Physics Institute, of describing the calibration procedure and of statistical analysis of precision of this sensor.

2. THE PRESSURE, HUMIDITY, TEMPERATURE - PHT SENSOR

Pressure measuring device is a general purpose microcontroller unit, designed for environmental measurements: pressure, temperature and humidity (see Figure 1). In addition to the main sensors mounted on the board, it has two auxiliary connectors with pinned out microcontroller input/output port pins, which can be used for other measurement and control purposes.

- It has two alternative interfaces to integrate it into a system: RS232 and half-duplex RS485.
- It has Frequency Modulated (FM) output TTL for compatibility with the existing Cosmic Ray The microcontroller software (firmware) supports all the mentioned sensors and interfaces and can be easily upgraded for additional measurements and control options.

Specific Features:

- Pressure sensor Motorola MPXA6115 (Freescale semiconductor. 2008) has 15 to 115 kPa measurement range with 1.5% maximum error in the 0 to 85°C temperature range. Using an external calibrating procedure, the error can be significantly decreased. The sensor is connected to a 16-bit ADC. The measured data is averaged in software to minimize the noise. The real pressure resolution depends on the averaging time and can be as good as 15-bit (~1/32000 of full scale).
- The ATMEL Atmega8-16AI microcontroller can be easily reprogrammed using the ATMEL standard serial programming protocol.
- The board has built-in +5V regulator, thus it can be powered by any regulated or unregulated power supply with 100mA current.

After ADC the digitized data is entering microcontroller Atmega8 and then via serial interface RS-385 – one of channels of 24-channel Neutron Monitor readout module. The code (or frequency) is converted in the output voltage and then to pressure (see Figure 2).

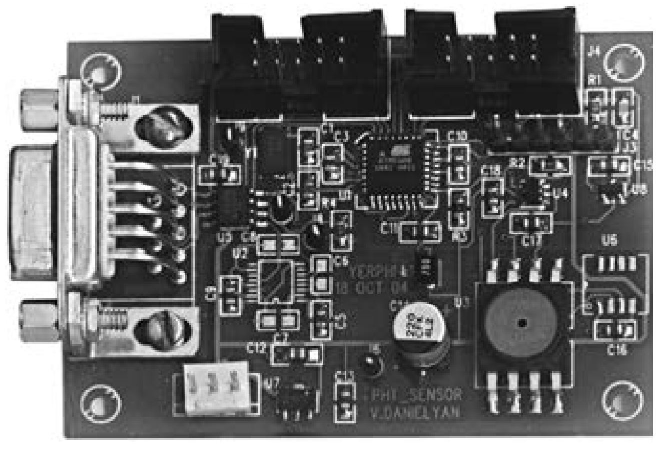

Figure 1. The Atmospheric Pressure measuring board

The sensor output is linear with respect to the pressure in the 780 to 820 mbar range. The correlation line equation is P(mbar) = 0.1429 N + 112.46 with a χ^2 fit of 0.9999

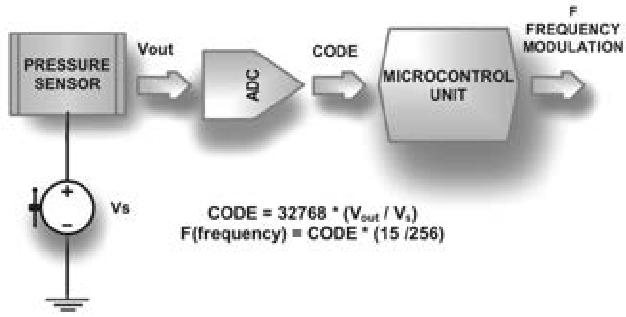

Figure 2. The scheme of Pressure measuring device

The atmospheric pressure is calculated from the sensor measurements by the following equations:

1 $$P = \frac{\frac{V_{out}}{V_s} + 0.095}{0.009} \pm \text{PressureError}$$

2 $$\frac{V_{out}}{V_s} = \frac{code}{32768} = frecuency \times \frac{256}{15}$$

3 $$P \approx \frac{frecuency \times \frac{256}{15} + 0.095}{0.009}$$

3. CHECKING OF THE PRESSURE SENSOR

Without calibration the atmospheric pressure measurements obtained from individual sensors can deviate from “true” value, according to the producer by 15 Mb.

To calibrate the pressure device, we place the PHT sensor in a special chamber in which we can vary and measure the pressure with high accuracy (0.05mbar) using a mercury barometer.

In Figure 3 the calibration curve for PHT sensor is depicted. The sensor output is a linear function of varying pressure in the range of 780 to 820 mbar. The correlation equation is P(mbar) = 0.1429 N + 112.46 with a χ 2 fit of 0.9999; where N is the sensor output.

To check the factory parameters and to obtain relative accuracy of the measurements (the one needed to calculate the accuracy of, so called, barometric coefficient) we locate at each research station 2 identical sensors.

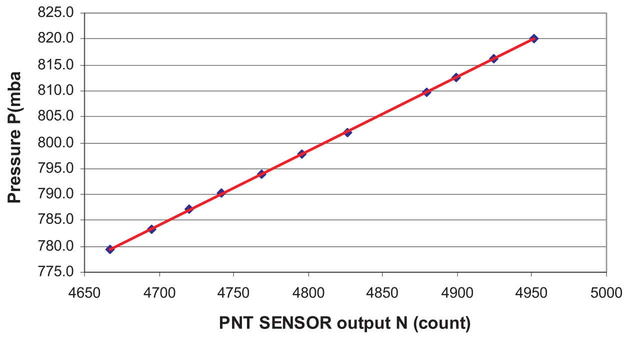

Figure 3. Calibration curve of the pressure sensor performed at Nor Amberd research station

As we can see from Figures 4 and 5 the measured atmospheric pressure by both sensors is highly coherent shifted from each other by a constant value 4 – 7 Mb, consistent with producer’s data.

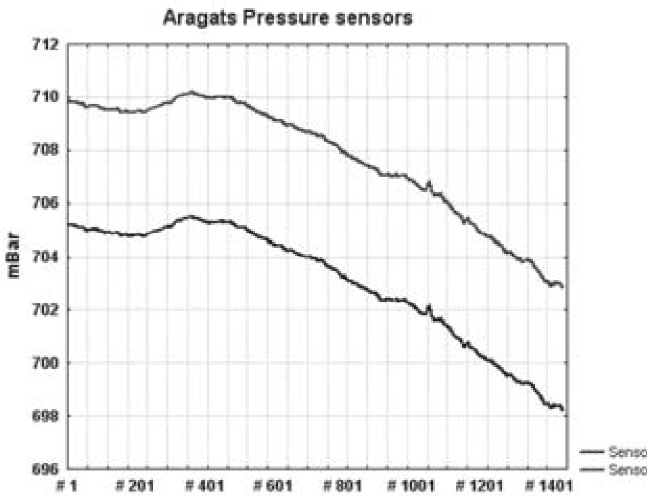

Figure 4. The daily variations of the atmospheric pressure measured at altitude 3200 m. by 2 independent pressure sensors of the same type.

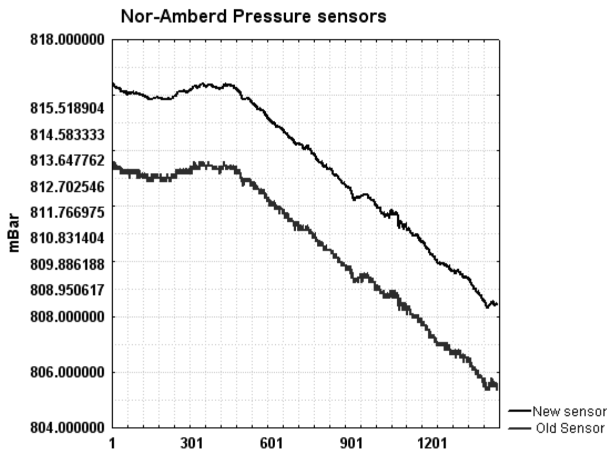

Figure 5. The daily variations of the atmospheric pressure measured at altitude 2000 m. by 2 independent pressure sensors of the same type.

The bias can be eliminated by taking into account the calibration with etalon precise sensor described in the beginning of section.

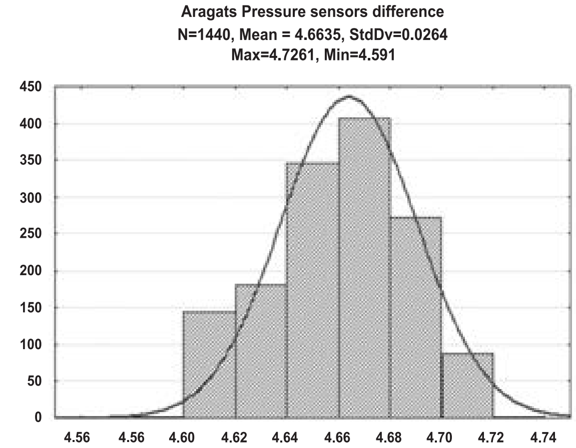

Figure 6. Thehe distribution of the differences of measurements of 2 similar pressure sensors located at altitute 3200 m.

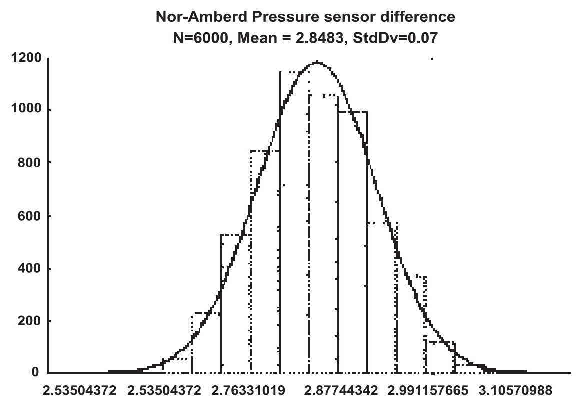

Figure 7. The distribution of the differences of measurements of 2 similar pressure sensors located at altitute 2000 m.

As we can see in Figures 6 and 7, the discrepancies (mean width on mean height) between sensors located at the same altitudes is rather stable and doesn't exceed 0.07 Mb. Therefore, the accuracy of the single pressure measuring device can be estimated as not worse than 0.05 Mb (see details in Dorman, 1975). As the barometric coefficients of both monitors located at Mt. Aragats are approximately -0.7 %/mb (increasing of atmosphere pressure by 1 Mb, leads to decrease of monitor's count rate by ~0.7%) and that accuracy of 1 minute count rate of monitors is ~ 0.6% we can conclude that obtained accuracy of the atmospheric pressure measuring device is far enough for performing pressure correction of the neutron monitor count rates.

To estimate the absolute accuracy of pressure measurements we should take into account also the accuracy of the calibration. The final absolute accuracy according to the measurements performs at Aragats and Nor Amberd with 4 serial sensors is not worse than ~0.05 Mb.

4. OPERATION OF THE PMT SENSOR ON HIGH ALTITUDE STATIONS AND IN YEREVAN

Starting from 2007 the count rates of the particle detectors belonging to the Aragats Space Environmental Center (Chilingarian et al, 2003, 2005) are routinely corrected for pressure before physical analysis. Among the brightest ASEC results is the discovery of the highest energy protons accelerated in the vicinity of the Sun on January 20, 2005 (Bostanjyan et al, 2007, Chilingarian, 2009). High precision of the pressure sensors allows also meteorological research. In Figure 8 we post the atmospheric pressure curves measured at 3 different latitudes in Armenia.

Pressure correction should be made also in studies of the diurnal variations of cosmic ray flux. The amplitude of diurnal variations at minimum of solar activity is not greater than 0.5%; therefore very precise analysis of the atmospheric pressure variability is needed to disentangle atmospheric pressure and solar-terrestrial connections effects.

In Figures 9 and 10 we can notice periodicity in the daily pressure variations, better expressed in Nor Amberd at altitude of 2000m. Harmonic variations of pressure peaked at ~ 7 and 20 UT with amplitude of ~0.05%. Taking into account the atmospheric pressure variation allows, as we can see in Figure 9 and 10, to emphasize the diurnal variations and estimates its amplitude and phase.

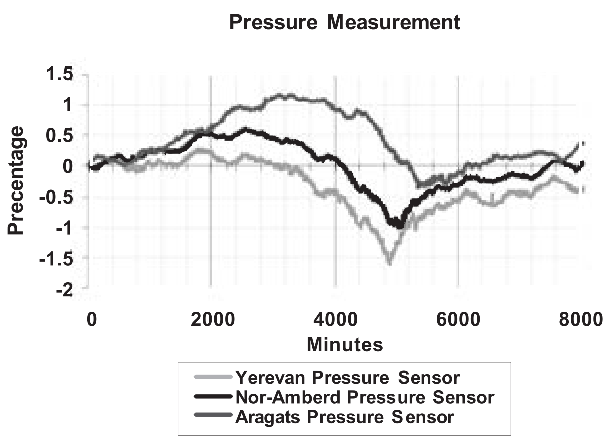

Figure 8. Measurements of pressure at different altitudes at 03 march 2009 till 09 march 2009

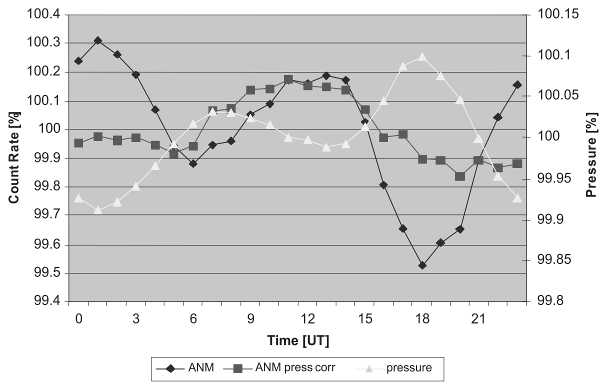

Figure 9. Daily variations of the atmospheric pressure and Aragats Neutron Monitor count rates. Note that correction to the pressure effects improves the shape of the daily count rates.

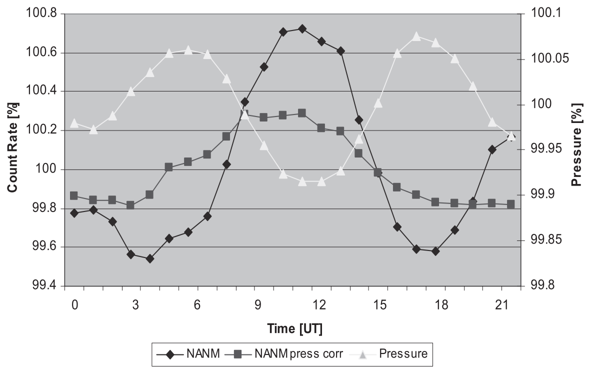

Figure 10. Daily variations of the atmospheric pressure and Nor Amberd Neutron Monitor count rates. Note that correction to the pressure effects improves the shape of the daily count rates

5. CONCLUSION

PHT sensor designed and fabricated in the Yerevan Physics Institute on basis of the pressure sensor Motorola MPXA6115. The device operates and supplies digitized data to the data acquisition systems of the Aragats Space Environmental Center at altitudes 1000, 2000, and 3200 m a.s.l. The accuracy of pressure measurements are not worse than 0.05 Mb, that is fully sufficient for the studies of the solar-terrestrial connections via variations of the secondary fluxes of the elementary particles detected on the Earth's surface. The device is reliable and simple in operation and can be recommended for the world- wide networks of particle detectors.

ACKNOWLEDGEMENT

Author thanks the staff of the ASEC for 24 hours year-around operation of the particle detectors, Babayan Valery for the useful discussions and valuable comments and Mailyan Bagrat for providing data on diurnal variations.

REFERENCES

Balabin Y. V., et al., Mountain-valley circulation effects in cosmic ray intensity. GEO, St. Petersburg 2008

Chilingarian A., Hovsepyan G., Arakelyan K., et al. Space environmental viewing and analysis network (SEVAN). Earth, Moon and Planets, 104, 195, 2009

Chilingarian, A., Arakelyan, K., Avakyan, K. et al. Correlated measurements of secondary cosmic ray fluxes by the Aragats Space-Environmental Center monitors. NIM, A543, 483- 492, 2005

Chilingarian A., Avakyan K., Babayan V. et al., Aragats space-environmental centre: status and SEP forecasting possibilities. J. Phys. G: Nucl. Part. Phys**.** 29, 9–951, 2003

Chilingarian A., Melkumyan L., Hovsepyan G., Reymers A., The response function of the Aragats Solar Neutron Telescope, Nuclear Instruments and Methods in Physics Research A 574, 255-263, 2007

Dorman L.I., Cosmic Ray Variations, Moscow State University Press, p. 54., Moscow, (in Russian), 1975.

Dorman L.I., Cosmic Rays, Variations and Space Exploration. North-Holland, Amsterdam, 1974

Dorman L.I., Rogava O.G., Shotashvili L.Kh., Planetary distribution of cosmic ray neutron component barometric coefficient during IQSY, Geomagnetizm and Aeronomy **8**, 166-167, (in Russian),1968

Malan* D.and Moraal H., The effect of wind on pressure correction of the SANAE neutron monitor counting rate, South African Journal of Science **98**, 2002

Thunderstorm Correlated Enhancements of Cosmic Ray Fluxes Detected at Mt. Aragats

A. Chilingarian, A. Daryan, K. Arakelyan, A. Reymers, L. Melkumyan

Cosmic Ray Division, Alikhanyan Physics Institute, Alikhanyan Brothers 2, Yerevan 375036, Armenia

Abstract: The cosmic rays ionize enough of the atmosphere to be questioned as possible triggers of the thunderstorms. A mechanism proposed by A. Gurevich and his collaborators suggest that showers of energetic particles produced by high-energy cosmic rays in the terrestrial atmosphere might provide a conductive path that initiates lightning. The positive feedback effect can increase the flux of electrons and photons by a factor of trillions, creating a large increase in conductivity that ultimately collapses the ambient electrical field via lightening. The Aragats Space Environment Center (ASEC) facilities allow measurements of the charged particles energy from 10 up to 100 MeV. In May – June 2009 we detect short count rate enhancements of low energy charged secondary cosmic rays. In the same time there were no peaks in time series of high energy muons. We present first attempts to calculate the energy spectra of the detected additional charged particles, connected with thunderstorm activity.

1. INTRODUCTION

A vast theoretical investigation of the processes taking place in thunderclouds was fulfilled by Gurevich et al. (1992).The proposed mechanism suggests that Extensive Air Showers (EAS) of energetic particles produced by high-energy cosmic rays in the terrestrial atmosphere might provide a conductive path initiating lightning. However, the electric fields inside the thunderstorm do not appear to be big enough to initiate a spark, therefore, it was postulated that the thunderstorm gave the cosmic-ray shower a boost by increasing the number of energetic electrons through a multiplication process initially called Runaway Breakdown (RB), and recently referred as Relativistic Runaway Electron Avalanche (RREA, Dwyer, 2007).

RREA mechanism can create large amounts of high-energy electrons, as well as X-rays and gamma rays. Unfortunately, this model has not yet been able to demonstrate creation of the hot plasma channel and lightning itself. A new RREA based model, involving positive feedback from positrons and high energy photons allows the runaway discharge to become self-sustaining and increase exponentially the number of avalanche electrons in very short time scales (Dwyer, 2003, Babich et al., 2005, Lidvanski & Khaerdinov, 2007). This mechanism, which shall be referred to as Relativistic Feedback Breakdown, (RFB, see Figure 1) allows runaway discharges in gases to become self-sustaining, dramatically increasing the flux of runaway electrons, the accompanying high-energy radiation, and resulting ionization. Using detailed Monte Carlo calculations, properties of relativistic feedback are investigated. It is found that once relativistic feedback fully commenced, electrical breakdown will occur and the ambient electric field, extending over cubic kilometers, will be discharged in as little as 2×10^{-5} s. Furthermore, it is found that the flux of energetic electrons and X rays generated by this mechanism can exceed the flux generated by the standard relativistic runaway electron model by a factor of 10^{13}, making relativistic feedback a good candidate for explaining terrestrial gamma-ray flashes and other high-energy phenomena observed in the Earth's atmosphere.

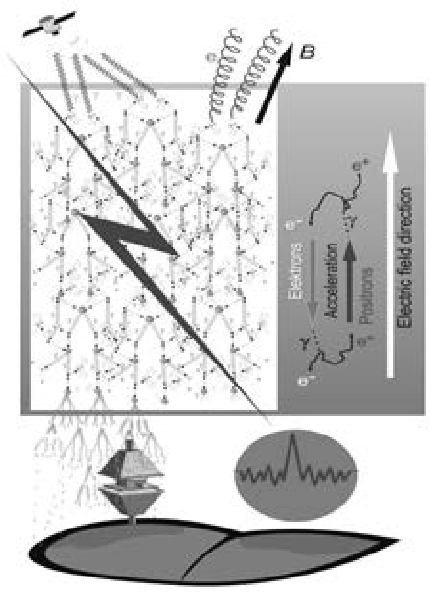

Figure 1. Relativistic Feedback Breakdown (RFB). Positive feedback is provided by the positrons bouncing back via column scattering and accelerating by electrical field and initiated up-going avalanches. The runaway electrons initiate avalanches

The corpus of experimental evidence supporting RREA and RFB models consists in detection of the enhancements of the cosmic ray flux on the Earth surface and Terrestrial Gamma-ray Flashes (TGB) observed by orbiting gamma-ray observatories (we will not discuss thunderstorm connected radio emission in this paper).

In experiments at the Baksan Neutrino Observatory of the Institute for Nuclear Research, Russian Academy of Sciences, the spectrum of cosmic rays are continuously measured along with precise measurements of the electric field and monitoring of thunderstorms (Khaerdinov et al., 2005). Characteristic enhancements of soft cosmic rays (below 30 MeV) and hard cosmic rays (>100 MeV) were studied. The detected enhancements of the soft component of cosmic rays are interpreted as runaway electrons. Events with fast exponential increase of intensity are interpreted as a positive feedback effect for runaway particles (RFB, Lidvanski & Khaerdinov, 2007). It was shown that the critical field and particle energy for this process are ~300 kV/m and ~10 MeV, respectively (Khaerdinov et al., 2005).

A radiation monitoring post in nuclear power plant of Japan reports on a comprehensive observation of a burst-like *gamma*-ray emission from thunderclouds, during strong thunderstorms. The detected emission, lasting for ~40 sec, preceded cloud-to-ground lightning discharges. The burst spectrum, extending to 10 MeV, the authors of (Tsuchiya et al., 2007) interpret as consisting of bremsstrahlung photons originating from relativistic electrons.

Sudden non-thermal gamma-ray emissions from upper atmosphere have been observed at equatorial latitudes by near-Earth satellites (Smith *et al.*, 2005). The spectra of the flashes are roughly expressed by power-law functions; some of them extending up to several tens of MeV. In (Dwyer et al., 2007) these events are interpreted as byproducts of massive number of runaway electrons being generated within or immediately above thunderstorms.

Mentioned experimental evidence leave no doubts that thunderstorms provide powerful accelerator operation in the atmosphere. However, many details of accelerator operations are still unclear due to discrepant random observation.

Planned TARANIS "Tool for the Analysis of Radiations from lightnings and Sprites" satellite project (Lefeurve et. al., 2008) dedicated to the study of impulsive transfers of energy between the Earth atmosphere and the space environment with 6 orbiting instruments will highly improve our understanding of the thunderstorm accelerators. Ground-based observations by a complex of surface particle detectors, measuring in a systematically and repeatable fashion, gamma quanta, electrons, muons and neutrons from atmospheric sources are compatible to space-born observation. Energy spectra and correlations between different particles, measured on the Earth's surface address the important issues of where this radiation and particles come from and what role it plays in thunderstorm and lightning processes. The particle detectors of the Aragats Space Environmental Center (ASEC) measure charged and neutral fluxes of secondary cosmic rays by variety of particle detectors located in Yerevan (1000 m a.s.l.) and on slopes of Mt. Aragats at altitudes 2000 and 3200 m. We present our first attempts to measure particles and radiation in correlation with thunderstorm activity.

2. LOW ENERGY CHARGED PARTICLE CALORIMETER AT ARAGATS

At Aragats Space Environment Center (ASEC, Chilingarian et al., 2003, 2005, Chilingarian &Reymers, 2007)) the Aragats Solar Neutron Telescope (see Figure 2) has been operating since 1997 as a part of the world-wide network of the same type of detectors coordinated by the group from Nagoya University (see details in Chilingarian et al, 2007). In 2006 with the installation of new Data Acquisition electronics (Arakelyan et al., 2009) facility was turned to a precise calorimeter for charged particles with energies up to 120 MeV.

Fluxes of particles with energies from 10 to 120 MeV under angles of incidence from 0 to 40 degree can be monitored with energy resolution not worse than 5 MeV. Histograms of the energy releases are taken and stored each minute providing exact pattern of changing fluxes of 10-120 MeV electrons & muons during solar transient events and also, during thunderstorms that are very often and strong at Aragats, 3200 m above sea level.

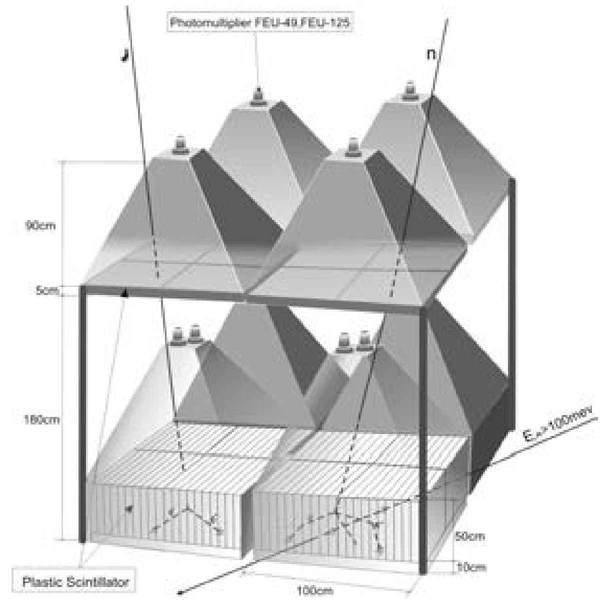

Figure 2. Aragats Solar Neutron Telescope (ASNT)

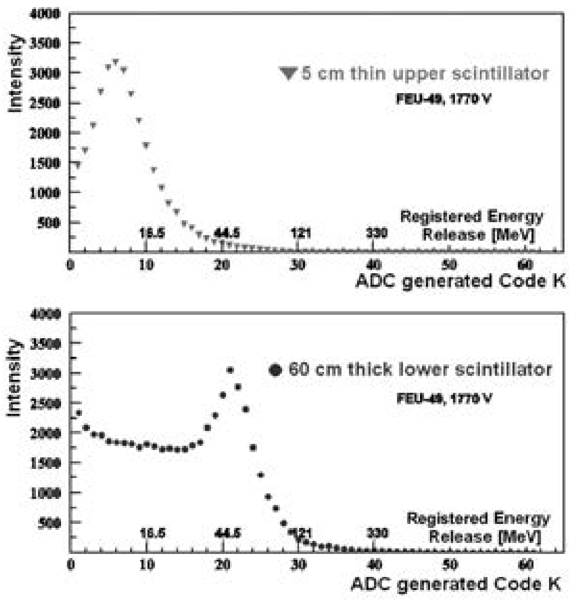

Figure 3. One-minute histograms of energy releases in thick and thick scintillators of ASNT

In Figure 3 are posted the 1-minute histograms of energy releases in 5 and 60 cm scintillators. Examining the histograms, measured and stored each minute, it is possible to determine the energy of particle forming enhancement and finally establish the energy spectrum of the “additional” particles. If a particle has energy less than 120 MeV it will release whole energy in thick scintillator. By integrating within definite codes (energies) we can obtain intensities of particles of different energies with resolution equivalent to one code of ADC. The ADC provides linearity in the code interval of [0<K<~80].

3. SEVAN PARTICLE DETECTORS

A network of particle detectors located at middle to low latitudes, SEVAN (Space Environmental Viewing and Analysis Network, Chilingarian and Reymers, 2008, Chilingarian et al., 2009), aims to improve fundamental research of the particle acceleration in the vicinity of the sun and the space environment. The new type of particle detectors will simultaneously measure changing fluxes of most species of secondary cosmic rays, thus turning into a powerful integrated device used for exploration of solar modulation effects. The first SEVAN modules are operating at the Aragats Space Environmental Center in Armenia, in Croatia and Bulgaria.

The basic detecting unit of the SEVAN network (see 4) is assembled from standard slabs of 50x50x5cm3 plastic scintillators. Between two identical assemblies of 100 x 100 x 5 cm3 scintillators (four standard slabs) are located two 100 x 100 x 5 cm^3 lead absorbers and thick 50 x 50 x 25 cm^3 scintillator assembly (5 standard slabs). A scintillator light capture cone and Photo Multiplier Tube (PMT) are located on the top, bottom and the intermediate layers of detector. The detailed detector charts with all sizes are available from http://aragats.am/SEVAN.

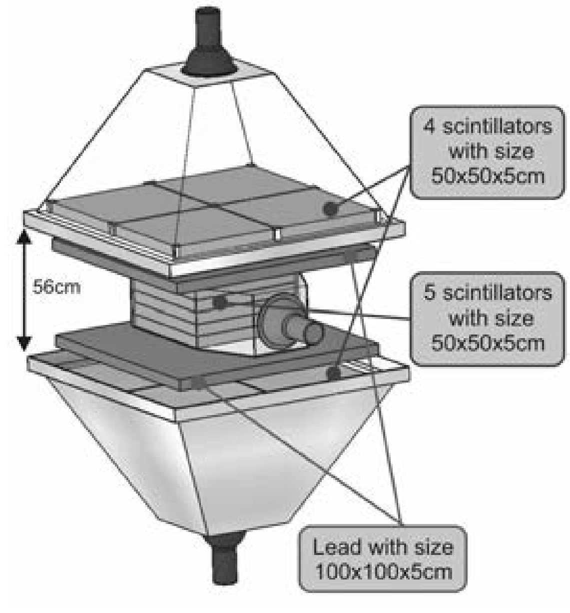

Figure 4. Basic detecting unit of the SEVAN network.

Incoming neutral particles undergo nuclear reactions in the thick 25cm plastic scintillator and produce protons and other charged particles. In the upper 5cm thick scintillator charged particles are registered very effectively; however for the nuclear interactions of neutral particles there is not enough substance. When a neutral particle traverses the top thin (5cm) scintillator, usually no signal is produced. The absence of the signal in the upper scintillators, coinciding with the signal in the middle scintillator, points to neutral particle detection. The coincidence of signals from the top and bottom scintillators indicates the traversal of high energy muons. Lead absorbers improve the efficiency of the neutral flux detection and filtered low energy charged particles. If we denote by “1” the signal from a scintillator and by “0” the absence of a signal, then the following combinations of the 3-layered detector output are possible:

111 and 101 – traversal of high energy muon;

010 – traversal of a neutral particle (gamma quanta or neutron);

100 – traversal of a low energy charged partice stopped in the scintillator or in the first lead absorber (energy less than ~100 MeV).

110 – traversal of a higher energy charged particle stopped in the second lead absorber.

001 – registration of inclined charged particles

Microcontroller-based Data Acquisition (DAQ) electronics and an Advanced Data Analysis System (ADAS) provide registration and storage of all logical combinations of the detector signals for further off-line analysis and for on-line alerts issuing. The slow control system of the ADAS subsystem allows providing the remote control of the PMT high voltage and important parameters of the DAQ electronics.

In the Figure 5 we can see that the neutral particles can be selected with rather high purity, but not very high efficiency. Muons are selected with both high purity and efficiency. Efficiency of electron selection is ~2 times less.

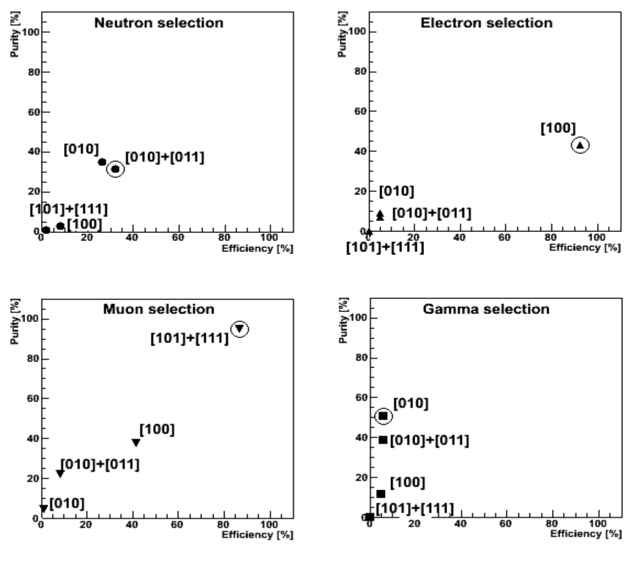

Figure 5. Particle “selection” by SEVAN module. In the circles are combination most appropriate for the selected particle.

4. DETECTION OF THE THUNDERSTORM CORRELATED COSMIC RAY FLUXES

In the time series of the ASEC monitor count rates registered on 3 levels: 1000 m (Yerevan Cosmic Ray Division headquarters), 2000 m (Nor Amberd research station) and 3200 m (Aragats research station) on slopes of Mt. Aragats several count rate enhancements connected with thunderstorm activity were detected. The most significant one was recorded on May 21, 2009 at Aragats research station. The count rate enhancement was observed by all detectors measuring low energy charged particles of secondary cosmic rays (see Figures 3-4). The shape of the enhancement was the same for ASNT and for particle detectors of Aragats Multichannel Muon Monitor (AMMM, low energy particles; detectors on the surface), located on the distance 700 m. from ASNT (see Figures 3 -6). Aragats research station is located on plateau 3200 m. above sea level near large lake. The southern peak (~3700 m hight) is located 4 km far to the north from the station; other 3 peaks of Aragats are located from 10 to 15 km. far.

The thunderstorm activity on Aragats is extremely strong in May-June. Sometimes lightning strokes the ground in the vicinity of the station continuously during an hour and more. In Figures 6 - 12 we present the observation of particle fluxes in correlation with extremely strong thunderstorm on May 21, 2009.

All particle detectors sensitive to the particles with energies greater than 10 MeV register profound enhancements lasting up to 15 minutes.

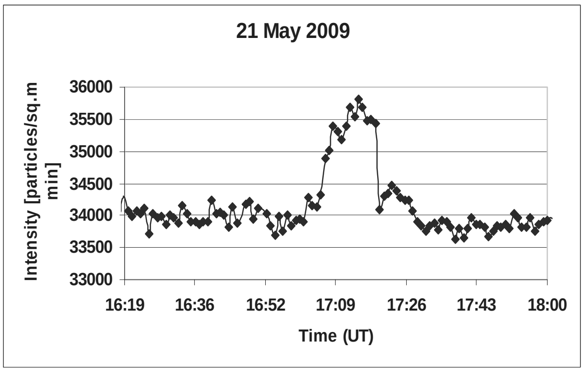

Figure 6. The 1 minute time series of ASNT at 21 May, 2009 (UT)

In Figure 6 the one minute time series measured by the ASNT are posted. Thick scintillators of ASNT give possibility to measure not only count rates, but also energies of the particles with accuracy of energy estimation ~ 1 Mev
at small codes.

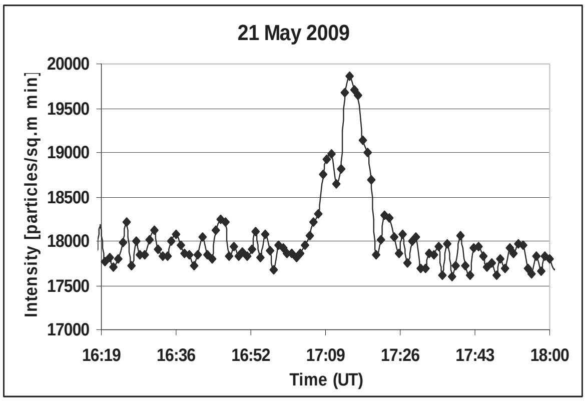

Figure 7. The 1 minute time series of SEVAN surface detector at 21 May, 2009

In Figure 7 the 1 – minute time series of the upper layer of the particle detector of new world-wide network named SEVAN (Chilingarian & Reymers, 2008, Chilingarian et al., 2009) are posted. Each module has 3 layers: the upper and bottom – 5 cm. this 1 m^2 area plastic scintillators; the middle 25 cm. thick 0.25 m^2 area plastic scintillators. Also the detector setup is interlayered by 5 cm. thick lead filters, see Figure 4.

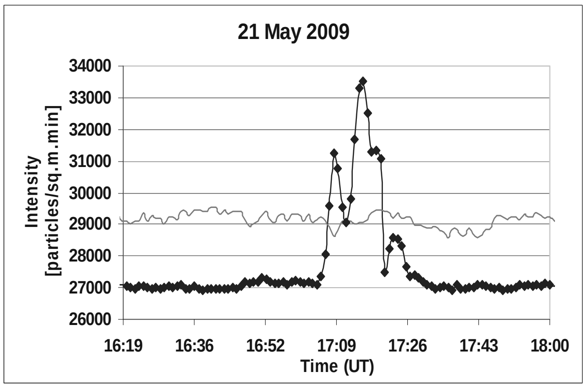

Figure 8. The 1 minute time series of AMMM surface detectors at 21 May, 2009; black line - low energy charged particles; grey - >5 GeV muons.

In Figure 8 we demonstrate 1 minute time series of the scintillators of surface array GAMMA, operating at Aragats (see details in Chilingarian et al., 2005). The black line – is the estimate of 1-minute intensity measured by 20 m^2 scintillators located on surface under 5 mm steel and 2 mm aluminum. The grey line corresponds to 90 m^2 area scintillators located at the underground hall under 14 meters of concrete and soil. The minimal energy of muons reaching detector is 5 GeV. Unfortunately, we did not have the electrical field meter, therefore we cannot correlate count rate enhancements with electrical field discharges. However, the world-wide lightning location network (WWLLN, http://webflash.ess.washington.edu/, Ramachandran et al, 2007) registered several lightings in the vicinity of Aragats precisely coinciding with the pattern of the particle flux enhancement, see Table 1.

Table 1 Detection of the Aragts lightings by WWLLN network

Date	Hour: minute	Latitude	Longitude	N of WWLLN stations
2009/05/21	17:07	40.9662	44.3817	5
2009/05/21	17:11	40.9210	44.4436	6
2009/05/21	17:20	41.0354	44.3013	5
2009/05/21	17:20	41.0236	44.5158	5

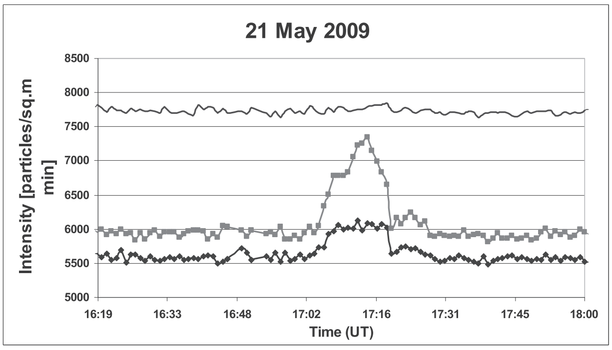

Figure 10. ASNT channels: 6-10 MeV (grey), 10-16 MeV (black), >30 MeV – black upper line

In Figure 9 we can see that the whole enhancement can be attributed to low energy particles; high energy particles do not demonstrate any enhancement.

In Figure 10 we present the energy spectra of enhancement fitted rather well by the exponential function. From the Figure we can see that at 30 MeV the particle flux is almost faded in agreement with expectations of RFB model (Dwyer, 2007) and Results of Baksan group (Lidvansky & Khaerdinov, 2007).

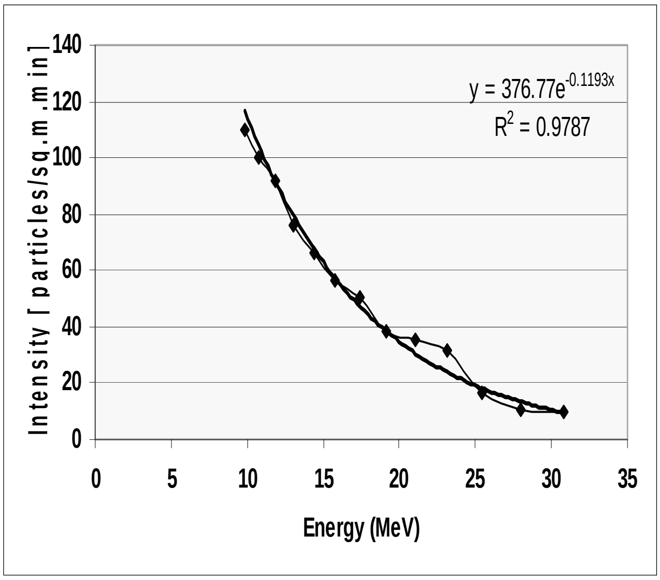

Figure 12 .Energy spectrum of the "additional" particles

In Figure 11 and 12 we use enhanced possibilities of the SEVAN detectors to select different species of secondary cosmic rays (see also Figure 5). Figure 11 compare fluxes of low energy charged particles (combination 100, energy threshold ~10 MeV) and high energy muons (combinations 111 and 101, minimal energy ~ 250 MeV). We want to point on the very stable maximal flux of electrons lasting 4 minutes (15% enhancement).

In Figure 12 we demonstrate that the enhancement in SEVAN module is due to gamma-quanta from electron-photon avalanche initiated by runaway electrons. Located in a few meters form SEVAN, Aragats neutron monitor did not demonstrate significant enhancement of count rate.

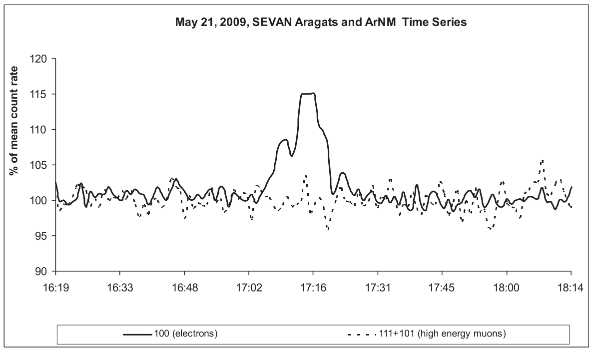

Figure 9. Comparison of low energy and high energy fluxes during thunderstorm activity

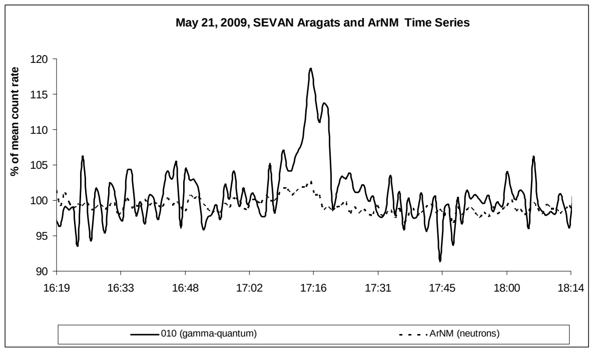

Figure 11. Comparison of neutron fluxes, measured by Aragats neutron monitor and neutral particles measured by nearby SEVAN module.

5. CONCLUSION

ASEC particle detectors have advanced possibilities to detect thunderstorm-cosmic ray correlations. The observations of ASEC monitors can me summaries as following:

- Detection simultaneously high energy gamma-quanta and electrons, proving existence of the electron photon cascade process in the atmosphere developing in the Earth direction;
- Detection of very long lasting additional particle flux, provided by chain cascade process;
- Measurement of the energy spectra of the additional particles;

We can conclude that positive feedback keeps the acceleration process for ~ 15 minutes despite discharge by lightening.

REFERENCES

Arakelyan K., Abovyan S.,Avetisyan A., et al., New electronics for the Aragats Space Environmental Center (ASEC) particle detectors, JASR, in press, 2009

Babich L.P., Donskoy E.N., Kutsyk I.M. The feedback mechanizm of runaway air breakdown, Geophys. Res. Let., 32, L09809, 2005

Chilingarian A.A., Avagyan K., Babayan V. et al. Aragats Space-Environmental Center: status and SEP forecasting possibilities. J.Phys. G:Nucl.Part.Phys. 29, pp. 939-952, 2003

Chilingarian A.A., Arakelyan K., Avagyan K., et al. Correlated measurements of secondary cosmic ray fluxes by the Aragats Space Environmental Center monitors. NIM, A543, pp. 483-496, 2005

Chilingarian A, Melkumyan L., Hovsepyan G., Reymers A., The response function of the Aragats Solar Neutron Telescope, Nuclear Instruments and Methods in Physics Research, A 574, (255-263), 2007

Chilingarian A. and Reymers A. Particle detectors in Solar Physics and Space Weather Research, Astropart. Phys., 27, pp. 465-472, 2007

Chilingarian A. and Reymers A. Investigations of the response of hybrid particle detectors for the Space Environmental Viewing and Analysis Network (SEVAN), Ann. Geophys., 26, pp. 249-257, 2008

Chilingarian A., Hovsepyan G., Arakelyan K., et al., Space environmental viewing and analysis network (SEVAN). Earth, Moon, and Planets, v.104, p. 195, 2009.

Dwyer J.R., Relativistic breakdown in planetary atmospheres, Physics of plazmas, 14, 042901, 2007.

Dwyer J.R., Grefenstette B.W., Smith D.M., High Energy electron beams launched into space by thunderstorms Geophys. Res. Letters, 35, L02815, 2007

Dwyer J.R. Geophys. Res. Letters, 30, 2055, 2003

Enoto T., and Tsuchiya H., PRL, 2007

Gurevich A.V., Milikh G.M., and Roussel-Dupre R., Phys. Lett. A, 165, 463, 1992

Gurevich A. and Zibin K. Runaway breakdown and electrical discharge in thunderstorms, Success in Physical Science 171, N 11, 1178 – 1199, 2001, in Russian

Lefeuvre F., Blanc E., Pincon J-L., et al., TARANIS—A Satellite Project Dedicated to the Physics of TLEs and TGFs, Space Sci Rev 137: 301–315, 2008

Lidvansky A.S, Khaerdinov N.S, Dynamics of Cosmic Rays in the electrical field of atmosphere and generation of particles in thunderstorms, Proc. Of Russiaon Academy of Science, physics series, 71, 1060-1062, 2007

Ramachandran, Prakash J. N., Deo A., and Kumar S. Lightning stroke distance estimation from single station observation and validation with WWLLN data Ann. Geophys., 25, 1509–1517, 2007

Khaerdinov N.S., Lidvansky A.S., and Petkov V.B., Cosmic Rays and Electric Field of Thunderclouds: Evidence for Acceleration of Particles (Runaway Electrons). Atmospheric Research, 76, pp. 346-354, 2005

Smith D. M. *et al.*, Science 307, 1085, 2005

Calculation of Mean Multiplicity Coefficients for ASEC Neutron Monitors

A. Hovhannisyan

Cosmic Ray Division, Alikhanyan Physics Institute, Alikhanyan Brothers 2, Yerevan 375036, Armenia
(e-mail: harmen@yerphi.am:)

1. INTRODUCTION

Network of particle detectors – neutron monitors located at different latitudes and longitudes operates as an integrating device measuring solar modulation effects. Among these effects, the so called ground level enhancements are of upmost interest. Some times (not more often than once a year), the beam of accelerated particles (Solar Cosmic Rays – SCR) from the sun is so intense and energetic that it can penetrate the magnetosphere and born copious secondary particles in interactions with atmospheric nucleolus. These secondary particles overcoming series of interactions reach mountain altitudes and are registered by particle detectors. Surface monitors "see" solar particles as an addition to the "background" count rates, i.e., flux of secondary particles initiated by the rather stable Galactic Cosmic Rays (GCR) incident on the terrestrial atmosphere. By statistical analysis of detected enhancements in time series of the count rates it is possible to isolate the contribution of the SCR and calculate the flux of secondary particles (neutrons, muons and electrons) above the detector. In this way solar flare/cme acceleration of nucleons over the energy range 1->20 GeV per nucleon can be investigated at any time (Simpson, 2000). This is far beyond the range of spacecraft facilities.

To "reconstruct" the primary flux above the atmosphere we need to make simulations of the particle traversal through the atmosphere.

After finding the "coupling functions" of the primary and secondary fluxes it is possible to determine the energy spectrum of the SCR

It is very important and interesting problem shedding light on the operation of the solar accelerators and most energetic processes in solar system – the solar flares.

Therefore it is necessary to measure the initial physical parameters – the fluxes of the secondary particles above the detector with good accuracy. Otherwise the errors will be multiplied during procedures of the primary flux reconstruction leading to the uncontrolled errors. In this work our aim is to calculate one of important parameters of the Neutron Monitor, namely the mean multiplicity coefficients.

At the Aragats Space Environmental Center (ASEC, Chilingarian et al., 2005) 2 Neutron Monitors operate (Nor Amberd Neutron Monitor – NANM at altitude 2000 m, and Aragats Neutron Monitor - ANM at altitude 3200). Both monitors are of type 18NM64, i.e. each NM consists of 18 channels, located below 5 cm of lead (producer) and 10 cm of polyethylene (moderator), see Figure 1. Secondary protons and neutrons in nuclear reactions in lead born numerous "evaporation" neutrons of smaller energies, which loss energy in polyethylene (thermalised) and enter in gaseous boron filled (enriched with 10-boron isotope 10BF3) proportional counter.

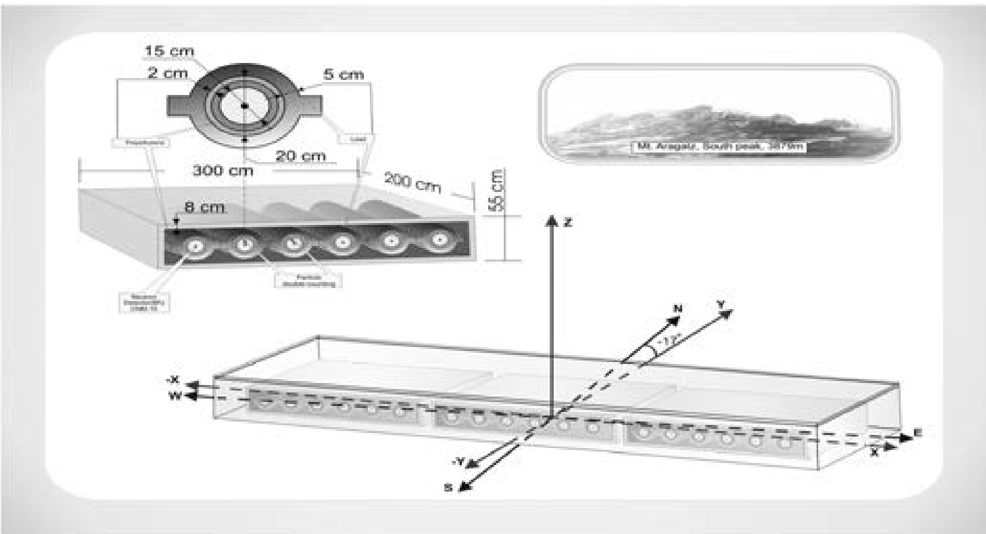

Figure 1. Aragats Neutron Monitor 18NM64, consisting of 3 separate sections 6 proportional chambers in each

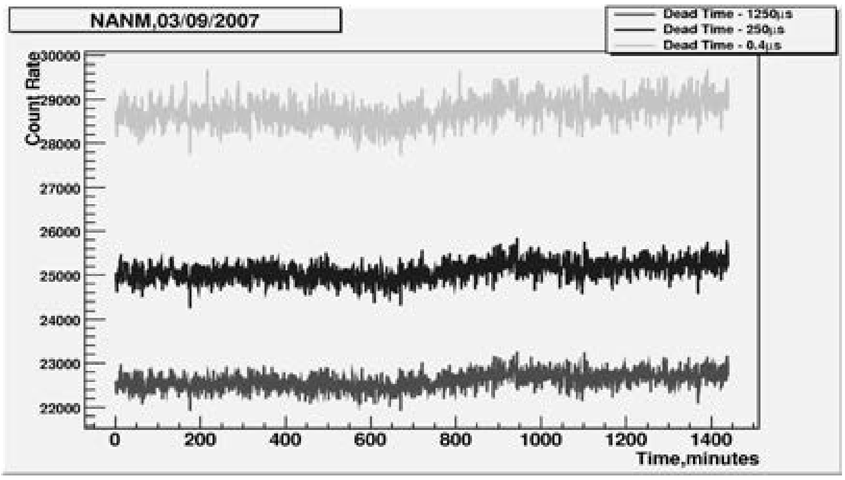

Figure 2. Time series of Nor-Amberd Neutron Monitor, Different Dead-Times

Table 1. NANM, Dead Time-1250mus, Correlation Matrix (%)

Det	1	2	3	4	5	6	7	8	9	10	11	12	13	14	15	16	17	18
1	100	15	4	3	3	5	1	-2	0	4	4	-1	-2	8	-1	2	3	1
2	15	100	14	4	4	-1	-1	0	2	3	3	1	1	3	0	5	3	2
3	4	14	100	12	5	3	1	2	3	2	0	6	2	1	-1	3	5	3
4	3	4	12	100	14	2	2	2	2	0	3	2	3	0	-2	2	2	4
5	3	4	5	14	100	16	4	3	5	0	6	2	7	1	6	6	6	2
6	5	-1	3	2	16	100	5	1	3	-1	2	1	2	3	8	3	1	4
7	1	-1	1	2	4	5	100	14	2	-1	-2	2	0	1	-2	0	0	0
8	-2	0	2	2	3	1	14	100	15	2	4	-1	3	2	-3	1	1	-1
9	0	2	3	2	5	3	2	15	100	18	6	5	-2	0	5	5	-3	0
10	4	3	2	0	0	-1	-1	2	18	100	16	4	1	2	3	3	2	-1
11	4	3	0	3	6	2	-2	4	6	16	100	17	6	3	3	3	2	4
12	-1	1	6	2	2	1	2	-1	5	4	17	100	3	0	1	-2	0	-1
13	-2	1	2	3	7	2	0	3	-2	1	6	3	100	17	5	3	-1	3
14	8	3	1	0	1	3	1	2	0	2	3	0	17	100	11	6	0	1
15	-1	0	-1	-2	6	8	-2	-3	5	3	3	1	5	11	100	12	5	5
16	2	5	3	2	6	3	0	1	5	3	3	-2	3	6	12	100	15	3
17	3	3	5	2	6	1	0	1	-3	2	2	0	-1	0	5	15	100	15
18	1	2	3	4	2	4	0	-1	0	-1	4	-1	3	1	5	3	15	100

Table 2. ARNM, Dead Time-1250mus, Correlation Matrix (%)

Det	1	2	3	4	5	6	7	8	9	10	11	12	13	14	15	16	17	18
1	100	14	2	-1	-4	5	0	-5	-4	-1	-3	2	4	2	1	3	3	-4
2	14	100	12	3	2	-1	0	-1	-4	-4	-4	-1	4	0	-1	1	2	4
3	2	12	100	10	5	-3	0	5	1	-1	-1	0	-2	1	-6	-2	-2	2
4	-1	3	10	100	10	7	5	9	0	-1	-2	0	-2	2	-4	-1	0	-2
5	-4	2	5	10	100	16	3	0	3	-1	-5	-1	1	-2	1	1	2	4
6	5	-1	-3	7	16	100	6	-1	1	-3	-1	6	-1	1	4	-1	0	2
7	0	0	0	5	3	6	100	15	10	1	3	-3	3	-5	2	-1	1	4
8	-5	-1	5	9	0	-1	15	100	19	6	1	1	-2	1	1	-1	-1	4
9	-4	-4	1	0	3	1	10	19	100	38	7	3	-1	-7	0	1	2	0
10	-1	-4	-1	-1	-1	-3	1	6	38	100	11	1	3	1	1	-2	2	0
11	-3	-4	-1	-2	-5	-1	3	1	7	11	100	15	3	-4	0	-1	0	0
12	2	-1	0	0	-1	6	-3	1	3	1	15	100	5	3	4	-2	0	-1
13	4	4	-2	-2	1	-1	3	-2	-1	3	3	5	100	12	8	1	6	1
14	2	0	1	2	-2	1	-5	1	-7	1	-4	3	12	100	12	5	3	-6
15	1	-1	-6	-4	1	4	2	1	0	1	0	4	8	12	100	11	3	1
16	3	1	-2	-1	1	-1	-1	-1	1	-2	-1	-2	1	5	11	100	19	7
17	3	2	-2	0	2	0	1	-1	2	2	0	0	6	3	3	19	100	16
18	-4	4	2	-2	4	2	4	4	0	0	0	-1	1	-6	1	7	16	100

Only a small percentage of the born in lead “evaporation“ neutrons 5.7% (Stocker et al., 2000) are absorbed by ^{10}B isotope, generating alpha-particle detected in proportional counter. The monitors are equipped with new electronics (Arakelyan et al, 2008) providing precise resolution of the proportional chamber output signal and, therefore, very short dead time of detector – 0.4 μs. For being comparable with world-wide network of neutron monitors we also measure time series with usually used dead-times of 250 and 1250 μs (see Figure 2). The first dead time of 0.4 μs collects almost all secondary neutrons reaching volume of the chamber and producing α-particle. The second and third dead times are miscounted additional neutrons which enters sensitive volume of proportional chamber after registering the first neutron. I.e. they the third, greatest, dead time registers only one signal to each hadron entering lead absorber, because the live-time of thermalized neutrons in neutron monitor is not greater that ~ 1millisecond.

Having these different time series, one, collected all neutrons entering proportional chamber and one - registering only one signal and suppressing detection of additional termalized neutrons entering sensitive volume of proportional chamber, we can calculate the mean multiplicity coefficient (Dorman, 2004) of neutrons in section of the Neutron Monitor:

$$\bar{m} = \frac{\sum_{m=1}^{M} mN_m}{\sum_{m=1}^{M} N_m}$$

Where m is multiplicity; N_m – number of events with multiplicity m and M is large number (proxy of infinity).

First assumption is that highest dead time is registering only one neutron in response to hadron falling on NM. (because the live time of thermalized neutrons we assume is ~ 1 millisecond).

Second assumption is that the shortest dead time is counted all termilized neutrons, entering the proportional chamber (all multiplicities till M).

Therefore, we can estimate the number of additional neutrons as difference of mean count rates corresponding to these dead times and the mean multiplicity coefficient will be ration of count rates corresponding to minimal and maximal dead times.

However, from Figure 1 we can see that a small amount of primary particles fallen on the border between 2 proportional chamber can be registered by both tubes, despite of any dead time. Therefore, a portion of neutrons can be registered in neighboring chamber and for calculation of the mean multiplicity coefficient we should take into account also these additional neutrons. Manifestation of these “neighboring” neutrons is significant inter-tube correlations apparent from the Table 1 and 2. Note that correlations between other counters are negligible. Therefore these additional “neighboring” events should be extracted from the count rate of Neutron Monitor section.

To understand how the correlations are related to the proportion of genetically connected events detected in 2 proportional chambers we develop a model of experimental situation.

Median Filtering Algorithms for Multichannel Detectors

A. Chilingarian, A. Hovhannisyan

Cosmic Ray Division, Alikhanyan Physics Institute, Alikhanyan Brothers 2, Yerevan 375036, Armenia
(e-mail:harmen@yerphi.am)

Abstract: Particle detectors of worldwide networks continuously measure various secondary particle fluxes incident on the Earth surface. At the Aragats Space Environmental Center (ASEC), 12 particle detectors with ~280 measuring channels, each minute send data on count rates of electrons, muons and neutrons via wireless bridges. These time series are used for the different tasks of off-line physical analysis and for online forewarning services. Usually long time series contain several types of errors (gaps due to failures of high or low voltage power supply, spurious spikes due to radio interferences, abrupt changes of mean values of several channels or/and slowly trends in mean values due to ageing of electronics components, etc). To avoid erroneous physical inference and false alarms of alerting systems we introduce offline and online filters to "purify" multiple time-series. In the presented paper we classify possible mistakes in time series and introduce median filtering algorithms for on-line and off-line "purification" of multiple time-series.

1. INTRODUCTION

The networks of the ground-based particle detectors measure time series of secondary particles born in the interactions of primary ions and solar neutrons in the terrestrial atmosphere. Galactic Cosmic Rays (GCR), mostly protons and heavier fully stripped nuclei), are accelerated in our Galaxy by shock waves originated in supernova explosions and by other exotic stellar sources. After traveling millions of years in our Galaxy, GCR arrive in the solar system as highly isotropic and stable flux. On the other hand, our Sun is a variable object changing intensity of radiation and particle fluxes several orders of magnitude within a few minutes. Because of the Sun's closeness these effects have a major influence on the Earth, including climate, safety and other issues.

The influence of the Sun on the GCR flux can be described as a modulation of the usually stable "background". The Sun modulates GCR in several ways. The explosive flaring processes on the Sun result in the ejection of huge amounts of solar plasma and in the acceleration of the copious electrons and ions. These particles comprise, so called, Solar Cosmic Rays (SCR). The SCR reach the Earth and initiate secondary elementary particles in the terrestrial atmosphere, increasing the count rates of particle monitors by several percents. This effect is called Ground Level Enhancement (GLE). The solar wind "blows out" the lowest energy GCR from the solar system, thus changing the GCR flux intensity inverse proportionally to the Sun activity. Huge magnetized plasma clouds and shocks initiated by the Coronal Mass Ejections (CME) travel in the interplanetary space tens of hours before reaching the Earth changing intensity and direction of the GCRs. On arrival at the Earth the magnetic field of the plasma cloud deplete the GCRs, measured as decrease in the count rates of the secondary cosmic particles (so called Forbush decrease).

Hybrid particle monitors at Aragats Space Environmental Center (ASEC, Chilingarian et al., 2003, 2005) measure both charged and neutral components of secondary cosmic rays; ASEC data provides good coverage of the violent Solar Energetic Particle (SEP) events of the 23rd cycle. The multivariate correlation techniques applied upon detected fluxes of charged and neutral particles are used for the study of geo-effective events, i.e. GLEs, Forbush decreases, Geomagnetic Storms; and for reconstruction of the energy spectra of SCR (Chilingarian & Reymers, 2007).

The particle monitors are located in the two research stations on the slopes of Aragats Mountain at altitudes 2000 and 3200 meters above sea level and are connected with the data analysis center in Yerevan by means of a radio networks. Additionally, there is an ongoing process of establishing a world-wide network of detectors called SEVAN operating at different latitudes, longitudes and altitudes (Chilingarian and et al., 2008).

During the 23rd solar activity cycle (1997-2008) the old type DAQ electronics used in ASEC had often malfunctioned and there were many errors in the time series (see Figure 1).

For the physical analysis we need to "purify" (correct, filter, smooth) the raw data. Filtering algorithms are usually based on the comparisons of data from identical measuring channels. Particle detectors of the world-wide network of Neutron Monitors (Clem & Dorman et al., 2000) usually consist of 3 sections, 6 identical proportional counters in each. If the ratio of count rates of different sections is changing within defined limits, the detector overall count rate is performed by simple summon of all sections. If ratio of one of sections is out of limits for the both other sections, the defected section is excluded from summation and the NM overall count rate is properly normalized. The same ideology can be applied for the counters within one section. However, this approach has several disadvantages. It is not fully automated, control parameters should be currently tuned, and algorithm did not correct abrupt jumps (Belov et al., 1988).

The algorithms based on median filtering are currently widely used in pattern recognition and smoothing in multimedia technologies and scientific applications. For instance, to maximize data output from single-shot astronomical images, the rejection of the cosmic ray background is important. Median algorithms are successfully used for these purposes (see Farage et al., 2005).

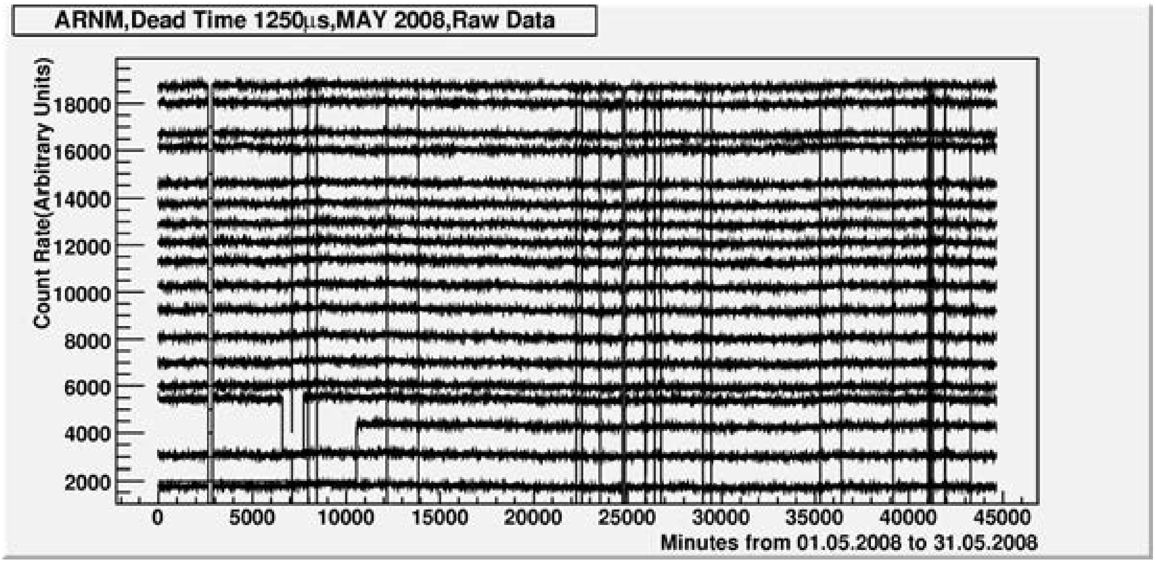

Figure 1. Aragats Neutron Monitor Data; totally 22 days; the time series are artificially shifter from each other; time is measured in

This paper consists of the following sections.

1. Classification of particle detector failures.
2. The description of "horizontal" median algorithm.
3. The description of "vertical" median algorithm.
4. The verification of the method and implementation of it to Nor-Amberd Neutron Monitor's data obtained during 23-rd solar cycle.
5. Monitoring of stability of measuring channels.

The advantages of the proposed method are

1. The algorithms are simple and do not need much computer resources for their realization.
2. They correct abrupt change of means of measuring channels as well as the spurious spikes.
3. Using obtained coefficients described in 3-rd section we can monitor the stability of measuring channels and reveal the even slow drifts of the channel-means.
4. The algorithms can be used not only for offline, but also for online data filtering.

2. TYPES OF PARTICLE DETECTOR FAILURES ENCOUNTER DURING COSMIC RAY FLUX MULTIYEAR MONITORING

Mainly there are 4 kinds of errors, as shown in Figures 2-5 and different combinations of these types.

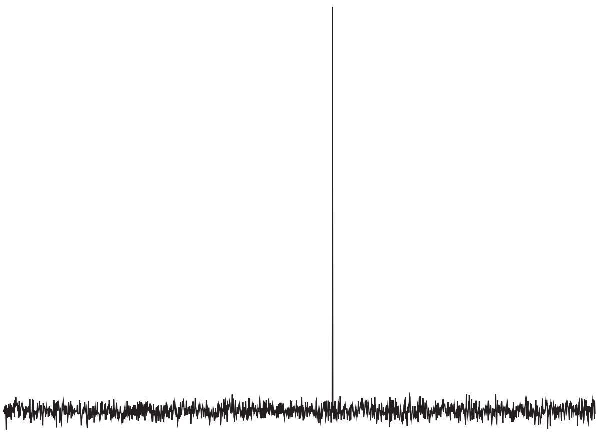

Figure 2. Abrupt Spike (jump)

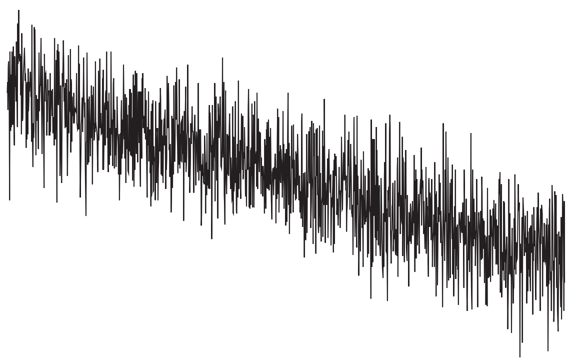

Figure 3. Slow Drift

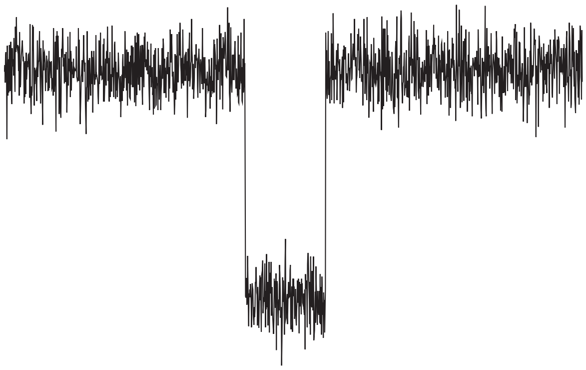

Figure 4. Abrupt change of mean continued with recovery

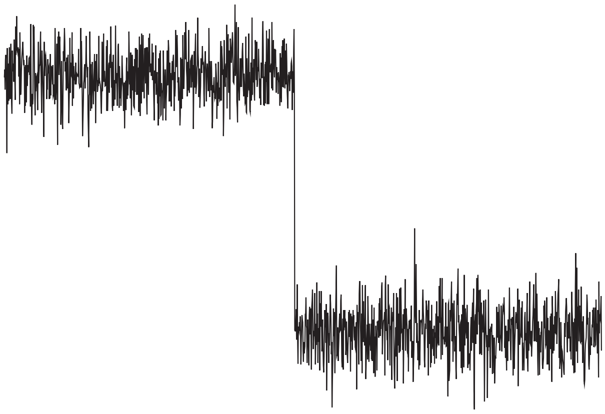

Figure 5. Abrupt change of mean without recovery

Mentioned errors in particle detector's operation can lead to erroneous estimation of the Fd magnitude; prevent detection of the GLE, (usually not very large at middle latitudes - 1.5-2%), etc. We introduce algorithms based on the stabilizing properties of the median for correction of multichannel detector's data. We heavily use the "overabundance" of ASEC data due to numerous identical channels measuring one and the same physical quantity (flux of particles of definite type).

3. MOVING MEDIAN FILTER (MMF) – "HORIZONTAL" MEDIAN.

Window of size L is "moving" from beginning to the end of time series with unit step; the median of L values falling within window is continuously calculated. If difference of the current time series and median is too large several actions are triggered:

a) *the outlier can be substituted by the median value;*
b) *the outlier can be substituted by the special code;*
c) *execution of program stops and an request to operator is send.*

Also MMF performs time series smoothing:

d) *All time series are substituted by the corresponding moving median values.*

If number of outliers exceed pre-chosen limit another filtering algorithm described in the next section is invoked.

Algorithm Description:

Notion:

- Time series of detector channel at moment i is denoted by small letter v_i; median of the L successive elements of time series started at i is denoted by $M_{i,L}$;
- Moving window width – L;
- Minimal and Maximal values of the window width – L_{min} and L_{max}; $L_{min} < L_{max}$;
- Maximal and minimal possible value of time series median – P_{max}, P_{min};
- Maximal possible deviation of time series from median value D_{max}.

In Figure 6 the schematic chart of MMF is presented.

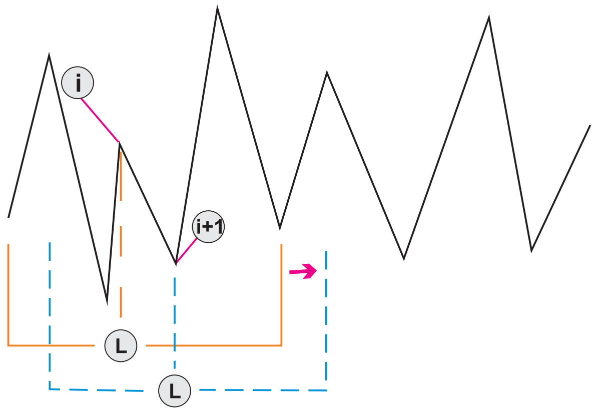

Figure 6. Schematic view of the "horizontal" window "moving" across time series.

Algorithm steps:

1. Select time series from database with N elements;
2. Start algorithm operation from the first of time series, assign i = 0;
3. Define $L = L_{min}$; if $i < N$, then assign $i = i+1$ and continue;
   otherwise write filtered time series into data base; calculate length of periods when algorithm substitute the time series by the median value, send to operator all messages and stop.
4. Select L-1 elements of time series to the right; calculate the median value $M_{i,L}$;
   if its value is in the limit of the predetermined values $M_{i,L}$ ε $(P_{min} – P_{max})$ then continue;
   otherwise, check if $L < L_{max}$ enlarge L by 2 and repeat steps 3,4;
   otherwise report about algorithm failure at point i and store algorithm parameters for i_{th} time series: (i, V_i, L_{max}); then go to 3
5. Check if $abs(V_i – M_{i,L}) < D_{max}$ then continue;
   Otherwise, report erroneous i-th time series, store algorithm parameters (i, v_i, $M_{i,L}$)
   and assign $v_i = M_{i,L}$ then go to 3

We describe algorithm operation for the option a), options b,c,d can be readily obtained by the minor changes of the described algorithm.

This filter is optimal for the time series containing spurious short spikes and abrupt changes of mean followed by recovery (Figures 2 and 4). It cannot correct smooth trends due to slowly changing parameters of particle detectors due to altering of Photomultiplier (PM) or/and electronics elements of Amplitude-to-Digital-Converter (ADC) and power supply (Figures 3, 5). Using MMF we can smooth time series, and get rid of short spikes, but it can't solve the problem when time series mean is changing gradually during large time span; another algorithm should be used to correct such defects using the data of other channels of the same monitor.

4. RELATIONAL MEDIAN FILTER FOR MULTICHANNEL MEASUREMENTS (RMF); "VERTICAL MEDIAN".

Let's suppose that detector consists of M identical channels, however due to individual characteristics of sensors used (photomultipliers, proportional counters, etc…) the mean count rates of channels $\overline{n}_j$, j=1, M are dispersed within definite (not very large) limits.

Notion:

- M – number of channels of the monitor;
- $\overline{n}_j$ - mean count rate of j-th channel;
- N_{total} – sum of mean values of all channels (detector mean count rate);
- med_i = $med\{F_i v_i^j\}_{j=1,M}$ – Median value of M channels at i-th minute; [1]
- F_j- the equalizing coefficient of j-th channel;
- v_i^j- i-th time series of j-th channel; $\mathbf{V}_i$ – estimate of the total detector count rate at moment i.

At the start of detector operation by assigning to each channel the appropriate coefficient F_j ; j=1, M it is possible to equalize the mean count rates:

$$F_j = \left(\frac{\overline{n}_j * M}{N_{total}} \right)^{-1}, \ j = 1, M \qquad (1)$$

Only after this "equalizing" operation, it is valid to calculate the median. The detector count rate at moment i can be calculated according to:

$$V_i = M \bullet med_i \qquad (2)$$

The median estimate of count rate is much more stable in the presence of outliers (bad channels) though its variance is greater comparing with mean value in absence of outliers.

Also if jth channel of detector is continuously and incoherently changing (operating unstable according to reports of MMF) its time series can be substituted by the median value:

$$v_i^j = med_i / F_j ; \ (3)$$

The possible scenario of implementation of both algorithms can be as follows:

1. For some initial period of detector operation possibly without any errors the mean count rates $\overline{n}_j$ and coefficients F_j are calculated and stored.
2. At the end of the day the data of all channels of detector are filtered with MMF algorithm;
3. If some channels operate unstable according to reports of the first algorithm RMF turns on, it reads the stored means and coefficients and corrects the malfunctioned channel data.
4. Channel means and appropriate coefficients are renewed and stored.
5. If second algorithm did not correct the data (which means that all or nearly all channels have been corrupted or detector was switched off due to some overall failure) system sends an e-mail to manager.

5. By automatically implementing both filtering algorithms each day and storing renewed mean values of channels and appropriate coefficients it is possible to correct all mentioned failures (demonstrated in Figures 2-5). The time history of the equalizing coefficients will help to outline non-stable channels and repair them. Below we demonstrate some examples of filtering by these algorithms.

In Figure 7 we present the corrected data of Aragats Neutron Monitor in May 2008 (see Figure 1 for raw data). Time series in the Figure are artificially shifted from each other for better assessment. The combination of MMF and RMF corrects data, eliminating spikes and filling corrupted periods. The Data in all graphs shown here has been smoothed by constant window L=60. The data of Nor-Amberd Neutron Monitor during 23rd solar cycle was smoothed by changing width of the window started from L=60 to Lmax=600 (if needed).

In Figure 8 the atmospheric pressure measurements performed at Nor- Amberd in 1997 are depicted. Using MMF algorithm it is easy to remove the spikes (due to failures of the pressure sensor) from that data, see Figure 9. The MMF algorithm only was used for correcting data.

- [1] This median is different from median used by MMF algorithm. MMF median "moves" along the time series therefore we name it "horizontal" median. Median used by RMF applied to different time series at the same minute. Because usually for display purposes different time series are stacked vertically (see figures 1,7) we name this median – "vertical".

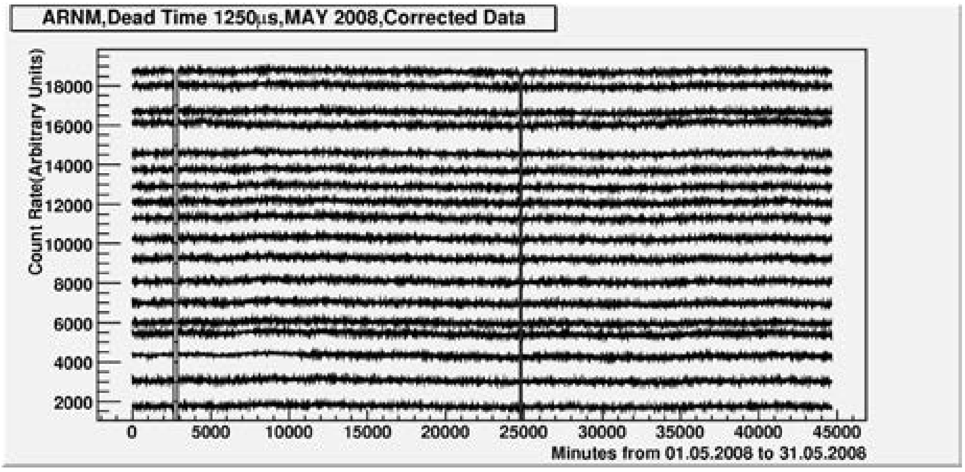

Figure 7. Aragats Neutron Monitor, MAY 2008 – after filtering

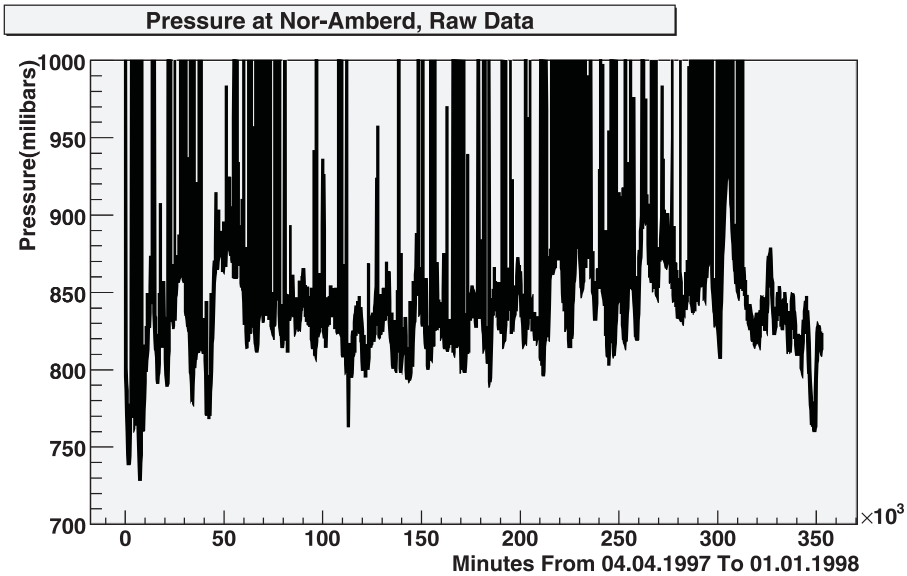

Figure 8. The pressure sensor time series at Nor-Amberd Station, before filtering

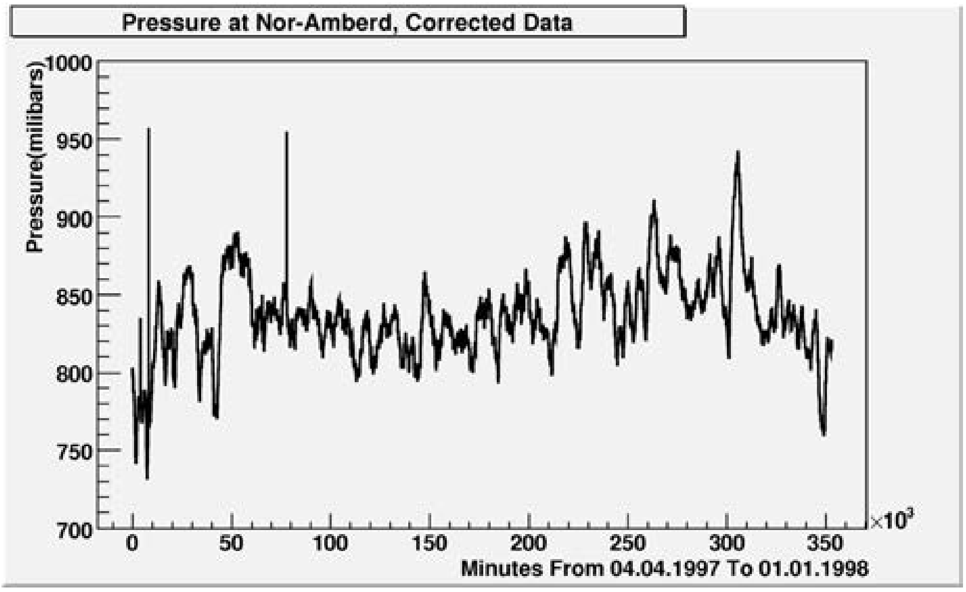

Figure 9. Pressure at Nor-Amberd Station, after filtering

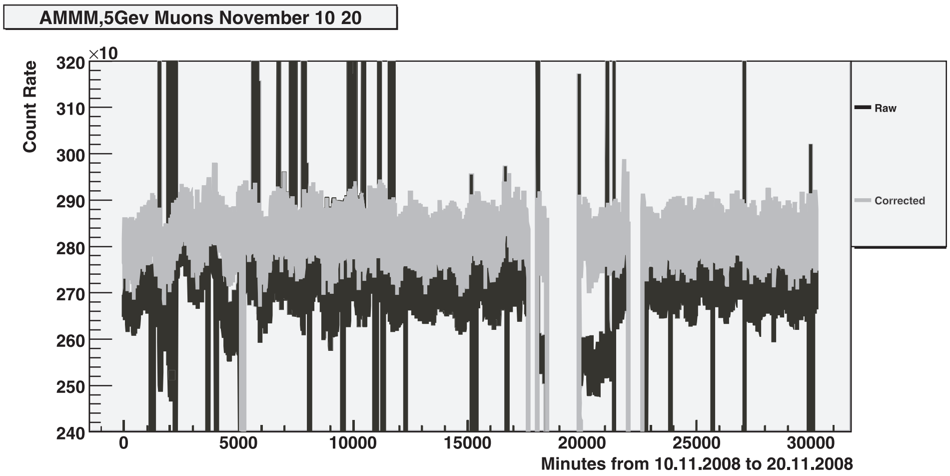

Figure 10. Correction of the AMMM time series, >5 Gev Muons

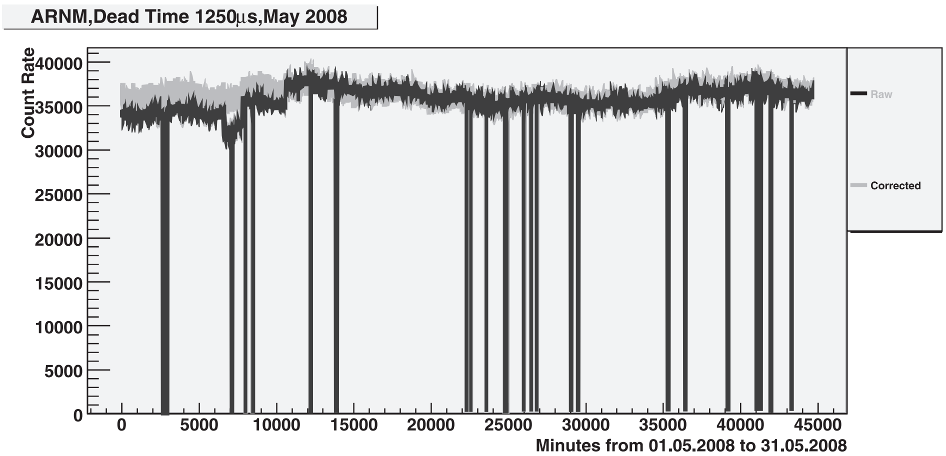

Figure 11. Correction of the ARNM time series

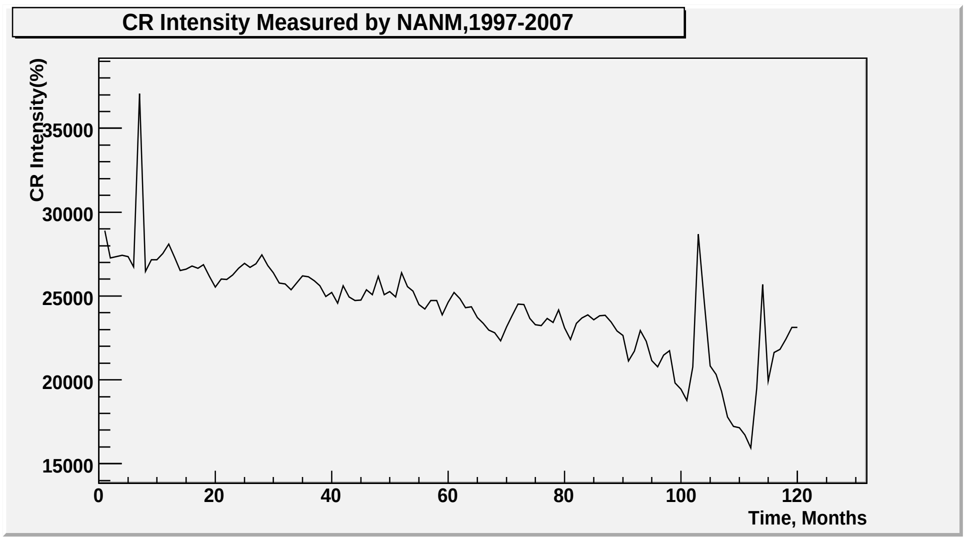

Figure 12. Cosmic Ray intensity modulation by NANM, 23rd solar cycle – before filtering

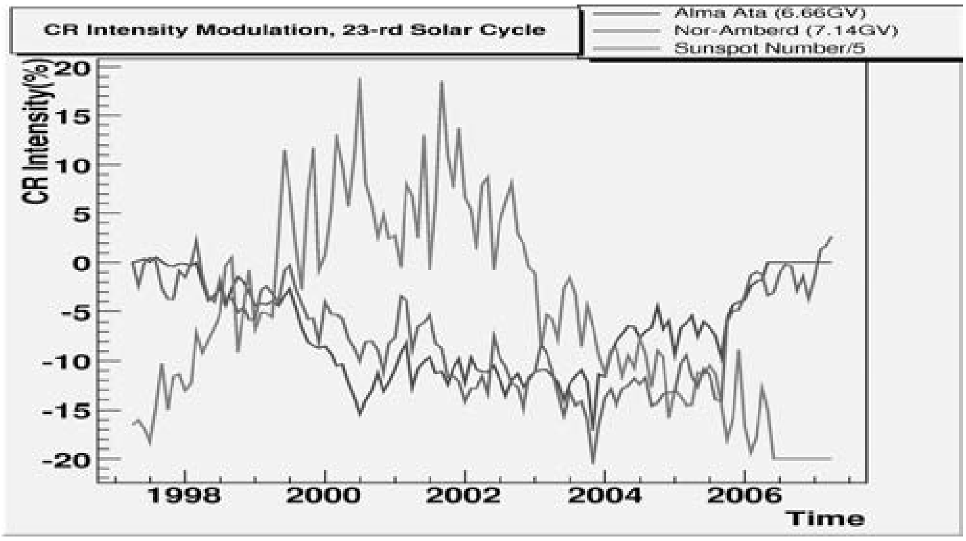

Figure 13. NANM, 23rd solar cycle – after filtering

.

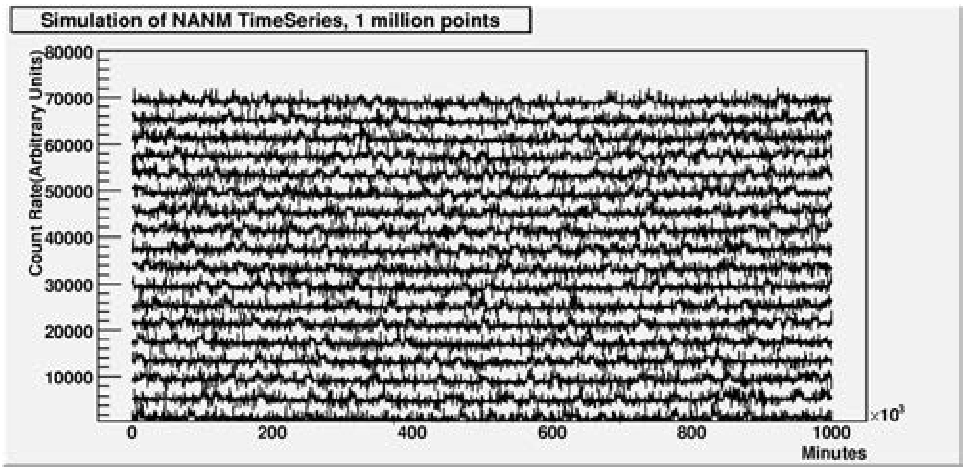

Figure 14. Simulated Time Series

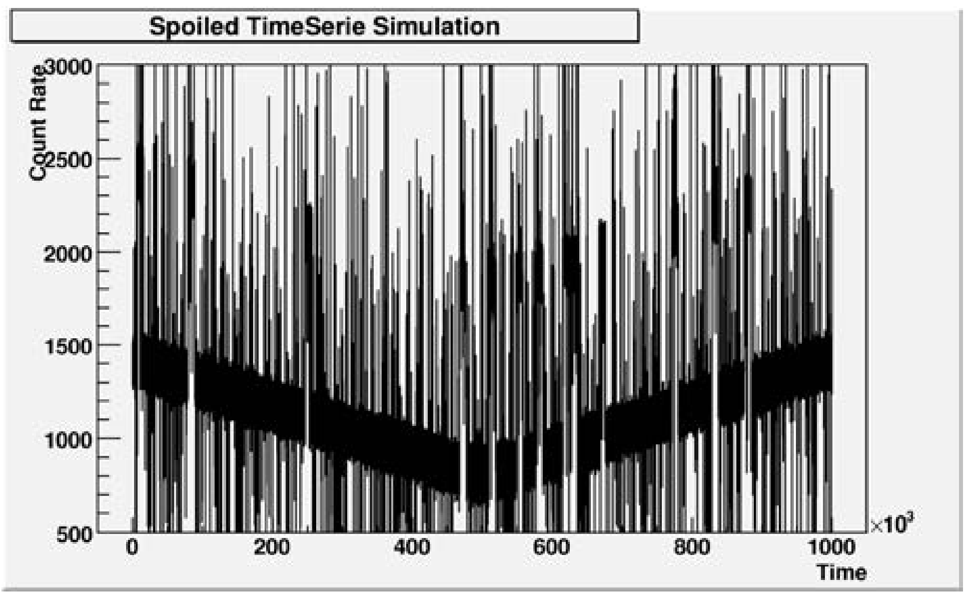

Figure 15. One of 18 simulated time series with modulation effect – before filtering

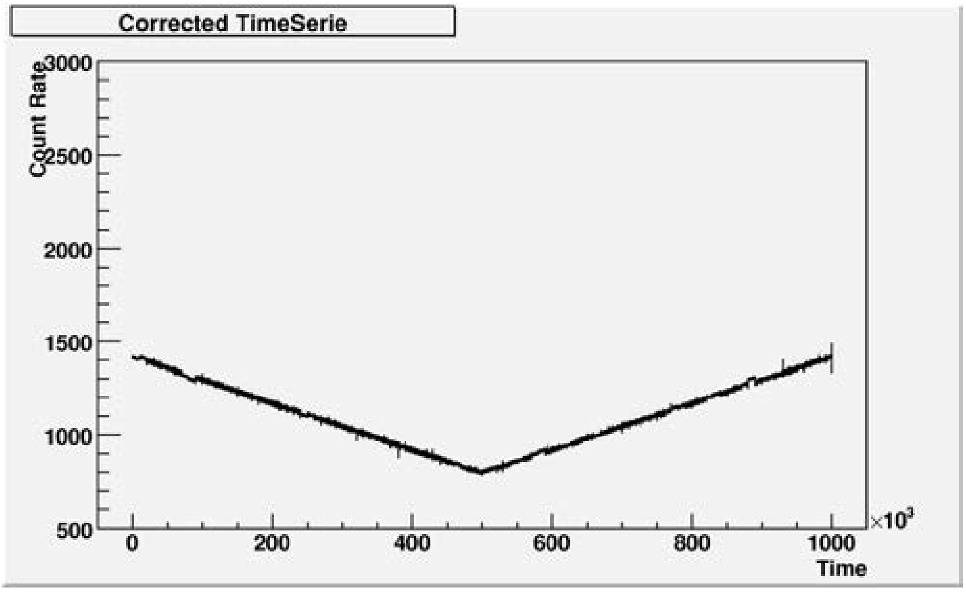

Figure 16. One of 18 simulated time series with modulation effect – after filtering

In Figures 10-11, we present correction algorithm operating according to equation (2). After finishing of its execution, the time series the MMF algorithm started operation. Although the variance of the filtered time series is larger comparing with initial ones, it corrects many mistakes apparent in the raw data (black – raw data, magenta – corrected).

In Figure 12 we present the Nor Amberd neutron monitor data as measured during 23rd solar cycle (1997-2007). Due to numerous failures of several detectors in the end of the cycle, there are significant biases in the count rate of monitor. Efficiency of several channels due to failures of high voltage supplies and aging effects of counters itself go down and overall count rate of monitor also go down.

As we can see in Figure 18 after applying filtering algorithms overall pattern of monitor count rate changes according the solar activity and comes very close to data of Alma-Ati Neutron Monitor located at altitude and latitude close to the Aragats ones.

6. VERIFICATION OF FILTERING ALGORITHMS

To check the suggested filtering techniques we perform simulation study with artificially corrupted time series. 18 time series with 1 million points have been simulated according to mean values and variances of the channels of Nor-Amberd Neutron Monitor. A trend has been introduced to time series to imitate solar modulation. Then all the 3 described types of failures were introduced in the time series (see Figure 15). In Figure 16 one can see that after correction with median algorithms all errors have been washed out and the solar “modulation” effect is apparently seen.

7. MONITORING OF THE STABILITY OF MEASURING CHANNELS

During multiyear operation of particle monitor’s mean count rates continuously alter not only by solar modulation or possible entering of regions where Galaxy arms are sending abundant GCR from supernovae explosions, but also by such prosaic effects as electronic components aging. Therefore, to identify instrumental failures and to avoid exploration of the artifacts instead of new physics we have to monitor carefully and continuously detector parameters.

In this paper, we present a simple method to do it by monitoring equalizing coefficients of monitor channels. The monthly (or decade) plots of coefficients will help to find unstable channels.

The channel mean count rates are changing due to solar modulation effects, in contrast, the equalizing coefficients (see section 3) should be stable despite changing means.

Therefore, it will be much easier to detect non-stable channels by monitoring the plots of coefficients, than changing channel means. Figures 17 and 18 are an example of our approach.

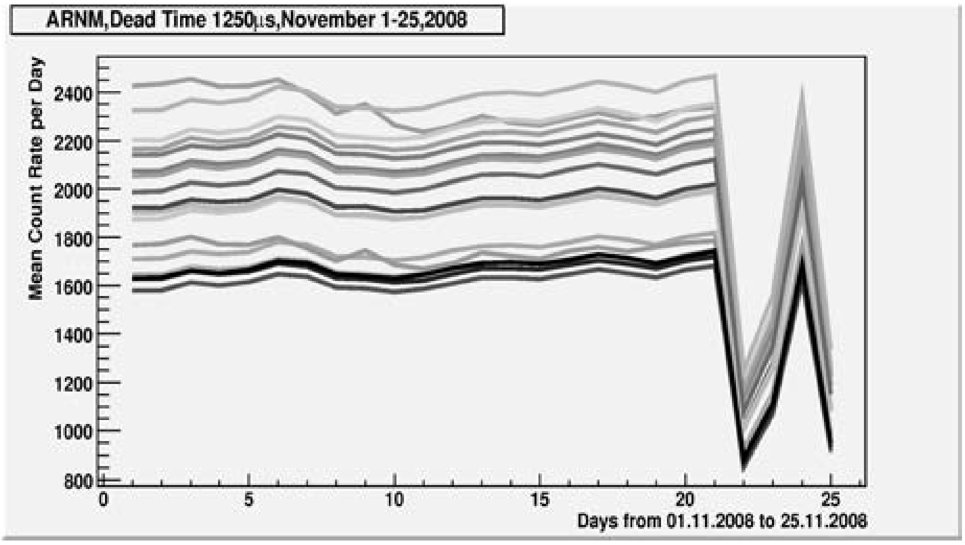

Figure 17. Day-to-day changes of the mean values of Aragats Neutron Monitor; at November 22 there were power supply cut

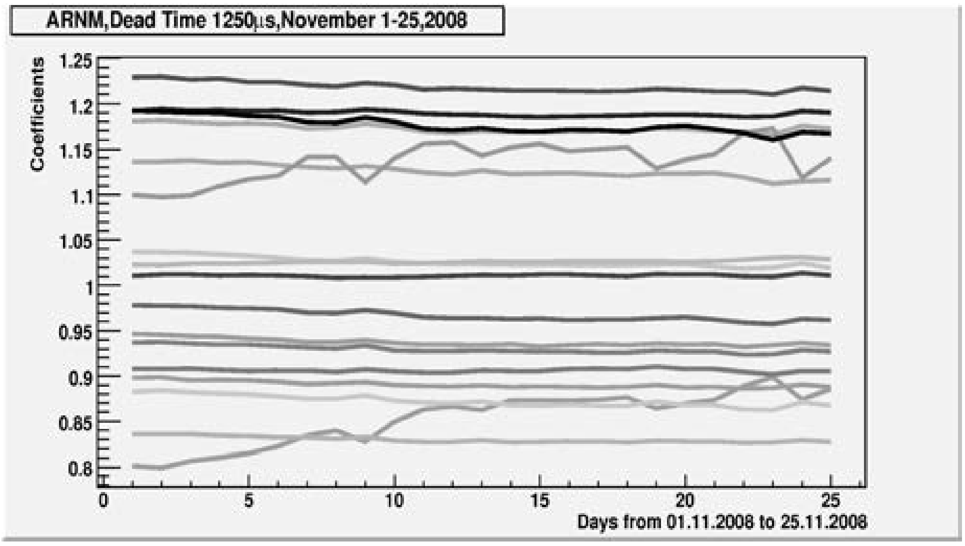

Figure 18. Day-today changes of the channel coefficients of Aragats Neutron Monitor

Although from Figure 17 we can notice that the variations of two channels are significantly larger than variations of the other 16, in Figure 18 the behavior of the corresponding coefficients demonstrate failure of two channels much more pronounced. The same method can be implemented to check data from numerous detectors. Several Eurasian countries joint the efforts to establish Neutron Monitor Data Base (NMDB, data available from the NMDB.eu). Data from numerous neutron monitors is gathered in NMDB and for the "housekeeping", it is necessary to run periodically tasks for checking if all monitors are adequate and data is correct and coherent. We select time series from several monitors participating in the NMDB project to run the "coherence" test (see Table 1).

Table 1 Neutron Monitors used in the "coherence" test

Neutron Monitor	Altitude,m	Rigidity, GV	Type
Alma Ata	3340	6.69	8NM64
Rome	60	6.32	7NM64
Aragats	3200	7.14	8NM64
Nor-Amberd	2000	7.14	8NM64
Moscow	200	2.46	4NM64
Oulu	0	0.81	9NM64
Athens	260	8.53	6NM64

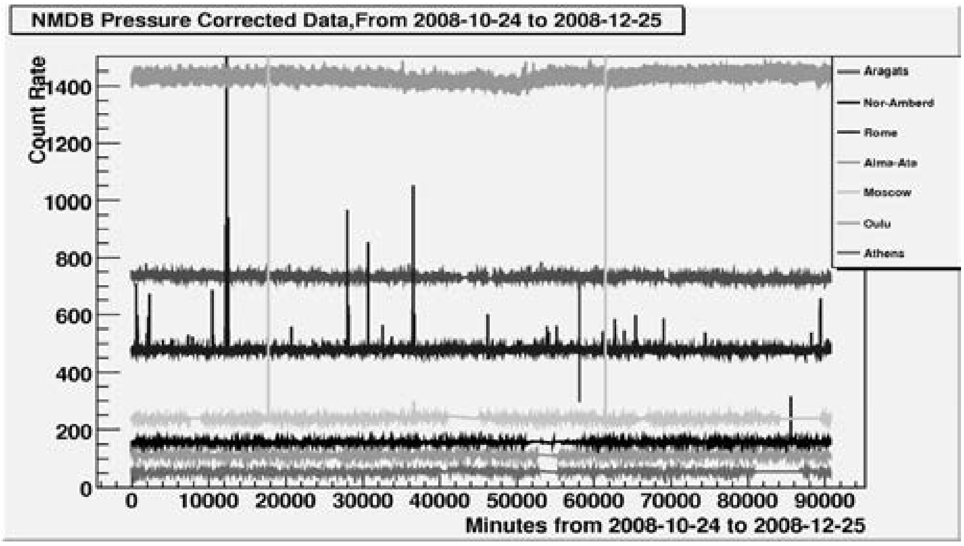

Figure 19 . Pressure Corrected Data from NMDB

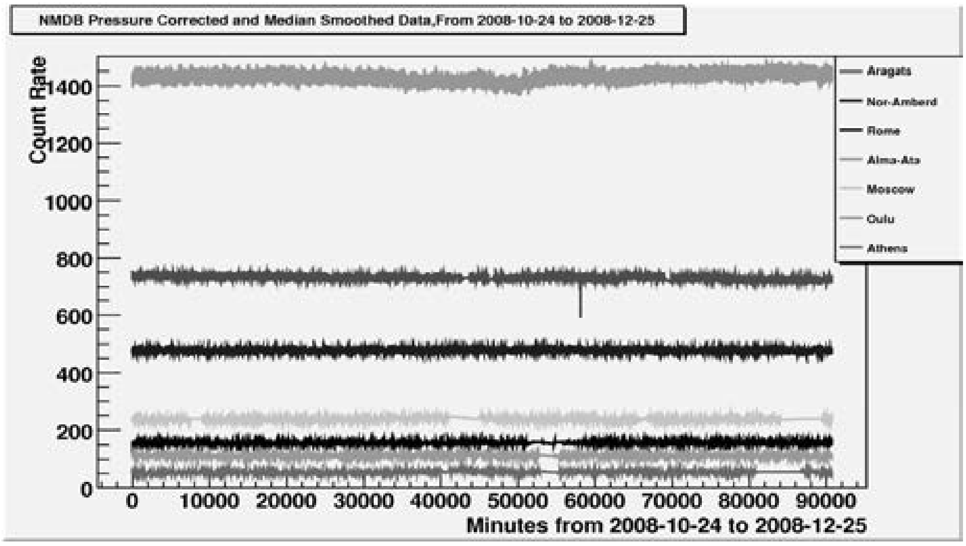

Figure 20. Pressure Corrected and Median Smoothed Data from NMDB

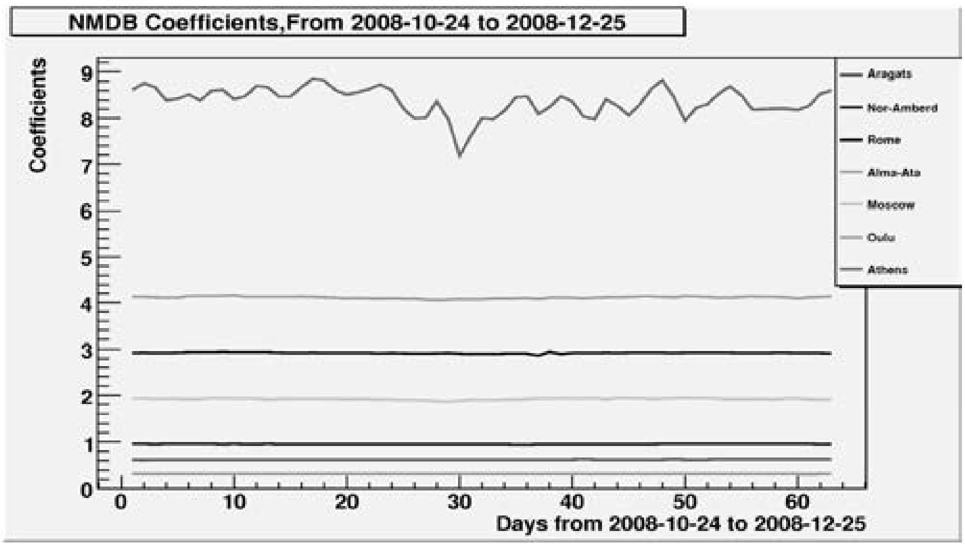

Figure 21. Equalizing coefficients of the NMDB facilities

We have taken pressure corrected data of these monitors for time period 24.10.2008-25.12.2008 and calculated coefficients for these seven time series, according to equations 1-3 . In Figure 19 the raw data are posted; in Figure 20 we present the median corrected, according to equation (3), data of NMDB Monitors (note, that the spikes in Nor Amberd and Izmiran monitors are filtered out and gaps are filled). In Figure 21 we present the "equalizing" coefficients for all the seven monitors calculated for each day of selected period. As you can see, 6 coefficients from 7 demonstrate very stable behavior, proving that all parameters of the neutron monitor chambers remain stable and constant. The calculated coefficients for the Athens monitor are much more variable. The high variability (non-coherence) of the Athens monitor's coefficient may be caused by drift of the electronics parameters (including pressure sensor) at the end of 2008. When dealing with multiple remote sensors it is of vital importance to develop a number of quality tests to check continuously the data coming from different remote destinations. Although the data from the NMDM network detectors are similar, different groups use different data acquisition electronics, pressure sensors and data transfer protocols. The time history of the "equalizing coefficients" is one of such tests to help keep NMDB data reliable and adequate for further physical inference.

8. CONCLUSION

Filtering of the multichannel data of particle detectors has operated for many years for the detection of the solar modulation effects and, maybe, sidereal modulation effects are of vital importance. During multiyear measurements, characteristics of detector undergo critical changes due to aging effects of sensors and discrete elements of electronics. Overabundance of the information allows introducing correction algorithms using stabilizing properties of the median of time series. Continuous storing and monitoring of the mean values of all channels along with their equalizing coefficient allows archiving the time-history of the behavior of all the channels. Examining the relative behavior of the channel means and coefficients during multiyear operation it became possible to distinguish the physical effects from instrumentation failures. See for example discussion in (Buetikofer & Flueckiger, 2008) and (Bieber et al., 2007). Also our approach allows not only the correction of mistakes due to hardware malfunction, but simple and efficient method of timely detection of non-stable channels or/and mistakes in data bases collecting time series from different remote detectors.

ACKNOWLEDGEMENT

We thank our colleagues from the Cosmic Ray (CRD) division of the Yerevan Physics Institute for the useful discussions on CRD seminars and colleagues from NMDB for posting and correcting data in NMDB.

Authors are grateful to the staff of Aragats and Nor Amberd research station for the uninterruptable operation of ASEC monitors. The work was supported by the grant RA610 and ISTC grantA-1554. The part of the research leading to these results has received funding from the European Community's Seventh Framework Programme (FP/2007-2013) under grant agreement no 213007.

REFERENCES

Buetikofer R., Flueckiger E.O., Long-term stability of Swiss neutron monitors. Private communication, 2008.

Belov A., Blokh Ya., Klepach E., et al. Primary Processing of Cosmic Ray Station Data: Algorithm, Computer Program and Realization. Kosmicheskie Luchi. 25, pp. 113-134, 1988 (in Rusian).

Bieber J. W., Clem J., Desilets D., Long-term decline of South Pole neutron rates. J. Geophys. Res., 112, A12102, doi:10.1029/2006JA011894 , 2007.

Chilingarian A., Reymers A., Particle detectors in Solar Physics and Space Weather research, Astroparticle Physics. Astropart. Phys., 27, pp 465-472 , 2007.

Chilingarian A., Avakyan K., Hovsepyan G., et al. Aragats Space-Environmental Center: Status and SEP Forecasting Possibilities. Journal of Physics G:Nucl.Part.Phys., 29 , pp 939-952, 2003.

Chilingarian A,, ,Babayan V., Arakelyan K., et al. Correlated Measurements of Secondary Cosmic Ray Fluxes by the Aragats Space- Environmental Center Monitors.NIM-A, 543, 483-496, 2005.

Chilingaryan S.,Chilingarian A., Danielyan V., et al. The Aragats data acquisition system for highly distributed particle detecting networks. Journal of Physics: Conference Series 119, 082001, 2008.

Clem J. M., Dorman L.,I. Neutron Monitor Response Function. Space Sci. Rev. 93, 335 -360, 2000.

Farage C., Pimbblet K. Evaluation of Cosmic Ray Rejection Algorithms on Single-Shot Exposures. Publications of the Astronomical Sociaty of Australia, 22, 249-256, 2005.

Data Visualisation Interactive Network for the Aragats Space-environmental Center

A. Chilingarian, A. Yeghikyan

Cosmic Ray Division, Alikhanyan Physics Institute, Alikhanyan Brothers 2, Yerevan 375036, Armenia
(e-mail: eghikyan@gmail.com)

Abstract: The ASEC (Aragats Space Environmental Center) facilities provide real time monitoring of cosmic particle fluxes with a number of particle detectors located at high-altitude research stations at Mt. Aragats, Armenia. To issue the warnings and alerts on sudden changing of the near-Earth radiation environments and for the detailed analysis of the most important solar modulation events we developed distributed data analysis interface with automatic data storage and processing. For the physical inference based on the changing particle fluxes the DVIN (Data Visualization Interactive Network) software was designed and implemented in the Cosmic Ray Division (CRD) of Yerevan Physics Institute. Data from ASEC monitors are accessible on-line from http://aragats.am/DVIN and currently is widely used in research of the solar physics and Space Weather. In the paper we illustrate how DVIN should be operated taking as an example the famous Halloween events of October 28 - November 2, 2003).

1. INTRODUCTION

Networks of particle detectors continuously monitor the changing fluxes of the particles reaching the Earth's surface. Charged and neutral particles are born in cascade processes initiated by protons and nuclei incident on the terrestrial atmosphere. Fast majority of these primaries are mostly from super-novae explosions in our galaxy (Galactic Cosmic Rays – GCR); GCRs travel tens of millions years and arrive to solar system as rather stable and isotropic population. Balloon and satellite facilities measure the GCR fluxes with rather high accuracy. Our nearest star, the sun, by disturbing interplanetary magnetic field and by accelerating protons and ions (producing so called Solar Cosmic Rays – SCR) is modulating the GCR flux, and as a result – the particle fluxes are measured by surface detectors. Among numerous sun modulation effects Ground Level Enhancements (GLE) is one of the most essentials, both from point of view of fundamental physics processes and the Space Weather effects.

The processes of particle acceleration in the Universe can be studied although on a much smaller scale, but much more detailed by measuring fluxes of protons and ions from solar accelerators. The satellite spectrometers due to tiny sizes can measure only huge fluxes of low energy particles; surface detectors are much larger, and they use atmosphere for the particle multiplication. Therefore, rather small highest energy fluxes of solar particles can be studied by measured secondary particle fluxes on the Earth surface.

The problem of revealing signal (for GLE detection signal is additional flux of secondary particles generated by the SCR) against an overwhelming background (the same particles generated by GCRs) is one of the most complicated, at least for particle detectors located at middle and low latitudes. We implement several data analysis procedures in DVIN for approaching this problem.

In addition to fundamental physics by measuring highest energy particles it will be possible to determine the spectra of the major solar event in progress. Hard spectra at highest energies will do manifest abundant SCR flux at low and medium energies and consequently radiation hazard to a crew of space stations, to space-born and surface industries. There is not much time for issuing warnings and alerts (15-45 minutes), therefore physical inference has to be made very fast. Physical analysis should invoke also data from space spectrometers and particle detectors from world-wide networks.

That's why DVIN is strategically important as a scientific application to help to develop space science and to foster global collaboration in solar physics and in space weather research. The system is highly interactive and exceptional information is easily accessible online. Data can be monitored and analyzed for desired time spans in a fast and reliable manner by the remote users world-wide.

2. PARTICLE DETECTORS OPERATING AT ASEC

The ASEC, (Chilingarian et al., 2003, 2005) consists of two high altitude stations on Mt. Aragats in Armenia and CRD headquarters in Yerevan. Geographic research stations located on slopes of mountain Aragats are: 40°30'N, 44°10'E. Cutoff rigidity: ~7.1 GV, altitude 3200m and 2000m; facilities in Yerevan are located at altitude ~1000 m. On these locations several monitors continuously measure the intensity of the cosmic ray fluxes and send data to the Internet in real time. The two *18NM-64 neutron monitors* (in operation at Nor-Amberd (2000m elevation), and at Aragats, (3200m elevation) research stations are the first particle detectors which started operation in 80-ths. The monitors are equipped with interface cards, providing time integration of counts from 1 second up to 1 minute. *The Aragats Solar Neutron Telescope (ASNT)* is in operation at the Aragats research station. The main detecting volume consists of four 1 m^2 surface, 60 cm thick scintillation blocks overviewed by photomultipliers type FEU-49 with 12 cm large photocathode.

The *Nor-Amberd Muon Multidirectional Monitor*, consists of two layers of plastic scintillators above and below two of the three sections of the Nor Amberd NM. The lead filter of the NM absorbs electrons and low energy muons. The threshold energy of the detected muons is estimated to be 250 MeV. The NAMMM consists of 6 up and 6 down scintillators, data acquisition system of the NAMMM can register all coincidences of detector signals from the upper and lower layers, thus, enabling measurements of the arrival of the muons from different directions.

In the underground hall, originally constructed for the ANI Cosmic Ray experiment 120 plastic scintillators are located with area of 1 m^2 each. The 6 m thick concrete blocks plus the 7 m soil filter the electrons and the low energy muons. Thus, only muons with energies > 5GeV reach the *Aragats Multichannel Muon Monitor*, comprised of 90 scintillators.

The *MAKET-ANI* surface array, consists of 92 particle density detectors formed from plastic scintillators with thickness of 5 cm. 16 of the 1 m2 continuously measure the count rates of low energy charged component of the secondary cosmic rays (energy threshold ~7 MeV).

The new world-wide particle detector network, named *SEVAN*, is under construction now in Armenia, Bulgaria, Croatia, Slovakia and India (Chilingarian & Reymers 2008, Chilingarian et al., 2008). 4 SEVAN detectors already operate on the slopes of Mt. Aragats at altitudes 3200, 2000, 1700 and 1000 meter and in Bulgaria and Croatia. SEVAN detectors also are measuring low energy charged particles, neutral particles (gammas and neutrons) and high energy muons.

Data from these particle detectors are automatically downloaded and stored in DVIN for joint analysis of data from ASEC monitors and SEVAN network. DVIN provides wide possibilities for sharing data and sending warnings and alerts to scientists world-wide, which have fundamental and practical interest in learning the space weather conditions.

DVIN gives an opportunity to remote groups to share the process of analyzing, exchange data analysis methods, prepare joint publications and maintain networks of particle detectors. DVIN gives users the set of online methods enabling physical interface from the time series of changing secondary particle fluxes.

3. OVERVIEW OF THE MAIN OPERATIONS

There are two main types of Operations so called moving and periodic operations.

The periodic and moving operations are calculated by 3 given values: the length of period, function type and offset. The difference between the moving and periodic operations is defined in the next portion of time series. In periodic operations the next portions are selected with the step given by the “Period” option and in the moving operations the step is always 1.

Periodic functions are as following:

- Average;
- Standard Deviation;
- Median;
- Linear Regression;
- Periodic re-binning (adding successive time series in larger time unit) of the initial time series

Periodic and moving operations provide a very flexible and powerful tool for the examination of the time series. User controls the time period, offset of period (start point of rebinning operation) and interpolation mode (within chosen time period) of time series. Using these options user can rebin (add) successive monitor counts for examining long time periods and reveal non-trivial structures in the time series. For example, adding initial (parent) 1-minute time series in 3 minute by the “Periodic sum operation” helps to discover the Ground Level Enhancement (GLE) detection on 20 January 2005 by the AMMM monitor (Bostanjyan et al., 2007, Chilinagarian, 2008), obscured by the large fluctuations of 1-minute time series. “Offset” option defines the particular grouping of initial time series. All the periodic operations have “Compatibility” option, leaving the number of elements in time series unchangeable. For example, if we interpolate 1 minute time series by hourly average, in each of 60 hourly minutes of transformed time series will be the same average value.

By subtracting one time series from another, user can obtain the residuals time series. By dividing obtained residuals to the variance (σ) we obtain the, so called, normalized residuals obeying the standard Gaussian law. By the time series of normalized residuals, we can select the outliers for the further analysis. The histograms of the residuals can be compared with standard Gaussian probability density function by χ^2 test. Large values of $\chi 2$ point on failures in detector channel operation. Therefore, the described operations modes of DVIN can be used for the check of detector channels.

After proving the “Gaussian” nature of the residuals, positive outliers are examined as candidates for the Ground Level Enhancement (GLE) events. Large positive deviations (greater than 3-4 σ values) pointed on the possible non-random character of the deviation from mean count rate, i.e. on the solar modulation effects.

4. SEARCH OF A GLE WITH AMMM DETECTOR DATA

The variety of the ASEC monitors “select” different populations of the primary energy spectra, due to different energy thresholds. Among ASEC monitors the Aragats Multidirectional Muon Monitor (AMMM) selects highest primary energies. Only muons with energy greater than 5 GeV can reach the detector location. The most probable energy of “parent” proton should be greater than 15 GeV to give birth to 5 GeV muon. These energies are extremely rare in SCR and if encounter lasting several minutes only. Therefore, in AMMM time series we look for very narrow peaks in coincidence with solar flares and GLEs detected by surface particle detectors sensitive to lower primary energies.

The 1- minute time series of the AMMM is presented in Figure 1. Enhancement of the count rate is seen at 11:12 - 11:14 UT. Unfortunately, 14 from 45 channels of the AMMM detector were not operational at the time, therefore only 31 m^2 of muon detectors were used to measure the high energy muon flux. The estimated mean count rate of the GCR, as measured by the 31 m^2 of the AMMM detector during the 10:40 – 11:40 UT time span, excluding the enhanced interval from 11:12 to 11:14 UT, was 92040 particles per minute.

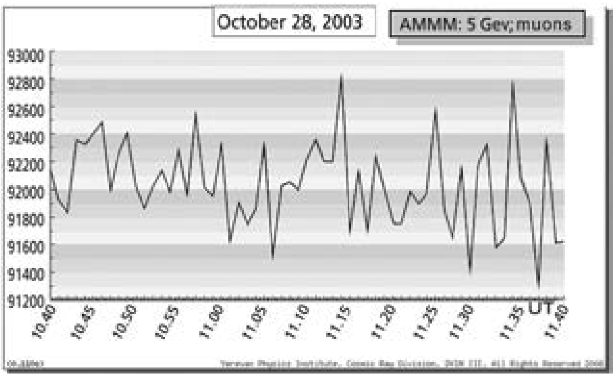

Figure 1. Minutely data of AMMM.

In the Table 1 are depicted the statistical parameters of one minute time series. To check significance of the GLE candidate we calculated standard Relative Mean Square Deviation (RMSD) of the AMMM at a time when there were no significant changes of detector count rates:

$$RMSD = \sqrt{\left(\frac{\sum_{i=1}^{i=N}(C_i - \bar{C})^2}{N-1}\right)} / \bar{C}, \; i = 1,60$$

Where Ci, are 1 minute count rates of the AMMM, $\bar{C}$ is hourly mean of the 1-minute count rates.

Table 1 Characteristics of the AMMM detection of GLE candidate (1 minute time series)

10:40-11:40 UT, October 28, 2003	Peak value	Hourly mean	MSD	RMSD	Number of σ
1min counts	92821	92040	315.45	0.34%	2.5

Maximal count rate during an hour of 10:40 – 11:40 is at 10:14 is – 92821. Therefore, we can calculate the enhancement (possible signal) as Δ = Peak value – Hourly mean =781. The relative enhancement $\Delta_r = \Delta / \bar{C}$ = 0.85%, correspondent to significance of $\sigma = \Delta_r$ / RMSD = 2.5.

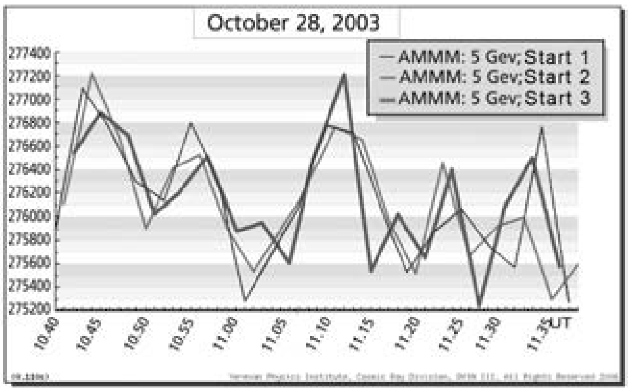

Figure 2. Three minutely time series corresponding to 3 different starts.

To emphasize the peak in the AMMM time series we group the 1 minute time series in the 3 minute time-intervals. In Figure 2 three different possibilities of regrouping of 1 minute time series in 3 are presented. All 3 demonstrate a slightly different temporal pattern of time series. The particular time series started from the second element (10:41) provide biggest peak.

For further calculation we remove the peak. To remove the peak we used "Up-Down Limit Cut" which replaces the points which are not located in the given range with Periodic Median. In Table 2 statistical parameters of the 3-minute time series are presented.

Table 2 Characteristics of the AMMM detection of GLE candidate (3 minute time series)

10:40-11:40 UT, October 28, 2003	Peak value	Hourly mean	MSD	RMSD	Number of σ
3 min counts	276620	275190	434	0.159 %	3.27

From the Table 2 we can calculate the significance of the 3 minute time series peak as we have done for the 1 minute time series. Nonetheless, the peaks of ~3.3 can occur several times a day occasionally without any noteworthy solar event. Therefore, we have to relate a detected peak with its possible trigger; i.e. a 4B/X17.2 solar flare located at S16 E08 that started ~ 11:01 with maximum at 11:10 UT. The earliest arriving particles were detected at Tsumeb, Namibia and Hermnus, South Africa (11:06 UT, Moraal et al, 2005); Cape Schmidt (11:14 UT) and Norilsk (11:14 UT, Miroshnichenko et al., 2005). The surplus of AMMM count rates can be related to primary protons with energy greater than 20 GeV. The fluxes of such great energies are very weak (and very short, we cannot expect duration greater than 3 minutes) and only relative large area of detector allows detecting weak signal. To be on the safe side, we can assume that protons of such energies can reach the Earth not later than 1 hour after the flaring process start and according to techniques described in (Chapman et.al., 2002, Chilinarian et al., 2006, Chilingarian, 2008) calculate the chance probability of obtaining random peak of 3.27σ within 1 hour. Because we made 3 attempts to obtain a highest peak, the total amount of attempts M will be 3 times 20 (number of 3-minute time series in one hour, M=60).

Calculated chance probability (see the techniques in Chilingarian, 2008) is equal to ~0.03; i.e. only once in 33 cases we can expect such an enhancement. Of course, if we assume more realistic maximal delay of an arrival of highest energy protons to 1 AU we will obtain much lower chance probability. However, in some sense arbitrary choice of the time delay and very weak fluxes of highest energies make further decrease of the delay dangerous for the quality of physical inference. Value of chance probability of 0.07 obtained in (Karapetyan, 2008) for the same event is due to different parameters used in calculations: 4 minute time series with maximal peak of 3.2σ and number of attempts M=100.

5. CORRELATION ANALYSIS

Correlation Analysis is a new tool for the physical inference on multiple time series. Different ASEC monitors are sensitive to different populations of the primary protons and ions. If Neutron Monitors are detecting neutrons generated by primary protons with energies just after cutoff rigidity, the 5 GeV muons are generated by >15 GeV protons. Furthermore, different channels of the Aragats Solar Neutron Telescope selected slightly different energy populations of primaries.

Therefore, measuring correlations between changing count rates of ASEC monitors we can get information about the energy spectra of the SCR, or about the nature of geomagnetic disturbance changing the actual value of the cutoff rigidity.

In Figure3 and Figure 4 the correlation matrices for two time periods, 29 October, 2003 are depicted which correspond to the very large Forbush decrease (correlations are very large, approaching ~1) and 3 May 2004, which corresponds to the calm phase of the Space Weather (no geomagnetic disturbances) there are no significant correlations detected.

6. DATA EXCHANGE BETWEEN USERS

Users of DVIN can interchange processed data and establish virtual collaboration. They interchange work areas using communication section. When a user gets data from another user, he can continue analyzing in the received work area or concatenate own work area with a new one. One can select other users from the list of DVIN users and selecting the list of available work-areas send him the processed data.

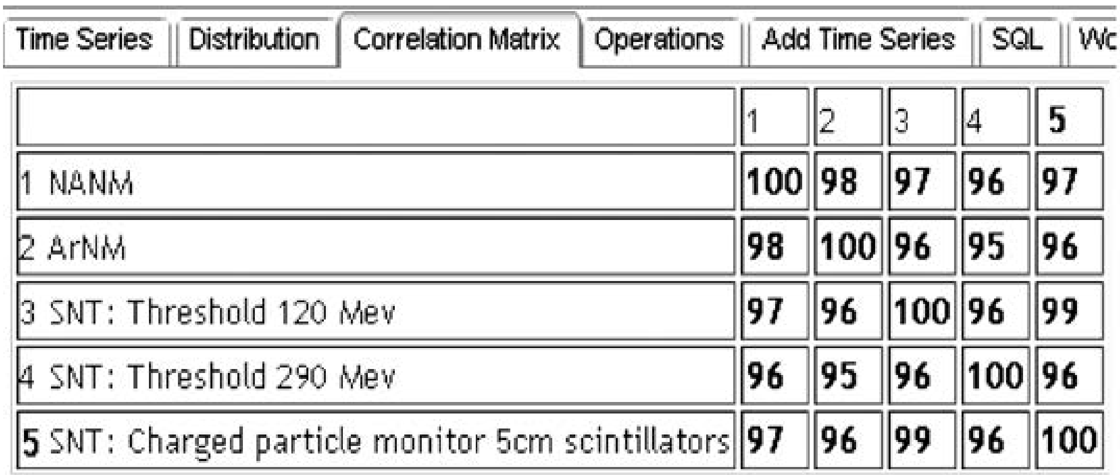

	1	2	3	4	5
1 NANM	100	98	97	96	97
2 ArNM	98	100	96	95	96
3 SNT: Threshold 120 Mev	97	96	100	96	99
4 SNT: Threshold 290 Mev	96	95	96	100	96
5 SNT: Charged particle monitor 5cm scintillators	97	96	99	96	100

Figure 3. Screenshot of correlation matrix of count rates of ASEC monitors at 29 October 2003, percents.

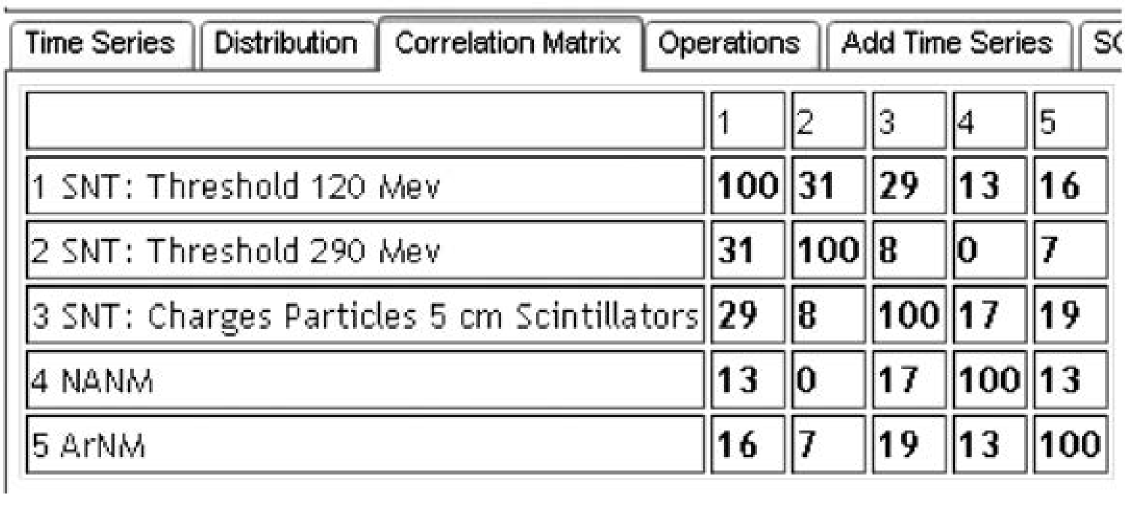

	1	2	3	4	5
1 SNT: Threshold 120 Mev	100	31	29	13	16
2 SNT: Threshold 290 Mev	31	100	8	0	7
3 SNT: Charges Particles 5 cm Scintillators	29	8	100	17	19
4 NANM	13	0	17	100	13
5 ArNM	16	7	19	13	100

Figure 4. Screenshot of correlation matrix of count rates of ASEC monitors at 3 May 2004, percents.

7. CONCLUSION

DVIN is the first online system developed in CRD allowing users to perform online collaborations not only on the level of information interchange but also on the level of physical analysis, using general interconnected platform. It allows scientists from different countries to exchange data, analysis methods and physical inferences.

ACKNOWLEDGMENT

We are grateful to Suren Chilingarian and Tigran Hovhannisyan for technical assistance, idea generation, ASEC members for stimulating interest and support, to Narine Khachatryan for improving quality of pictures and to Arthur Reymers and CRD students for reporting bugs in DVIN.

REFERENCES

Chapman, S.C., Rowlands, G., Watkins, N.W. Extremum statistics – a framework for data analysis. Nonlin. Process. Geophys. 9, 409–418, 2002

Chilingarian A., Avakyan K., Babayan V., et al. Aragats space-environmental centre: status and SEP forecasting possibilities. J. Phys. G: Nucl. Part. Phys. 29, 939–951, 2003

Chilingarian A., Arakelyan, K., Avakyan, K. et al. Correlated measurements of secondary cosmic ray fluxes by the Aragats Space-Environmental Center monitors. NIM, A 543, 483-292, 2005

Chilingarian A., Gharagyozyan, G., Karapetyan, G., Hovsepyan, G., Statistical methods for signal estimation of point sources of cosmic rays. Astropart. Phys. 25, 269–276, 2006

Eghikyan A.R. and Chilingarian A.A., Data Visualisation Interactive Network for Aragats Space Environmental Center, in the Proceedings of the Second International Symposium Solar Extreme Events, Nor Amberd, Armenia, 245-251, Yerevan, 2006

Chilingarian A. and Reymers A. Investigations of the response of hybrid particle detectors for the Space Environmental Viewing and Analysis Network (SEVAN). Ann. Geophys., 26, 249-257, 2008

Chilingarian A., Statistical study of the detection of solar protons of highest energies at 20 January 2005. J. Adv. Space Res., doi:10.1016/j.asr.2008.10.005, 2008

Chilingarian A., Hovsepyan G., Arakelyan K., et al., Space environmental viewing and analysis network (SEVAN). DOI: 10.1007/s11038-008-9288-1, 2009

Karapetyan G.G., Detection of high energy solar protons during ground level enhancements, Astropart. Phys. Doi:10.1016/j.astropartphys.2008.09.007, 2008

Miroshnichenko, L. I., K.-L. Klein, G. Trottet, P. Lantos, E. V. Vashenyuk, Y. V. Balabin, and B. B. Gvozdevsky. Relativistic nucleon and electron production in the 2003 October 28 solar event, *J. Geophys. Res.*, 110, A09S08, doi:10.1029/2004JA010936, 2005

Moraal H., McCracken K.G., Schoeman C.C., Stoker P.H., The Ground Level Enhancement of 20 January 2005 and 28 October 2003. 29th ICRC, Pune, 1, 101-103, 2005

List of Participants

Alaverdyan	Anna	Armenia	Alikhanyan Physics Institute	anna_alaverdyan@yerphi.am
Arakelyan	Karen	Armenia	Alikhanyan Physics Institute	karen@yerphi.am
Asatryan	Gagik	Armenia	Alikhanyan Physics Institute	gagik_asatryan@yerphi.am
Bostanjyan	Nikolay	Armenia	Alikhanyan Physics Institute	nikolai@yerphi.am
Carlson	Herbert	United Kingdom	EOARD	
Chilingarian	Ashot	Armenia	Alikhanyan Physics Institute	chili@aragats.am
Chilingarian	Suren	Armenia	Alikhanyan Physics Institute	Suren.Chilingarian@ipe.fzk.de
Gesayan	Lilit	Greece	University of Athens	dvornikov@iszf.irk.ru
Gopalswamy	Nat	United States	NASA GSFC	n_gopalswamy@yahoo.com
Ivanov	Vitali	Armenia	Alikhanyan Physics Institute	vitali@mail.yerphi.am
Hippler	Rainer	Germany	University of Greifswald	gavrilova.istc.ru
Hovsepyan	Gagik	Armenia	Alikhanyan Physics Institute	hgg@yerphi.am
Hovhannisyan	Armen	Armenia	Alikhanyan Physics Institute	harmen@yerphi.am
Karapetyan	Grigory	Armenia	Alikhanyan Physics Institute	gkarap@yerphi.am
Karapetyan	Tigran	Armenia	Alikhanyan Physics Institute	ktigran79@yerphi.am
Khachatryan	Narine	Armenia	Alikhanyan Physics Institute	narine_ khachatryan@yerphi.am
Korepanov	Valery	Ukraine	Lviv Centre of Institute of Space Research	lev@crd.yerphi.am
Kozliner	Lev	Armenia	Alikhanyan Physics Institute	lev@yerphi.am
Kudela	Karel	Slovakia	Institute of Experimental Physics	kkudela@kosice.upjs.sk
Lazutin	Leonid	Russia	SINP MSU	lll@srd.sinp.msu.ru
Lucas	Caro	Iran	University of Tehran	lucas@ipm.ir
Mailyan	Bagrat	Armenia	Alikhanyan Physics Institute	bagrat_mailyan@yerphi.am
Mamidjanyan	Erik	Armenia	Alikhanyan Physics Institute	nasc@web.am
Maricic	Darije	Croatia	Astronomical Observatory Zagreb	darije.maricic@zg.htnet.hr
Parsapoor	Mahboobeh	Iran	Islamic Azad university Science and Research Branch,Tehran, Iran	marjin@taspd.sinp.msu
Peroomian	Vahe	USA	UCLA	vahe@igpp.ucla.edu
Petrosyan	Vahe	USA	Stanford University	vahe@astronomy.stanford.edu
Reymers	Arthur	Armenia	Alikhanyan Physics Institute	artur@yerphi.am
Rosa	Dragan	Croatia	Astronomical Observatory Zagreb	drosa@hpd.botanic.hr
Rushanyan	Geim	Armenia	Alikhanyan Physics Institute	geim@yerphi.am
Spilantini	Pierro	Italy	Scientific Attache of Italian embassy in Russia.	spillantini@fi.infn.it
Stozhkov	Yuri	Russia	Lebedev Physical Institute	stozhkov@ian.fiandns.mipt.ru
Tserunyan	Sargis	Armenia	Alikhanyan Physics Institute	sargis@yerphi.am
Taroyan	Youra	United Kingdom	University of Sheffield, UK, Post Doctoral Research Fellow Department of Applied Mathematics	y.taroyan@sheffield.ac.uk
Yeremian	Anahid	USA	SLAC	anahid1@sonic.net
Zazyan	Mary	Armenia	Alikhanyan Physics Institute	mary@mail.yerphi.am

The International Workshop: “Forecasting of Radiation and Geomagnetic Storms by networks of particle detectors” (FORGES-2008) was held from 29 September to 3 October, 2008 in the International Conference Center in Nor Amberd, Armenia, 40 km from Armenia's capital Yerevan. The foci of the meeting were the drivers of space weather and the possibility that the networks of particle detectors by measure flux changes of neutral and charged particles can provide warning of impending severe radiation and geomagnetic storms. Some 40 scientists and students from Germany, Italy, Great Britain, Croatia, Greece, Ukraine, Russia, USA, Costa-Rica and Armenia listened to eight invited lectures and 25 original papers. Modern society depends heavily on a variety of technologies that are susceptible to the extremes of space weather—severe disturbances of the upper atmosphere and of the near-Earth space environment that are driven by the magnetic activity of the Sun. The charged-particle radiation and geomagnetic storm can degrade GPS navigation, disrupt radio communications, and trigger continent-wide blackouts lasting hours and days. That's why the forecast space weather storms are of upmost importance. The surface particle detectors can be compatible to excellent measuring facilities located on a fleet of spacecraft around the Earth and in the interplanetary space. Ground based particle detectors measure time series of secondary particles born in cascades originating in the atmosphere by protons and ions accelerated in the Galaxy and in vicinity of Sun. The networks of particle detectors can predict upcoming geomagnetic storms hours before the arrival of Interplanetary Coronal Mass Ejections (ICMEs) at the ACE and SOHO spacecraft. The less than one hour lead time (the time it takes for the ICME to travel from the spacecraft to the magnetosphere) provided by measurements made at ACE and SOHO is too brief to take effective mitigating actions to protect satellites and surface industries from the harm of major geomagnetic storms.